The dynamical evolution of massive black hole triplets in stellar systems

Thesis submitted in accordance with the requirements of the University of Liverpool for the degree of Doctor in Philosophy by

Xiuming Xu

School of Mathematics and Physics
Xi'an Jiaotong-Liverpool University
Saturday 22$^{\mathrm{nd}}$ July, 2023

Declaration

This work has not been submitted in substance for any other degree or award at this or any other university or place of learning, nor is being submitted concurrently in candidature for any degree or other award. This thesis is being submitted in partial fulfilment of the requirements for the degree of PhD. This thesis is the result of my own independent work/investigation, except where otherwise stated. Other sources are acknowledged by explicit references. The views expressed are my own. I hereby give consent for my thesis, if accepted, to be available for photocopying and for inter-library loan, and for the title and summary to be available for outside organizations.

Abstract

Observational studies suggest that supermassive black holes (SMBH) are located in the centers of galaxies. When two galaxies merge, their SMBHs migrate toward each due to dynamical friction. Similarly, some massive star clusters may host intermediate-mass black holes (IMBHs). When such clusters merge, their IMBHs also migrate toward the center of the merged cluster. After arriving in the center, the two black holes (BHs) form a tight binary system. When sufficiently tight, gravitational wave emission may lead to a BH-BH merger. This process is time-consuming, so it is possible that a tertiary BH will join the center of the merger system, resulting in strong gravitational three-body interactions. However, the influence of a massive tertiary BH on the gravitational-wave merger timescale of the progenitor binary in a stellar environment is still unknown, and the aim of this thesis is to investigate this situation. We first investigate the dynamical evolution of SMBH triplets with different mass ratios in galaxy centers. We analyze the effect of a tertiary SMBH on the gravitational wave merger timescale of a binary SMBH after galaxy mergers. We find that a tertiary SMBH can shorten the merger timescale of a progenitor binary SMBH up to several orders of magnitude via two mechanisms: the tertiary SMBH drives the binary SMBH's eccentricity up via chaotic binary-single interactions. The triplet may also form a hierarchical triple system and increase the binary SMBH's hardening rate. We subsequently investigate the dynamical evolution of IMBH triples with different mass ratios in the centers of realistic star clusters and analyze the effect of a tertiary IMBH on the gravitational wave merger timescale of a binary IMBH in a star cluster. We find that a tertiary IMBH does not necessarily shorten the merger timescale of binary IMBH due to the often rapid ejection of the tertiary IMBH. Finally, we investigate the dynamical evolution of equal-mass IMBH triplets in rotating star clusters with different global properties. We analyze the effect of a tertiary IMBH on the merger timescale of a binary IMBH and how it varies with the degree of cluster rotation and central concentration. We find that the presence of a tertiary IMBH can greatly shorten the semi-major axis of the binary IMBH in clusters with equal-mass stars, but it is not the case in clusters with an IMF. The hardening rate of a binary IMBH increases with central concentration but decreases with increasing cluster rotation. The presence of a tertiary IMBH does not necessarily shorten the merger timescale of binary IMBH due to the stochastic nature of the eccentricity of the binary IMBH.

大质量三黑洞系统在天体系统中的动力学演化

摘要

超大质量黑洞和中等质量黑洞已经被观测发现处在不同天体系统的中心，其中包括星系和不同种类的星团。星系之间和星团之间的合并过程已经被观测结果所确认。与之同时，在这些系统中的超大质量黑洞和中等质量黑洞也会形成一个稳定的双体系统并最终合并为一个超大质量黑洞。但这个合并过程极其的漫长，使得两个系统合并的时候几乎不可避免地导致会有第三个系统加入这个合并过程，在这个合并过程中会形成一个三体黑洞系统。为了探究第三个黑洞对于之前形成的双黑洞系统的合并过程的影响，我们有必要研究在星团和星系中的大质量黑洞的演化过程。本课题呈现了不同质量的第三个黑洞对于在不同环境下不同质量双黑洞系统的合并过程的影响。我们首先研究了在星系中心的不同质量的三体超大质量黑洞系统的演化过程。通过对于双黑洞系统的引力波合并时间的计算，我们可以得出以下结论：第三个超大质量黑洞至多能够缩短双黑洞合并时间到原时间的$1/10^7$. 第三个超大质量黑洞可以通过与双黑洞系统的随机的交换，以及与双黑洞系统稳定的绑定来缩短双黑洞系统的合并时间。之后我们研究了在星团内第三个中等质量黑洞对于双中等质量系统的合并时间影响。我们发现由于在星团中第三个中等质量黑洞很容易逃逸，所以第三个中等质量黑洞对于双中等质量黑洞的合并时间没有显著影响。在这之后我们探究了在旋转星团内第三个中等质量黑洞对于双中等质量黑洞系统的合并时间影响，并探究了不同的旋转星团性质对于合并事件的影响。我们发现在等质量星团中，第三个中等质量黑洞可以显著缩短双中等质量黑洞系统的轨道半长轴，但在加入初始质量函数后第三个中等质量黑洞没有显著效果。星团的中心密度越大，旋转的速度越低，轨道缩减越明显。但由于双中等质量黑洞系统的离心率变化是混沌的，所以第三个中等质量对于合并时间的影响并不显著。

Acknowledgements

I would like to thank KaiBo Mao, who is currently a civil servant in the Bureau of Statistics. Comprehensive discussion with her greatly strengthen my confidence in finishing this Ph.D degree study. I would also like to thank Renjie Cui, who introduce me to KaiBo Mao.

I would like to thank my supervisor, Thijs Kouwenhoven, and our collaborator, Rainer Spurzem, Peter Berczik, and Hao wei for their fruitful discussion during the teeminar. Hao wei provided me with his talent and passion in coding.

I would also like to thank my colleagues in MB319 and MB321, especially Kai Wu. Discussion with them makes me feel less stressful.

I would like to thank my parents for their nurture, precepts and deeds during the past 29 years.

I would like to thank Min Zhao, a friend of mine, for her hospitality during my academic visit to Beijing in 2019. Discussion with her deepen my understanding of balance between teaching and academic research.

I would like to thank Shu qi, for his hospitality during the academic visit to Beijing in 2019.

I would like to thank Yanren Chen and his wife, Tianyu Yang, for their hospitality treatment during the COVID-19 pandemic.

I would like to thank sihan Wan and sijin Li, for their inspiration on my teaching duty.

Last but not least, I would like to thank Xiaojun Zhu and Zhehao Zhang, for their invaluable inspiration.

Contents

List of Figures

List of Tables

Chapter 1

Introduction

This thesis discusses the dynamical evolution of massive black hole (MBH) triplets in three types dense stellar systems. The three scenarios are galactic centers, non-rotating star clusters, and rotating globular clusters. The concept of MBH refers to supermassive black holes (SMBHs) and intermediate-mass black holes (IMBHs). The main goal of this thesis is to investigate the effect of a tertiary MBH on the gravitational wave merger timescale of an MBH binary in different stellar environments.

1.1 Supermassive black holes

The concept of a black hole originates from Newton's classical description of light as particles. If the light is composed of microscopic particles, then light can be slowed down by gravitational forces. If the body's surface gravity is so huge that even light can only circulate it, then this body was considered as a "dark star," which we can not observe directly (de Laplace & Harte 1830, Michell 1784). The concept of a "dark star" was far beyond the recognition of scientists in that era, so it is more of a theoretical prediction than a solidified proof. The modern idea of a black hole arose from the theory of general relativity (Einstein 1916a). After establishing the theory of general relativity, Karl Schwarzschild solved Einstein's field equation under the assumption of spherical symmetry, no net charge, and no spin. The so-called Schwarzschild solution describes an astronomical body with slow rotation. Schwarzschild black hole is a derivative of Schwarzschild solution (Penrose 1996).

There are several solutions to Einstein's Field Equations. The simplest solution is the "Schwarzschild solution," describing the space-time around a spherical body with zero spin and electric charge (Schwarzschild 1999). If the spherical body contains electric charge and no spin, then the Schwarzschild solution expands to Reissner-Nordström solution (Nordström 1918, Reissner 1916). A more realistic solution for astronomical observation was proposed by Kerr (1963), describing the space-time geometry around a spherical body with net spin and no electric charge. Ezra Newman and Roy Kerr provided a complete solution describing a spherical body with net electric charge and spin in 1965 (Newman et al. 1965).

A quasar is an astronomical object with a very high luminosity, even higher than its host galaxy. The enormous luminosity of quasars required explanation. Lynden-Bell (1969) proposed the idea of a supermassive black hole (SMBH), stating that a quasar is powered by gas and stars accreted to SMBHs. This theory has been widely accepted as the reason for radiation and emission from active galactic nuclei (AGNs). SMBHs are believed to reside in the centers of almost all the galaxies (Kormendy & Richstone 1995). A confirmed SMBH detection that lies at the center of the Milky Way with a mass of about $4 \cdot 10^6 \mathrm{M}_\odot$ has proven this hypothesis (Genzel, Eisenhauer, & Gillessen 2010, Ghez et al. 2008).

1.2 Galaxy mergers

The idea of galaxy merger comes from the book of Halton Arp named *Atlas of Peculiar Galaxies* (Arp 1966). Initially, it was believed that irregular galaxies described in this book were exploding, but it became clear later that these are signatures of galaxy mergers. Most galaxy mergers are hard to detect due to their large distance from Earth, so studying nearby galaxy mergers became very important. Our Milky Way is known to migrate towards Andromeda. The merger timescale of these two galaxies was estimated by van der Marel et al. (2019), measuring the proper motion of Andromeda. The study concluded that the merger timescale is about 4.5 Gyr, comparable to the earlier estimate by Kahn & Woltjer (1959). But the time required for the two galaxies to complete the merger process is still under debate, because of the uncertainty of proper motion and their masses (Schiavi et al. 2020).

1.3 Intermediate-mass black holes

Black holes in the mass range between 10^2 and 10^5 $\mathrm{M}_\odot$ are known as intermediate-mass black holes (IMBHs). Observations have shown that supermassive black holes (SMBHs) and stellar-mass black holes (SBHs) are common throughout the Universe (Abbott et al. 2019, Casares 2007, Kormendy & Ho 2013, Sahu et al. 2022). However, detecting and confirming intermediate-mass black holes (IMBHs) is significantly more challenging, and only a handful of candidates have been reported (see Greene, Strader, & Ho 2020).

1.4 Globular clusters

A globular cluster is defined as a self-gravitating system with $10^4 - 10^7$ stars. Usually, their stellar density profile is high (with a density $\geq 10^4$ $\mathrm{M}_\odot$ pc^{-3} in the cluster core). With such a high core stellar density, the core of a globular cluster becomes an ideal place for studying collisions and gravitational interactions between stars (Sigurdsson & Phinney 1993).

Globular clusters are commonly believed to form in an environment with relatively high interstellar medium density (Elmegreen & Efremov 1997). Early studies suggest that globular clusters can be treated as a system with a simple stellar population, with only their mass being different (Bruzual A. 2010a). However, other studies suggest that a global initial mass function (IMF) may not exist (Bruzual A. 2010b). The first reported discovery of a globular cluster was found by Abraham Ihle in 1665 (Wilson 2003). Our Milky way is believed to host ~ 160 globular clusters, with ~ 20 globular cluster remains undiscovered (Ashman & Zepf 1992). In the past, globular clusters are believed to be non-rotating, spherical systems. However, the utilization of advanced detectors, such as Gaia, and modern data processing tools have proven that classically non-rotating globular clusters are indeed rotating, allowing the revelation of global rotation and individual star motion (Vasiliev 2019).

1.5 Gravitational waves

The original idea of gravitational wave described by Albert Einstein was analogous to the electromagnetic wave that is described by Maxwell's equations of electromagnetic fields. Although the idea and Einstein's publication in 1916 are now considered the Rosetta Stone of gravitational wave astronomy (Einstein 1916b), the existence of gravitational waves was a long-term debate that lasted for multiple decades. The concept of gravitational waves was initially considered as a by-product of mathematical derivations with no corresponding physical phenomena (Cervantes-Cota, Galindo-Uribarri, & Smoot 2016). However, the first indirect detection of gravitational waves provided by Hulse & Taylor (1975) provided preliminary proof of the existence of gravitational waves. Abbott et al. (2016) confirmed the existence of gravitational waves and brought the field of gravitational wave astronomy into a new era. The merger of two MBHs can create gravitational wave events that can be detected. However, in realistic scenarios such as galaxy and globular cluster mergers, the binary MBH system does not evolve in isolation but interacts with surrounding stellar population.

.

1.6 Research Questions to be answered

Owing to the long duration of the binary MBH merger process, a tertiary MBH with comparable mass may intrude and affect the merge process via complex three-body interaction. The effect of a tertiary MBH on the merge timescale of a binary MBH system has been investigated extensively. However, the effect of a tertiary MBH on the merger process of a binary MBH embedded in a stellar population is a topic that has not been studied in detail. This thesis aims to discover how a tertiary MBH affects the hardening of a binary MBH embedded in different stellar systems.

There are many questions that require further investigation. How does a triple SMBH system evolve? If a tertiary SMBH arrives, how does it affect the evolution of the progenitor SMBH binary? How does a tertiary IMBH affect the evolution of pre-existing IMBH binary in a realistic merged cluster, and how does the cluster affect the properties of IMBH? How does a tertiary IMBH affect the evolution of pre-existing binary IMBH in a rotating star cluster? And how does the triple IMBH system affect the global properties of the host cluster?

This thesis aims to answer these questions, and is organized as follows:

- Chapter 2 provides a comprehensive overview of the relevant literature within the scope and context of our study. The numerical methods for our study are also described.
- Chapter 3 investigates the effect of a tertiary SMBH with different mass ratios on the gravitational wave merger timescale of a binary SMBH system with different masses ratios in galactic centers.
- Chapter 4 investigates the effect of a tertiary IMBH with different mass ratios on the gravitational wave merger timescale of a binary IMBH with different mass ratios in

globular clusters, with an IMF, stellar evolution, and a tidal field incorporated. The global properties of host clusters were also investigated, as well as the correlation between the cluster properties and IMBH properties.

- Chapter 5 investigates the dynamical evolution of equal-mass IMBH triplets in rotating star clusters with different central concentrations and degrees of rotation, along with the global properties of host clusters.
- Chapter 6, we present our conclusions and discuss potential future projects.

Chapter 2

Literature review

2.1 Supermassive black holes

2.1.1 Mass of SMBHs

The mass of an SMBH can in principle be derived from the Eddington luminosity, which can be obtained by equating the gravitational attraction on electrons and protons to the radiation pressure arising from Thompson scattering. If we assume spherical, non-rotating accretion onto an SMBH, then the Eddington luminosity is

$$L_{\mathrm{eddington}} = \frac{4\pi G M m_{\mathrm{p}} c}{\sigma_{\mathrm{T}}} = 1.51 \times 10^{39} \frac{M}{10^8 M_{\odot}}\ W \quad .$$

Here, G is the gravitational constant, M is the mass of the black hole, m_{p} is the proton mass, and the σ_{T} is the cross-section for Thompson scattering. With the luminosity of an object measured, its theoretical mass can be determined. The observation of quasars with a redshift $z \sim 6$ showed the evidence for the existence of SMBHs with mass up to $10^9 \mathrm{M}_{\odot}$ (Fan 2006).

2.1.2 Formation of SMBHs

Contrary to the confirmed existence of SMBH, the mechanism of SMBH formation remains elusive. Most SMBHs reside in the center of galaxies and grow over time through gas accretion. The surrounding gas spirals in and forms an accretion disc. If the SMBH has a net spin, then a relativistic jet may form from the interaction between the surrounding plasma and the SMBH. But the SMBH located in the center of the Milky Way hardly accretes any surrounding material, leading to no existing relativistic jet. The jet from an SMBH may disturb the surrounding gas and empty the gas supply (Silk & Rees 1998). Supernovae can also suppress the growth of SMBH via a similar negative feedback mechanism. With the exception of mergers with stellar-mass objects, SMBHs require gas accretion to increase in mass, but supernovae may drive the gas disc away with a speed of ≈ 200 km/s, leaving little gas in the center, and thus hindering the growth of an SMBH (Dubois et al. 2015). In addition to the mechanisms mentioned above, The ejection of an SMBH from a galaxy center may also be a hurdle to the growth of SMBH. The shallow potential well of a dwarf galaxy may allow an SMBH to wander around in a dwarf galaxy (Bellovary et al. 2019), or get ejected from the galaxy center via relativistic kicks from the GW emission of a binary SMBH merger (Gualandris & Merritt 2008) or complex three-body interactions (Valtonen et al. 1994).

2.2 SMBH mass measurements

The mass of SMBH can be determined using four approaches, as outlined below

2.2.1 Stellar dynamical approach

The first method is to measure the orbital motion of surrounding stars. The mass of the central SMBH can be determined by estimating the orbital parameters of its surrounding stellar population. The mass of Sagittarius A* (Sgr*) in the center of our Milky Way is measured by determining the orbital parameters of a surrounding star named S2. The precise mass of Sgr* is $4.14 \pm 0.06 \cdot 10^6 \mathrm{M}_\odot$ (Ghez et al. 2008). This method is the most accurate method, but the limitation is obvious: it can only be used for our Sgr* A, because of its proximity. To measure the mass of other SMBH in distant galaxies, other methods must be applied.

2.2.2 Reverberating mapping

Another alternative method is Reverberation mapping. This technique is essentially measuring the lag between radiation variation from surrounding region (Cackett, Bentz, & Kara 2021, Peterson 1993). This method relies on three assumptions:

- Broad emission line region (BLR) come from a source that can be treated as a point source.
- The relation between ionized flux and observed flux can be described by a simple function.
- The light-travel time is much longer than the gas recombination timescale.

If we assume a time delay t_d between the emission line and continuum emission, then the size of BLR is $R_\mathrm{BLR} = ct_\mathrm{d}$, where c is the speed of light. The BLR size r can be used to measure the mass of SMBH with velocity dispersion σ, where σ is the root-mean-square velocity of the gas around the SMBH in the broad line emission region. The mass of SMBH is $M = r\sigma^2/G$. From this point of view, the mass of SMBH can be rewritten as:

$$M = fct_\mathrm{d}\sigma^2/G, \tag{2.1}$$

where the f is a factor that accounts for the geometry of the BLR source (Peterson & Wandel 1999). But this method may result in underestimation of the SMBH mass in high Eddington-rate source because of the ignoring of radiation pressure.

2.2.3 Photoionization modeling

The idea of photonionization modeling is to manufacture emission line intensity by changing model parameters to suit the observations. This model requires knowledge of three parameters:

- the geometry of the ionized emission-line cloud
- the chemical composition of the gas
- the distance between the central source and the cloud

The thickness of the cloud is also important when considering emission by a hard X-ray continuum (Davidson & Netzer 1979).

According to Ferland & Mushotzky (1982), The photonionization modeling is specified by the geometry of the ionized emission-line cloud, the chemical composition of the gas, the distance between the central source and the cloud, and the ratio of ionized photon density to the particle density U: The ionization parameter is defined as:

$$U = \frac{q}{4\pi R^2 nc}, \tag{2.2}$$

where q is the rate of ionized photon produced, R is the distance from the emission line gas cloud, and n is the particle density. Dietrich et al. (2002), Vanden Berk et al. (2004) states that the ratio U and particle density n are roughly the same for all AGNs. If we assume the luminosity L is proportional to the ionization photon production rate q, then it is obvious that $R \propto \sqrt{L}$. This relation allows interpretation of BLR size r via measuring the luminosity L. This relation allows the interpretation of the Broad emission Line Region (BLR) region from luminosity L although it is too simplified for BLR. This R-L relation is only well calibrated for Hβ line emission, but Kaspi et al. (2007) extend this method to CIλ1549 and UV continuum. Laor (1998) and Wandel, Peterson, & Malkan (1999) were the pioneer studies in applying this method to measure the mass of SMBH. But some other observations, such as those of Kollmeier et al. (2006), McLure & Jarvis (2002), Vestergaard (2002, 2004), Vestergaard & Peterson (2006), extend this method to ultraviolet emission lines MgIIλ2798 and CIVλ1549.

2.2.4 Radio interferometry

The successful measurement of SMBH mass in the M87 galaxy brings a newly proposed method to a practical application using high-resolution radio interferometry. The essence of this method is to observe the edge of the region where photons pass through the event horizon of the SMBH and get plunged into the SMBH. The region where photon does not emit but orbit around SMBH is called the photon sphere, and the size of this region is called photon capture radius R_c. For a non-rotating black hole, the $R_\mathrm{c} = 1.5R_\mathrm{s}$, where R_s is the Schwarzschild radius of the SMBH. The observed size of SMBH from an infinite distance called R_inf is:

$$R_\mathrm{inf} = R_\mathrm{c}\left(1 - \frac{R_\mathrm{s}}{R_\mathrm{c}}\right). \tag{2.3}$$

After simplification, R_inf is $= 3\sqrt{3}R_\mathrm{s}/2$ (Schwarzschild 1999). For a rotating black hole, the photon capture radius depends on the shape of black hole and its spin vector. The rotation of SMBH may result in the photons' geodesic orbiting around SMBH and emitting radiation from surrounding plasma. These radiations from plasma constitute the observable

”photon ring” (Event Horizon Telescope Collaboration et al. 2019a). The relation between the size of the ring and the mass of the SMBH is as follows:

$$M_{\mathrm{SMBH}} = \frac{ac^2\theta D}{G} \quad , \tag{2.4}$$

Where G is the gravitational constant, D is the distance from the SMBH to the observer, θ is the angular radius of photon ring, and c is the speed of light. For a non-rotating SMBH, the value of a is $\sqrt{3}/9$. For a Kerr SMBH, the value of a requires additional general relativistic magneto-hydrodynamic simulation for calibration (Event Horizon Telescope Collaboration et al. 2019b).

2.3 SMBH mass function and correlation with host galaxy properties

The SMBHs in the center of each galaxy greatly impact on the surrounding environment and evolve with their host galaxy (Gültekin et al. 2009, Kauffmann & Haehnelt 2000). Several correlations between SMBHs and host galaxy properties have been discovered, such as the mass of SMBH and the mass of the bulge of the host galaxy, abbreviated as the M-M_{bulge} relation. Kormendy & Ho (2013) used least-square fits, the same method applied in Tremaine et al. (2002), to obtain the following M-σ and M-L_{bulge} relation:

$$\frac{M}{10^9\mathrm{M}_\odot} = \left(0.542^{+0.069}_{-0.061}\right)\left(\frac{L_{\mathrm{K,bulge}}}{10^{11}L_{\mathrm{K}_\odot}}\right)^{1.21\pm0.09} \quad , \tag{2.5}$$

$$\frac{M}{10^9\mathrm{M}_\odot} = \left(0.309^{+0.037}_{-0.033}\right)\left(\frac{\sigma}{200\mathrm{km/s}}\right)^{4.38\pm0.29} \quad , \tag{2.6}$$

M-M_{bulge} relationship was also obtained:

$$\frac{M}{10^9\mathrm{M}_\odot} = \left(0.49^{+0.06}_{-0.05}\right)\left(\frac{M_{\mathrm{bulge}}}{10^{11}\mathrm{M}_\odot}\right)^{1.16\pm0.08} \quad . \tag{2.7}$$

The correlation between SMBH and their host galaxy remains elusive. However, some conclusions can be drawn. SMBHs with masses between $10^6\mathrm{M}_\odot$ and $10^8\mathrm{M}_\odot$ are usually located in Serfeyt Galaxies, with a total mass between $10^{10}\mathrm{M}_\odot$ and $10^{11}\mathrm{M}_\odot$. These SMBHs usually has a thin accretion disk with a high radiation efficiency. Their host galaxies usually has a high stellar surface luminosity. In this case, SMBHs does not gain their fuel via tidal interaction or major merger, but grow themselves via gas transport. Typical elliptical galaxies with masses between $10^{11}\mathrm{M}_\odot$ and $10^{12}\mathrm{M}_\odot$ host SMBHs with masses higher than $10^{8}\mathrm{M}_\odot$. These AGNs are classified as jet-mode AGNs. These AGNs emit high-energy outflow, but themselves does not have a high radiation. These AGNs are fuelled by hot gas that are excited by these jets (Heckman & Best 2014).

2.4 Observations of binary SMBHs

Since SMBHs are ubiquitous in the center of galaxies, the detection of SMBH binaries in the centers of a galaxies is important for understanding galaxy merging and evolution. Usually, the detection of an SMBH binary requires additional fingerprints and proofs to confirm its existence, but in some galaxies, the SMBH binary can be spatially resolved.

2.4.1 Direct observations of binary SMBHs

2.4.1.1 NGC3393

With the Chandra X-ray telescope, Fabbiano et al. (2011) discovered a binary SMBH system in the central region of NGC3393. The distance between two SMBHs is about 135 parsec. Both SMBHs have a mass $\approx 10^{6}\mathrm{M}_\odot$.

2.4.1.2 Galaxy 0402+379

Maness et al. (2004) stated that there are two bright components are observed in the radio galaxy 0402+379, using a very long baseline array telescope (VLBA). The two components were further studied, confirming that they are two SMBHs with a projected separation of 7 parsec and a total mass of $1.5 \times 10^{8}\,\mathrm{M}_\odot$ (Rodriguez et al. 2006).

2.4.2 Indirect evidence for SMBH binary detection

After the merger process of two galaxies, the binary SMBH is expected to migrate into the center of the newly-formed galaxy. There are certain observable phenomena that can indicate the migration of SMBHs (for further details, see Komossa (2006)).

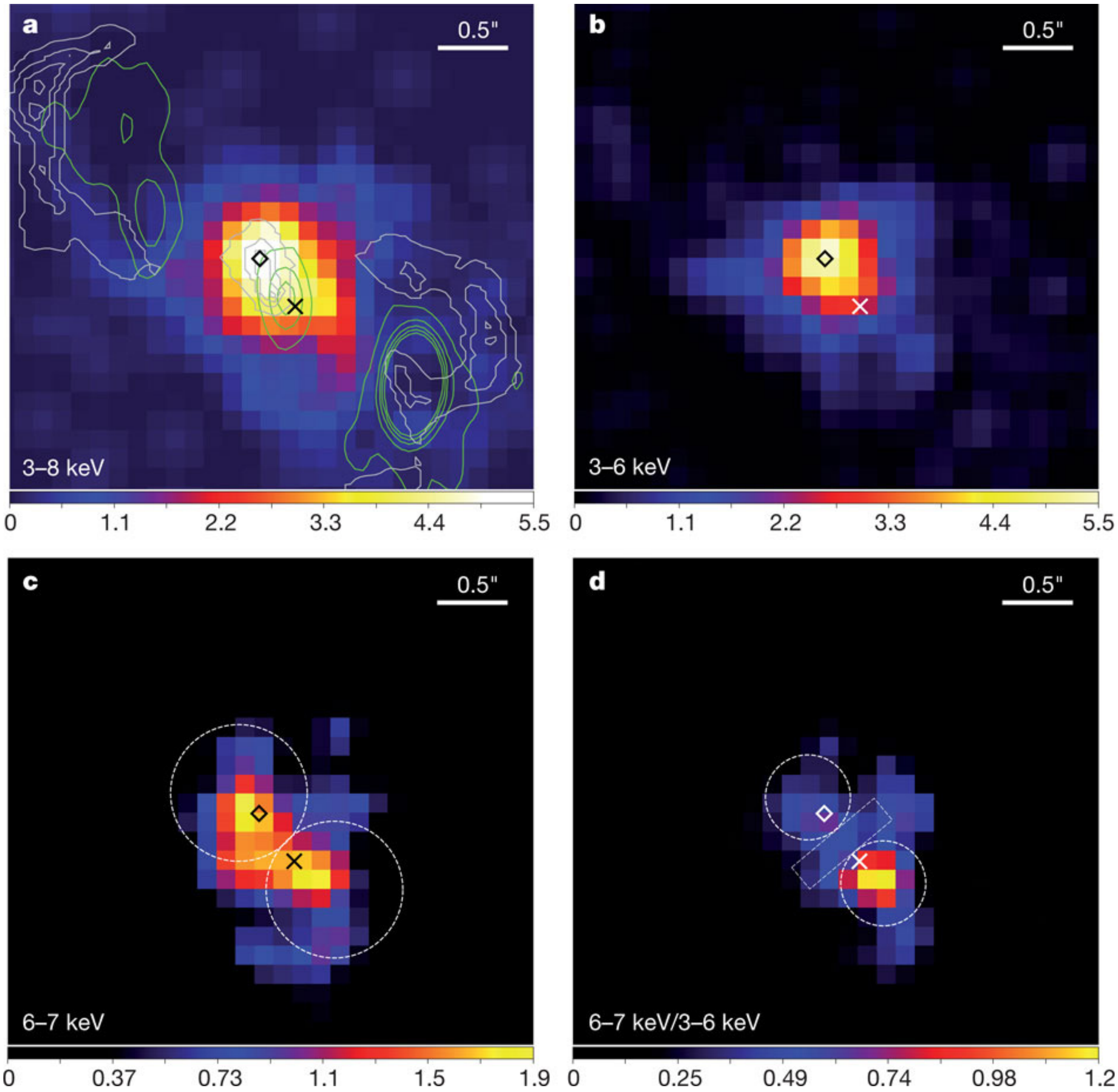

Figure 2.1: Chandra ACIS-S images of the NGC 3393 nuclear region. Image credit: Fabbiano et al. (2011).

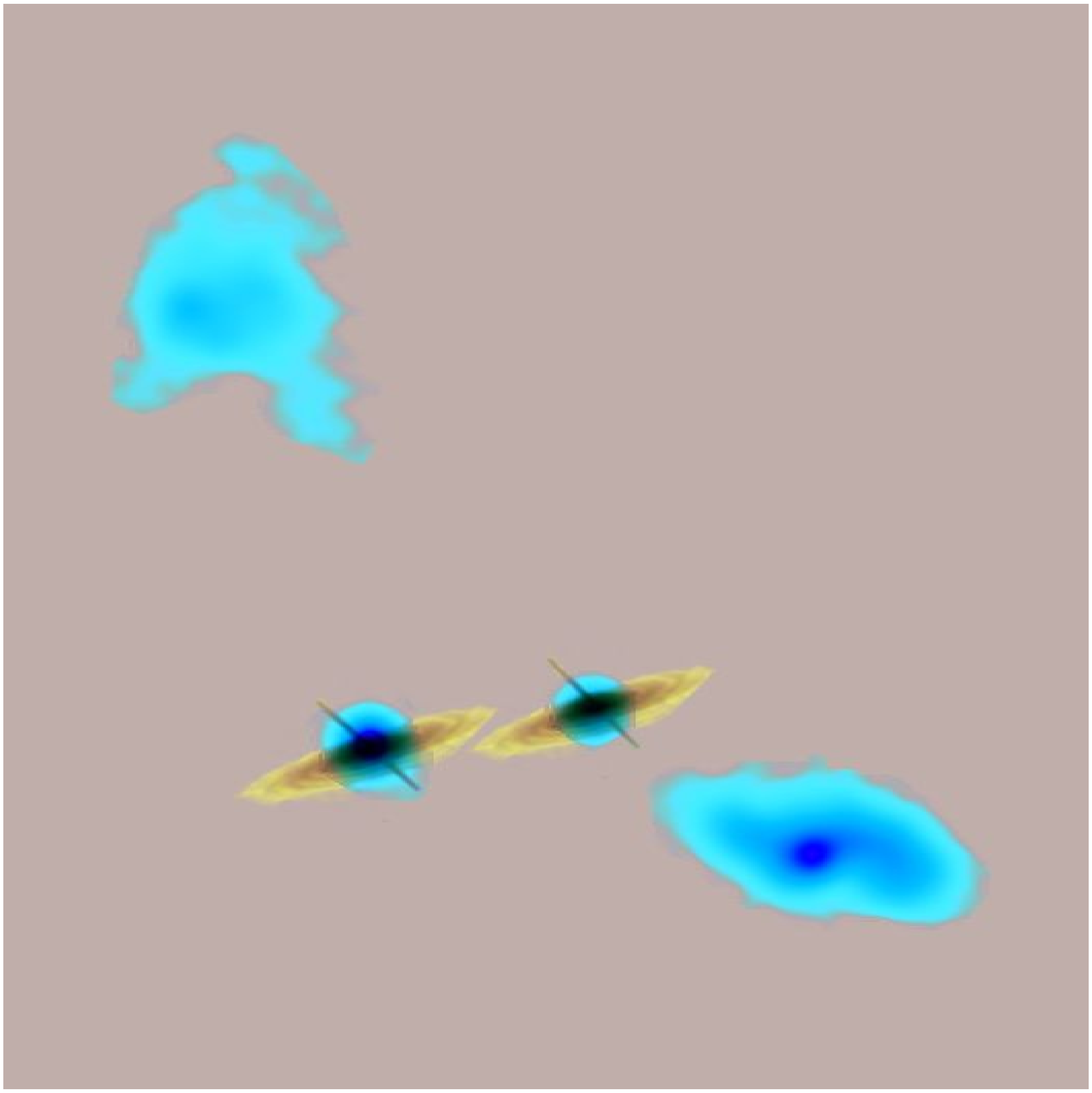

Figure 2.2: VLBA 2-cm image of the radio galaxy 0402+379 which hosts two SMBHs at its center. Image credit: Rodriguez et al. (2006), NRAO Archives.

2.4.2.1 X-shape jet

An X-shape jet is an indicator for identifying SMBH mergers. When the radio jet change direction abruptly, X-shape pattern forms (Parma, Ekers, & Fanti 1985). According to Zier (2005), If a radio jet in one of the two galaxies with a primary SMBH, then the SMBH merger process may change the spin axis of the primary SMBH, causing the radio jet to deviate its direction from its original path.

2.4.2.2 Symmetric double-lobed structure

Radio galaxies with a symmetric double-lobed structure are called "Double-Double" radio galaxies. Schoenmakers et al. (2000) suggest that the "Double-Double" phenomenon originates from the interruption of jet production in the inner structure. Liu, Wu, & Cao (2003) further investigated this problem, suggesting that the "Double-Double" phenomenon was the remnant of coalescence binary SMBH.

2.4.2.3 Periodic jet deviation

A periodic jet deviation was observed in a lot of quasars, including 3C 273, 3C449, BL Lac, and 4C73.18. Roos, Kaastra, & Hummel (1993) interpret the periodic deviation in the direction of the jet as the evidence for proving the existence of a binary massive black hole. It is currently the most plausible explanation, although Rieger (2004) discussed the alternative mechanism that can explain this phenomenon.

2.4.2.4 Periodic lightcurve variations

Another phenomenon that indicates the existence of binary SMBH is a periodic change in the light curve. OJ 287 was one of the most bright quasars. OJ 287 has an outburst period of 11.86 years (Valtonen et al. 2008). Lehto & Valtonen (1996) proposed that the oscillation in lightcurve variation probably originates from secondary SMBH passing through the accretion disk of primary SMBH. The mass of secondary SMBH is $10^8\,\mathrm{M}_\odot$, and the primary SMBH has a mass of $1.7 \times 10^{10}\,\mathrm{M}_\odot$. Valtonen et al. (2008) added Post-Newtonian terms to the binary orbit and succeeded in predicting the next outburst.

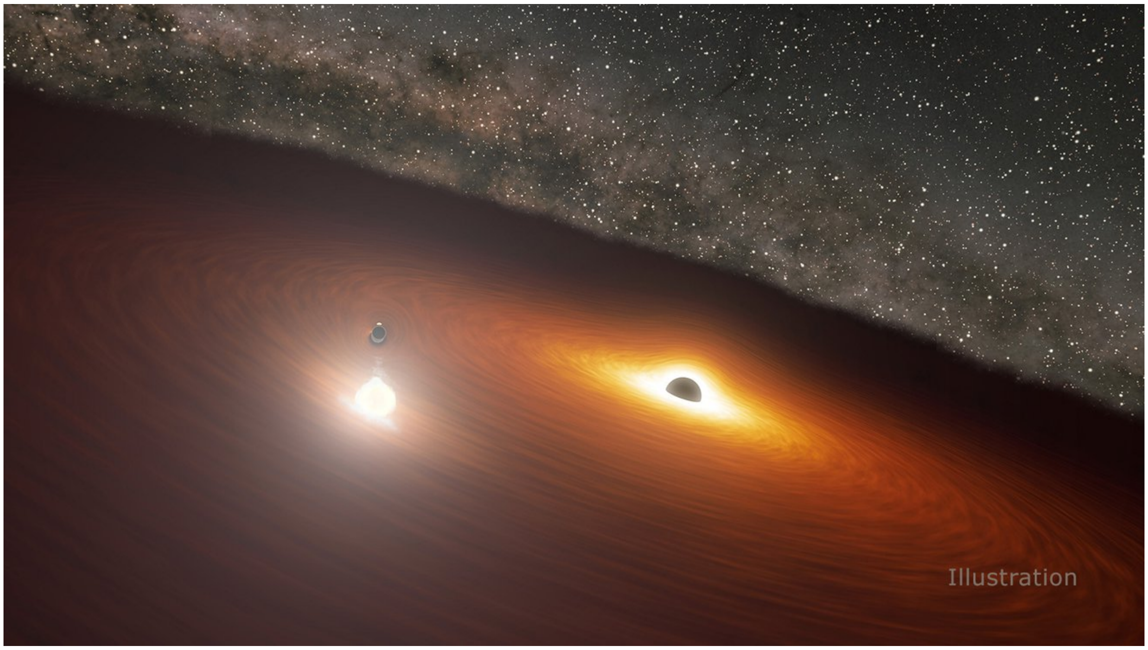

Figure 2.3: Animation of binary SMBH system OJ 287. image credit: NASA/JPL-Caltech.

2.4.2.5 Double peak emission lines

A binary SMBH with a very small separation may be observed as an object with two broad emission line systems due to the orbit motion of the binary SMBH. Boroson & Lauer (2009) reported a quasar SDSS J153636.221 044127.0 as a potential SMBH binary system. Its component has a mass of $\approx 10^{7.3}\,\mathrm{M}_{\odot}$ and $\approx 10^{8.9}\,\mathrm{M}_{\odot}$ with a separation of $\approx$ 0.1 parsec and an orbital period of $\approx$ 100 years.

2.4.2.6 Unobservable central cusps

Another indicator of the existence of the SMBH binary is the surface brightness profile. Kormendy et al. (2009) derived the relation between brightness and radius for all known elliptical galaxies. It shows that the relation can be fit using the Sersic profile. Elliptical galaxies with absolute magnitude $\leq$ -21.66 tend to have a core with surface brightness less than its exterior part. This phenomenon probably originates from the slingshot ejection of stars, expulsed by the hardening process of the SMBH binary.

2.4.3 SMBH binary candidates with sub-parsec separations

Although there is a fair amount of SMBH binary that can be observed, the separation of SMBH binary is still relatively distant. A candidate that has a separation of less than 1 parsec is rare. Here we indicate a list of signatures of SMBH binary that has a sub-parsec separation, in addition to the criteria mentioned above.

- Continuum deficit
- Gas dynamics of circumbinary disk
- Signals from polarized spectra
- Change-looking AGN

(Wang & Li 2020). The first SMBH candidate that has a separation of less than 1 parsec was reported by Bon et al. (2012) in the center of NGC 4151. It was identified by the oscillation of light and radial velocity curve with a period of roughly 15.9 years and a redshift of $z = 0.0033$. The separation of the SMBH binary is about 0.01 pc. Other SMBH binary candidates were identified using a periodic variation of orbital elements and optical photometry with sub-parsec separation, including Graham et al. (2015), Li et al. (2016, 2019), Zheng et al. (2016).

Other criteria for identifying SMBH binary include gas dynamics of nuclei, radio image, continuum deficit, and flux drops in the tidal disruption event (Wang & Li 2020). The formation mechanism of a counter-rotating disk in NGC 1068 remains a mystery and challenge to explain. Two layers of the disk have different rotating directions. The inner region ($r \leq 1.5$ pc) rotates prograde, but the outer region ($3 - 7$ pc) rotates retrograde. The region between the prograde part and retrograde part cannot be described by Kelvin-Helmholtz instability. But the introduction of an SMBH binary may help solve this dilemma by carrying away the angular momentum of a retrograde part. The binary SMBH is expected to have a total mass of $1.3 \times 10^7\,\mathrm{M}_\odot$ with a mass ratio of 0.3. By using VLBA (very long baseline interferometry), Kharb, Lal, & Merritt (2017) identified a pair of SMBH with a separation of ≈ 0.35 pc. The total mass of the SMBH binary is $3.6 \times 10^7\,\mathrm{M}_\odot$ with a mass ratio $q \approx 1$. In 2015, Yan et al. (2015) identified a quasar in the center of MrK 231 with a redshift of $z = 0.0422$. The UV spectrum of the quasar has a discontinuity that cannot be explained by extinction or absorption. This dilemma was solved by adopting a binary

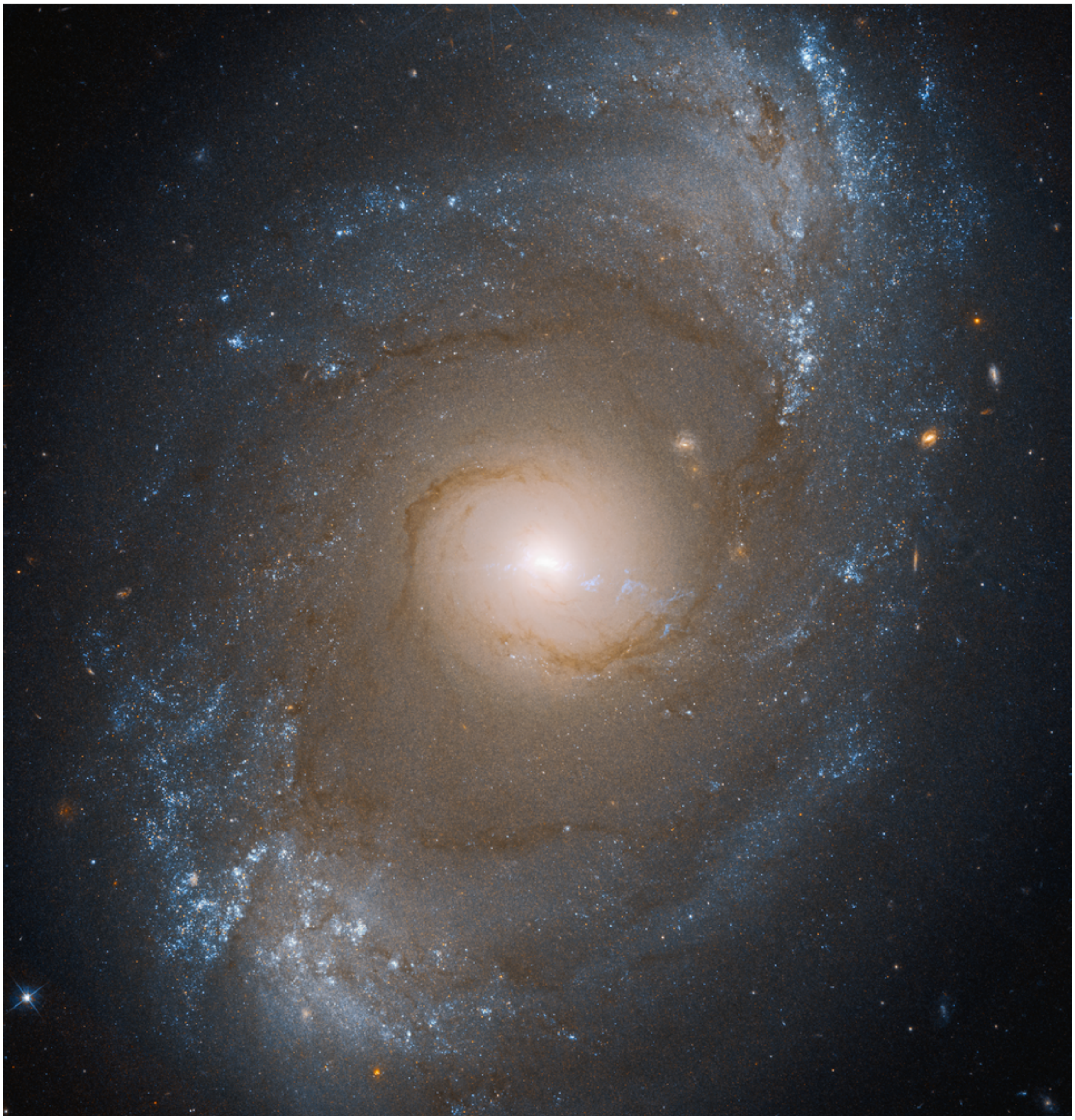

Figure 2.4: UVIS observation of NGC 4151. Image credit: Hubble Space Telescope.

SMBH model with a circumbinary disk and mini-disk around each SMBH. The mass of the primary SMBH is $\approx 1.5 \times 10^8\,\mathrm{M}_\odot$, and the secondary SMBH has a mass of $4.5 \times 10^6\,\mathrm{M}_\odot$.

2.5 Dynamical evolution of SMBH binaries

The dynamical evolution of binary SMBH can be described as a combination the processes described below.

1. As two galaxies merge, the central SMBHs migrate towards the center of the newly formed with dynamical friction from surrounding stars and gas (Begelman, Blandford & Rees 1980). Dynamical friction is the net force exerted on a massive object by surrounding stars. Assuming field stars have an isotropic velocity distribution, the surrounding stars will decelerate the massive body with a negative acceleration:

   $$\frac{dv_\mathrm{m}}{dt} \approx -16\pi^2 G^2 M m_\mathrm{a} \ln\Lambda \left[(\int_0^{v_\mathrm{m}} dv_\mathrm{a} v_\mathrm{a}^2 f(v_\mathrm{a})) \right] \left| \frac{\vec{v}_\mathrm{m}}{v_\mathrm{m}^3} \right| \tag{2.8}$$

   (Chandrasekhar 1943). Here, M is the mass of the massive object, m_a is the mass of surrounding stars, v_a is the velocity of surrounding stars, v_m is the velocity of the massive object, and $\ln\Lambda$ is the Coulomb logarithm, respectively. The typical values of the Coulomb logarithm vary according to different systems and different positions in the system. The Coulomb logarithm at the half-mass radius of a globular cluster is 12.0 and 23.9 for an elliptical galaxy (Binney & Tremaine 1987). The dynamical friction timescale can be estimated if we neglect the variation in the Coulomb logarithm. The dynamical friction timescale is:

   $$T_\mathrm{fric} = \frac{19\ \mathrm{Gyr}}{\ln\Lambda} \left(\frac{r_\mathrm{i}}{5\ \mathrm{kpc}}\right)^2 \frac{\sigma}{200\ \mathrm{km/s}} \frac{10^8\ \mathrm{M}_\odot}{M} \quad , \tag{2.9}$$

   where the σ is the velocity dispersion, r_i is the size of the galaxy, and M is the mass of the subject. If we assume a galaxy center as a singular isothermal sphere with N stars and a density $\rho = \sigma^2/(2\pi G r_c^2)$, then the dynamical friction timescale is:

   $$t_\mathrm{fric} \sim 2 \times 10^8 \frac{1}{\ln(N)} \left(\frac{10^6\ \mathrm{M}_\odot}{m}\right) \left(\frac{r_c}{100\ \mathrm{pc}}\right)^2 \left(\frac{\sigma}{100\ \mathrm{km\ s}^{-1}}\right) [\mathrm{yr}] \tag{2.10}$$

   (Sobolenko, Berczik, & Spurzem 2021), where r_c is the core radius, and σ is the velocity dispersion. During this stage, dynamical friction is the dominant factor.

2. When the SMBHs migrate to a separation below their own influence radius, the SMBH binary is defined as "bound." Consider a Keplerian orbit consisting of two SMBH, ignoring the force contribution from surrounding stars. The semi-major axis and eccentricity are defined as:

$$\frac{1}{a} = \frac{2}{R} - \frac{v^2}{G(M_1 + M_2)} \quad , \tag{2.11}$$

$$e = \sqrt{1 + \frac{2h^2}{G(M_1 + M_2)} \left[\frac{v^2}{2} - \frac{G(m_1 + m_2)}{R}) \right]}. \tag{2.12}$$

The binding energy is:

$$E = \frac{GM_1M_2}{2a} \quad . \tag{2.13}$$

The influence radius, $a_{\rm inf}$, is defined as:

$$a_{\rm inf} \equiv \frac{G(M_1 + M_2)}{\sigma_{\rm c}^2} \tag{2.14}$$

(Aarseth, Tout, & Mardling 2008), where $\sigma_{\rm c}$ is the velocity dispersion of surrounding stars. M_1 and M_2 are the masses of the two SMBHs, respectively. During this stage, dynamical friction and three-body scattering between surrounding stars and SMBH help shrink the orbit of binary SMBH.

3. As the SMBH binary continues orbital decay, the binary becomes hard. "Hard binary" was defined in multiple ways. The first one was defined in Binney & Tremaine (1987), saying that the binding energy of binary $E_{\rm b}$ is larger than $m_{\rm s}\sigma^2$. The second one states that a hard binary gets harder through the interaction with surrounding stars, and a soft binary gets softer. These two statements are equivalent. Either one of these is called Heggie's law. The third one is a derivative of the first two statements. It suggests that a hard binary harden at a constant rate that is only dependent on the properties of surrounding stars. When applying to the massive black hole binary, in our studied scenario, the third statement is adopted. We may define the mass ratio $q \equiv \frac{M_1}{M_2}$, $\mu \equiv \frac{M_1 M_2}{M_1 + M_2}$. We also define a_h as the semi-major axis below which the binary

is considered "hard".

$$a_{\mathrm{h}} = \frac{G\mu}{4\sigma^2} \quad . \tag{2.15}$$

Here σ is the one-dimension velocity dispersion of surrounding stars. In this stage, the orbital evolution of the SMBH binary is determined solely by surrounding stars. Surrounding stars help take away the energy and angular momentum of the MBH binary orbit. Usually, the hardening rate is written as $s = \frac{da}{dt}$. Theoretically, the binary hardening rate can be written as:

$$H = \frac{\sigma}{G\rho} \frac{d}{dt} \frac{1}{a} \quad . \tag{2.16}$$

Two more parameters can be developed to characterize the evolution of SMBH, mass ejection rate and eccentricity change rate. The mass ejection rate is:

$$J = \frac{1}{M_{\mathrm{BH}}} \frac{dM_{\mathrm{ej}}}{d\ln(\frac{1}{a})} \quad , \tag{2.17}$$

Where dM_{ej} is the mass ejection rate and M_{BH} is the mass of the black hole. The eccentricity change rate is:

$$K = \frac{de}{d\ln\left(\frac{1}{a}\right)} \quad . \tag{2.18}$$

The three parameters are usually determined by isolated three-body scattering experiments (Bonetti et al. 2020, Quinlan 1996, Rasskazov & Merritt 2017, Rasskazov & Kocsis 2019, Sesana, Haardt, & Madau 2006, 2007, 2008). But these values cannot represent a real system such as a galactic center and globular cluster very well. One reason is that stars in the galactic center have a mass spectrum that is not consistent with the single-mass condition assumed in the scattering experiment. Another reason is that the amount of stars supplying to interact with binary SMBH is assumed to be infinity, inconsistent with a real system. Here we introduce the concept of "loss cone." The loss cone radius is the larger one of the tidal disruption radius and radius of capture for a star around SMBH. The angular momentum of such a star with respect to the SMBH is:

$$L_{\mathrm{lc}} \approx \sqrt{2GMr_{\mathrm{lc}}} \quad , \tag{2.19}$$

where G is the gravitational constant, M is the mass of the star and r_{lc} is the loss cone radius. The collection of the orbit of stars that has angular momentum $L \leq L_{\mathrm{lc}}$

constitutes a loss cone (Merritt 2013). A schematic description of star orbits in a triaxial galaxy is illustrated in Figure 4.

4. When the orbit of SMBH becomes sufficiently tight, gravitational wave emission takes over the spot of three-body scattering and dominates their own orbital decay. The critical value of the orbit's semi-major axis is:

$$a_{gr} = \left(\frac{256}{5} \frac{G^2 \mu M_{12}^2 \sigma}{c^5 \rho H} \right)^{0.2} \tag{2.20}$$

(Quinlan 1996). Here, μ is the reduced mass of BIMBH, M_{12} is the total mass of the SMBHB. Usually, the value of a_{gr} is $\approx 10^{-2}$ pc for SMBH with a mass of $10^6 \mathrm{M}_{\odot}$. This process may ultimately result in a coalescence of the two SMBHs, and the resulting burst of gravitational waves may be observed. The coalescence time of a binary black hole can be written as:

$$\begin{aligned} t_{\mathrm{merge,binary}} \simeq 2.9 \times 10^{12} \mathrm{yr} \left(\frac{m_0}{10^6 \mathrm{M}_{\odot}} \right)^{-1} \left(\frac{m_1}{10^6 \mathrm{M}_{\odot}} \right)^{-1} \left(\frac{m_0 + m_1}{2 \times 10^6 \mathrm{M}_{\odot}} \right)^{-1} \\ \left(\frac{a_1}{10^{-2} \mathrm{pc}} \right)^{4} f(\mathrm{e}_1)(1 - \mathrm{e}_1^2)^{7/2} \quad , \end{aligned} \tag{2.21}$$

where

$$f(e) = \left(1 + \frac{73}{24} \mathrm{e}^2 + \frac{37}{96} \mathrm{e}^4 \right)^{-1} \tag{2.22}$$

(Blaes, Lee, & Socrates 2002). Equation 2.21 treats the binary SMBH as a Keplerian binary, which is usually not the case when the separation does not allow the neglection of general relativistic effect. The corrected timescale, including Post-Newtonian correction, is listed in Zwick et al. (2020):

$$T_{\mathrm{corr}} = T_{\mathrm{merge,binary}} 8^{1-\sqrt{1-e_1}} \exp \left(\frac{2.5 r_s}{a_0 (1 - e_1)} \right) \quad , \tag{2.23}$$

With e_1 being the eccentricity of the binary and r_s being the ”equivalent” Schwarzschild radius of the binary system.

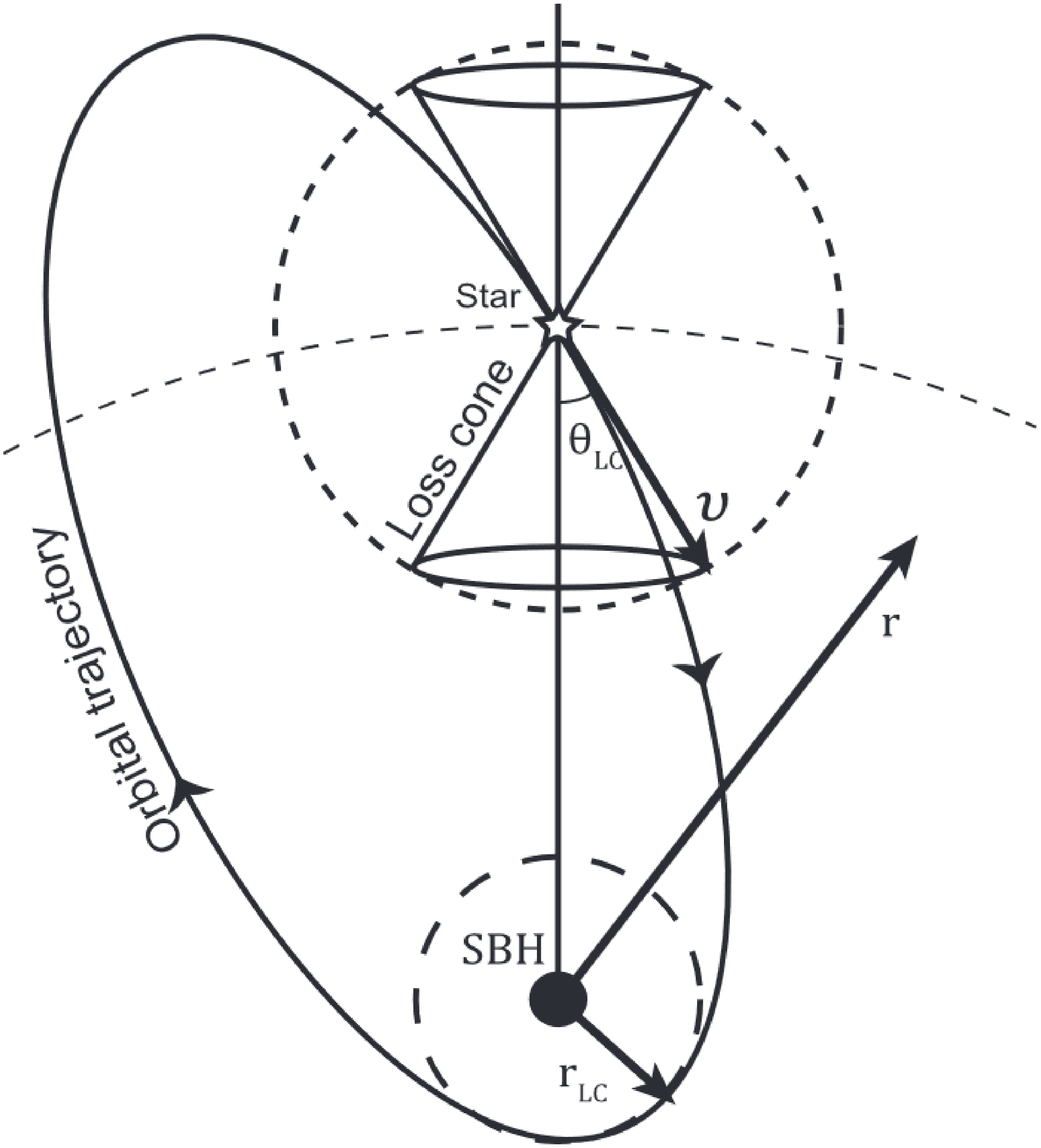

Figure 2.5: A schematic description of loss cone. Image credit: Merritt (2013).

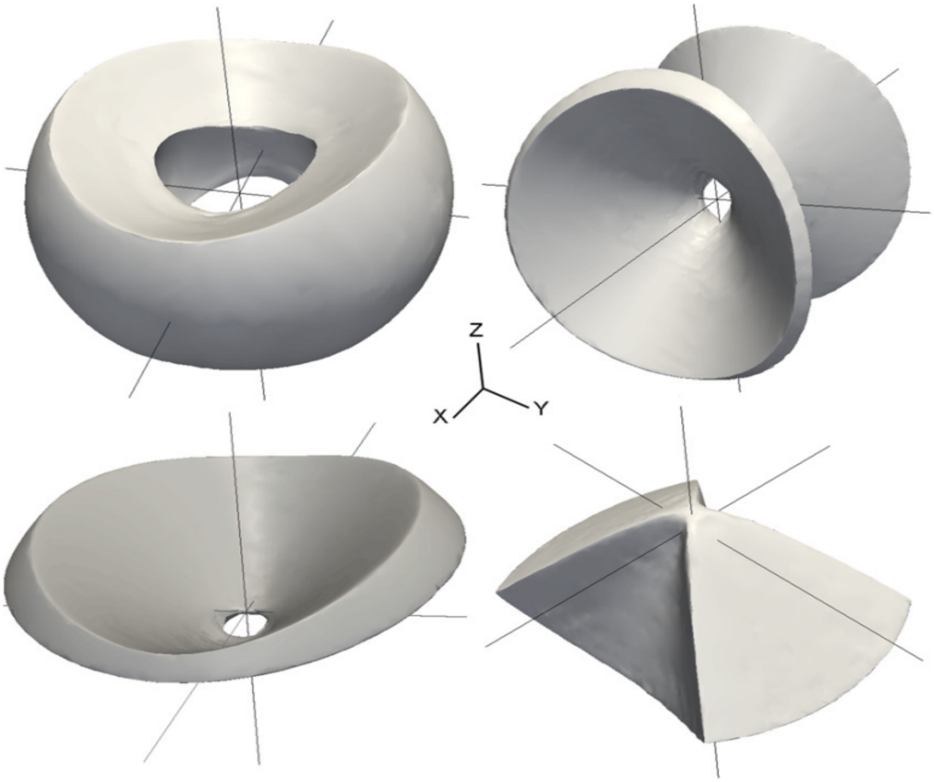

Figure 2.6: Orbit family of stars in triaxial galaxy. Image credit: Vasiliev (2014).

2.6 The Final Parsec Problem

Recent development in computational facilities and algorithms allows simulations of large-scale phenomena to be conducted on a realistic timescale. The study of the dynamics of SMBH binary systems has become a very hot topic. A pioneering study of simulation of supermassive black hole binary was conducted in Ebisuzaki, Makino, & Okumura (1991). It use GRAPE-2 with modified NBODY3 code on it to simulate the merging of two galaxies in order to study the effect of two SMBHs on the evolution of two galaxies. It conclude that the core radius of the galaxies enlarged with central SMBH. Fukushige, Ebisuzaki, & Makino (1992) studied the orbit decay of supermassive black hole binary in merging galaxies, with dynamical friction force modelled by a simple analytic formula. It shows that the SMBH binary may coalescence in $\leq 10^7$ yrs. Makino et al. (1993) simulate SMBH binary in a galaxy with N-body simulation. The coalescence time for SMBH binary is $\approx 10^9$ years. The transition between the third and fourth stages of evolution of binary SMBH described in section 2.5 has been proposed to be the main obstacle in binary SMBH coalescence. As SMBHs form a binary, it ejects stars with orbits that intersect the orbit of binary SMBH. In a spherical galaxy, the only way of refilling surrounding stars is two-body relaxation. The relaxation timescale is about 10^{11} years for a real galaxy. Thus if no stars is supplied to the SMBH binary, then the SMBH binary may stall, and its coalescence timescale is longer than a Hubble time. This phenomenon is called ”Final Parsec Problem.”

The Final Parsec Problem is a long-term problem brought about by the galaxy merger process. This problem was first brought up by Milosavljević & Merritt (2001). It argues that the shrink of the orbit of SMBH binary with each component has a mass of $\approx 10^6\,M_\odot$ in a spheroidal galaxy may stall at $0.01 - 1$ pc. This problem was later formally stated as the ”Final-parsec problem” by Milosavljević & Merritt (2003). Makino & Funato (2004) numerically confirmed the problem of insufficient stars interacting with the SMBH binary. It shows that the hardening rate depends on the particle number of the system when the particle number exceeds 2×10^5, a similar conclusion reached by Berczik, Merritt, & Spurzem (2005). The findings provided by the previous N-body simulation is in contradiction with observations of SMBH binary with separation ≤ 1 pc. Thus several solutions are provided to solve the ”Final Parsec Problem.” One method to solve the ”Final Parsec Problem” is to eccentricize the orbit of the binary SMBH. If the orbit of binary SMBH has a very high eccentricity, then the periastron of the binary SMBH would be very short, so that general relativistic effect takes over the place of Keplerian motion and destroy Kozai mechanism

(Holman, Touma, & Tremaine 1997). The merger timescale is shortened when the inner binary's eccentricity is excited. The Kozai mechanism is a robust mechanism that can drive the binary SMBH's eccentricity to a very high value. The other method is refilling the loss cone of the binary SMBH efficiently until the general relativistic effect becomes important.

2.7 Solution to the final-parsec problem: refilling the loss cone

The existence of SMBH binary candidate with separation ≤ 1 parsec has been proven true. To solve the contradiction between the "Final-parsec problem" and observed SMBH binary with milliparsec separation, several approaches have been proposed by previous studies. Chatterjee, Hernquist, & Loeb (2003) investigated whether binary SMBH can merge through the gravitational wave emission in a spherical bulge. The binary SMBHs are affected by stellar dynamical interaction alone. It shows that in a fair fraction of simulations, binary SMBH can coalesce within a Hubble time. But this study utilized self-consistent field expansion rather than direct summation, which introduced some non-spherical terms.

- Random walk of SMBH binary to ensure more interaction with surrounding stars (Milosavljević & Merritt 2001, 2003).
- The time-independent solution of the Fokker-Planck equation may cause an underestimate of the stars' refilling rate. Thus time-dependent solution may introduce a higher refilling rate (Milosavljević & Merritt 2003).
- Secondary slingshots may result in multiple interactions between stars, unable to escape from SMBH (Milosavljević & Merritt 2003). This approach was later proved to be trivial in a triaxial galaxy. The non-conservation of angular momentum probably results in stars leaves away from loss cone (Vasiliev, Antonini, & Merritt 2014).
- Gas in a circumbinary disk may accelerate the merger process, either by applying a torque on the SMBH binary to lose its angular momentum (Cuadra et al. 2009, Dotti et al. 2007, Escala et al. 2004, 2005) or keep forming new stars to ensure high enough re-population rate (Mayer et al. 2007). But modeling gas environment is rather difficult compared to direct N-body simulation. Also, it is not guaranteed to solve the "Final Parsec Problem (Lodato et al. 2009).

- External massive perturbers, such as a tertiary black hole, giant molecular cloud, and dwarf galaxy. The tertiary black hole may increase the eccentricity of the inner binary through the Kozai-Lidov mechanism (Iwasawa, Funato, & Makino 2006) hence decreasing the GW merger timescale. The giant molecular cloud may increase the inner binary hardening rate by increasing the two-body relaxation rate and driving more stars into the loss cone (Perets & Alexander 2008). The migration of a tertiary galaxy may increase the number of stars with a boxy orbit and refill the loss cone of pre-existing binary (Naab, Khochfar, & Burkert 2006). These stars in the tertiary galaxy with centrophilic orbit may get ejected by the pre-existing binary and shrink the orbit of the pre-existing binary (Roos 1988). Matsui & Habe (2009) states that the dwarf galaxy may disturb the stellar orbit in the center of the host galaxy. Both stars in the dwarf galaxy and the central region of the host galaxy repopulate into the loss cone of SMBH binary. The repopulation of the loss cone results in rapid shrink of the SMBH binary orbit and decrease the coalescence time to much less than a Hubble time.

- Non-spherical shape. Norman & Silk (1983) and Poon & Merritt (2001) state that a SMBH may put a constraint on the stellar orbit, limiting the triaxiality of galactic nuclei. Both theoretical (Holley-Bockelmann & Sigurdsson 2006, Merritt & Poon 2004, Norman & Silk 1983, Yu 2002) and numerical (Berczik et al. 2006, Khan et al. 2013, Khan, Just, & Merritt 2011, Preto et al. 2011) studies have shown that non-spherical shape of the central region of galaxy allows bankrupt of angular momentum conservation for stellar orbit, thus increase stellar supply rate and the categories of stellar orbit.

- Introduce PN correction (Preto et al. 2009).

  With a set of N-body simulations, Khan et al. (2012) show that mergers of non-spherical galaxies with different mass ratios introduce triaxiality and drive unequal mass SMBH binary to coalescence. The hardening rate of SMBH binary in galaxies with steep cusps is much higher than SMBH binary in galaxies with shallow cusps. Khan et al. (2012) and Khan, Berczik, & Just (2018) suggest that a steeper stellar density profile greatly enhances the hardening rate. With the incorporation of the IMF, the hardening rate is higher. But the eccentricity does not change much for a single-mass spectrum (SMF) system, while different randomization in SMF case can greatly vary the value and evolution of eccentricity. The eccentricity of the SMBH binary with an extreme mass ratio was studied by Iwasawa et al. (2011). It proposed two mechanisms to solve the Final Parsec Problem:

1. Kozai mechanism under a non-axisymetric potential
2. selective ejection of prograde orbits

2.8 Rotation factor

To simulate a more realistic galaxy merger process, it is necessary to include the rotation factor for galaxies. There are several studies about the effect of galaxy rotation on the evolution of binary SMBH. Sesana, Gualandris, & Dotti (2011) investigated the effect of the degree of galaxy rotation on the eccentricity evolution of binary SMBH. It suggests that isotropic cusp counter-rotating cusp would eccentricize the binary orbit. Co-rotating cusp would circularize the binary orbit. Holley-Bockelmann & Khan (2015) investigated the coevolution of binary SMBH and galaxy rotation. It found that the evolution of SMBH is independent of particle number. Galaxy rotation helps harden the SMBH binary even more than the factor of inherent galaxy geometry. Mirza et al. (2017) found that the initial orbit plane orientation and eccentricity can drive the SMBH inspiral time to decrease by one order of magnitude. These studies suggest that in general, host galaxy rotation is an aid in eccentricizing the binary orbit and reducing the gravitational wave merger timescale.

In Vasiliev, Antonini, & Merritt (2015), the Final Parsec Problem under the context of collisionless relaxation with arbitrary galaxy shape was studied. It uses the Monte-Carlo approaches to deal with collisional and collisionless dynamics. It was concluded that axisymmetry alone was not enough to deal with the depletion of stars in the loss cone region, but a small degree of triaxiality can drive the SMBH binary to coalescence in a Hubble time. It proves that the timescale of coalescence of SMBH binary in any triaxial galaxy is ≤ 1 Gyr.

It is observed that one of the most massive BH lies in the center of NGC1277, roughly $1.7 \times 10^{10}\,\mathrm{M}_\odot$. The orbit of such a massive binary BH should stall at the parsec scale. Khan, Holley-Bockelmann, & Berczik (2015) performed direct N-body simulations to study the dynamical evolution of such a massive binary BH, finding out that the coalescence of the massive binary BH is governed by dynamical friction, followed by gravitational wave radiation emission. The coalescence timescale for the massive binary is very rapid and efficient, bypassing the 3-body scattering phase with surrounding stars.

Bortolas et al. (2016) suggest that the Brownian motion of the SMBH binary is not important when the particle number exceeds 1 million, but Brownian motion is important when the particle number is between 10^4 and 10^6. Varisco et al. (2021) proved that rotation factor alone can circularize the orbit of the SMBH binary and speed up the hardening rate of the SMBH binary.

2.9 Solution to the final parsec problem: a tertiary SMBH

2.9.1 Observational evidence for triple SMBH systems

The existence of a triple SMBH system is much rare than a binary SMBH system. Deane et al. (2014) first identified SDSS J150243.091111557.3, a quasar at $z = 0.39$, as a triple SMBH system. The separation of the close binary is about 7 parsec. NGC 6240 is a well-studied galaxy system that is considered in the process of merging. Kollatschny, et al. (2020) discovered that NGC 6240 contains not only 2 but 3 nuclei, with close binary separation as close as 198 pc. Pfeifle et al. (2019) discovered that a triple AGN lies in the SDSS J084905.51+111447.2.The mutual separation of the triple AGN is ≤ 10 kpc. Foord et al. (2021) discovered a triple AGN, SDSS J0849+1114, and a triple merger, SDSS J0858+1822. Recent observations have proved the existence of a wandering SMBH that ejected ~ 39 Myr ago, with a velocity of ~ 1600 km/s. Such a runaway SMBH is probably ejected after a violent three-body interaction with a progenitor binary SMBH (van Dokkum et al. 2023).

2.9.2 Kozai mechanism

In 1961, Lidov studied the orbit evolution of an artificial satellite driven by an outer potential. Kozai studied how an inclined asteroid in the Solar system gets affected by the gravitational perturbation of Jupiter. Both of their systems can be simplified as a relatively close binary (with one as a test particle) and an outer distant tertiary body. Both Kozai and Lidov found that the inclination and eccentricity of the test particle oscillate. The period of oscillation of eccentricity and inclination is much longer than its orbital period (Kozai 1962, Lidov 1962). This mechanism is called Kozai mechanism. When assuming a secondary test particle with negligible mass compared to the primary object and a distant tertiary particle in an isolated three-body system,the equation of motion for the secondary is such that the quantity $\sqrt{1-e_1^2}\cos i$ is conserved, where i is the mutual inclination between the

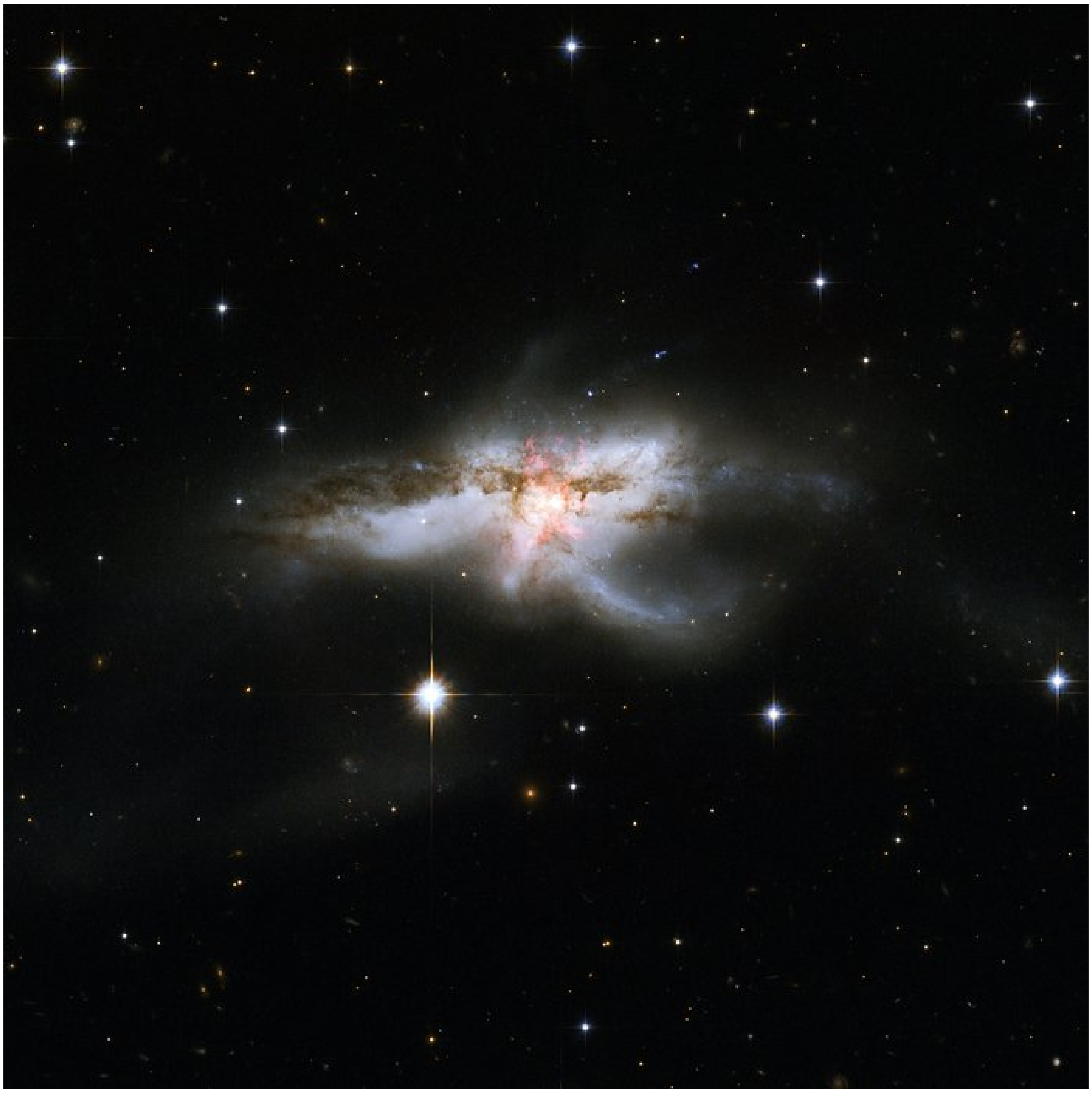

Figure 2.7: Hubble space telescope observation of NGC 6240. Image credit: NASA, ESA, the Hubble Heritage Team (STScI/AURA)-ESA/Hubble Collaboration and A. Evans (University of Virginia, Charlottesville/NRAO/Stony Brook University).

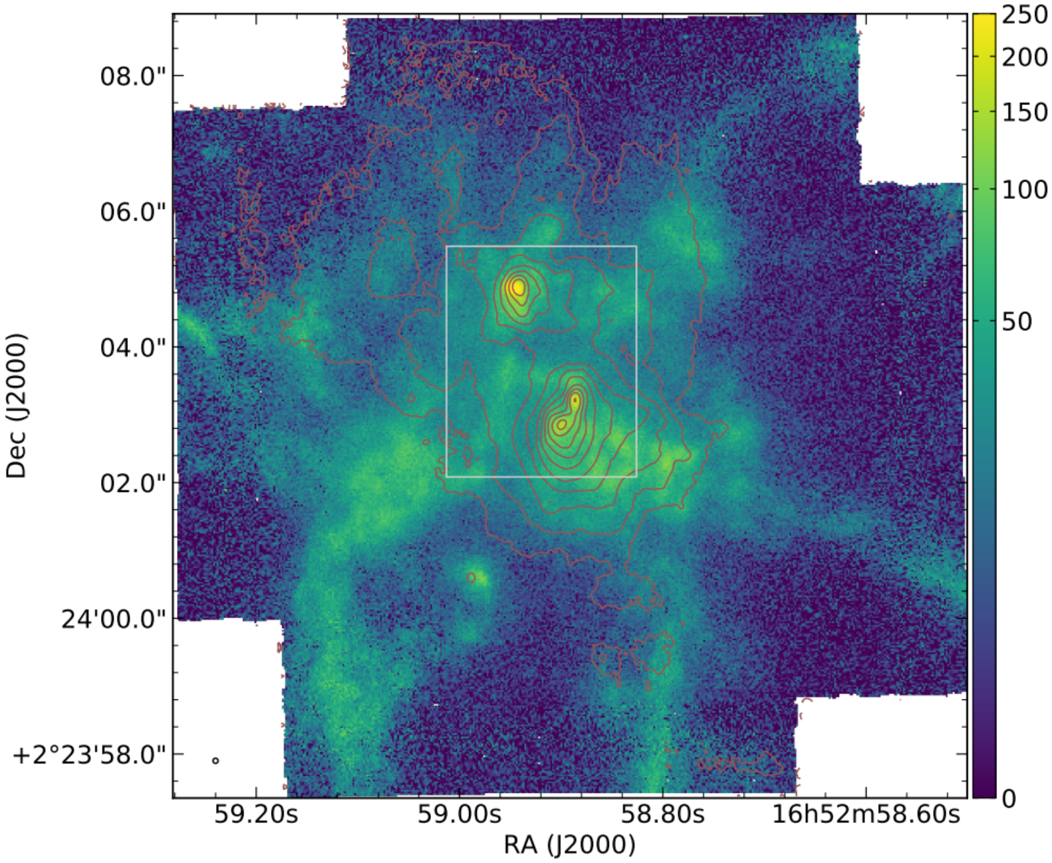

Figure 2.8: Hα/[NII] image of the gas in NGC 6240. Reference: Kollatschny, et al. (2020).

inner and outer orbital planes:

$$\cos i = \frac{\vec{L}_{\mathrm{in}} \cdot \vec{L}_{\mathrm{out}}}{\left|\vec{L}_{\mathrm{in}}\right| \cdot \left|\vec{L}_{\mathrm{out}}\right|} \quad , \tag{2.24}$$

where $\vec{L}_{\mathrm{in}}$ and $\vec{L}_{\mathrm{out}}$ is the relative angular momentum of the mutual closest neighbour and the binary consists of the tertiary object and the mass center of the mutual closest neighbour, respectively. The minimum mutual inclination required for Kozai oscillations is $i \approx 39.2^{\circ}$. Here, a_2, and e_2 are the semi-major axis and eccentricity of the outer orbit, and m_1, and m_3 are the mass of the primary and tertiary objects, respectively. P_{out} and P_{in} are the period of the outer and inner orbits. The orbital parameters of the system then oscillate, and this oscillation period is called the Kozai timescale. According to Antognini (2015), the Kozai-timescale can be approximated as follows:

$$t_{\mathrm{KL}} \approx \frac{16}{15} \left(\frac{{a_3}^3}{a_1^{\frac{3}{2}}} \right) \sqrt{\frac{m_1}{G m_3}} (1 - e_2^2)^{\frac{3}{2}} \quad , \tag{2.25}$$

or

$$t_{\mathrm{KL}} \approx \frac{8}{15\pi} \left(1 + \frac{m_1}{m_3}\right) \left(\frac{P_{\mathrm{out}}^2}{P_{in}}\right) (1 - e_2^2)^{\frac{3}{2}} \quad , \tag{2.26}$$

where the a_2, and e_2 are the semi-major axis and eccentricity of the outer orbit, m_1, and m_3 are the mass of the primary and tertiary object, respectively. a_1 is the semi-major axis of the inner binary orbit. P_{out} and P_{in} is the period of the outer and inner orbit. Chen et al. (2011) find that the Kozai-Lidov precession rate can be expressed as

$$\dot{\omega}_{\mathrm{KL}} \quad \simeq \quad \begin{cases} \frac{15\pi q_1}{2\sqrt{2}P(a_1)} \left(\frac{r_t}{a_1}\right)^{-1/2} \left(\frac{a_2}{a_1}\right)^{2} & (a_2 < a_1/2) \\ \frac{15\pi q_1}{32P(a_1)} \left(\frac{r_t}{a_1}\right)^{-1/2} \left(\frac{a_2}{a_1}\right)^{-3/2} & (a_2 \geq a_1/2) \end{cases} . \tag{2.27}$$

where q_1 is the mass ratio of the inner binary, $P(a_1)$ is the orbital period, a_2 is the semi-major axis of the tertiary object's orbit, and r_{t} is the tidal disruption cross section (see Chen et al. 2011, for details).

2.9.3 General relativistic precession

General-relativistic precession can hinder the Kozai resonance and stop the eccentricity oscillation in an isolated three-body system. The criterion for Kozai resonance not to be destroyed by general-relativistic precession is

$$\frac{a_2}{a_1} < 34 \left(\frac{a_1}{10^{-2}\,\mathrm{pc}}\right)^{\frac{1}{3}} \left(\frac{m_1+m_2}{2\cdot 10^6\,\mathrm{M}_\odot}\right)^{-\frac{1}{3}} \left(\frac{2m_3}{m_1+m_2}\right)^{\frac{1}{3}} \left(\frac{1-e_1^2}{1-e_2^2}\right)^{\frac{1}{2}} \quad . \tag{2.28}$$

The general-relativistic precession rate is

$$\dot{\omega}_{\mathrm{GR}} \simeq \frac{6\pi G M_1}{(1-e_2^2)c^2 a_2} P(a_2)^{-1} = \frac{3\pi}{2P(a_1)} \left(\frac{r_{\mathrm{s}}}{r_t}\right) \left(\frac{a_2}{a_1}\right)^{-3/2} \quad , \tag{2.29}$$

where a_2 is the semi-major axis of the tertiary object. r_{s} is the Schwarzschild radius of primary object, and r_t is the tidal disruption cross section of the primary object. c is the speed of light and e_2 is the eccentricity of the tertiary object. The ratio between the Kozai-Lidov precession rate and the general relativistic precession rate is

$$\frac{\dot{\omega}_{\mathrm{KL}}}{\dot{\omega}_{\mathrm{GR}}} \sim \frac{m_3}{m_1+m_2} \left(\frac{a_1}{a_2}\right)^3 \frac{a_1}{r_{\mathrm{S,inb}}} \frac{(1-e_1^2)^{1/2}}{(1-e_2^2)^{3/2}} \quad , \tag{2.30}$$

where $r_{\mathrm{S,inb}}$ is the "equivalent" Schwarzschild radius of the inner binary (Bonetti et al. 2016, Chen et al. 2011). The Kozai-Lidov mechanism is only effective when $\dot{\omega}_{\mathrm{KL}} \geq \dot{\omega}_{\mathrm{GR}}$.

2.9.4 Mass precession

The assumption of the Kozai mechanism and its prohibition by general relativity includes an Keplerian isolated three-body system. However, in a realistic scenario such as a hierarchical black hole merger in a globular cluster, the general relativistic precession can be ignored for a hierarchical stellar triple embedded in a stellar population with a large separation. In this case, the Newtonian mass precession may be a hurdle to the Kozai resonance.

In a self-gravitational system with a density profile $\rho(r) = \rho_0\,(r/r_0)^{-\gamma}$, where γ is a constant and r_0 is the scale of the system, the mass-precession rate is

$$\dot{\omega}_{\mathrm{MP}} = -V_r G_m(e,\gamma)\sqrt{1-e_2^2}\left[\frac{M_*(a_2)}{M_0}\right] \quad , \tag{2.31}$$

(Haardt et al. 2016). Here, M_0 is the mass of the object that undergoes orbital precession.

The quantity $V_r = 2\pi/P = a^{-3/2}\sqrt{GM_0}$ is the radial velocity with P being the orbital period. $M_*(a_2)$ is the mass enclosed within the outer semi-major axis a_2. Equation (3.1) shows the initial mass distribution in the Plummer sphere. The mass enclosed in the orbit of the triple SMBH is thus

$$M(< a_2) = Ma_2^3 \left(a_2^2 + a_{\text{scale}}^2\right)^{-3/2} \quad , \tag{2.32}$$

where a_2 is the outer semi-major axis of the triple system. The enclosed mass for a SMBHB is often small. For example, if $a_2 = 0.02$ N-body units, then enclosed mass of the triple orbit for the outer semi-major axis is merely 0.003% of the entire system. The factor $G_m(e, \gamma)$ in Equation (2.31) is

$$G_m(e_2, 2) = (1 + \sqrt{1 - e_2^2})^{-1} \quad . \tag{2.33}$$

When $\gamma = 2$. For $\gamma \neq 2$,

$$G_m(e_2, \gamma) \approx \frac{2}{2-\gamma}\alpha(\gamma) \quad . \tag{2.34}$$

When the eccentricity is low, $\alpha(\gamma) = \alpha_1$,

$$\alpha_1(\gamma) \approx \frac{3}{2} - \frac{79}{60}\gamma + \frac{7}{20}\gamma^2 - \frac{1}{30}\gamma^3 \quad , \tag{2.35}$$

and when the eccentricity is high, $\alpha(\gamma) = \alpha_2$, where

$$\alpha_2(\gamma) \approx \frac{3}{2} - \frac{29}{20}\gamma + \frac{11}{20}\gamma^2 - \frac{1}{10}\gamma^3 \quad . \tag{2.36}$$

Mass-precession is effective in hindering the Kozai resonance when the mass-precession timescale is much shorter than the Kozai timescale.

2.10 Stellar evolution

Stellar evolution has been a hot research topic for a long period of time. This section provides a schematic description of star formation and stellar evolution. Protostars originates from the condensation of interstellar medium (ISM) in hydrostatic equilibrium. Because of inhomogenity in the internal structure of large mass molecular cloud, gravitational collapse take place and molecular cloud break into small cores to achieve These small cores accrete surrounding gas and collapse again in order to achieve hydrostatic equilibrium. After a number of iterations of this process, a star forms. Stars in this stage is very convective with a low temperature and high luminosity. Its luminosity increase dramatically with nearly constant effective temperature. When a radiative core forms, star leaves the Hayashi track and increase its effective temperature with convective shell contracts until the fusion of hydrogen release enough energy to resist gravitational forces. This point is the beginning of Zero age main sequence (ZAMS). During the main sequence evolution, star transform its Hydrogen to Helium by nuclear fusion. The primary factor controlling this process is mass. The luminosity is dependent on its mass. With a certain chemical composition, the relationship between luminosity and mass can be approximated:

$$\frac{L}{L_\odot} \simeq \begin{cases} 0.23\left(\frac{M}{M_\odot}\right)^{2.3} (M \leq 0.43M_\odot) \\ \left(\frac{M}{M_\odot}\right)^{4} (0.43M_\odot \leq M \leq 2M_\odot) \\ 1.4\left(\frac{M}{M_\odot}\right)^{3.5} (2M_\odot \leq M \leq 55M_\odot) \\ 32000\left(\frac{M}{M_\odot}\right) (M \geq 55M_\odot) \end{cases} . \tag{2.37}$$

(Cuntz & Wang 2018, Duric 2003, Salaris & Cassisi 2006) The nuclear timescale is the time required for all the hydrogen to burn into helium.

$$\tau_{nuc} = \frac{\epsilon M c^2}{L} q \tag{2.38}$$

q is the fraction of mass used for nuclear fusion. M is the mass of star. c is the speed of light. ϵ is the amount of mass converted into energy. From the two equation above, it is clear that star with higher mass burn faster. After the exhaustion of hydrogen in the core, the radius of star increase greatly and decrease its effective temperature. This process is named subgiant branch. With decreased effective temperature, opacity increases and convective envelope grows. The process of envelope grows is called giant branch. Hydrogen burning shell keeps adding helium to the core and mixing core helium with surface. When the temperature of core become sufficiently high, helium start burning as fuel source of nuclear fusion. When helium are exhausted, the asymptotic giant branch begins. On the AGB, helium shell keeps adding carbon to the carbon core. When the helium shell touches the hydrogen envelope, the hydrogen shell get re-ignited and cause release of luminosity. The radius of star become very large on the AGB phase, decrease its gravity on the surface and loss its mass. Low mass star will evolve into a white dwarf and high mass stars will evolve into neutron stars. Even higher mass stars will directly collapse into a black hole (Hurley, Pols, & Tout 2000). The evolution pathway of a star ultimately depends on its initial mass and chemical composition. Hertzsprung-Russell diagram (HRD) is a very important tool in analyzing the evolution of a star. It contains information about luminosity (L) and effective temperature (T_{eff}). The lifetime of a star is dependent on its initial mass and its metallicity. Pre-main sequence stars are stars that have achieved hydrostatic equilibrium. The mass spectrum of pre-main sequence stars has three key points: $0.5\,\mathrm{M}_{\odot}$, $3\,\mathrm{M}_{\odot}$, and $10\,\mathrm{M}_{\odot}$. Stars with less than $0.5\,\mathrm{M}_{\odot}$ masses are convective when they enter the main sequence process. Stars with a mass between $0.5\,\mathrm{M}_{\odot}$ and $3\ \mathrm{M}_{\odot}$ remain convective in the pre-main sequence but become radiative in one region when they enter the main sequence. Stars with a mass between $3\,\mathrm{M}_{\odot}$ and $10\,\mathrm{M}_{\odot}$ are radiative in the pre-main sequence. Stars with a mass of more than $10\,\mathrm{M}_{\odot}$ enter the main-sequence directly (Palla 2012).

The relation between luminosity and temperature that describe the transition from PMS to MS is called the Hayashi track on HRD (Hayashi 1961). During the MS phase, stars with a mass between 0.08 $\mathrm{M}_{\odot}$ and 0.5 $\mathrm{M}_{\odot}$ are convective, while stars with a mass between 0.5 $\mathrm{M}_{\odot}$ and 1.5 $\mathrm{M}_{\odot}$ consist of a radiative core and a convective mantle. Other stars with a mass of more than 1.5 $\mathrm{M}_{\odot}$ have a radiative mantle and a convective core (Hansen & Kawaler 1994). Hayashi (1961) suggests that stars with a mass between 0.01 $\mathrm{M}_{\odot}$ and 0.08 $\mathrm{M}_{\odot}$ will fail to ignite their hydrogen. These stars are brown dwarfs (Kumar 1962). Stars between 0.08 $\mathrm{M}_{\odot}$ and 8 $\mathrm{M}_{\odot}$ will end up with a white dwarf. A single white dwarf will evolve into a black dwarf, but under certain circumstances, a white dwarf may end up with a type I supernova (Mazzali et al. 2007). Stars between 8 $\mathrm{M}_{\odot}$ and 25 $\mathrm{M}_{\odot}$ (Heger et al. 2003) will evolve into neutron stars (Woosley & Janka 2005). In 1939, Oppenheimer and Volkoff demonstrated that the maximum mass of a neutron star is 3 $\mathrm{M}_{\odot}$ (Oppenheimer & Volkoff 1939). One type of neutron star, known as ”pulsars”, can under specific conditions, be detected using gravitational wave detectors such as IPTA. Stars with a mass of more than 25 $\mathrm{M}_{\odot}$ also collapse, but the final product is a black hole. Figure 2.10 shows the Hayashi track for pre-main sequence stars.

2.11 Detection of Stellar-mass black holes

Einstein’s theory of general relativity states that gravity is the curvature of space-time. Therefore, massive objects distort the fabric of space-time around it. Light travel through

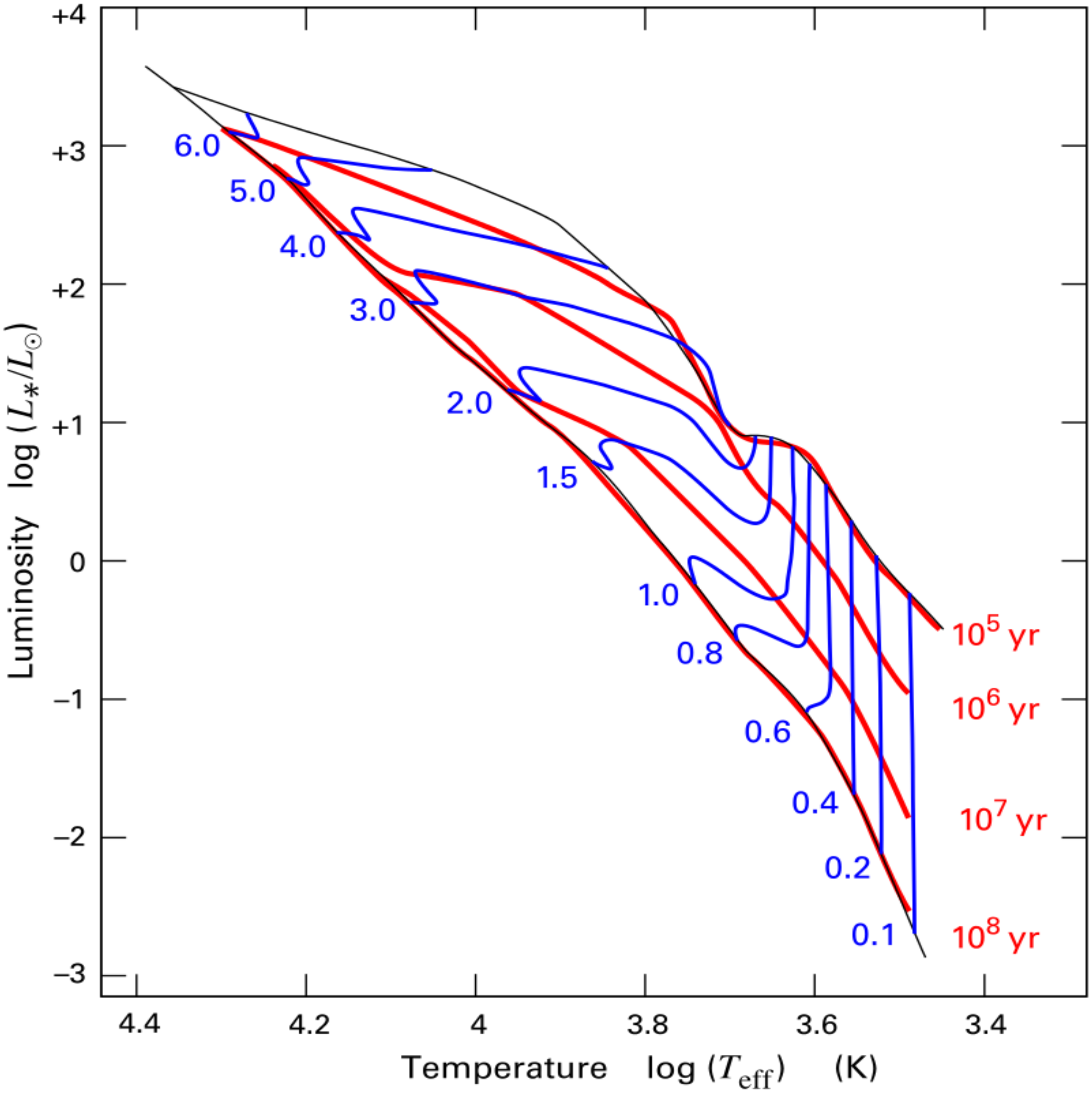

Figure 2.9: Track for Pre-main-sequence stars. Vertical lines are Hayashi tracks. The track on the left of the Hayashi track are Henyey track. More massive stars does not have Hayashi track (Henyey, Lelevier, & Levée 1955). The end of Henyey track represents the mass in $M_\odot$ on the main sequence. Red curves are isochrone at given age. Image credit:Stahler & Palla (2004).

the shortest distance between two points in the space time. The paths that light travel in curved space-time are called geodesics. Usually the issue of light bending is negligible. In this case, first order approximation of Einstein's formula is sufficient for dealing with light bending. But the issue of light bending become significant when light pass through neutron star or black holes. Einstein's equation requires higher order approximation to deal with very strong deflection of photon when light bypass astronomical object with very high density. The detection of stellar-mass black hole has been a long time. Stellar-mass black hole binaries can be measured by either dynamical mass measurement or from the remnant of gravitational-wave event (Abbott et al. 2016, Sahu et al. 2022, Özel et al. 2010).

2.12 Formation of stellar mass BHs

Stellar mass BHs are usually considered as a product of stellar evolution of massive stars. An alternative formation mechanism of BH is the gravitational collapse process during the early stage of Universe. Two important processes of the formation of BHs are supernova explosions and stellar winds. Stellar winds are very important for the study of compact remnant because the outcome of supernova explosion is highly dependent on the total mass and metallicity of stars. Abbott (1982) mentions that stellar wind mass loss rate $\dot{M}$ is proportional to the power of α of metallicity Z_α, with multiple scattering of photon ignored. Vink, de Koter, & Lamers (2001) included multiple scattering effect of photon and conclude that stellar wind mass loss rate $\dot{M}$ is proportional to Z_α, where $\alpha = 0.85$. The effective temperature range is 12500 K - 50000 K, with bi-stability jump at 25000 K.

2.13 Mass gap of stellar mass black holes

The discovery of stellar black holes leaves dilemma to the theory of stellar evolution. Stellar evolution theory suggests that massive stars with helium burning core in the mass range of 64-135 $M_\odot$ end their lives with pair instability supernovae with no remnant. If the helium core is in the mass range of 32-64 $M_\odot$, self-generated pulse may enhance the mass-loss rate before supernovae. This process is called pulsational pair-instability supernovae. This process may result in the absence of stellar mass BH in the range of 32-64 $M_\odot$. The upper and lower bound of mass gap is highly uncertain or even not exist, but it is highly dependent on the parameter of star, including metallicity, rotation speed and the rate of carbon-oxygen nuclear reaction. Including more factors complicate the mass gap problem, such as stellar wind and core overshooting (Belczynski et al. 2010).

2.14 Physics of gravitational waves

Consider a binary system with two component masses M_1 and M_2. The characteristic strain amplitude is

$$h = \left(\frac{128\pi^{\frac{1}{3}}}{15}\right)^{\frac{1}{2}} \frac{M_{\mathrm{c}}^{\frac{5}{3}}}{r} f^{\frac{2}{3}} \quad , \tag{2.39}$$

where quantity M_{c} is the chirp mass, r is the luminosity distance, and f is the frequency of the gravitational wave. It may also be written as:

$$h = 4.1 \cdot 10^{-22} \left(\frac{\mu}{\mathrm{M}_\odot}\right)^{\frac{1}{2}} \left(\frac{M_1 + M_2}{\mathrm{M}_\odot}\right)^{\frac{1}{3}} \left(\frac{100\mathrm{MPc}}{R}\right) \left(\frac{100\mathrm{Hz}}{f_{\mathrm{c}}}\right)^{\frac{1}{6}} \tag{2.40}$$

(Hawking & Israel 1989).
SMBH binaries with mass ranging from $10^5\,\mathrm{M}_\odot$ to $10^{10}\,\mathrm{M}_\odot$ are expected to be the loudest gravitational wave source within the frequency band from 10^{-4} mHz to 1 mHz. Using a gravitational wave observatory helps observe these phenomena. Since SMBH binaries are commonly lying in the center with gas and stars crowded, the observation of SMBH binary coalescence is usually coupled with an electromagnet counterpart. Understanding these phenomena helps in understanding the co-evolution of galaxies and SMBHs.

2.15 Detection of gravitational waves

One century from now, Einstein predicted the existence of gravitational waves (Weinstein 2016). However, the existence of gravitational waves from binary black holes was not proved until 2015 (Abbott et al. 2016). The first gravitational wave event was observed by Laser Interferometer Gravitational-Wave Observatory (LIGO) on September 14th, 2015, named GW150914. The initial binary black hole masses are 36 $\mathrm{M}_\odot$ and 29 $\mathrm{M}_\odot$, respectively. Abbott et al. (2017) discovered a gravitational wave event with component mass of 12 $\mathrm{M}_\odot$ and 7 $\mathrm{M}_\odot$. It was the lightest companion until the discovery of GW170817. On August 17th, 2017, LIGO observed the gravitational wave signal of the inspiral of double neutron stars with an electromagnetic counterpart. The component mass of the binary neutron star is in the range of 1.17 $\mathrm{M}_\odot$ - 1.60 $\mathrm{M}_\odot$, with a total mass of 2.74 $\mathrm{M}_\odot$. This is the first detection of

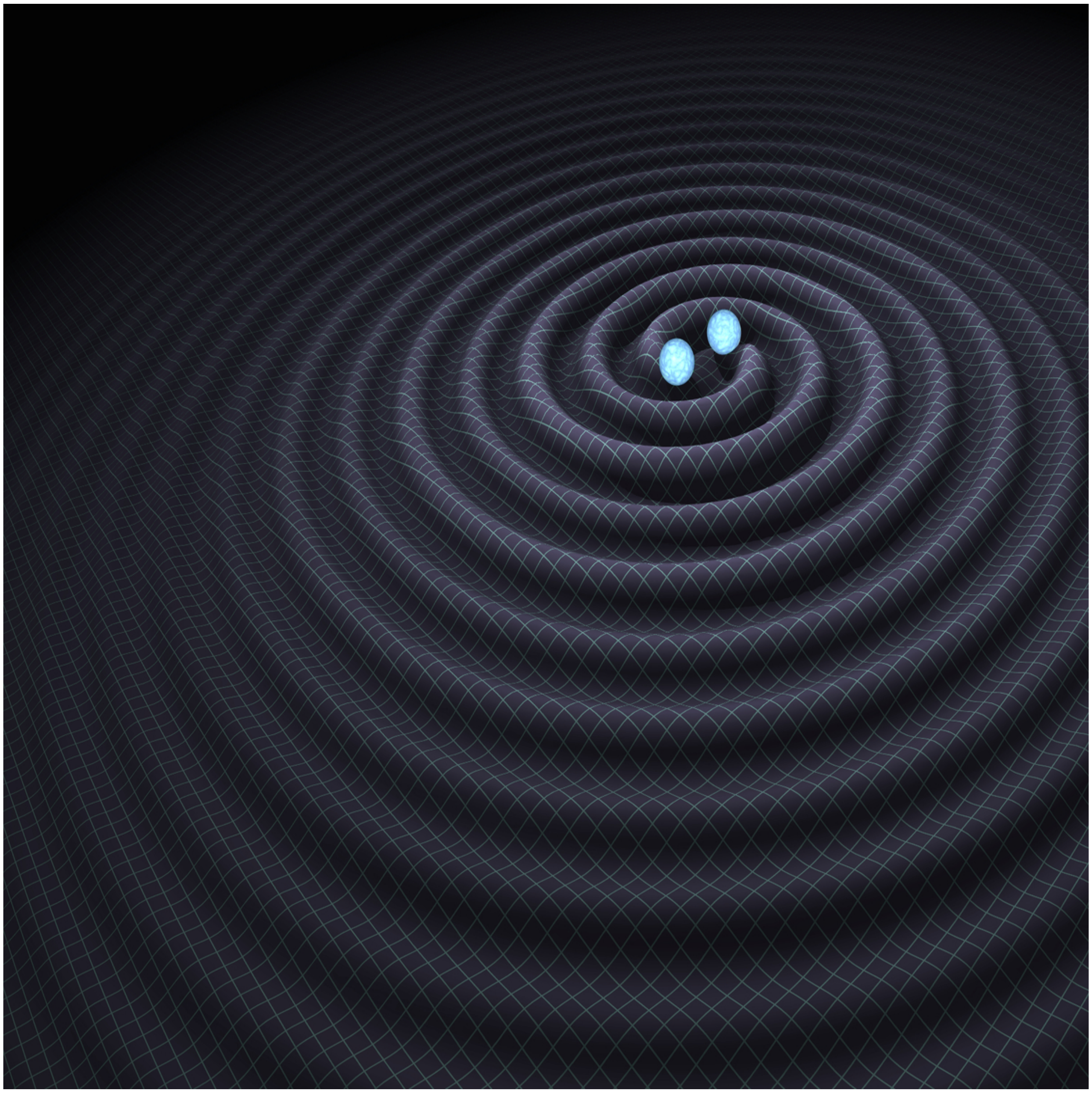

Figure 2.10: The final stage of binary black hole merger process. image credit: LIGO scientific collaboration.

Table 2.1: A collection of representative gravitational wave events detected. The unit of each component is in $M_\odot$.

Gw event ID	M_1	M_2	M_{final}	Type of GW event
GW150914	32-41	25-33	58-67	BH-BH (Abbott et al. 2016)
GW151226	11-23	5-10	19-27	BH-BH (Abbott et al. 2016)
GW170104	25-40	13-25	46-57	BH-BH (Abbott et al. 2017)
GW170608	5-9	9-19	18-24	BH-BH (Abbott et al. 2017)
GW170814	28-36	21-28	51-56	BH-BH (Abbott et al. 2017)
GW170817	1.36-2.26	0.86-1.36	2.73-3.29	NS-NS (Abbott et al. 2017)
GW190412	24.4-34.7	7.4-10.1	33.1-41.1	BH-BH (Abbott et al. 2020)
GW190425	1.61-2.52	1.12-1.68	3.3-3.7	NS-NS (Abbott et al. 2020)
GW190521	85	66	142	BH-BH (Abbott et al. 2020)
GW190814	23	2.6	25.6	BH-unknown (Abbott et al. 2020)

a binary neutron star merger. Figure 2.11 shows a simulation of the GW170817 event. The GW190521 was the first gravitational wave event, with the remnant being an intermediate massive black hole. The mass of the remnant is 142 $M_\odot$ (Abbott et al. 2020). A list of GW events detected is included in Table 2.1. Figure 2.15 shows a schematic simulation of binary black hole merging. GW200105 and GW200115 are the first two neutron star-black hole merger events. The component of the source of GW200105 is 8.9 $M_\odot$ and 1.9 $M_\odot$. The source of GW200115 consists of a neutron star with 1.5 $M_\odot$ and a black hole with 5.7 $M_\odot$ (Abbott et al. 2021). The GW170104 event was the first event that measured the spin of a remnant.

The compact binary in GW190814 has the most unequal mass ratio. The light companion is either the heaviest neutron star or the lightest black hole . In the observation of GW190412, the more massive black hole has a spin magnitude between 0.22 and 0.6 while its companion does not rotate . In the observation of GW190425, the masses of two companions are measured, but the type of these two dense object cannot be determined .

2.16 Instruments for detecting gravitational waves

2.16.1 LISA and eLISA

Laser Interferometer Space Antenna (LISA) and evolved Laser Interferometer Space Antenna (eLISA) are designed to detect gravitational wave sources from massive black hole binaries. eLISA can detect black hole binaries with a mass range from $10^4 M_\odot$ to $10^7 M_\odot$ (eLISA

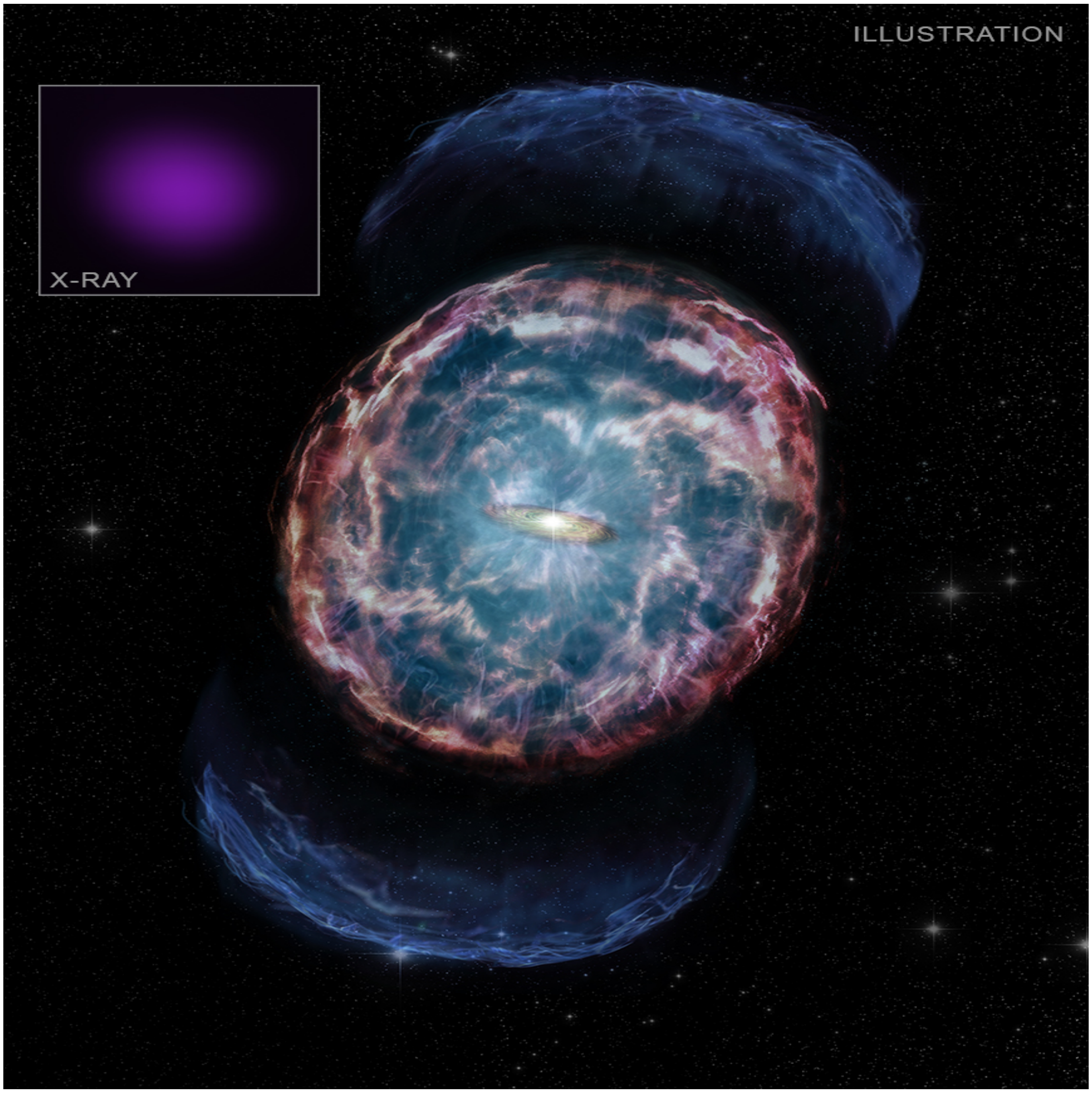

Figure 2.11: Simulation of GW170817. image credit: LIGO scientific collaboration.

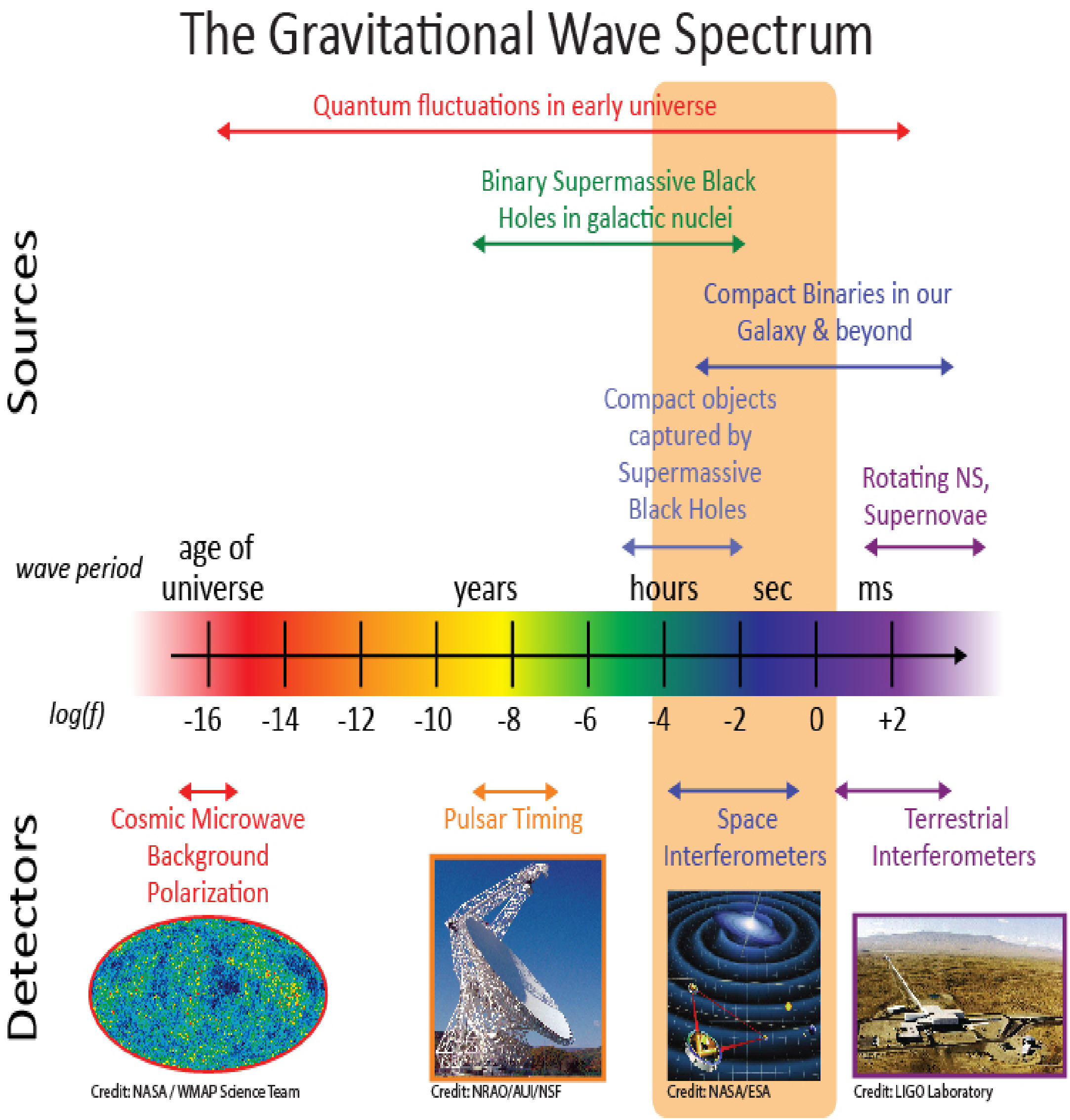

Figure 2.12: Gravitational wave spectrum and corresponding detection technique. image credit: LISA.

Consortium et al. 2013). Figure 2.13 shows the orbits of LISA satellites. Figure 2.14 shows the sensitivity curve of LISA.

2.16.2 Taiji

The taiji program, like LISA, consists of three GW detectors in an equilateral triangle shape. By measuring the phase difference between the sent signal and received signal, change in arm length with respect to time can be measured, find the GW signal. The best target for the Taiji program are MBHBs, but it can also be utilized to detect GW signal from EMRI, IMRI, compact binaries, universe inflation, and heating/preheating. Figure 2.16 shows the schematic description of Taiji.

2.16.3 Tianqin

The mission design of TianQin is analogous to LISA. They share the same frequency. TianQin is more like a gravitational wave detector rather than an observatory. It shares the same frequency band detectable by LISA and only detects the gravitational wave emitted from LISA-verified binaries, such as J0806 (Luo et al. 2016). Figure 2.17 shows a description of the mission design of TianQin.

2.16.4 International Pulsar Timing Array

Pulsars are highly magnetized neutron stars with a rotation period of several milliseconds. Such a stable rotation makes any ripples in space-time become visible to high-precision telescopes. The slight distortion in space-time is not sufficient for direct detection of GW events, but it can help separate GW signal from background detector noise with different pulsars, given a relatively long period of time (several years). The distance between Earth and the pulsar is served as the effective arm length of the detector, allowing indirect detection of GW signal from SMBHB. The international Pulsar Timing array (IPTA) consists of the European Pulsar Timing Array (EPTA), the North American Nanohertz Observatory for Gravitational Waves (NANOGrav), the Indian Pulsar Timing Array (InPTA), and the Parkes Pulsar Timing Array (PPTA) (Dahal 2020).

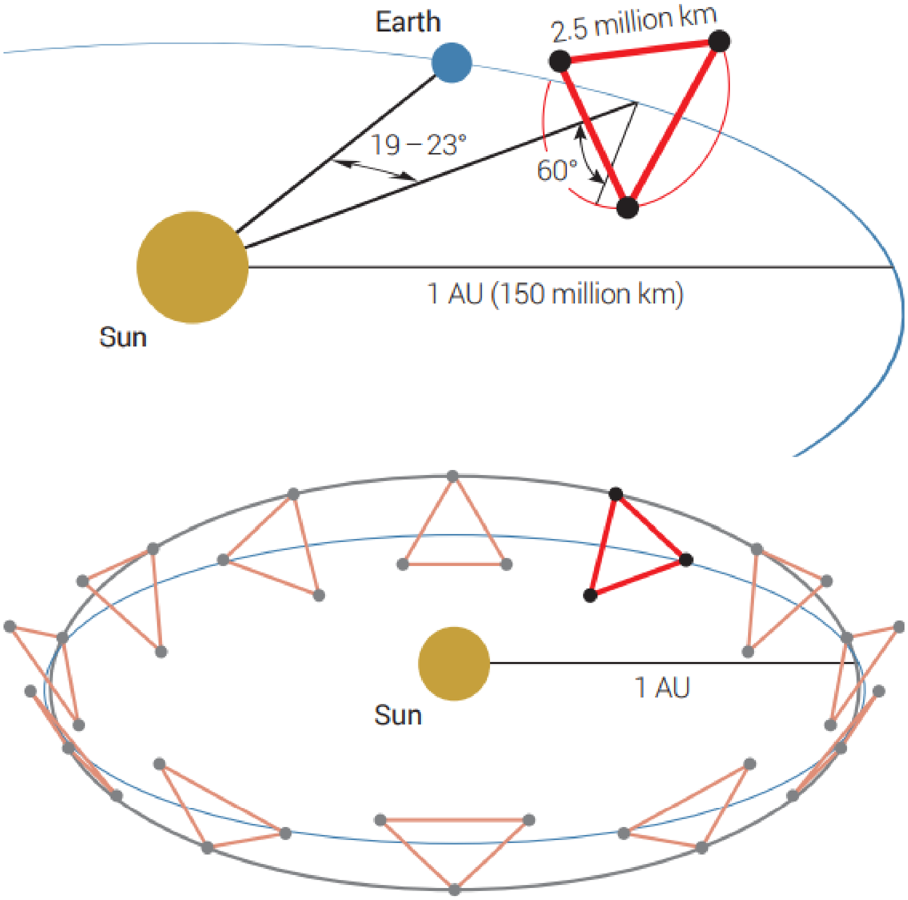

Figure 2.13: Orbits of the LISA satellites.

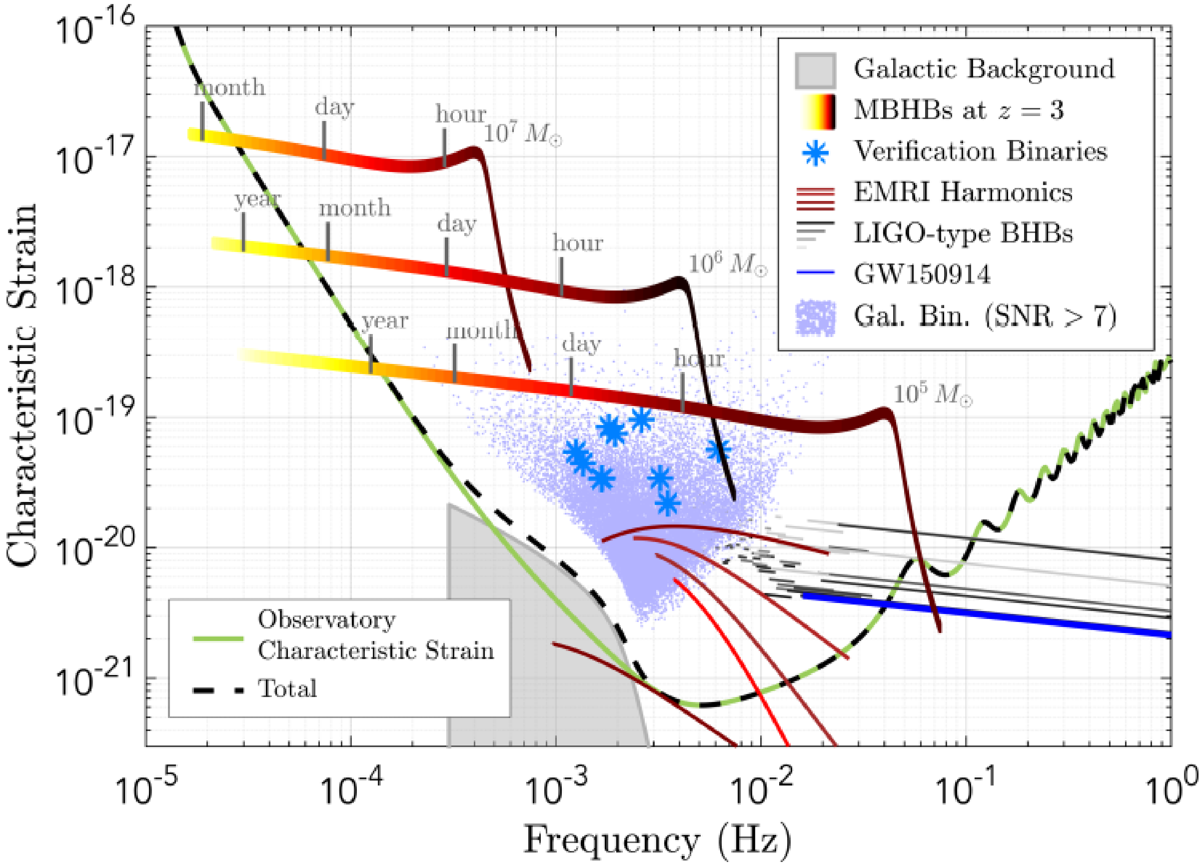

Figure 2.14: Characteristic strain vs. frequency of gravitational wave detectable by LISA, The green curve indicates the sensitivity.

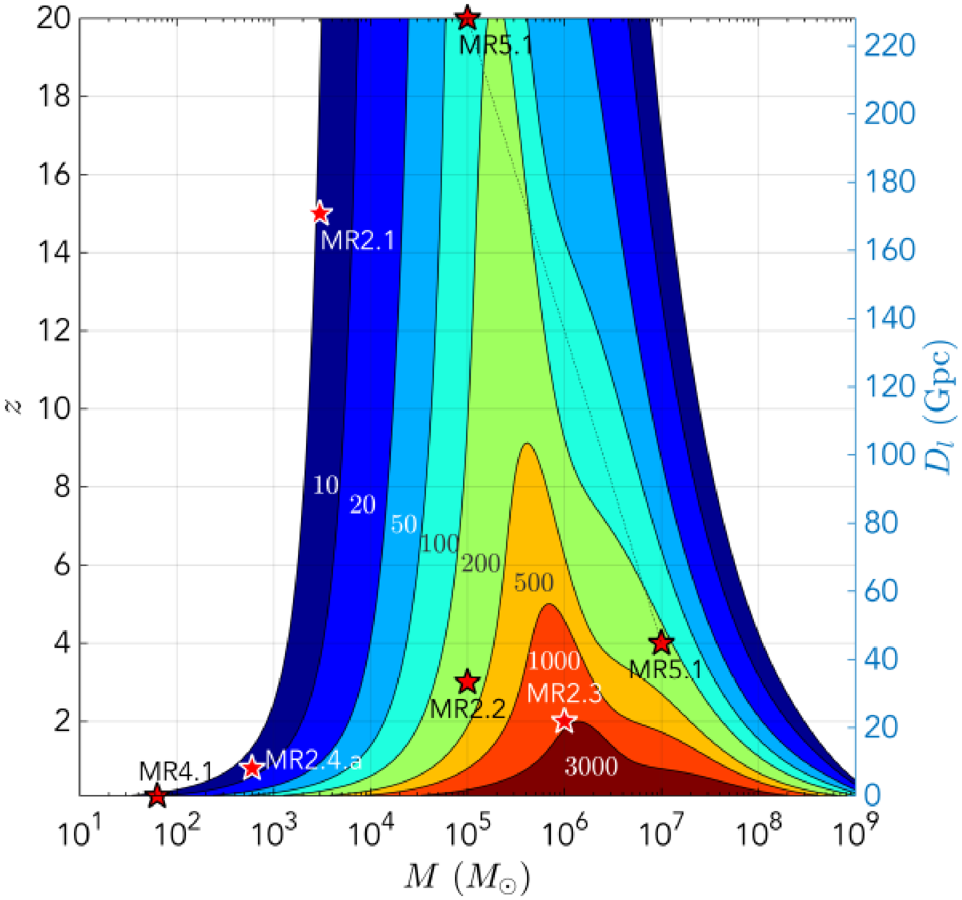

Figure 2.15: Constant signal-to-noise ratios as a function of redshift, luminosity distance and total mass of the binary black hole. Image credit: Amaro-Seoane et al. (2017).

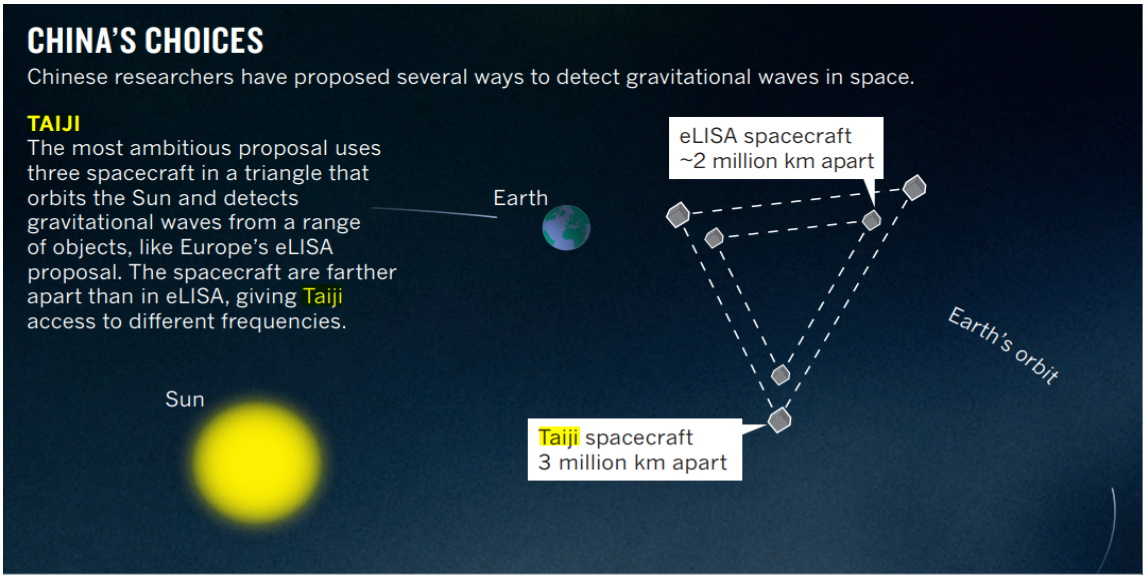

Figure 2.16: Detailed schematic description of Taiji. Image credit: Ruan et al. (2020).

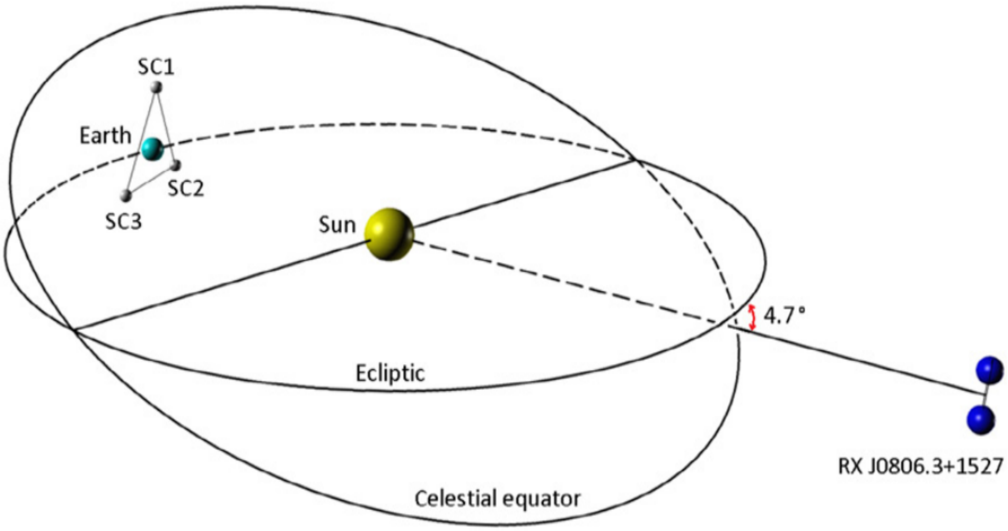

Figure 2.17: Tianqin and its reference object for detecting gravitational wave.

2.17 Observation and scarcity in detecting IMBHs

Drawbacks for dynamical modeling of SMBH are very obvious, including difficulty in distinguishing between orbit anisotropy and mass, degeneracy between stellar mass-to-light ratio and black hole, incomplete stellar orbit libraries, and the bankruptcy of axisymmetric assumption. In a low-mass system, four additional challenges occur. If we need to detect an IMBH with a mass of $10^5 \mathrm{M}_\odot$, then the angular size of the region containing IMBH is roughly 0.2", which is very small. Mass-to-light ratio factor can also be disguised due to ongoing star formation. The brightness of individual stars can bias the stellar dispersion of the measured region by influencing the light output of the measured area. Last but not least, the difference between an IMBH and a group of stellar remnant is small, making confirmation of IMBH even harder. IMBHs are widely considered the seeds of SMBH formation. However, detections of IMBHs is rare. The merger product of GW190521 is a confirmed IMBH with a mass at the low end of the IMBH mass spectrum. The first detection of an IMBH with a mass in the range $10^2\,\mathrm{M}_\odot - 10^3\,\mathrm{M}_\odot$ is the merger product of a gravitational wave event GW190521. The signal of GW190521 originates from a binary stellar-mass black hole with a primary black hole of 85 $\mathrm{M}_\odot$ and a secondary mass of 66 $\mathrm{M}_\odot$ (Abbott et al. 2019). The formation process of such a binary system is still under debate. The primary black hole may have formed through stellar collapse or a hierarchical BHs/massive stars merger in a star cluster (Abbott et al. 2020). The scenario of this event has been discussed extensively, including hierarchical mergers in a star cluster (Abbott et al. 2020) and the first generation of Population III stars (Liu & Bromm 2020).

The most confirming candidate, although it still remains elusive, is HLX-1. The IMBH candidate HLX-1 has a mass range of 6300-50900 $\mathrm{M}_\odot$ if it has no spin, and the mass range of this candidate is 16900-191700 $\mathrm{M}_\odot$ with maximum spin (Straub et al. 2014). HLX-1 has been proven to lie in a star cluster (Farrell et al. 2014). Another IMBH candidate with a mass at the high end of the mass spectrum is located in B023-G78, the most massive globular cluster in M31. It has been proved to have a dynamical mass of roughly $9.1 \cdot 10^4 \mathrm{M}_\odot$ (Pechetti et al. 2022). The scarcity of IMBH observation and the wealthy observation of SMBH brings up a question: how does IMBH grow into SMBH? If we consider a BH with a mass of 100 $\mathrm{M}_\odot$ accrete at the Eddington limit with no interruption, then the time for it to grow to $10^9 \mathrm{M}_\odot$ is about 0.8 Gyr, far less than a Hubble time. This is a viable approach to creating an SMBH at $z \approx 6$. But the constant Eddington limit accretion does not necessarily happen. The accretion rate can either be sub-Eddington or super-Eddington.

The alternative is to start with a more massive IMBH (Haiman 2013). Barth et al. (2003) derived the mass of a black hole lies in the quasar SDSS J114816.64+525150.3 with a redshift $z = 6.4$. It suggests that a stellar-mass black hole can grow to a SMBH with Eddington accretion if the stellar-mass black hole is distant enough. The formation of massive black holes (MBH) can come either from stellar origin or cosmological origin.

The theoretical formation mechanism of IMBH can be divided into six parts:

- Remnant of Population III stars
- Gas dynamical processes
- Stellar collision
- Hierarchical black hole merger
- Primordial black hole
- Cosmic loop string

(Volonteri, Habouzit, & Colpi 2021). Population III stars are stars from the condensation of zero-metallicity gas and are expected to form SMBH. The mass of first star is $\approx 10^6$ $M_\odot$. If the first star is very massive until the end of its life, then it will collapse very fast. Low-metallicity massive stars (25 $M_\odot$ - 140 $M_\odot$) tend to form very light black holes under a direct collapse process, while heavier stars (140 $M_\odot$ - 260 $M_\odot$) undergo pair-instability supernovae, burn their fuel, and explode with no remnant. Stars heavier than 260 $M_\odot$ undergo another process. The energy burn is not enough to resist the implosion before photon disintegration instability and forms a black hole with all the heavy elements swept inside.

Another proposed mechanism for MBH formation is dense gas contraction. It was suggested that efficient gas collapse only occurs in massive metal-free halo with virial temperature $T \geq 10^4 K$. These gas were cooled by atomic hydrogen to nearly 4000 K and then contracted adiabatically. Substantial angular momentum transport is required for gas to contract to form an MBH, even with the aid of efficient gas cooling. Quick angular momentum shedding can be achieved by global dynamical instabilities. When the rotation speed of a self-gravitating gas cloud exceeds a threshold value, it becomes unstable and transports angular momentum outward via gravitational and hydrodynamical torque and reduces its radius. This process is a positive feedback loop (Volonteri 2010).

Black hole seeds in globular clusters with a mass between $10^4 M_\odot$ and $10^7 M_\odot$ may grow to an IMBH via repeated mergers with other seeds (Giersz et al. 2015). Due to their high masses, they sink to the center via the aid of dynamical friction. In the center of a cluster, close interaction between IMBHs may result in the ejection of bound binary IMBH, stopping the merger process (Sigurdsson & Hernquist 1993). The main obstacle of this IMBH formation approach is the GW-recoil velocity kick to the merged product that can kick the merged IMBH out of the cluster (Lousto et al. 2010).
MBH can also form via stellar collision (Freitag, Gürkan, & Rasio 2006, McMillan et al. 2004, Portegies Zwart et al. 2004). In this process, a very massive star (VMS) forms in a low metallicity dense stellar cluster via runaway collision. Then the VMS collapses to an IMBH with a similar mass (Mapelli 2016, Reinoso et al. 2018). A massive star with mass in the range of 800 $M_\odot$ -3000 $M_\odot$ form through stellar merger and sink to the center of star clusters very quickly. The massive star later collapsed to an IMBH (Madau & Rees 2001). The formation mechanism of IMBHs has been widely discussed. The first proposed scenario is the growth of massive stars via physical collision in the center of a cluster that have migrated with the aid of mass segregation (Freitag, Gürkan, & Rasio 2006, Gürkan, Fregeau, & Rasio 2006, Portegies Zwart & McMillan 2000, Portegies Zwart et al. 2004). Giersz et al. (2015) suggest that an IMBH may form from the remnant of a supermassive star produced by the merger of massive stars in the center of a globular cluster. IMBHs can also form through multiple merger processes of SBHs (Miller & Hamilton 2002). Another IMBH formation channel is the direct collapse of Population III stars or gas clouds. The mass range of IMBH originates from the gas cloud is 10^4-10^6 $M_\odot$ (Madau & Rees 2001), while IMBH produced by the collapse of Population III stars has a mass range of ≈ 100 $M_\odot$ (Fryer, Woosley, & Heger 2001).

Although a lot of numerical studies have been conducted to simulate the formation scenarios of IMBH, The confirmed detection of IMBH at the low end of the mass spectrum is rare. Currently, the component of GW190521 was explained with several proposed approaches:

- Formation of population III stars (Liu & Bromm 2020, Tanikawa et al. 2021)
- Binary evolution (Belczynski 2020)
- Stellar collision (Rizzuto et al. 2021)
- Hierarchical merger in a young massive cluster, nuclear cluster, globular cluster, and

active galactic nuclei (Mapelli et al. 2021)

2.18 Numerical methods

It is impossible for the analytic and semi-analytic models to describe the complexity of the evolution of the physical properties of a globular cluster. The major obstacles for realistic globular cluster simulation are the calculation of forces between stars and short half-mass relaxation time. The evolution of globular cluster is very sensitive to initial conditions, so various models with different initial conditions are required for a systematic study of the dynamical evolution of globular clusters (Aarseth 1999).

2.18.1 Collisional and collisionless systems

All gravitational systems can be divided into two subgroups: collisional and collisionless systems. Good examples of collisionless systems are dark matter halos and galaxies, while good examples of collisional systems are galactic centers and globular clusters. The criteria for classifying collisional and collisionless systems is the two-body relaxation timescale. The two-body relaxation timescale can be written as

$$T_{\mathrm{relax}} = \frac{0.13\sigma^3}{G^2 m \rho \ln \lambda} \tag{2.41}$$

(Spitzer 1987), where the σ is the velocity dispersion of stars, m is the mass of an individual star, ρ is the stellar density, and $\ln \lambda$ is the impact parameter. In a collisional system, the two-body relaxation timescale is shorter than the lifetime of the system. In contrast, in a collisionless system, the two-body relaxation timescale is much longer than the lifetime of the system.

2.18.2 Formulation of the N-body problem

"Direct N-body" means that the forces acting on one particle is calculated using the standard Newton's law. The equation of motion is:

$$\vec{F_{\mathrm{ij}}} = -\frac{G m_{\mathrm{i}} m_{\mathrm{j}} \vec{r_{\mathrm{ij}}}}{|r_{\mathrm{ij}}|^3} \quad ; \tag{2.42}$$

$$\vec{F_{\rm ij}} = -\sum_{\rm j}^{\rm i \neq j} \frac{G m_{\rm i} m_{\rm j} \vec{r_{\rm ij}}}{|r_{\rm ij}|^3} \quad . \tag{2.43}$$

When the particle number N is 2 or less, this set of equations of motion has an analytical solution, but this set of the equation of motion can not be solved analytically when the particle number N is more than 2, so it is necessary to apply a numerical method to solve. The pioneering study of N-body simulation was conducted by Holmberg (1941), who used light bulbs to represent the encounter of stellar in nebulae and study the effect of nebulae tidal capture. The pioneer computational simulation of a stellar system was brought by von Hoerner (1960), with particle number $N = 16$. When the distance between two particles is too small, the singularity may occur during the computation process. It was first solved by using a softening potential. Aarseth (1963) simulated the dynamical evolution of clusters of galaxies with a suite of software named NBODY1 using a softening potential. It found that the mass of the central region increases. Inspired by NBODY1, ϕGRAPE was created (Harfst et al. 2007). Later, ϕ-GPU was developed from ϕGRAPE (Berczik et al. 2011). ϕ-GPU uses Graphical processing unit (GPU) as a device for the acceleration of force calculation, enabling utilization of multiple GPU cores on each node of computing clusters.

2.18.3 Direct N-body methods

2.18.3.1 Hermite scheme and individual timestep

In theory, the position and velocity at any arbitrary time can be calculated by the integration of net force. However, information on position and velocity can only be obtained at a certain time t with a timestep δt. Acceleration for one particle is defined as:

$$\vec{a_{\rm i}} \equiv \frac{\vec{F_{\rm i}}}{m_{\rm i}} \quad ; \tag{2.44}$$

$$\vec{v_{\rm i}}(t_{\rm k}) = \vec{v_{\rm i}}(t_{\rm k-1}) + \vec{a_{\rm i}}(t_{\rm k-1})\delta t \quad ; \tag{2.45}$$

$$\vec{r_{\rm i}}(t_{\rm k}) = \vec{r_{\rm i}}(t_{\rm k-1}) + \vec{v_{\rm i}}(t_{\rm k-1})\delta t \quad . \tag{2.46}$$

The complexity of the calculation above is $O(N^2)$. To obtain a realistic position and velocity of each particle, δt must be very small, which means that the computational cost is very high. When simulating galaxies and cosmological events, the amount of calculation becomes extremely high, so it is impossible to simulate stellar systems in a realistic computational time. To deal with this dilemna, several approaches have been proposed. The Hermite scheme is applied to deal with the operations that has high computational resource costs. This scheme maintains the same accuracy with a much larger time step. It is based on the Taylor expansion of position and velocity with the prediction-correction method incorporated. Usually, 4^{th} order is the optimal order for this scheme. The position and velocity vector under the Hermite scheme can be calculated with $\vec{a}_i(t_{\mathrm{k-1}})$ and $\vec{a}_{\mathrm{i}}^{(1)}(t_{\mathrm{k-1}})$. $\vec{a}_{\mathrm{i}}^{(1)}(t_{\mathrm{k-1}})$ are calculated as:

$$\vec{a}_{\mathrm{i}}^{(1)}(t_{\mathrm{k-1}}) = -G \sum_{j}^{N;i\neq j} \left(\frac{m_{\mathrm{j}}\vec{v}_{\mathrm{ij}}}{|r_{\mathrm{ij}}|^3} + 3\frac{m_{\mathrm{j}}\vec{r}_{\mathrm{ij}} \cdot \vec{v}_{\mathrm{ij}}}{|r_{\mathrm{ij}}|^2} \frac{\vec{r}_{\mathrm{ij}}}{|r_{\mathrm{ij}}|^3} \right) \quad . \tag{2.47}$$

The $\vec{a}_i(t_{\mathrm{k-1}})$ is calculated using equation. The $\vec{v_{\mathrm{i}}}(t_{\mathrm{k}})$ and $\vec{r_{\mathrm{i}}}(t_{\mathrm{k}})$ are calculated using equation below:

$$\vec{v_{\mathrm{i,p}}}(t_{\mathrm{k}}) = \vec{v_{\mathrm{i}}}(t_{\mathrm{k-1}}) + \vec{a}_{\mathrm{i}}(t_{\mathrm{k-1}})\delta t + \frac{1}{2}\vec{a}_{\mathrm{i}}^{(1)}(t_{\mathrm{k-1}})\delta t^2 \quad ; \tag{2.48}$$

$$\vec{r_{\mathrm{i,p}}}(t_{\mathrm{k}}) = \vec{r_{\mathrm{i}}}(t_{\mathrm{k-1}}) + \vec{v_{\mathrm{i}}}(t_{\mathrm{k-1}})\delta t + \frac{1}{2}\vec{a}_{\mathrm{i}}(t_{\mathrm{k-1}})\delta t^2 + \frac{1}{6}\vec{a_{\mathrm{i}}^{(1)}}(t_{\mathrm{k-1}})\delta t^3 \quad . \tag{2.49}$$

The Taylor expansion of $a_i(t_{\mathrm{k}})$ and $\vec{a}_{\mathrm{i}}^{(1)}(t_{\mathrm{k}})$ are:

$$\vec{a}_i(t_{\mathrm{k}}) = \vec{a}_i(t_{\mathrm{k-1}}) + \vec{a}_i^{(1)}(t_{\mathrm{k-1}})\delta t + \frac{1}{2}\vec{a}_i^{(2)}(t_{\mathrm{k-1}})\delta t^2 + \frac{1}{6}\vec{a}_i^{(3)}(t_{\mathrm{k-1}})\delta t^3 \quad ; \tag{2.50}$$

$$\vec{a}_i^{(1)}(t_{\mathrm{k}}) = \vec{a}_i^{(1)}(t_{\mathrm{k-1}}) + \vec{a}_i^{(2)}(t_{\mathrm{k-1}})\delta t + \frac{1}{2}\vec{a}_i^{(3)}(t_{\mathrm{k-1}})\delta t^2 \quad . \tag{2.51}$$

The higher order term $\vec{a}_i^{(2)}(t_{\mathrm{k-1}})$ and $\vec{a}_i^{(3)}(t_{\mathrm{k-1}})$ can be calculated using following equations:

$$\vec{a}_i^{(2)}(t_{\mathrm{k-1}}) = (-6(\vec{a}_i(t_{\mathrm{k-1}}) - \vec{a}_{\mathrm{i,p}}(t_{\mathrm{k}})) - (4(\vec{a}_i^{(1)}(t_{\mathrm{k}}) + (\vec{a}_{i,P}^{(1)}(t_{\mathrm{k}}))\delta t))\frac{1}{\delta t^2} \quad ; \tag{2.52}$$

$$\vec{a}_i^{(3)}(t_{\mathrm{k-1}}) = (12(\vec{a}_i(t_{\mathrm{k-1}}) - \vec{a}_{\mathrm{i,p}}(t_{\mathrm{k}})) - (6(\vec{a}_i^{(1)}(t_{\mathrm{k}}) + (\vec{a}_{i,P}^{(1)}(t_{\mathrm{k}}))\delta t))\frac{1}{\delta t^3} \quad . \tag{2.53}$$

With $\vec{a}_i^{(3)}(t_{\mathrm{k-1}})$ and $\vec{a}_i^{(2)}(t_{\mathrm{k-1}})$, $r_{\mathrm{i}}(t_{\mathrm{k}})$ and $v_{\mathrm{i}}(t_{\mathrm{k}})$ can be calculated:

$$\vec{r}_{\mathrm{i}}(t_{\mathrm{k}}) = \vec{r}_{\mathrm{i,p}}(t_{\mathrm{k}}) + \frac{1}{24}\vec{a}_i^{(2)}(t_{\mathrm{k-1}})\delta t^4 + \frac{1}{120}\vec{a}_i^{(3)}(t_{\mathrm{k-1}})\delta t^5 \quad ; \tag{2.54}$$

$$\vec{v}_{\mathrm{i}}(t_{\mathrm{k}}) = \vec{v}_{\mathrm{i,p}}(t_{\mathrm{k}}) + \frac{1}{6}\vec{a}_i^{(2)}(t_{\mathrm{k-1}})\delta t^3 + \frac{1}{24}\vec{a}_i^{(3)}(t_{\mathrm{k-1}})\delta t^4 \quad . \tag{2.55}$$

With the Taylor expansion of acceleration and first-order derivative of acceleration, higher order of acceleration can be achieved.

2.18.3.2 Block timestep

The integration method introduced in 2.18.3.1 uses individual timesteps. The computing time and relative error of simulation are highly dependent on δt. The complexity of computing the orbit of each star in a star cluster is $O(N^2)$ for each time step. To save computing resources, the idea of the block time step was proposed.

The density of stars in the center of a star cluster is much higher than the halo, so the stars in the center of a star cluster experience much higher forces and much more frequent force variation. If a uniform time step is adopted, then computation time would be the bottleneck for a realistic star cluster simulation. The basic idea of the block time step is to set different time steps for stars at a different position. Stars in the central region of the star cluster are assigned small δt, and stars in the halo share big δt. Here we define the maximum time step δt_{max}. The timestep for each star is reduced by order of 2:

$$\delta t_{\mathrm{n}} = \frac{\delta t_1}{2^{\mathrm{n}-1}} \quad . \tag{2.56}$$

Usually n is less than 12 for $N \leq 1000$. n can be increased by a few order if $N \approx 10000$.

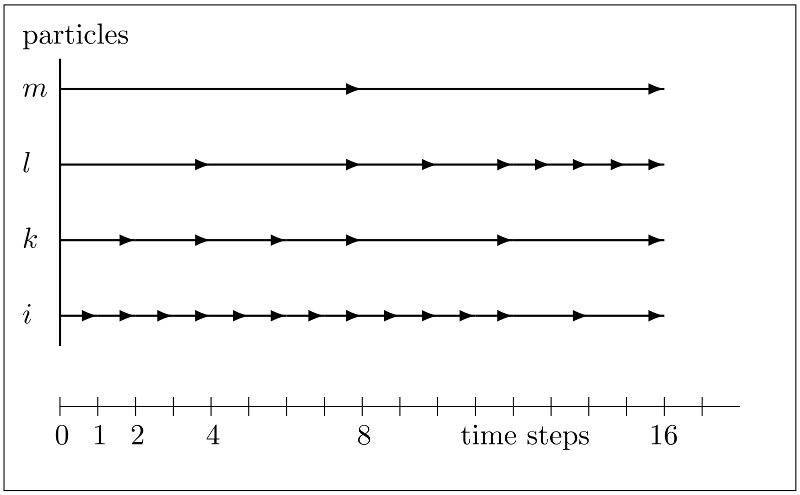

Figure 2.18: Block time steps exemplary for four particles.

2.18.3.3 Ahmad-Cohen neighbour scheme

The calculation of gravitational forces is very computationally expensive. Ahmad & Cohen (1973) proposed a new algorithm called the "Ahmad-Cohen neighbour scheme" to accelerate N-body calculation. It divides the force act on a particular particle i, F_i into neighbour part (irregular part) and distant part (regular part). The timestep for the neighbour particles is small, making computation cost relatively low. The optimal number of neighbour particles is very small compared to total number N. The optimal neighbour particle number is determined by the following formula:

$$N_{\rm n} = \left(\sqrt{\frac{\eta_{\rm n}}{\eta_{\rm d}}} \frac{N}{4} \right) \quad , \tag{2.57}$$

$\eta_{\rm n}$ and $\eta_{\rm d}$ are the accuracy parameters for the stepsize of neighbour steps and distant steps, respectively (Makino & Hut 1988). The regular part of force calculation is very time-consuming. But with very large time steps, the computational cost could also be greatly reduced. The amount of time reduced is proportional to $N^{0.25}$ (Makino & Aarseth 1992).

2.18.4 Close interacting binary treatment

Close encounters and binaries are very important subjects in realistic globular cluster simulation. The strong interaction in close binaries and encounters may lead to very short timestep δt, which may result in a very long computation time. The finite precision of values saved in computer storage may result in an unacceptable numerical error. Very short timesteps originate from very short distances between close encounters and binaries. There are two approaches to dealing with this dilemma. One is called softening, and another one is called regularization.

Kustaanheimo & Stiefel (1965) provided a regularization approach that transforms the equation of motion into an oscillating equation. The so-called KS regularization was a generalization of the Levi-Civita transformation.

$$\epsilon = \begin{bmatrix} u_1 & -u_2 & -u_3 & u_4 \\ u_2 & u_1 & -u_4 & -u_3 \\ u_3 & u_4 & u_1 & u_2 \\ u_4 & -u_3 & u_2 & -u_1 \end{bmatrix} \tag{2.58}$$

$$dt = Rd\tau \quad ; \tag{2.59}$$

$$R = u_1^2 + u_2^2 + u_3^2 + u_4^2 \quad . \tag{2.60}$$

$$\tag{2.61}$$

The component of R is R_1,R_2,R_3 and R_4, which can be written in this form:

$$R_1 = u_1^2 - u_2^2 - u_3^2 + u_4^2 \quad ; \tag{2.62}$$

$$R_2 = 2(u_1u_2 - u_3u_4) \quad ; \tag{2.63}$$

$$R_3 = 2(u_1u_3 + u_2u_4) \quad ; \tag{2.64}$$

$$R_4 = 0 \quad ; \tag{2.65}$$

$$\tag{2.66}$$

$$p_{90} = \frac{2G(m_1 + m_2)}{v_\infty^2} \quad . \tag{2.67}$$

The criteria for a binary to be considered as a KS binary is listed as follows:

- First, the distance between the two particles is less than $r_{\rm min}$
- Second, their timestep is less than $\delta t_{\rm min}$, where the $\delta t_{\rm min}$ is calculated as follows:

$$\delta t_{\rm min} = \kappa\Big(\frac{\eta}{0.03}\Big)\sqrt{\Big(\frac{r_{\rm min}^3}{\langle m\rangle}\Big)} \quad . \tag{2.68}$$

  k is a numerical factor. η is the general time step factor. $\langle m\rangle$ is the average stellar mass in the system.

- Two more criteria are set to search for KS binary:

  $$\mathbf{R} \cdot \mathbf{V} > 0.1\sqrt{(G(m_1 + m_2)R} \quad ;$$
  $$\gamma := \frac{|\mathbf{a}_{\text{pert}}| \cdot R^2}{G(m_1+m_2)} < 0.25 \quad .$$

  $\mathbf{R}$, $\mathbf{V}$, and R are the distance in vector form, velocity vector, and scalar distance of the binary pair, respectively. $\mathbf{a}_{\text{pert}}$ is the vector form of force applied by other perturbing particles.

KS regularization avoids the possible singular computation of close encounters and reduces the computation effort of distant particles because F is proportional to r^{-3} (Aarseth 2003). Its advantages include improved numerical stability, possible error reduction by rectification, and further study of tidal interaction from two-body orbital elements. Stimulated by Kustaanheimo & Stiefel (1965), Aarseth & Zare (1974) provided a regularization method of a three-body problem by introducing two KS transformations and allowing computers to simulate one particle colliding with the other two. To deal with a four-body system, the Chain regularization method was proposed by Mikkola & Aarseth (1990) using KS variable and time transformation. Mikkola & Aarseth (1993) provided a general formulation of Mikkola & Aarseth (1990) and included external perturbation. The application of Mikkola & Aarseth (1993) can be used in 3 applications:

1. Compact subsystem in a stellar system
2. Hard binaries-single star interaction and binary-binary interaction.
3. Dynamical friction and drag force

An improvement of the regularization method in Mikkola & Aarseth (1993) was provided in Mikkola & Aarseth (1996) for higher speed in the numerical integration of close binaries in an N-body system. Its basic principle is to slow down the motion of the binary artificially but still keep the correct treatment of the secular and long-term effect of the binary's motion. Mikkola & Aarseth (1998) provided a new method for computing the motion of perturbed binaries in the KS regularization by expanding the solution in the Taylor series with a combination of Stumpff functions. The new method achieves high accuracy in computation with a small number of terms.

2.18.5 FOPAX

FOPAX is a powerful tool that can be used to simulate a rotating cluster. The tool was developed and tested by Einsel & Spurzem (1999). The method applied is a sequel to the part III of Goodman (1983). This method models the distribution function of a rotating stellar system as a function of energy E and z-component angular momentum, with a third integral of motion neglected. By utilizing the method from Lupton, Gunn, & Griffin (1987), the distribution function for rotating King models is expressed as:

$$f_r(E, J_z) = Constant \times (e^{-\beta E} - 1) \times e^{-\beta \Omega J_z} \quad , \tag{2.69}$$

where $\beta \equiv 1/(m{\sigma_c}^2)$, and the dimensionless angular velocity $\omega = \Omega\sqrt{9/4\pi G n_c}$, to be specified for each model. The dimensionless potential parameter $W_0 = -\beta m(\phi - \phi_t)$, with ϕ and ϕ_t being the central King potential and the King potential at the cut-off radius. The dimensionless potential parameter and angular velocity is computed using method from Henyey et al. (1959), Cohn (1979), and Spurzem (1994, 1996).

2.18.6 Implementation of parallel computing

To perform an N-body simulation with a large particle number in a reasonable time, parallelization of the N-body code is necessary. Fortunately, the most time-consuming part of N-body simulation is force calculation, which can be parallelized. The parallel computing version of NBODY6 is called NBODY6++, developed by Spurzem (1999).

2.18.7 N-body stellar evolution

The stellar evolution recipes applied in NBODY6++GPU have undergone a long evolution path. NBODY6++GPU was first implemented by Wang et al. (2015). The Stellar evolution recipes implemented in NBODY6++GPU originate from Hurley, Pols, & Tout (2000), Hurley, Tout, & Pols (2002), Tout et al. (1997). In 2021, major updates on stellar evolution recipes were incorporated into a new version of NBODY6++GPU. An overview of new stellar evolution recipes is listed in Kamlah et al. (2022). The stellar evolution phase modeled in NBODY6++GPU is listed as follows:

- 0 for fully convective stars with mass ≤ 0.7 M$_\odot$
- 1 for main sequence star with mass > 0.7 M$_\odot$

- 2 for Hertzsprung Gap
- 3 for first giant branch
- 4 for core helium burning
- 5 for early asymptotic giant branch
- 6 for thermally pulsing asymptotic giant branch
- 7 for Naked helium star for main sequence star
- 8 for Naked helium star for Hertzsprung gap stars
- 9 for Naked helium star for giant branch star
- 10 for Helium white dwarf
- 11 for Carbon-oxygen white dwarf
- 12 for Oxygen-Neon white dwarf
- 13 for Neutron star
- 14 for Black hole
- 15 for Mass-less remnant

In the updated version of NBODY6++GPU, several new features are included. A derivative of NBODY6, named NBODY6TT, was developed by Renaud & Gieles (2015), Renaud, Gieles, & Boily (2011), Renaud & Gieles (2013) to include a time-dependent galactic tidal field.

2.19 Star cluster dynamics

2.19.1 The virial theorem

If an isolated system is in equilibrium, then its state satisfies the following equation

$$2K + U = 0 \quad , \tag{2.70}$$

where K is the total kinetic energy of all the stars in the system, and U is the potential energy of the system. The virial ratio can be defined as

$$Q \equiv \left| \frac{K}{U} \right| \quad . \tag{2.71}$$

When $Q = 0.5$, it means that the system is in virial equilibrium. When $Q < 0.5$, the system will contract to a size when it regain virial equilibrium. When $Q > 0.5$, the system will expand to achieve virial equilibrium at a later stage.

2.19.2 Time scale and length scale

Two timescales are pivotal for the study of the dynamical evolution of star clusters: crossing timescale and relaxation timescale. Crossing timescale is defined as the timescale for a star to move through the galaxy once. When the subject star crosses the galaxy quite a few times, its velocity will be changed by surrounding encounters. The time for the subject star to change velocity by the order of original velocity is relaxation time. The crossing time is calculated using the equation below:

$$t_{\mathrm{c}} = \frac{R_{\mathrm{h}}}{\sigma_{\mathrm{h}}} \quad , \tag{2.72}$$

where R_{h} is the half-mass radius and σ_{h} is the velocity dispersion at R_{h} (Spitzer 1987). If virial equilibrium is reached, then the velocity dispersion is $\approx \sqrt{GM_{\mathrm{h}}/R_{\mathrm{h}}}$. The crossing timescale can be written as:

$$t_{\mathrm{c}} = \sqrt{\frac{r_{\mathrm{h}}^3}{GM_{\mathrm{h}}}} \quad . \tag{2.73}$$

Spitzer (1987) defines the relaxation timescale for a test particle in a gravitationally bound system:

$$t_{\mathrm{r}} \equiv \frac{1}{3} \frac{v_{\mathrm{m}}^2}{\langle((\Delta v_{\parallel})^2)\rangle_{v=v_{\mathrm{m}}}} = \frac{0.065 v_{\mathrm{m}}^3}{n m^2 G^2 \ln \Lambda} \quad , \tag{2.74}$$

where v_{m} is the velocity of the subject star, and $\langle(\Delta v_{\parallel}^2)\rangle$ is the velocity component of the subject star parallel to the velocity of encounters. m is the local star mass. n is the local number density. G is the gravitational constant. Λ is $\approx 0.4N$ in a system with SMF, uniform density, and isotropic velocity distribution. Λ is smaller in a system with a mass spectrum. Since the density profile in a gravitationally bound system varies with a different model, half-mass relaxation timescale t_{rh} is a parameter that is more useful for describing the stage of evolution of a whole star cluster. It is defined as the t_{r} at the half-mass radius of a star cluster.

$$t_{\mathrm{rh}} = 0.138 \frac{N^{0.5} r_{\mathrm{h}}^{1.5}}{m^{0.5} G^{0.5} \ln \Lambda} \tag{2.75}$$

t_{r} can also be written in term of t_{c}:

$$t_{\mathrm{r}} \approx \frac{0.138N}{\ln \Lambda} t_{\mathrm{c}} \tag{2.76}$$

where N is the particle number of the system. The virial radius is the size of a self-gravitational system. It can be calculated from the potential energy of the system:

$$R_{\mathrm{v}} = \frac{G m_{\mathrm{system}}}{2\,|U|} \tag{2.77}$$

Where m_{system} is the mass of the system and $|U|$ is the potential energy of the system.

2.19.3 Mass segregation

In a gravitationally bound system, heavier particles tend to move into the center of the system and lighter particles tend to move farther away from the center. This phenomena is called mass segregation. It originate from the close encounter of any 2 members with unequal mass. The lighter member tend to move faster and move away from the center. This process occur on a timescale of:

$$t_{\mathrm{ms}} = \frac{\langle m \rangle}{m} \frac{0.138N}{\ln(0.11M/M_{\mathrm{max}})} \sqrt{\frac{{r_{\mathrm{h}}}^3}{GM}} \quad , \tag{2.78}$$

Here N denotes the number of particles, r_{h} is the half-mass radius, G is the gravitational constant, and $\langle m \rangle$ is the average stellar mass. The m is the mass of the IMBH, and M is the mass of the star cluster (Spitzer & Hart 1971).

2.19.4 Core collapse

The contraction of the center of an isolated cluster is called core collapse (Binney & Tremaine 2008). This is different from the concept of the ”core collapse” of a massive star. During the contraction process, the inner region of the cluster eject stars at a high speed while the stars in the outer region eject stars at a low speed. The process that a star cluster strip off its stars in the halo is called evaporation. This process will reduce the mass of the cluster slowly until the cluster is completely disintegrated. The time for a star to evaporate from the star cluster, called evaporation timescale is $\approx t_{\mathrm{rh}}^{0.75} t_{cr}^{0.25}$, where t_{rh} is the half-mass relaxation timescale and t_{cr} is the crossing time (Baumgardt 2001). It is worth noting that the evaporation process still occur regardless of the existence of a tidal field (Heggie & Hut 2003). The calculation of the central density of an isolated cluster in the early stage did not take binary star interaction into account, resulting in a singularity of the central density (Cohn 1980). Takahashi (1995) solved this problem by solving the orbit-averaged Fokker-Planck equation for an isolated spherical cluster with uniform mass for every member without primordial binaries, starting from a Plummer model. He was able to follow the evolution of the central density to the factor of 10^{13}. The core collapse will eventually be halted by binary stars. It is because binary stars add heat to the core and eliminate the temperature gradient.

(Heggie & Hut 2003) derived the core collapse timescale:

$$t_{\mathrm{cc}} \approx \frac{v^3}{\eta G^2 m^2 n \log \Lambda} \quad , \tag{2.79}$$

Where v is the typical velocity of stars in the core, m is the mass of a star, n is the number of particle in the core, η is a numerical coefficient that varies with time, and Λ is the Coulomb logarithm of the core.

2.19.5 Stationary equilibrium

Close interaction between stars in star clusters is very important and complicated. However, an idealized model that ignores the effect of encounters can be utilized as an approximation of evolution of star cluster. The stationary equilibrium of such a model, stated as ”zero order”, has three underlying postulates:

- Smooth gravitational potential over the whole gravitational bound system
- Quasi-steady state for the evolution of physical properties of the model, such as the distribution function of position and velocity
- Spherical symmetry. The gravitational potential, distribution function, and velocity depend only on the distance vector r.

(Spitzer 1987). With the three postulations above, the collisionless Boltzmann equation can be derived:

$$\frac{\partial f}{\partial t} + \sum_i a_i \frac{\partial f}{\partial v_i} + \sum v_i \frac{\partial f}{\partial x_i} = 0 \tag{2.80}$$

(Spitzer 1987). Poisson's Law can be applied to this scenario:

$$\nabla^2 \phi(r,t) = 4\pi G \rho \tag{2.81}$$

(Spitzer 1987). If we assume an isotropic velocity distribution of the gravitational bound system, then we may construct a distribution function:

$$f(x) = \begin{cases} C_1(-E)^p & E < 0 \\ 0 & E > 0 \end{cases} \tag{2.82}$$

C is a constant. The density profile for this model is:

$$\rho(r) = C_2[-\phi(r)]^{p+\frac{3}{2}} \quad . \tag{2.83}$$

2.19.6 Fokker-Planck equation

If encounters between stars are considered, then the Boltzmann equation is used:

$$\frac{Df}{Dt} = \frac{\partial f}{\partial t} + \sum_{\mathrm{i}} a_{\mathrm{i}} \frac{\partial f}{\partial v_{\mathrm{i}}} + \sum_{\mathrm{i}} v_{\mathrm{i}} \frac{\partial f}{\partial x_{\mathrm{i}}} = \left(\frac{\partial f}{\partial t}\right)_{\mathrm{enc}} \tag{2.84}$$

$\left(\frac{\partial f}{\partial t}\right)_{\mathrm{enc}}$ is the effect of encounters.

Here we define an integral of a probability density function $\Phi(v, \delta v)$ as the probability of a particle with velocity v obtaining a change of velocity δv. $\Phi(v, \delta v)d\delta v$ is the probability of the particle that obtain velocity change within the range $d\delta v$. The integration of $\Phi(v, \delta v)d\delta v$ gives a systematic drift $\langle \delta v_{\mathrm{i}} \rangle$:

$$\langle \delta v_{\mathrm{i}} \rangle = \int \Phi(v, \delta v) d\delta v \quad . \tag{2.85}$$

Similarly, $\langle \delta v_{\mathrm{i}} \delta v_{\mathrm{j}} \rangle$ is

$$\langle \delta v_{\mathrm{i}} \delta v_{\mathrm{j}} \rangle = \int \Phi(v, \delta v) \delta v_{\mathrm{i}} \delta v_{\mathrm{j}} d\delta v \quad . \tag{2.86}$$

The encounter term can be expanded using Taylor expansion:

$$\left(\frac{\partial f}{\partial t}\right)_{\mathrm{enc}} = -\sum_{\mathrm{i}=1}^{3} \frac{\partial}{\partial v_{\mathrm{i}}}(f\langle \delta v_{\mathrm{i}}\rangle) + \frac{1}{2}\sum_{\mathrm{i,j}=1}^{3} \frac{\partial^2}{\partial v_{\mathrm{i}} \partial v_{\mathrm{j}}}(f\langle \delta v_{\mathrm{i}} \delta v_{\mathrm{j}}\rangle) \quad . \tag{2.87}$$

The equation above is a simplified description of the effect of the encounter. A more comprehensive version is proposed by Larson (1970). Here we assume a system with spherical symmetry in polar coordinates r, ϕ, θ, u, v, and w as corresponding velocity components. $\langle u\rangle, \langle v\rangle, \langle w\rangle$ is the mean tangential velocity component. For this system, we assume a distribution function $f(r, u, v, w, t)$, the Boltzmann equation is:

$$\frac{\partial f}{\partial t} + u\frac{\partial f}{\partial r} + \dot{u}\frac{\partial f}{\partial u} + \dot{v}\frac{\partial f}{\partial v} + \dot{w}\frac{\partial f}{\partial w} = \left(\frac{\partial f}{\partial t}\right)_c \quad , \tag{2.88}$$

where $\dot{u}$,$\dot{v}$,$\dot{w}$ are:

$$\begin{aligned} \dot{u} &= -\frac{\partial \phi}{\partial r} + \frac{u^2 + w^2}{r} \\ \dot{v} &= -\frac{uv}{r} + \frac{w^2}{r\tan\theta} \\ \dot{w} &= -\frac{uw}{r} - \frac{vw}{r\tan\theta} \quad . \end{aligned} \tag{2.89}$$

$$\begin{aligned} \frac{\rho}{t} + \frac{1}{r^2}\frac{\partial}{\partial r} r^2 \rho \langle u\rangle &= 0 \\ \frac{\partial \langle u\rangle}{\partial t} + \langle u\rangle \frac{\partial \langle u\rangle}{\partial r} + \frac{1}{\rho}\frac{\partial}{\partial r}\rho\alpha + \frac{2}{r}(\alpha - \beta) + \frac{\partial \Phi}{\partial r} &= 0 \\ \frac{\partial \alpha}{\partial t} + \langle u\rangle \frac{\partial \alpha}{\partial r} + 2\alpha \frac{\partial \langle u\rangle}{\partial r} + \frac{1}{\rho}\frac{\partial}{\partial r}\rho\epsilon + \frac{2\epsilon}{r}\left(1 - \frac{2\beta}{3\alpha}\right) &= \left(\frac{\partial \alpha}{\partial t}\right)_c \\ \frac{\partial \beta}{\partial t} + \langle u\rangle \frac{\partial \beta}{\partial r} + 2\beta \frac{\partial \langle u\rangle}{\partial r} + \frac{\frac{1}{3}}{\rho}\frac{\partial}{\partial r}\frac{\beta}{\alpha}\rho\epsilon + \frac{4\epsilon\beta}{3\alpha r} &= \left(\frac{\partial \beta}{\partial t}\right)_c \\ \frac{\partial \epsilon}{\partial t} + \langle u\rangle \frac{\partial \epsilon}{\partial r} + 3\epsilon \frac{\partial \epsilon}{\partial r} + 3\alpha \frac{\partial \alpha}{\partial r} + \frac{1}{\rho}\frac{\partial}{\partial r}\rho\epsilon + 2\epsilon\left(1 - \frac{\beta}{\alpha}\right) &= \left(\frac{\partial \epsilon}{\partial t}\right) \\ \frac{\partial \varepsilon}{\partial t} + \langle u\rangle \frac{\partial \varepsilon}{\partial r} + 4\varepsilon \frac{\partial \langle u\rangle}{\partial r} + 6\epsilon \frac{\partial \alpha}{\partial r} + 4\alpha \frac{\partial \epsilon}{\partial r} &= \left(\frac{\partial \varepsilon}{\partial t}\right)_c \end{aligned} \tag{2.90}$$

2.19.7 Tidal field

The tidal force is necessary to include in the simulation of a star cluster. The net gravitational force exerted on a star is not uniform because of its finite length, so there exists a stretching force in the gravitational field. The strength of the tidal force is proportional to r^{-3}, where r is the distance to the source. The timescale for stars to cross the tidal radius r_t is calculated by Fukushige & Heggie (2000):

$$t_{\mathrm{e}} = \frac{\pi}{8}\frac{\sqrt{-2E_{\mathrm{crit}}}r_{\mathrm{t}}}{E - E_{\mathrm{crit}}} \quad . \tag{2.91}$$

The escape energy $E_{\mathrm{crit}} \equiv GM/r_{\mathrm{t}}$. This equation assumes a scenario with smooth galactic potential and a steady tidal field in galaxy. However, the tidal field of a galaxy is usually not time-independent. We adopt a standard solar neighborhood tidal field for our simulation of star clusters:

$$r_t = \left[\frac{GM}{4A(A-B)}\right]^{\frac{1}{3}} \quad , \tag{2.92}$$

where A and B are Oort Constants. The value of A and B are 14.4 ± 1.2 $\mathrm{km \cdot s^{-1} kpc^{-1}}$ and -12.0 ± 2.8 $\mathrm{km \cdot s^{-1} kpc^{-1}}$ (Kerr & Lynden-Bell 1986). A describes the tangential motion of the galaxy, and B describes the rotation of the galaxy.

2.19.8 The Plummer model

The Plummer model is a model that is widely used in the modeling of star clusters and galaxies. It is proposed by Plummer (1911). Two free parameters are in the model, total mass M and scale radius a. Its density profile within radius r of the sphere is:

$$\rho(r) = \frac{3M}{4\pi a^3}\left(1 + \frac{r^2}{a^2}\right)^{-\frac{5}{2}} \quad . \tag{2.93}$$

Its enclosed mass within radius r is:

$$M(r) = M\left(1 + \frac{a^2}{r^2}\right)^{-\frac{3}{2}} \quad . \tag{2.94}$$

Its specific potential is:

$$\phi(r) = -\frac{GM}{a}\left(1 + \frac{r^2}{a^2}\right)^{-\frac{1}{2}} \quad . \tag{2.95}$$

a is the scale length of the Plummer sphere:

$$a = \frac{3\pi}{16} R_{\mathrm{virial}} \quad . \tag{2.96}$$

Applying equation 2.94, the half-mass radius is 0.768 R_{Virial}. Usually, the Plummer model is used for practical calculation, while the King model is important for observation.

2.19.9 The King model

The distribution function of the King model is:

$$f = \begin{cases} f_0(\exp(-2j^2 E) - \exp(-2j^2 E_0)) & E < E_0 \\ 0 & E > E_0 \end{cases} \tag{2.97}$$

Where the E_0 is the escape energy. The density profile for the King model is:

$$\rho = k \left\{ \frac{1}{\sqrt{1 + \left(\frac{r}{r_{\mathrm{c}}}\right)^2}} - \frac{1}{\sqrt{1 + \left(\frac{r_{\mathrm{t}}}{r_{\mathrm{c}}}\right)^2}} \right\}^2 \quad . \tag{2.98}$$

It is not only a model with finite mass and radius, which is attractive, but also a good approximation to a solution of the Fokker-Planck equation. A third parameter can be used to characterize King's model: $W_0 = 2j^2(E - E_0)$ $c = \lg\left(\frac{r_t}{r_0}\right)$ where r_{t} is the tidal radius and E is the energy of a star at rest at the center. The size of the central region can be characterized by 'core radius', r_{c} (King 1966).

2.19.10 The initial mass function (IMF)

Initial mass function (IMF) is the distribution of stellar masses after they form. Since stars form at different times and the time for a star to form is very long, it is an idealized model for describing the mass of a star cluster. If we denote the number of stars in a mass range (m,$m + dm$) as dN, then dN obeys the following probability distribution:

$$dN \propto \epsilon(m) dm \quad , \tag{2.99}$$

where ϵ is often in the form of m^{α} A pioneering study conducted by Salpeter (1955) provided the first initial mass distribution function, where $\epsilon(m)$ is $m^{-2.35}$. His work was extended by

Miller & Scalo (1979) to lower than $1\,\mathrm{M}_\odot$, suggesting that α approaches 0 in the low mass region. Kroupa, Tout, & Gilmore (1993) proposed an improved initial mass distribution function:

$$\epsilon(m) = \begin{cases} 0.035 \cdot m^{-1.3} & 0.08M_\odot \leq x \leq 0.5M_\odot \\ 0.019 \cdot m^{-2.2} & 0.5M_\odot \leq x \leq 1.0M_\odot \\ 0.019 \cdot m^{-2.7} & 100M_\odot \leq x \leq \infty \end{cases}$$

Kroupa, Tout, & Gilmore (1993) proposed an improved description of the IMF. It extended the mass range down to $0.01\,M_\odot$, although the confidence interval was not determined:

$$\epsilon(m) \propto m^{-\alpha} \tag{2.100}$$

$$\alpha = \begin{cases} 0.3 \pm 0.7 & 0.01M_\odot \leq m \leq 0.08M_\odot \\ 1.8 \pm 0.5 & 0.08M_\odot \leq m \leq 0.5M_\odot \\ 2.7 \pm 0.3 & 0.5M_\odot \leq m \leq 1M_\odot \\ 2.3 \pm 0.7 & 1M_\odot \leq m \end{cases}$$

(Kroupa 2001). Although it is reasonable to provide an IMF for a star cluster, current observation of star formation in the long and thin filaments is a challenge to the gravo-turbulent theory of the IMF. Recent observation also shows that the shape of the IMF depends on metallicity and local stellar density. Therefore, constraining the variations of IMF will be an important task to conduct (Kroupa & Jerabkova 2019).

2.19.11 Star clusters and IMBHs

The detection of IMBHs in globular clusters can be obtained if the IMBHs accrete material from a nearby star, or surrounding gas. When a star gets very close to a black hole, the star will be torn apart, resulting in a tidal disruption event. Its remnant will accelerate towards black hole and heat up. The heat radiates into space in the form of X-ray emission, which can be detected by detectors such as Chandra X-ray telescope. The accretion disk is composed of material around the IMBHs, such as plasma, dust and gas. Gravitation and frictional force heat the disk up and emit electromagnetic radiation. The frequency of electromagnetic radiation is dependent on the mass of the central body. The frequency of electromagnetic radiation from accretion disk is smaller when the mass of the central body is larger. Observational results from the Hubble Space Telescope show that the Antennae Galaxy and Arp 220 contain many star clusters that have formed in a short period of time. These clusters are gravitationally bounded and form a cluster complex with a high number density (Wilson et al. 2006, Zhang, Fall, & Whitmore 2001). It has been shown that IMBH can form in the center of a star cluster after repeated collisions and mergers of stars (Gürkan, Fregeau, & Rasio 2006, Miller & Hamilton 2002, Portegies Zwart et al. 2004). Although there is no solid observational evidence of IMBHs in globular clusters, the high frequency of stellar collisions and runaway mergers of stellar-mass BH may result in IMBH formation in the center of a globular cluster (Inayoshi, Visbal, & Haiman 2020). It is believed that IMBHs are located in globular clusters, such as G1 in the Andromeda galaxy (Kong et al. 2010, Pooley & Rappaport 2006, Ulvestad, Greene, & Ho 2007), and 47 Tucanae in the Milky Way (Freire et al. 2017, Kızıltan, Baumgardt, & Loeb 2017, Ridolfi et al. 2016). Notable IMBH candidates in globular clusters includes HLX-1 and M82 X-1. The very high likelyhood of an IMBH located in the center of NGC 4395 and 47 Tucanae make these two globular clusters well-known and distinct from other globular clusters (Koliopanos 2017).

2.19.12 Scaling relation for IMBHs and their host clusters

Although IMBHs are much harder to detect than SMBHs, the search for IMBHs in globular clusters has extrapolated the scaling relation between IMBH and the host globular cluster to a lower mass. Lützgendorf et al. (2013) studied the scaling relation between IMBH mass and the properties of host globular cluster. Unlike galaxies and their SMBHs, globular clusters experience mass loss during their evolution which cannot be ignored, so the slope of the scaling relation may change over time.

2.19.13 Violent relaxation

Violent relaxation is a process that occurs in the dynamical evolution of a collisionless system (Lynden-Bell 1967). With an initial bulk rotation, the shape of the system (moment of inertia) will change over time, with its potential energy change. The change in the potential of the cluster results in a redistribution of stars: stars in the outer region expand slowly, while the inner region and core contract at a much higher rate. The contraction may result in an unstable core caused by the gravo-thermal and gravo-gyro catastrophe. The violent relaxation process would occur later with a higher degree of rotation (Fiestas, Spurzem, & Kim 2006).

2.19.14 Gravothermal and gravogyro catastrophe

The idea of a gravogyro catastrophe originates from Antonov (1961). He found that when the difference between central density ρ_c and density at the edge of a cluster ρ_e is below a certain value ($\frac{\rho_e}{\rho c} < \frac{1}{709}$), then this system has no maximum entropy at any given energy. Lynden-Bell & Wood (1968) further stated that the heat capacity of the cluster becomes negative when the density contrast is $\approx \frac{3}{100}$ and reaches zero when the density contrast reaches the value predicted by Antonov (1961). The system is stable when the density contrast is between $\frac{1}{709}$ and $\frac{3}{100}$, with negative heat capacity. If we consider an isothermal gas sphere that expands adiabatically, then the gas sphere would have a core with a much higher density than the edge. The edge of the gas sphere would decrease much faster than the core. When the heat capacity of the core is negative, the core contracts. The heat flows from the core to the halo, but the halo has a positive heat capacity, so the halo would expand. The continuous contraction of the core and continuous expansion of the halo is called a gravothermal catastrophe. When applying a star cluster as an analogy, the center of the cluster should have a very high density which is in contradiction with current observation. This dilemma is called core collapse. The core collapse dilemma has been solved by the inclusion of the binary and hierarchical system (triple and quadruple systems). The energy released from the binary and hierarchical system results in energy exchange between the core and halo, producing an isothermal system for gravothermal catastrophe to occur. If we further include the stellar evolution, natal kick, and escaper, then these factors would accelerate the gravothermal catastrophe and leave only hard-binary stars behind (Padmanabhan 1990). Hachisu (1979) utilized the stability criteria from Inagaki & Hachisu (1978) and proved that a rotating isothermal gas cylinder is an unstable system with a negative moment of inertia. When the contraction of the gas element is large enough, its angular speed may increase. This phenomenon is the gravogyro catastrophe. Akiyama & Sugimoto (1989) utilized the NBODY2 code (Aarseth 1985) to study a rotating cluster with particle number $N = 1000$. It found that the star cluster evolution follows this procedure:

1. Violent relaxation
2. Gravogyro catastrophe from transportation of angular momentum caused by negative moment of inertia of the system
3. Decrease of the gravogyro instability originate from the transport of angular momentum by gravothermal instability

4. A more violent gravothermal catastrophe

2.20 N-body units

The idea of a standard unit and time scale comes from Heggie & Mathieu (1986). By setting the gravitational constant G and the initial total mass of the system to be 1, other physical properties of a system can be determined. This unit system is called the N-body unit system. In this system, the initial total energy of this system is set to be $\frac{1}{4}$. The generic equation for the total energy of a system is $E = K + W$, where K is the total kinetic energy of the system. The total potential energy W for the Plummer model is:

$$W = -\frac{3\pi}{32}\frac{GM^2}{R} \quad . \tag{2.101}$$

Then we apply the Virial theorem. the total energy of a Plummer sphere model is:

$$E = -\frac{3\pi}{64}\frac{GM^2}{R} \quad . \tag{2.102}$$

In the Plummer model, the virial radius is defined to be 1 N-body unit length.

2.21 Monte Carlo methods

Because of the high computational costs of direct N-body simulations, the Monte Carlo method become an alternative approach to study the dynamical evolution of star clusters. Dynamical Monte Carlo method use statistical method to solve Fokker-planck equation, with each particle represent a group of stars with same position and velocity. The potential can be calculated using super particles and velocity can be calculated using Poisson's equation. Carrying out simulations using the Monte Carlo method costs much less time than when using the direct N-body method, but it requires modeling additional diffusion process to change the orbit of particles and simulate strong interaction. The orbit-averaged Monte Carlo method uses energy and angular momentum to represent the status of stars. This method avoids the integration of orbit so it uses much less time to simulate the evolution of a globular cluster. Modern Monte-Carlo code are developed by Joshi, Rasio, & Portegies Zwart (2000) and Giersz et al. (2013). Miholics, Webb, & Sills (2016) utilized NBODY6TT to conduct N-body simulation of star clusters in galaxy mergers. So techniques that take time-dependent tidal field into account is required.

2.22 Comparison between N-body and other methods

Aarseth, Henon, & Wielen (1974) compared the result of three methods that simulate the evolution of a spherical cluster. The three approaches are Monte-Carlo method, N-body method and fluid dynamical approach. The Monte-Carlo method evolve 1.5 times faster than the direct N-body approach. The fluid dynamical approach is two to three times faster than the N-body approach (Sesana & Khan 2015).

2.23 Studies on rotating star clusters

A lot of effort has been devoted to the theoretical modelling of rotating star cluster. Currently, direct N-body simulations of globular cluster are still scarce (Kamlah et al. 2022, Livernois et al. 2022, Tiongco, Vesperini, & Varri 2022). Kamlah et al. (2022) investigated the effect of stellar evolution and initial rotation on the evolution of rotating cluster, concluding the gravothermal-gyro catastrophe occurs later and more violent in the simulated cluster without stellar evolution. The simulated cluster without stellar evolution also form a more concentrated bar with higher triaxiality. However, this study does not contain IMBHs, which are believed to locate in the centers of some star clusters. Currently, the dynamical evolution of IMBHs in globular clusters is still a field that requires much investigation.

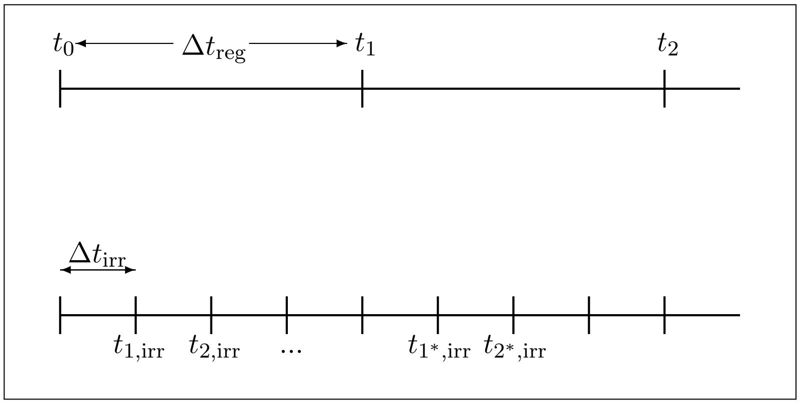

Figure 2.19: Regular and irregular time steps (Makino & Aarseth 1992).

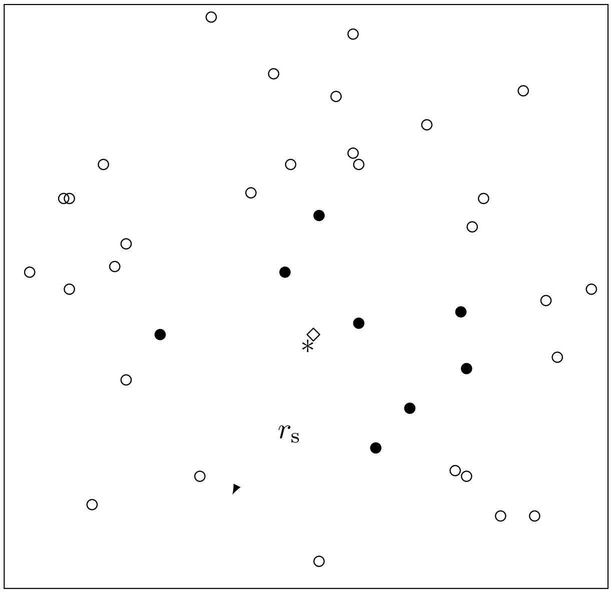

Figure 2.20: Illustration of the neighbour scheme for particle i marked with the asterisk (Aarseth 1985).

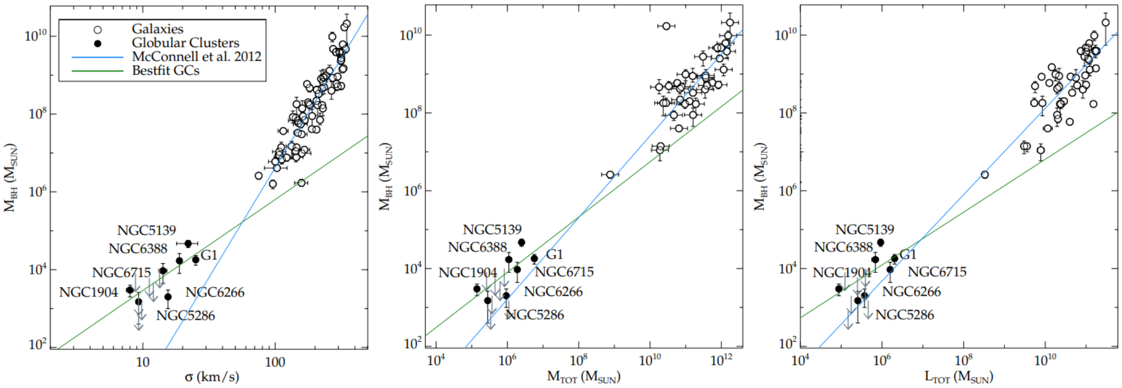

Figure 2.21: Scaling relation between globular cluster and IMBH mass. Image credit: Lützgendorf et al. (2013).

Chapter 3

Dynamical evolution of triple supermassive black holes in galactic centers

This chapter is based on the paper ”The dynamical evolution of unequal-mass supermassive black hole triplets in galaxy centers” submitted to the Monthly Notices of the Royal Astronomical Society.

3.1 Introduction

Supermassive black holes (SMBHs) are commonly found in the centers of massive galaxies (e.g., Begelman, Blandford & Rees 1980). Galaxy mergers and the role of SMBHs in such phenomena have received much attention in recent years. eLISA and the Pulsar Timing Array can probe such events, and can be utilized to observe the evolution of SMBH binaries (SMBHBs) (eLISA Consortium et al. 2013). The dynamical evolution of SMBHBs during a galaxy merger can be roughly divided into three phases. When the merger process starts, the SMBHs are still in the cores of their host galaxies. During the galaxy merger process itself, the SMBHs migrate towards the center of the merged galaxy as a consequence of violent relaxation. Following the dynamical friction provided by surrounding stars and gas, the two SMBHs rapidly form a bound binary system (e.g., Begelman, Blandford & Rees 1980). This process may be strongly affected by the properties of the surrounding environment. After the formation of a SMBHB, the binary system interacts with the surrounding stars, releasing energy through three-body scattering, and the orbit consequently shrinks. The SMBHB is considered hard when the semi-major axis of the binary system approaches a value $a_h \approx G\mu/4\sigma^2$, where the G is gravitational constant, μ is the reduced mass of binary SMBH, and σ is the velocity dispersion of field stars. If the local stellar density is sufficiently high, the binary system continues to shrink its orbit through expelling stars until the semi-major axis of the binary reaches a value approximating $a_{\rm gr} \approx 10^{-2}$ pc. From that moment onward, the shrinking of the orbit of a SMBHB is dominated by gravitational wave emission. This process may ultimately result in the coalescence of the two SMBHs (Quinlan 1996). The accompanying burst of gravitational waves may be observed with present-day gravitational wave detectors (e.g., Amaro-Seoane et al. 2017).

In many situations, the phase of gravitational wave emission is not reached. When the encounter rate between a SMBHB and neighbouring stars is insufficient, the energy exchange between the SMBHB and the stellar population becomes negligible, and the hardening process halts. This problem is often referred to as the *final parsec problem* (e.g., Milosavljević & Merritt 2001). The *final parsec problem* was computationally identified in Berczik, Merritt, & Spurzem (2005). Although the phenomenon occurs in idealised spherical galaxies, there is evidence suggesting that the *final parsec problem* may not be relevant in realistic systems, due to the triaxial nature of galaxies. Berczik et al. (2006) found that the *final-parsec problem* does not exist in triaxial galaxies, due to the efficient refilling mechanism of stars interacting with the SMBHB. Chatterjee, Hernquist, & Loeb (2003) examined the *final-parsec problem* by studying the Brownian motion of a binary's center of mass interacting with surrounding stars. They demonstrated that the *final-parsec problem* can be solved by incorporating the Brownian motion factor. The *final-parsec problem* can also be solved by introducing gas in a circumbinary disk (e.g., Cuadra et al. 2009, Dotti et al. 2007, Escala et al. 2004, Mayer et al. 2007), although this is not a guarantee for solving the *final parsec problem* (Lodato et al. 2009). Another approach to solve the *final parsec problem* is to introduce a third black hole, or another massive perturber, such as a giant molecular cloud (e.g., Milosavljević & Merritt 2003, Perets & Alexander 2008).

Recent observations have shown that a hierarchical triple SMBH systems with a SMBHB in the final stage of merging occur in nature (Kollatschny, et al. 2020). Although observations are rare, there exist numerous studies on the dynamics of SMBH triplets. Blaes, Lee, & Socrates (2002), for example, carried out the first theoretical study on black hole triples, where general-relativistic precession and first Post-Newtonian terms are integrated into the orbit-averaged Hamiltonian of an isolated hierarchical triple point mass system. The orbit-averaged Hamiltonian was derived using secular perturbation theory to expand to octupole order. This suggests that an intruding third black hole can accelerate the orbital shrinking rate of a SMBHB by one order of magnitude. Iwasawa, Funato, & Makino (2006) conducted a Newtonian N-body study of SMBH triples in realistic galaxy models, with the inclusion of energy loss through gravitational waves. This suggests that a high eccentricity of a SMBHB orbit may reduce the gravitational wave merger timescale. Such high eccentricities are thought to originate primarily from two mechanisms: (i) frequent exchanges between SMBHBs and single SMBHs, and (ii) the Kozai mechanism (Kozai 1962, Lidov 1962).

Hoffman & Loeb (2007) studied massive black hole triplets that are embedded in a stellar background. The study use a Hernquist profile stellar potential superimposed dark matter halo to represent the galactic model. This study suggests that an intruding third black hole may shorted the merger time of a SMBHB. Iwasawa, Funato, & Makino (2008) conducted a similar Newtonian N-body simulation to investigate the evolution of galaxies with binary and triple SMBHs. This study suggests that triple SMBHs may enlarge the cusp and reduce its density. Amaro-Seoane et al. (2010) utilized the black hole triplet system in Hoffman & Loeb (2007) to study phenomena of massive black hole triples that are detectable by the Pulsar Timing Array, assuming a certain fraction of SMBH binaries originate from black hole triplet interactions.

The studies of Bonetti et al. (2016), Bonetti et al. (2018a), Bonetti et al. (2018b), and Bonetti et al. (2019) investigated the Post-Newtonian evolution of SMBH triplets. These studies suggest that the presence of a third SMBH may speed up the hardening rate of a SMBHB (and hence result in a gravitational wave emission event), but they also show that the presence of this third SMBH may lead to the ejection of one of the black holes from the system. Mapelli et al. (2021) investigated the effect of metallicity, spin, and cluster properties on gravitational wave emission. It is suggested that with three black holes in a galaxy merger, a slingshot ejection event of at least one of the black holes is possible (see also Mikkola & Valtonen 1990, Valtonen et al. 1994).

Although many pioneering studies have been carried out, most of these are three-body simulations that involve only the three black holes themselves, while ignoring the influence of the surrounding stellar population. Iwasawa, Funato, & Makino (2006) and Iwasawa, Funato, & Makino (2008) included the surrounding stellar population, but only study the situation in which the three black holes have identical masses; such a situation is unlikely to occur in nature. The dynamical evolution of SMBH triples in dense stellar environments

Table 3.1: N-body unit conversion for our reference model.

N-body unit	Physical scaling
1 length unit	1374 pc
1 mass unit	10^{10} $\mathrm{M}_{\odot}$
1 velocity unit	177 $\mathrm{km\,s^{-1}}$
1 time unit	7.61 Myr

with different mass ratios currently remains a poorly studied topic.

How will an unequal-mass SMBH triple system in a galaxy centre evolve? To answer this question, and to constrain the merger timescale of binary black holes, we carry out a number of N-body simulations of galaxy centers containing three SMBHs. This study aims to determine the dynamical evolution of black hole triplets, with a focus on exchanges and the evolution of the binding status of binary and triple black holes. The implications for gravitational wave emission and hardening of binary black holes are also discussed. This chapter is organized as follows. In Section 3.2 we describe the initial conditions of the stellar population and the three black holes in our simulations, as well as the numerical methods we employ in the study. In Section 3.3 we present and analyze our findings. Finally, in Section 3.4, we present and discuss our conclusions.

3.2 Methodology and initial conditions

3.2.1 Physical scaling

We carry out a numerical analysis of the evolution of SMBH triplets in galaxy centers using N-body simulations. The stellar population represents the core of an elliptical galaxy without gas. The N-body simulations are scale-free, and initial results are obtained in N-body units (see, e.g., Heggie & Mathieu 1986, Hénon 1971). Prior to scaling to from N-body units to physical units, the relaxation time of the system only depends on the number of particles. After the simulations have been carried out, we scale the results to the desired physical dimensions (length, time, and mass) of the system. After scaling, the gravitational wave merger timescale is determined.

The conversion from N-body units to physical units for our reference model are listed Table 3.1. We assume that the mass of the central SMBH is $\sim 1\%$ of the total mass of the system. The stellar velocity dispersion is then calculated using the M-σ relation described in Kormendy & Ho (2013). The corresponding conversion factor between N-body velocity and physical velocity is then determined. The conversion factor for length is $R = GM/v^2$, where M is the total mass of the system and v is the velocity conversion factor. The conversion factor between N-body time and physical time is $T = \sqrt{R^3/GM}$. The speed of light speed in physical units is $c = c_{\rm n}\sqrt{GM/R}$, where $c_{\rm n}$ is the speed of light in N-body units.

3.2.2 Initial conditions - stellar population

We model a galaxy center consisting of a population of 64 000 particles, with three particles representing the SMBHs. All remaining $N = 63\,997$ particles in the system have identical masses. Hereafter, we refer to these particles as "stars".

We integrate the system for 100 N-body time units. When converted to a physical timescale for our reference model, this corresponds to $\sim$ 760 Myr (see Section 3.2.1). We do not include an external tidal field, nor do we include primordial binaries. Stellar evolution is not enabled in our simulation. We do not include the effects of general relativity in the N-body simulations, as these are unimportant at the physical scales under consideration in this work.

The Plummer (1911) model with $n = 5$ polytrope is used to initialize the stellar system, with a virial radius of $R_{\rm v} = 1$ (in N-body units). The system is initialized in virial equilibrium ($Q = 0.5$). The half-mass radius of the Plummer model can be obtained from the virial radius of the Plummer model, $R_{\rm h} \approx 0.768 R_{\rm v}$, and the virial radius of the Plummer model is related to the scale length, $a_{\rm scale}$, of the Plummer model, $R_{\rm v} \approx 1.7 a_{\rm scale}$ (see, e.g., Heggie & Hut 2003). The mass enclosed within radius r for the Plummer model is

$$M(r) = M \frac{r^3}{(r^2 + a_{\rm scale}^2)^{3/2}} \quad , \tag{3.1}$$

where M is the total mass of the cluster. This allows us to calculate the circular velocity at the half-mass radius, which is $V_{\rm c} = \sqrt{GM/2R_{\rm h}} \approx 0.806$. The corresponding density profile is

$$\rho(r) = \frac{3M}{4\pi a_{\rm scale}^3} \left(1 + \frac{r^2}{a_{\rm scale}^2}\right)^{-5/2} \quad . \tag{3.2}$$

In the Plummer model, the density profile in the core is constant ($\gamma = 0$). With an SMBH system located at the centre of the cluster we thus obtain $\alpha_1 = \alpha_2 = 3/2$.

Equation (2.31) then simplifies to

$$\dot{\omega}_{\mathrm{MP}} = -V_r \frac{3}{2}\sqrt{1-e_2^2}\left(\frac{M_*(a_2)}{M_0}\right) \quad . \tag{3.3}$$

The study of Iwasawa, Funato, & Makino (2006) on equal-mass triple black holes suggests that particle number, when sufficiently large, has little effect on the evolution of the massive black hole triplet. The choice for the number of particles determines three processes to a certain extent: the relaxation time, the timescale of dynamical friction, and the hardening rate of the central SMBH system. The relaxation time for a system consisting of N particles of mass $m = M/N$ scales as $t_{\mathrm{rlx}} \propto (\ln N)^{-1}(N/m)^{1/2}$. The relaxation time for our model with 64 000 particles is 578 N-body units, while for a more realistic system with 10^{10} particles the relaxation time would be 4×10^8 N-body units. Both values are much longer than the duration of the simulations. Within the timescale adopted in our simulations, the particle number thus has little influence on the evolution of the stellar system itself. The SMBHs sink to the centre of the system on a timescale that is roughly the mass segregation timescale, $t_{\mathrm{ms}} \propto m\, t_{\mathrm{rlx}} \propto (\ln N)^{-1}$. This weak dependence indicates that the dynamical friction timescale used in our model is somewhat overestimated. In other words, the SMBH migration process occurs faster in realistic models. The hardening timescale of an SMBHB is proportional to ρ^{-1} the inverse of the mass density of the surrounding stellar population (see Section 3.3.1). Since $\rho \propto mN$ and $m = M/N$, we do not expect a significant dependence of the hardening rate on the chosen particle number.

In the absence of other perturbing processes, the SMBHB will eventually deplete its loss cone, and stall without further evolution. The depletion of the loss cone is the hypothetical problem in which the SMBH binary ejects almost all stars in its neighbourhood, so that the hardening process stalls and the phase of gravitational wave emission is significantly delayed. This implies that SMBHBs in such environments are unlikely to merge within a Hubble time through interactions with field stars and gravitational wave emission alone (Makino & Funato 2004). However, the presence of a tertiary SMBH affects the hardening rate of an SMBHB through refueling the SMBHB's loss cone and through three-body scattering events involving the SMBHs (see below).

The interaction between an SMBH triplet and the stellar population is chaotic. Small differences in the initial conditions can lead to different outcomes. To better understand the fate of SMBH triplets, additional simulation with different initial conditions for the stellar population were conducted (see Section 3.3.7).

Table 3.2: Initial mass ratio scheme for triple SMBHs. Column 1 denotes the identifier of each model. Columns 2 to 4 list the mass of each of the three SMBHs (in N-body units). Column 5 lists the mass ratio, q, of the SMBH triplet (see Equation 3.4).

Model ID	m_1	m_2	m_3	q
A	0.01	0.010	0.010	2.000
B	0.01	0.010	0.007	1.400
C	0.01	0.010	0.005	1.000
D	0.01	0.010	0.003	0.600
E	0.01	0.010	0.002	0.400
F	0.01	0.010	0.001	0.200
G	0.01	0.007	0.007	1.700
H	0.01	0.007	0.005	1.214
I	0.01	0.007	0.003	0.728
J	0.01	0.007	0.002	0.486
K	0.01	0.007	0.001	0.243
L	0.01	0.005	0.005	1.500
M	0.01	0.005	0.003	0.900
N	0.01	0.005	0.002	0.600
O	0.01	0.005	0.001	0.300
P	0.01	0.003	0.003	1.300
Q	0.01	0.003	0.002	0.867
R	0.01	0.003	0.001	0.433
S	0.01	0.002	0.002	1.200
T	0.01	0.002	0.001	0.600
U	0.01	0.001	0.001	1.100

3.2.3 Initial conditions - SMBHs

Each simulation contains three SMBHs. The first black hole is assigned a mass $m_1 = 0.01$ (in N-body units). We adopt a range in masses for m_2 and m_3, with $m_3 \leq m_2 \leq m_1$, down to $m_3 = 0.001$. The masses of the SMBHs in each model are summarized in Table 3.2. Black hole m_1 is placed at rest at the center of the cluster. Black holes m_2 and m_3 are placed at the half-mass radius of the cluster at equal distances and at opposite locations from the centre, and are assigned circular orbits. The initial positions and velocities of each SMBH are listed in Table 3.3.

Inspired by Blaes, Lee, & Socrates (2002), the first detailed study of the black hole triple systems, we define the mass ratio q of the SMBH triplet as the ratio between m_3 and

Table 3.3: Initial positions and velocities of the three SMBHs.

	Black hole 1	Black hole 2	Black hole 3
Position $\vec{r}_0$	(0,0,0)	($R_{\rm h}$,0,0)	($-R_{\rm h}$,0,0)
Velocity $\vec{v}_0$	(0,0,0)	(0,$V_{\rm c}$,0)	(0,$-V_{\rm c}$,0)

reduced mass of m_1 and m_2:

$$q \equiv \frac{m_3}{\mu_{12}} = \frac{m_3(m_1+m_2)}{m_1 m_2} = \frac{m_3}{m_1} + \frac{m_3}{m_2} \quad . \tag{3.4}$$

We use this mass ratio to quantify how the tertiary intruder affects the inner binary orbit. The definition of $0 < m_3 \leq m_2 \leq m_1$ sets the constraint $q \in \langle 0, 2]$, where the limit $q = 0$ corresponds to the situation where m_3 is absent (i.e., the situation of a SMBH binary), and the highest value ($q = 2$) is obtained in the case of an equal-mass triplet, $m_1 = m_2 = m_3$. Note that $q \geq 1$ in all situations where $m_3 = m_2 \leq m_1$.

The initial conditions for the three SMBHs were inspired by the earlier study on triple SMBHs by Iwasawa, Funato, & Makino (2008). The choice for the initial conditions has little influence on our general conclusions: Amaro-Seoane et al. (2010) found that the three black holes lose memory of their initial conditions after the first round of secular evolution.

3.2.4 Numerical method

We carry out the N-body simulations using the N-body code `NBODY6++GPU` (Wang et al. 2015), a parallelized version of Aarseth's `NBODY6` code (Aarseth 1999). It is also an offspring of `NBODY6++` (Spurzem 1999), with utilization of GPUs (Graphical Processing unit) incorporated. `NBODY6++GPU` uses Kustaanheimo-Stiefel (KS) regularization to treat close binaries instead of introducing softening parameters (Kustaanheimo & Stiefel 1965). Initial conditions for the stellar populations of the clusters were generated using `McLuster` (Küpper et al. 2011), and the three SMBHs were manually added to the input file that was parsed to `NBODY6++GPU`.

3.2.5 Classification of binary and triple SMBH systems

The dynamical configuration of the three black holes at a given moment in time can be classified as either (i) three unbound black holes, (ii) a binary system with an unbound single black hole, or (iii) a hierarchical triple black hole system. To analyze the dynamical evolution of the SMBH triplet, we identify at each time whether or not the SMBHs are gravitationally bound. If an inner binary exists, we denote its two components as $m_{\rm a}$ and $m_{\rm b}$, with $m_{\rm b} \leq m_{\rm a}$. The third SMBH is denoted as $m_{\rm c}$. To identify the inner binary system, we measure the mutual distance between each pair of black holes. Mutually-closest neighbors are defined as the inner binary when the pair is gravitationally bound. In the case of a binary system, we determine the relative distance vector between the components of the binary $\vec{r}_{\rm rel}$, the relative velocity vector of binary $\vec{v}_{\rm rel}$, and the binding energy of the binary $E_{\rm ab}$,

$$E_{\rm ab} = \frac{1}{2}\mu_{\rm ab}\, v_{\rm rel}^2 - \frac{Gm_a m_b}{r_{\rm rel}} \quad . \tag{3.5}$$

The pair of SMBHs is considered a binary system when $E_{\rm ab} < 0$. In that case, the semi-major axis of the binary a_1, is

$$a_1 = -\frac{Gm_{\rm a}m_{\rm b}}{2E_{\rm ab}} \quad , \tag{3.6}$$

and the eccentricity of the inner binary is

$$e_1 = \left[\left(1 - \frac{r_{\rm rel}}{a}\right)^2 + \frac{(\vec{r}_{\rm rel}\cdot\vec{v}_{\rm rel})^2}{a\,G\,m_{\rm ab}}\right]^{\frac{1}{2}} = \sqrt{1 + \frac{2E_{\rm ab}L_{\rm ab}^2}{\mu(Gm_a m_b)^2}} \quad , \tag{3.7}$$

where $m_{\rm ab} = m_{\rm a} + m_{\rm b}$ is the total mass of the inner binary and $\mu_{\rm ab} = m_{\rm a}m_{\rm b}/(m_{\rm a} + m_{\rm b})$ is its reduced mass. The angular momentum of the inner binary is

$$L_{\rm ab} = \left[\frac{G}{m_{\rm ab}}\, a_1\,(1 - e_1^2)\right]^{\frac{1}{2}} m_a\, m_b \tag{3.8}$$

(see, e.g., Kroupa 2008).

The black hole triplet is defined as in a binary-single system when the third body is not gravitationally bound to the inner binary, i.e., $E_{\rm ab} < 0$ and $E_{\rm ab/c} > 0$. Conversely, the three black holes are considered as a triple system when both $E_{\rm ab}$ and $E_{\rm ab/c}$ are negative.

3.3 Results

In this section we present the results of our simulations and analyse the dependence of the orbital parameters of the inner binary black hole system on the mass ratio, q. The main results for all simulations are presented in Figures 3.5-3.34. We discuss the implications for the merger process and gravitational waves. Throughout this section, we define the "center" of the system as the coordinate origin (i.e., the center of the star cluster).

3.3.1 Theoretical background

The dynamical evolution of a SMBH triple in a stellar environment without gas can be roughly divided into three stages: (i) the dynamical friction stage, (ii) the hardening stage, and (iii) the gravitational wave emission stage. Our analysis primarily focuses on the second stage, and particularly on how this phase of evolution is affected by the presence of a third SMBH.

During the first stage, the SMBHs are unbound and gradually move towards the centre via dynamical friction from surrounding stars of the cluster and approach each other. The dynamical friction timescale can be estimated as

$$t_{\rm fric} \sim 2 \times 10^8 \frac{1}{\ln(N)} \left(\frac{10^6\ {\rm M}_\odot}{m}\right) \left(\frac{r_c}{100\ {\rm pc}}\right)^2 \left(\frac{\sigma}{100\ {\rm km\ s}^{-1}}\right) [{\rm yr}] \quad , \tag{3.9}$$

(e.g., Sobolenko, Berczik, & Spurzem 2021). The center of the galaxy is assumed to be an isothermal sphere with core density $\rho = \sigma^2/(2\pi G r_{\rm c}^2)$, where σ is the velocity dispersion, r_c is the core radius, and m is the mass of the SMBH.

When two of the SMBHs reach the core of the cluster, they form a gravitationally-bound pair with a semi-major axis roughly equal to the influence radius of a SMBH. The influence radius is defined as the radius of the sphere centered around a SMBH that contains a total stellar mass equal to the mass of the SMBH. The initial separation between newly-formed binary SMBHs is thus $r_b \approx GM/\sigma^2 \approx 174$ pc, where σ is the one-dimensional stellar velocity dispersion at the center.

When the semi-major axis of the SMBHB decreases to $a_{\rm h} = G\mu/4\sigma^2$, the SMBHB enters the stellar hardening phase, where three-body scattering involving stellar particles is the dominant mechanism in driving the shrinking of the SMBHB. The hardening rate is useful for quantifying the evolution of the system after dynamical friction is no longer the dominant factor in driving binary orbit to shrink. The inverse semi-major axis, a^{-1}, can be used as a proxy for the binding energy of the inner binary. Here we define the hardening rate of inner binary $s(t)$ as

$$s(t) \equiv \frac{d(a_1^{-1})}{dt} \quad , \tag{3.10}$$

where $a_{\rm ab}$ is the semi-major axis of the inner binary. The timescale for SMBHB hardening can be estimated as

$$t_{\rm h} \approx 70 \left(\frac{\sigma}{100~{\rm km~s^{-1}}}\right)\left(\frac{10^4~{\rm M_\odot~pc^{-3}}}{\rho}\right)\left(\frac{10^{-3}~{\rm pc}}{a}\right)~[{\rm Myr}] \quad , \tag{3.11}$$

(Sobolenko, Berczik, & Spurzem 2021). The scaling factor was calculated using the $M-\sigma$ relation from Kormendy & Ho (2013).

During the final stage, when the two SMBHs are sufficiently close, gravitational wave emission carries away energy from the SMBHB, and shrinks and circularizes the orbit of the SMBHB. The gravitational wave merger timescale is estimated as

$$\begin{aligned} t_{\rm merge} \approx 2.9 \times 10^{12}\,{\rm yr}\, &\left(\frac{m_1}{10^6\,{\rm M_\odot}}\right)^{-1}\left(\frac{m_2}{10^6\,{\rm M_\odot}}\right)^{-1} \\ &\left(\frac{m_1+m_2}{2\times10^6\,{\rm M_\odot}}\right)^{-1}\left(\frac{a_1}{10^{-2}\,{\rm pc}}\right)^{4} F(e) \quad , \end{aligned} \tag{3.12}$$

where

$$F(e) = \left(1 + \frac{73}{24}e_1^2 + \frac{37}{96}e_1^4\right)\left(1-e_1^2\right)^{\frac{-7}{2}} \tag{3.13}$$

(Blaes, Lee, & Socrates 2002). When including Post-Newtonian perturbations, the corrected timescale for Peters' merger timescale is

$$T_{\rm corr} = T_{\rm merge} 8^{1-\sqrt{1-e_1}} \exp\left(\frac{2.5 r_{\rm s,inb}}{a_1(1-e_1)}\right) \quad , \tag{3.14}$$

(Zwick et al. 2020), where $r_{\rm s,inb} = 2GM/c^2$ is the effective Schwarzschild radius of the binary system, M is the mass of the binary system, and c is the speed of light. Equation (3.14) shows that both the semi-major axis and eccentricity strongly influence the merger timescale.

3.3.2 SMBH kinematics

The evolution of the kinematical properties of the three SMBHs in each of the simulations share many similarities. In all simulations, black holes 2 and 3 migrate towards the center (where black hole 1 is located), until a SMBH binary is formed, as shown in the third panels of Figures 3.5-3.34. In most cases, the newly-formed binary consists of the two most massive black holes.

The SMBH migration timescale observed in the simulations is consistent with the relation described in Equation (3.9), and shows the expected relation with mass: $t_{\mathrm{fric}} \propto m^{-1}$. For example, in simulation C (Figure 3.1), the theoretical dynamical friction timescale is 1.11×10^2 Myr, or roughly 14 N-body time units. The numerical value estimated from the second panel of Figure 3.1 is roughly 15 N-body time units. This indicates that the numerical value is comparable with the theoretical value. Following the short period of migration, a new SMBH binary is formed in each of the simulations.

3.3.3 Classification of evolutionary pathways

Since two SMBHs (m_2 and m_3) migrate towards the center of the merged system where the other SMBH (m_1) is located, a three-body interaction involving the SMBHs is inevitable. In the majority of the simulations, the two most massive SMBHs form a binary system, and this system is perturbed by the third, least massive SMBH. Strong dynamical interactions between the three SMBHs often result in exchanges involving the binary system. How frequently exchange-reactions between the inner binary and the third body occur, depends on the initial conditions of the system; notably on the mass ratio. By inspecting the evolution of the inverse semi-major axis in simulation B, shown in the bottom panel of Figure 3.2, we find that there are frequent jumps. On the other hand, there is no spike in the evolution of inverse semi-major axis in simulation F, as shown in the bottom panel of Figure 3.3. This suggests that the exchange of inner binary companions occurs very frequently in simulation B, but there are no exchanges with the inner binary in simulation F.

After inspection of the dynamical evolution of the SMBH triplet, we can classify the systems into two categories. Systems in Category (1) show nearly no exchanges with the inner binary system. This includes simulations E, F, I, J, K, M, N, O, R and T. Category (2) contains the systems in which exchanges of the inner binary system frequently occur. This includes simulations A, B, C, D, G, H, L, P, Q, S and U.

In general, we find that the models in Category (1) have $q \lesssim 1$, and those in Category (2) have $q \gtrsim 1$. Figure 3.4 shows the number of exchanges of inner binary companions in each triple SMBH system. Exchanges of inner binary companions in Category (2) are more frequent than in Category (1). In Category (2), we observe oscillation behavior when the mass ratio increases. This is unexpected but reasonable. Milosavljević & Merritt (2003) introduced the concept named "secondary slingshot", suggesting that stars with an orbital period shorter than the binary orbit decay timescale can be reintroduced in the loss cone and take away energy. The oscillating behavior of exchange of inner binary may originate

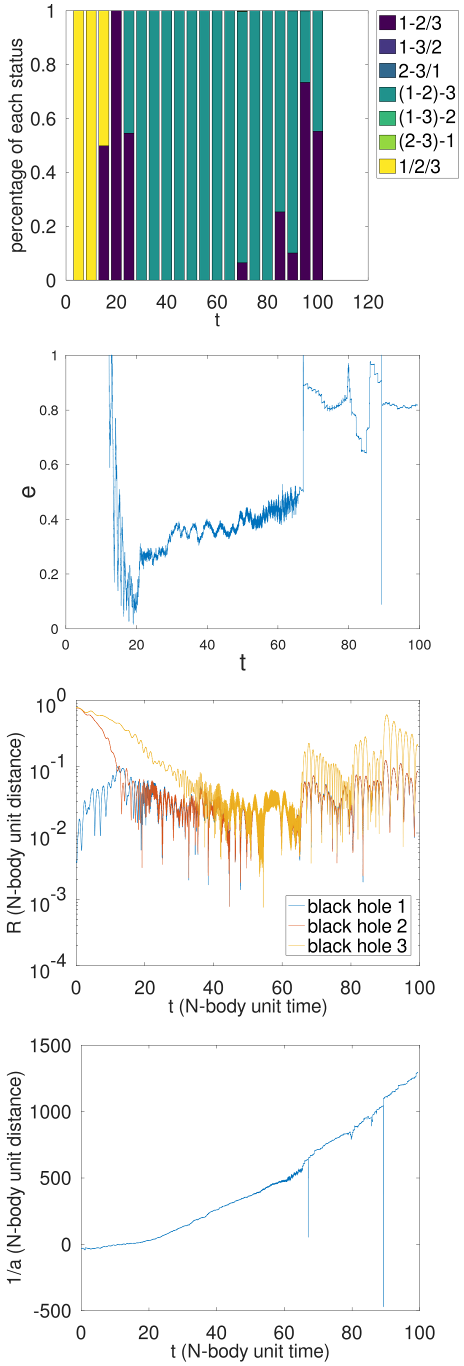

Figure 3.1: Evolution of inner binary black holes in simulation C.

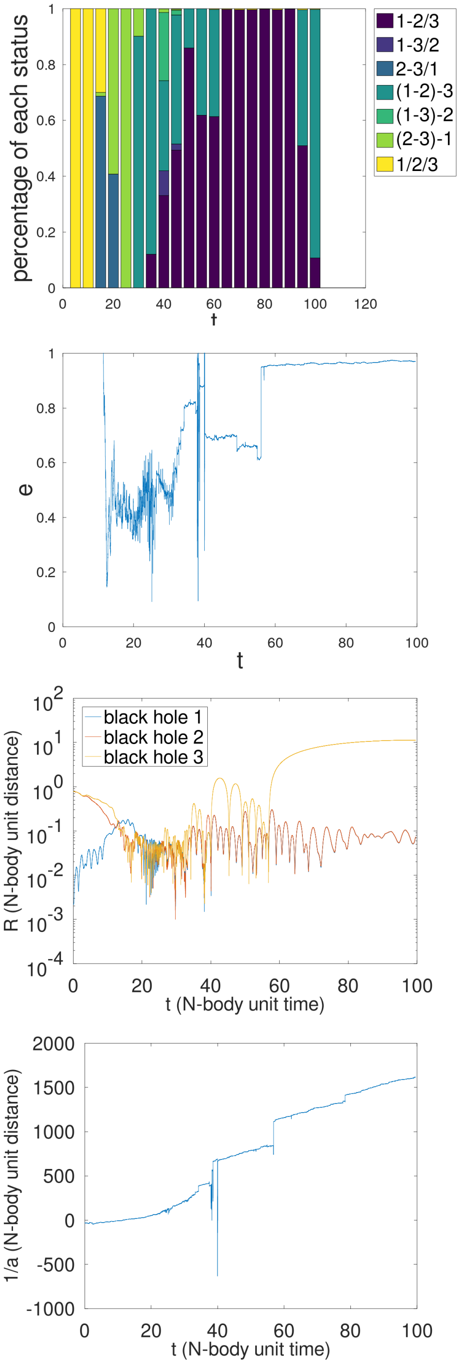

Figure 3.2: Evolution of inner binary black holes in simulation B.

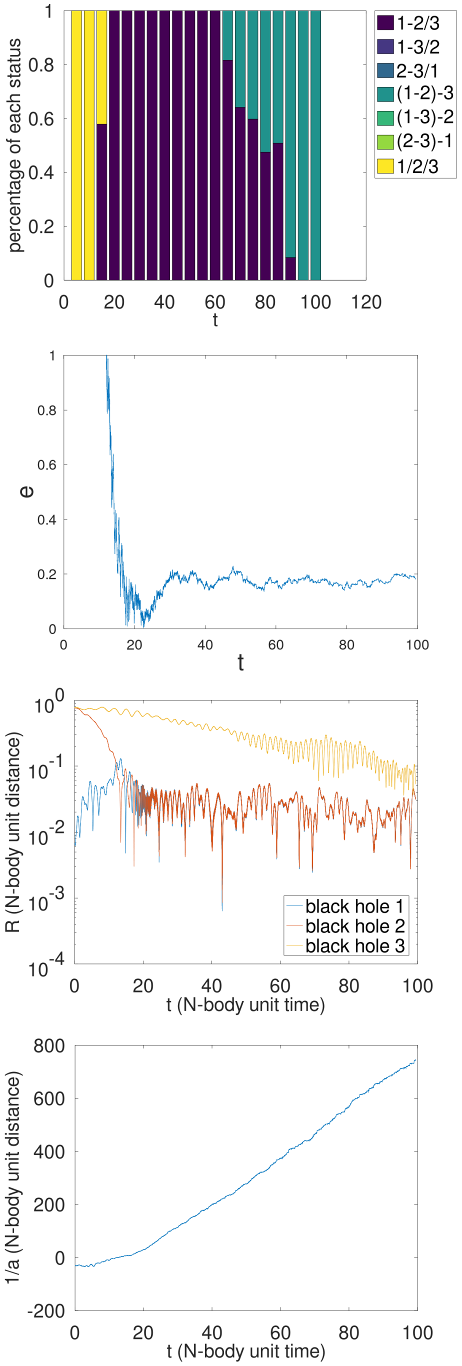

Figure 3.3: Evolution of inner binary black holes in simulation F.

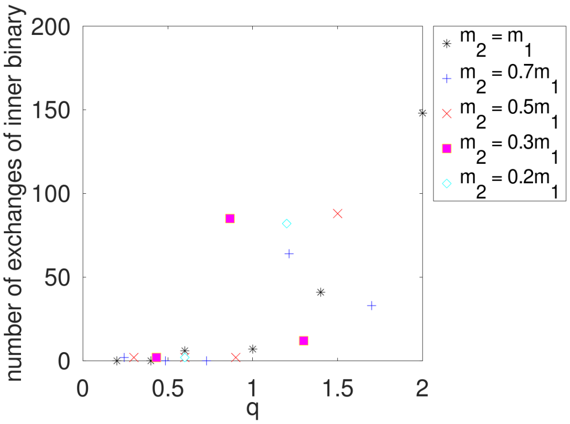

Figure 3.4: The number of exchanges of the inner binary in each of the simulations. The horizontal axis denotes the mass ratio q (see Equation 3.4). The vertical axis indicates the number of times that one of the SMBHs of the inner binary is exchanged with the third SMBH, within the simulated time.

from the ”secondary slingshot”. The SMBH with smaller mass needs to interact with the inner binary so that the energy and angular momentum of the inner binary can be extracted efficiently.

3.3.4 Slingshot ejections of one SMBH

Strong dynamical interactions between the three SMBHs occasionally result in the dynamical ejection of one of the SMBHs from the triplet. For example, in both simulations A and B, one SMBH was ejected. In simulation A, however, the SMBH was permanently ejected, while simulation B one of the SMBHs was ejected but later returns to the core of the cluster.

Below we inspect simulations A and F in detail, in order to determine how three-body exchanges between the SMBHs affect the evolution of the inner binary orbit. The third panel of Figure 3.5 shows the evolution of the distance of the three SMBHs from the center for simulation A. The semi-major axis and eccentricity are those of the orbit of the inner binary (see Equations 3.6 and 3.7). Initially, the three SMBHs are mutually unbound. At $T \approx 10$ N-body units, two of the SMBHs form a bound pair, and the inverse semi-major axis becomes positive. The dramatic jumps in the inverse semi-major axis and eccentricity indicates exchanges between inner binary companions and the third SMBH. This results a decrease in the semi-major axis and an increase in the eccentricity. At $T \approx 70$ N-body units, black hole 3 is ejected from the system. After the ejection of black hole 3, the eccentricity of the inner binary gradually decreases to a nearly constant value around $e \approx 0.3$. The inverse semi-major axis also shrinks rapidly due to a phase of complex three-body interactions with the stellar population.

Figure 3.3 shows the evolution of the triple black hole system in simulation F. Simulation F has identical initial conditions as Simulation A, apart from the mass of the third black hole. In simulation F, there is no ejection of an black hole, and stable binary-single configuration emerges which lasts until the end of the simulation. No jumps occur in the evolution of the inverse semi-major axis, and there is no exchange of the inner binary companion. The eccentricity decreases from $e \approx 1$ to $e \approx 0$, and then increases to $e \approx 0.2$ at $T \approx 30$. It oscillates around this value for the remainder of the simulation. In general, the simulations indicate that a more massive tertiary body has a stronger perturbing influence on the evolution of the inner binary, and shrinks the inner binary orbit, followed by a slingshot ejection of one of the SMBHs.

Another example, shown in Figure 3.2, presents the evolution of the distance of the SMBHs from the cluster center, and semi-major axis and eccentricity of the inner binary in simulation B. In this simulation, one of the SMBHs is expelled from the core but still remains bound to the system. The figure shows that the lowest-mass SMBH (m_3) is expelled from the center of the system, but the velocity at which it is expelled is sufficiently small for it to return, given sufficient time. As a consequence of the three-body interaction that leads to the ejection, the semi-major axis of the inner SMBH binary experiences a sharp drop, and the eccentricity of inner binary increases substantially.

3.3.5 Three-body interaction with nearly no exchanges

Exchanges between the inner binary and the tertiary SMBH are absent or nearly absent in a subset of the simulations. Figure 3.7 shows the evolution of the triple black hole system in simulation E. The evolution of the inverse semi-major axis in simulations E and F is similar. The eccentricity evolution is also similar. However, the inverse semi-major axis in simulation is higher than in simulation F at the end of the simulation.

Hardening rates for simulations E and F are obtained by applying linear regression. The hardening rate (in N-body units) is 12.73 for simulation E and 9.67 for simulation F. Although the tertiary SMBH does not become bound to the inner binary, it still affects the hardening rate. Here we may conclude that a more massive tertiary body can help increase

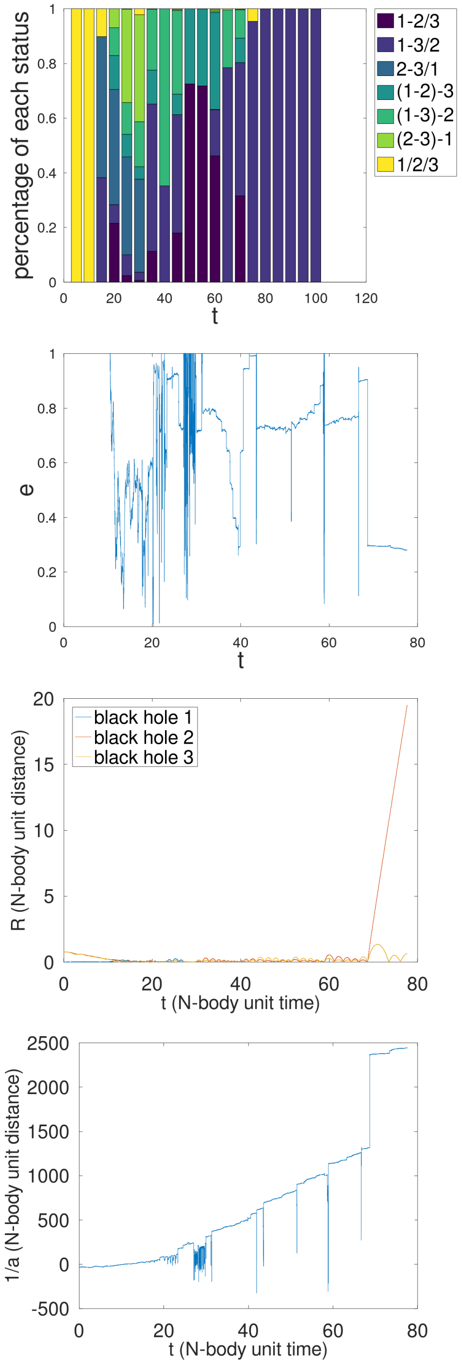

Figure 3.5: Evolution of inner binary black holes in simulation A. The top panel indicates which of the three black holes are bound in a binary or triple system, versus time. The second, third, and fourth panels show the evolution of the eccentricity, the distance to the center, and the inverse semi-major axis.

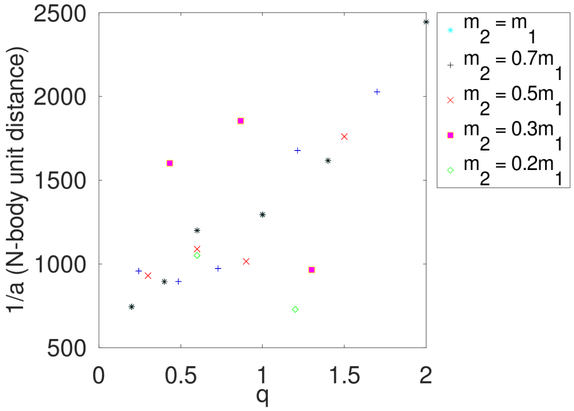

Figure 3.6: The final inverse semi-major axis of each simulation (in N-body units) versus the mass ratio q of the SMBH triplet.

the inner binary hardening rate and further shrink the orbit of inner binary.

By analyzing the relationship between the final inverse semi-major axis and mass ratio q, the relationship between the projected merger timescale and mass ratio can be determined. Figure 3.6 shows the relationship between final inverse semi-major axis and mass ratio q, at time $T = 100$. In general, the inverse semi-major axis at the end of the simulations is higher for systems with higher mass ratios q, which results in a shorter gravitational wave merger timescale.

The bottom panels of Figures 3.1, 3.7 and 3.3 show the evolution of the inverse semi-major axis of the inner binary black hole in simulations C, E, and F, respectively. The results of simulation C show that the timescale of chaotic three-body interactions is short, indicating that there is nearly no chaotic three-body interaction. In this case, the mechanism introduced in Section 3.3.4 is no longer valid in this scenario. The top panels in Figures 3.1, 3.7 and 3.3 show that fraction of time that the three SMBHs in simulation C spend in a bound triple system is more than in simulations E and F. The fraction of time in simulation E that the SMBHs spend in a bound triple system is higher than in simulation F. Figure 3.8 shows the evolution of the inverse outer semi-major axis of the triple SMBH system. This confirms the mechanism proposed by Blaes, Lee, & Socrates (2002) which states that tertiary black holes bound to the inner binary may enforce the binary to interact with surrounding stars more frequently, and hence increase the hardening rate.

In simulation C, $\dot{\omega}_{\rm KL}$ is always larger than $\dot{\omega}_{\rm GR}$. The $r_{\rm S,inb}$ for a binary SMBH with

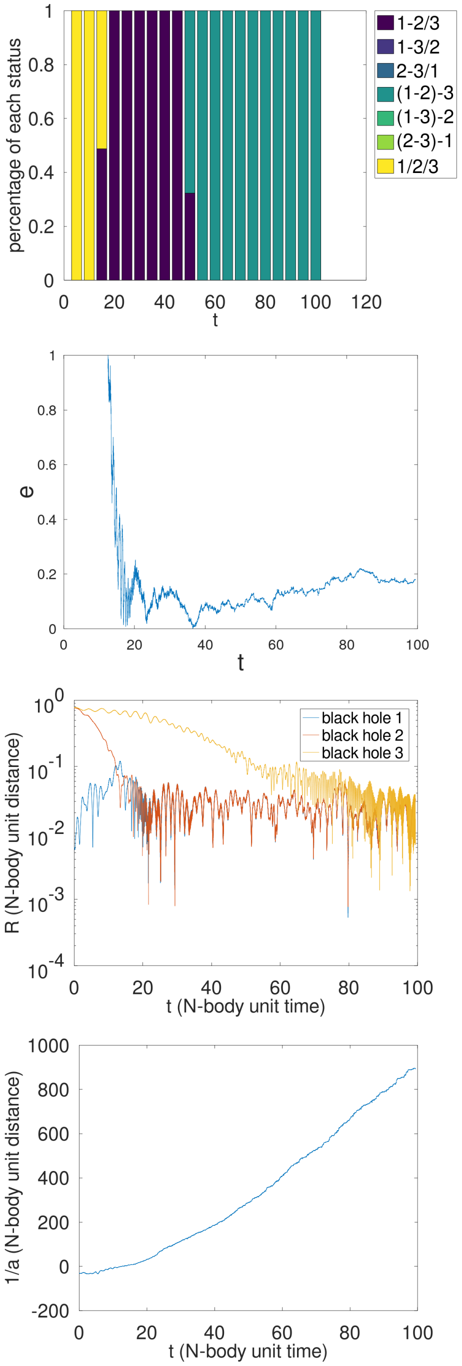

Figure 3.7: Evolution of inner binary black holes in simulation E.

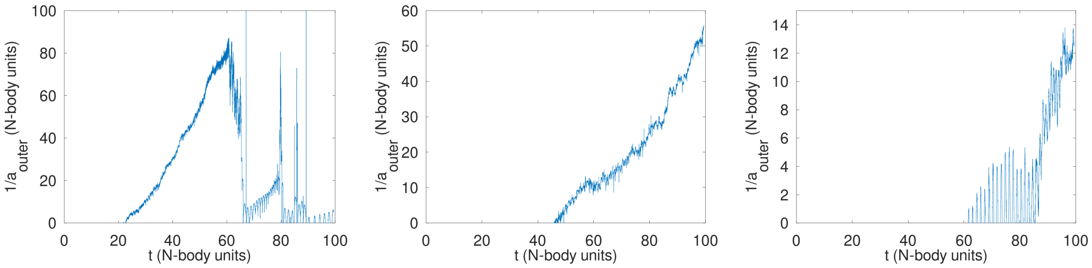

Figure 3.8: The evolution of the inverse outer semi-major axis of the SMBH triplets in simulations C (*left*), E (*middle*) and F (*right*). Quantities are shown in N-body units.

a component mass of $10^8\,\mathrm{M}_\odot$ is on the order of several astronomical units, much smaller than the semi-major axis of the inner binary, and $\dot{\omega}_{\mathrm{KL}}$ is thus much larger than $\dot{\omega}_{\mathrm{GR}}$. In simulation C, for example, the mass precession rate during the Kozai resonance is always smaller than the Kozai precession rate (see the discussion below).

The second panel of Figure 3.1 shows the eccentricity evolution of inner binary SMBH. Eccentricity oscillations occur at $T \approx 40$, consistent with the oscillation of mutual inclination in Figure 3.10. At $T = 60$, the eccentricity increases, without a clear oscillation pattern. However, the oscillation of eccentricity and inclination between $T \approx 40$ and $T \approx 60$ are very weak. In order to determine whether this is caused by the Kozai mechanism, we plot in Figure 3.9 the Kozai timescale, which is roughly 0.63 N-body time units (about 4.8 Myr) at $T \approx 55 - 60$. Figures 3.10 and 3.1 show that seven oscillations occur in the interval $T \approx 55 - 60$. The period of oscillation in this time span is therefore 0.71 N-body time units (5.4 Myr). This oscillation period agrees with the estimated Kozai timescale, suggesting that the SMBH triplet is in a Kozai resonance. The agreement between the Kozai timescale and eccentricity oscillation timescale implies that the Kozai resonance operates, but it is very weak. It is possible that Kozai resonance may be hinder by mass-precession. Figure 3.9 compares the mass precession timescale and the Kozai timescale for simulation C. Both timescales vary significantly over time. Between $T = 40$ and $T = 60$, the mass-precession timescale is longer than the Kozai timescale, indicating that mass-precession does not hinder the Kozai resonance significantly during this period. Figure 3.10 shows the mutual inclination of the inner binary to the outer binary orbital plane in simulation C. The mutual inclination is nearly constant between $T = 40$ and $T = 60$, with very weak oscillations. In combination with Figure 3.9, this suggests that the Kozai-mechanism is suppressed, and does not play an important role in the evolution of the triple SMBH system in simulation C. In

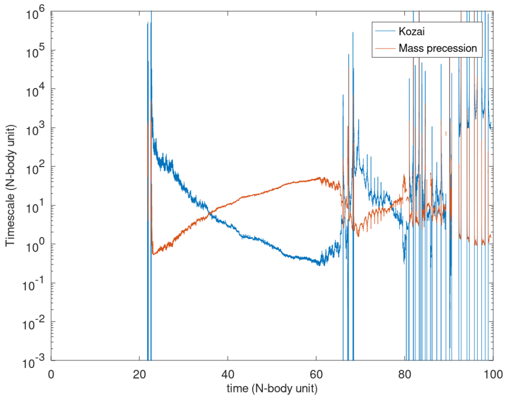

Figure 3.9: Comparison between the Kozai timescale and the mass-precession timescale in simulation C.

simulations C, E and F, We do not observe a clear pattern of oscillations in the eccentricity; in these systems, the Kozai-Lidov mechanism does not play an important role.

3.3.6 Implications for the gravitational wave merger timescale

Equation (3.12) shows that the extrapolated gravitational wave merger timescale of a SMBH binary depends strongly on both semi-major axis and eccentricity. The merger timescale of the inner binary in each simulation is calculated and presented in Figure 3.11. These values are calculated directly from Equation (3.12) and represent the timescale at which such a binary would merge if the system were to evolve in isolation.

It can be inferred from Figure 3.11 that in general, the merger timescale decreases when larger values of q are selected as initial conditions. The increase in the merger timescale probably originates from the decrease in the eccentricity of the inner binary. It is expected that the SMBH binary will reach the necessary separation to trigger coalescence in less than a Hubble time ($\sim 10^{10}$ years) with the intrusion of third SMBH under certain conditions.

Figure 3.12 shows the gravitational wave merger timescale of simulations with varying secondary mass and fixed tertiary mass. It is observable that on the upper-left panel, the corresponding extrapolated merger timescale for $q = 0.3$ is lower than the timescale when $q = 0.5$, then increase for all three time snapshots. In the other panels there are no clear trend of a decreasing merger timescale as as q increases, for any the three time snapshots. This indicates that the ratio between secondary and primary mass does not affect the

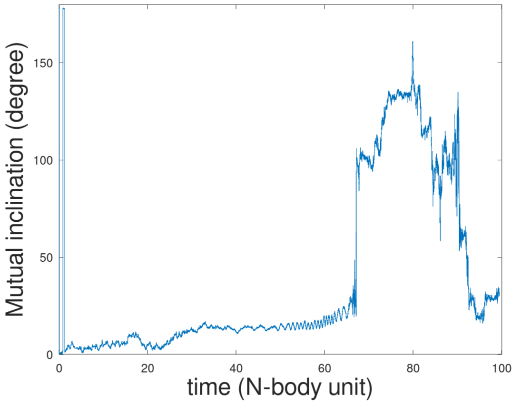

Figure 3.10: Evolution of the mutual inclination of the SMBH triplet in simulation C. The mutual inclination angle of a triple system is the angle between the orbital planes of the inner binary and the outer binary. When the SMBHs do not form a gravitationally-bound triple system, the mutual inclination is calculated the plane in which the closest pair orbits, and the plane in which the third body orbits relative to this pair.

merger timescale of inner binary.

3.3.7 Effects of stochasticity

The interaction between three black holes is generally chaotic, so that small differences between initial conditions may result in significant differences in the outcome. This is most notable in the equal-mass case ($q = 2$). For this reason, we carry out nineteen additional simulations with the same mass in simulation A with different random number seeds, which determine how the stellar positions and velocities are initialized from the Plummer model.

Figures 3.13-3.17 show the evolution of the distance to the center of the three SMBHs in the nineteen additional simulations with different random seeds. One SMBH escapes from the system in five of the twenty simulations, while in the other fifteen simulations all SMBHs remain bound to the cluster core. Although our simulated time is limited, the ongoing chaotic interactions suggest that additional SMBHs may escape at later times. This would imply that a free-floating SMBHs may be relatively common, which is in agreement with the findings of Iwasawa, Funato, & Makino (2006).

When comparing the bottom panels of Figures 3.1, 3.7 and 3.3, we see that when the tertiary SMBH mass is small compared to that of the binary SMBH, such as in simulations E

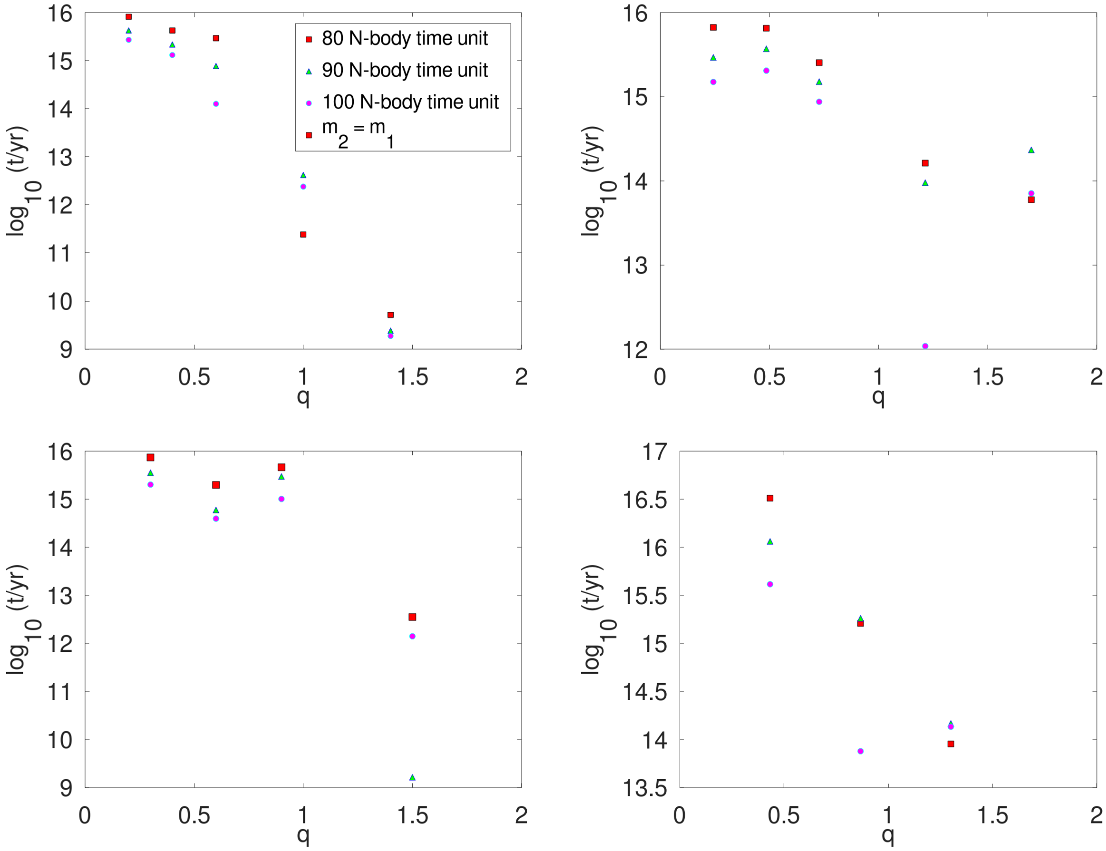

Figure 3.11: The extrapolated gravitational wave merger timescale at different times, for systems with different mass ratios, q (see Equation 3.4).

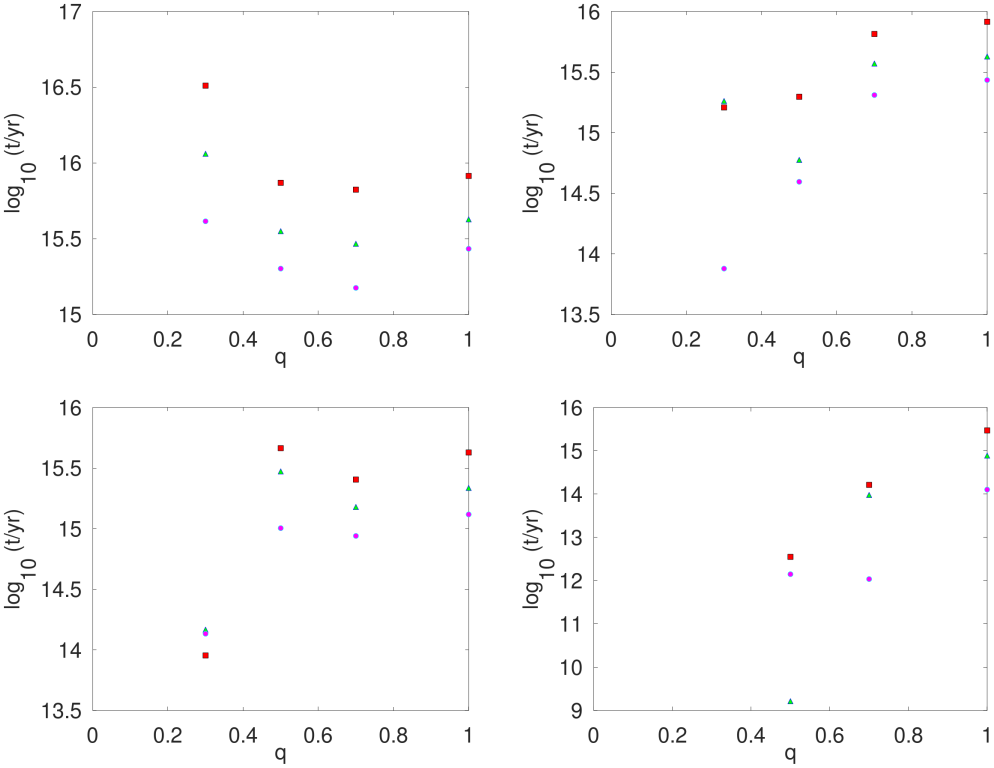

Figure 3.12: The predicted evolution of the inner SMBH binary systems, with secondary mass variable and tertiary mass fixed. The vertical axis denotes time in years. The quantity q stands for the mass ratio between secondary mass and primary mass. Panels show the extrapolated gravitational wave merger timescale for simulation with $m_3 = 0.001$ (top-left), $m_3 = 0.002$ (top-right), $m_3 = 0.003$ (bottom-left), and $m_5 = 0.005$ (bottom right). The labels in legend denote the extrapolated gravitational wave merger timescale measured at each time snapshot.

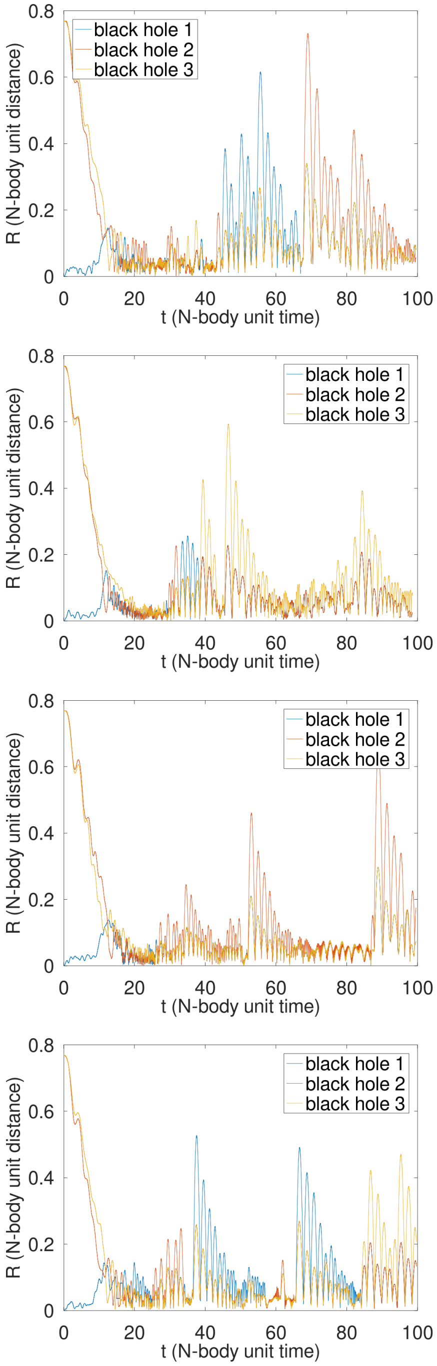

Figure 3.13: The evolution of triple black hole system in simulations with different random seeds for the initial stellar distribution. In these four simulations, no SMBH was ejected from the core.

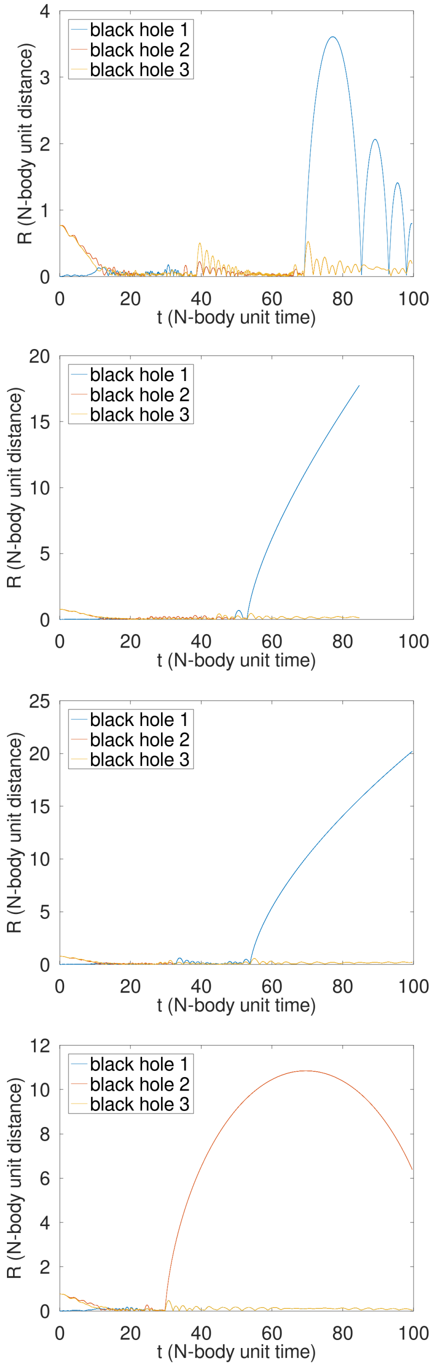

Figure 3.14: Same as Figure 3.13, for different random seeds. In these four simulations, one of the SMBHs was expelled from the core with a speed below the escape velocity of the system.

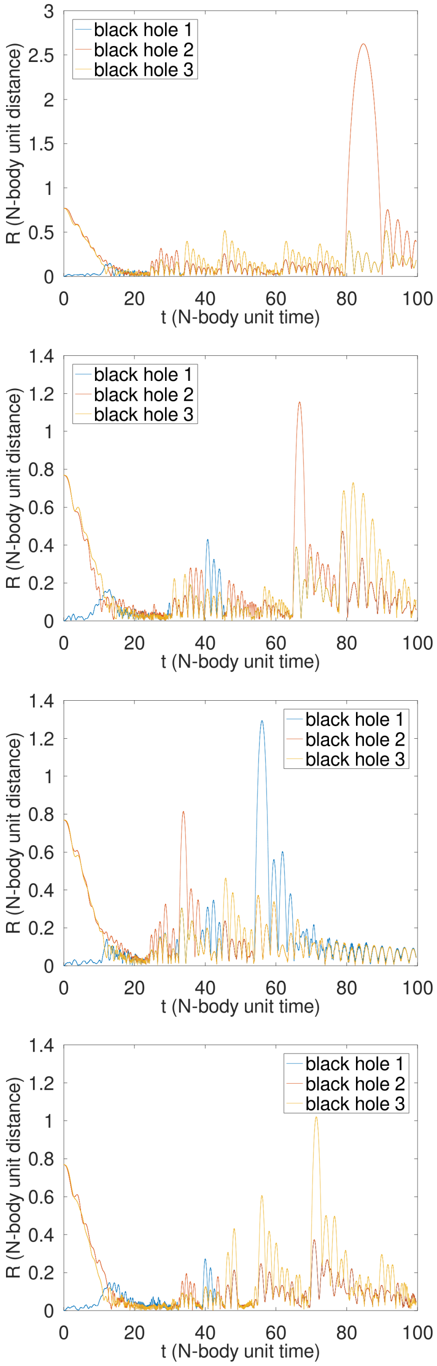

Figure 3.15: Same as Figure 3.14, for different random seeds. In each of these four simulations, one SMBH was expelled from the core, with a speed below the escape velocity. In each of these cases, the expelled SMBH returns to the core during or after the simulation.

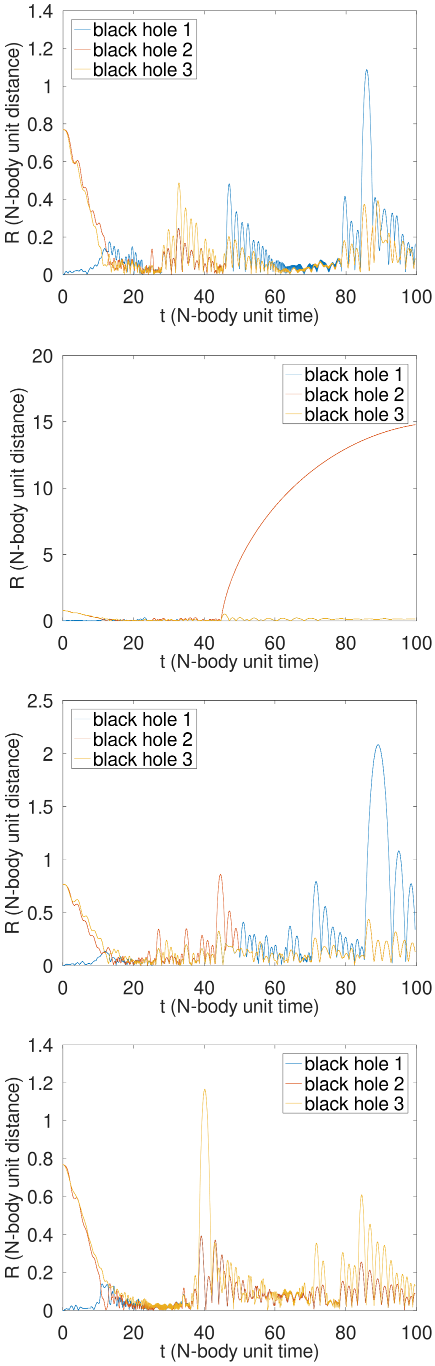

Figure 3.16: Same as Figure 3.14, for different random seeds. one SMBH was expelled from the core, with a speed below the escape velocity. In each of these cases, the expelled SMBH returns to the core during or after the simulation.

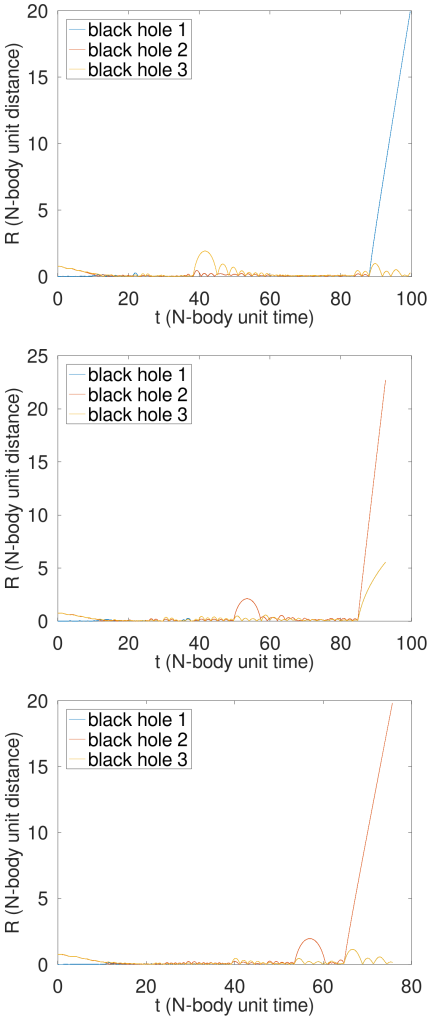

Figure 3.17: Same as Figure 3.14, for different random seeds. In these three simulations, at least one SMBH was ejected from the core. In the first and third panel, one SMBH is ejected. In the second panel, one SMBH is ejected and one SMBH is expelled but returns.

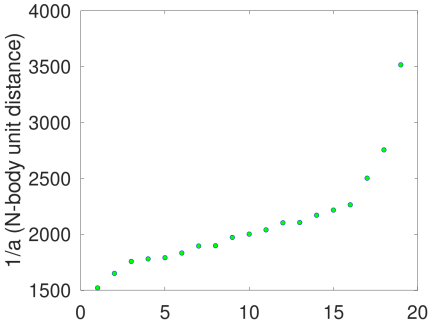

Figure 3.18: The final semi-major axis (at $T = 100$ N-body units) of twenty simulations with equal-mass SMBH triplets ($q = 2$). The horizontal axis indicates the different realizations. All simulations have identical (global) initial conditions, but differ in the random seed that is used to initialise positions and velocities of the stellar population.

and F, strong three-body interactions do not take place. Instead, the tertiary SMBH orbits the inner binary and increases the hardening rate of the inner binary SMBH.

Equation (3.12) shows that the gravitational wave merger timescale depends the semi-major axis as $t_{\rm merge} \propto a^4$, but also that it has a much stronger dependence on the eccentricity. For a given semi-major axis, an increases in the eccentricity from $e = 0.2$ to $e = 0.8$ shortens the merger timescale by a factor of 31. As mentioned in Section 3.3.5, the high eccentricity of the inner binary SMBH is generally not a result of the Kozai mechanism, but is instead caused by binary-single interactions involving the three SMBHs. The latter process is highly chaotic, and its general outcome is therefore difficult to predict using analytic methods or numerical approaches.

Figure 3.18 shows the inverse of the final semi-major axes of twenty simulations with equal-mass SMBH triplets, but with different random seeds. The final inverse semi-major axis of the twenty simulations with equal-mass SMBH triples varies by up to a factor of two, with a maximum of $a^{-1} \approx 3500$ and a minimum of $a^{-1} \approx 1500$ N-body units. These variations originate from the stochastic nature of the stellar population.

3.4 Conclusions and discussion

We present a study on the dynamical evolution of triple SMBH systems in galaxy centers, with the aim of constraining the influence of a third SMBH companion on the evolution of a SMBH binary system. We have performed a series N-body simulations of SMBH triples with different mass ratios in a stellar environment using the N-body code `NBODY6++GPU`. Our main conclusions can be summarized as follows.

1. The three initially-unbound SMBHs with masses $m_1 \geq m_2 \geq m_3$ experience migration through dynamical friction within several crossing times. This process is followed by strong three-body scatterings, and the rapid formation of an SMBH binary system that usually consists of the two most massive SMBHs (m_1 and m_2).

2. For given masses m_1 and m_2, a more massive tertiary black hole (m_3) tends to result in a higher hardening rate, $s(t)$. A more massive tertiary SMBH generally leads to a shorter (extrapolated) gravitational wave merger timescale of the inner binary SMBH system, shorter than a Hubble time. The inclusion of a tertiary SMBH with a mass comparable to the components of the binary SMBH can be a great aid in shrinking the semi-major axis of the inner binary SMBH to a value smaller than 1 pc, hence bypassing the *final parsec problem.*

3. In the cases where $m_1 = m_2$, an increase in the tertiary black hole mass increase from $10^7 \mathrm{M}_\odot$ to $7 \times 10^7 \mathrm{M}_\odot$, results in a reduction of the merger timescale of inner binary SMBH by several orders of magnitude.

4. The ratio m_2/m_1 has no significant effect on the extrapolated gravitational wave merger timescale of the inner binary SMBH, when embedded in a galaxy core.

5. Small changes in the initial conditions of the stellar population may result in different outcomes in terms of SMBH ejections. In several simulations, SMBHs are ejected form the system, while in others SMBHs may be temporarily ejected from the core. Repeated ejections of SMBHs from the center of galaxy merger remnant may occur.

6. Two mechanisms drive the orbital shrinking of the inner SMBH binary: (i) the interacting third SMBH pushes the inner binary around and enhances the hardening rate by further driving inner binary to interact with surrounding stars, and (ii) slingshot ejections of one of the SMBHs tend to harden the inner SMBH binary.

7. Repeated dynamical interactions between the tertiary SMBH and the inner binary SMBH may result in repeated hardening events of the inner SMBH binary, in which its semi-major axis shrinks abruptly. Both the frequency of inner binary exchange and the final semi-major axis value have a positive correlation with the mass ratio, $q = m_3/\mu_{12}$, of the SMBH triplet.

In our study have approximated the surrounding stellar population with a limited number of particles. Future simulations in which individual stars are modeled may provide further insights in how the stellar population drives the shrinking of both the inner and outer orbits of triple SMBH systems. Our system also did not include rotation of the stellar population, which may be worth studying in the follow-up work. Our findings may help computational astronomers to have a rough estimation of the gravitational wave merger timescale of a triple SMBH and provide an alternative solution to the ”final-parsec problem”. Our simulation may provide an aid to observational studies in predicting the evolution of the observed triple nucleus in a galaxy center.

3.5 Evolution of triple SMBH systems

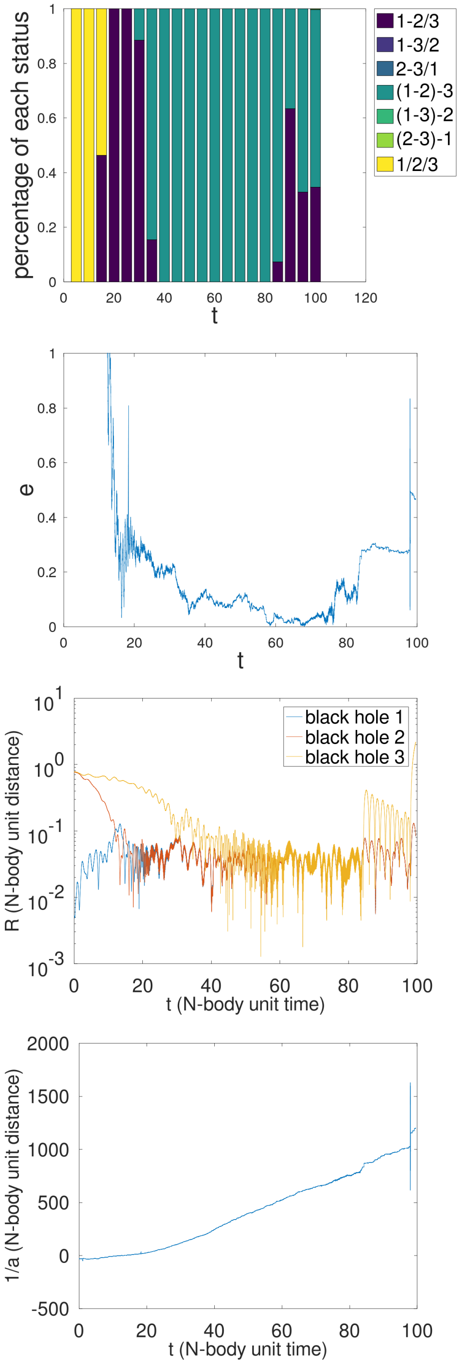

Figure 3.19: Evolution of inner binary black holes in simulation D.

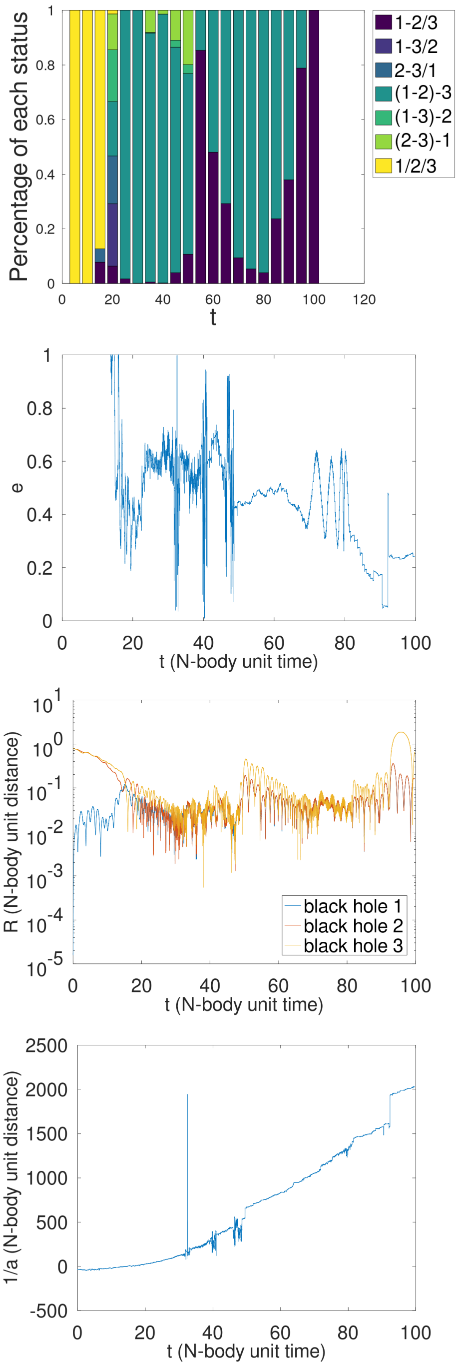

Figure 3.20: Evolution of inner binary black holes in simulation G.

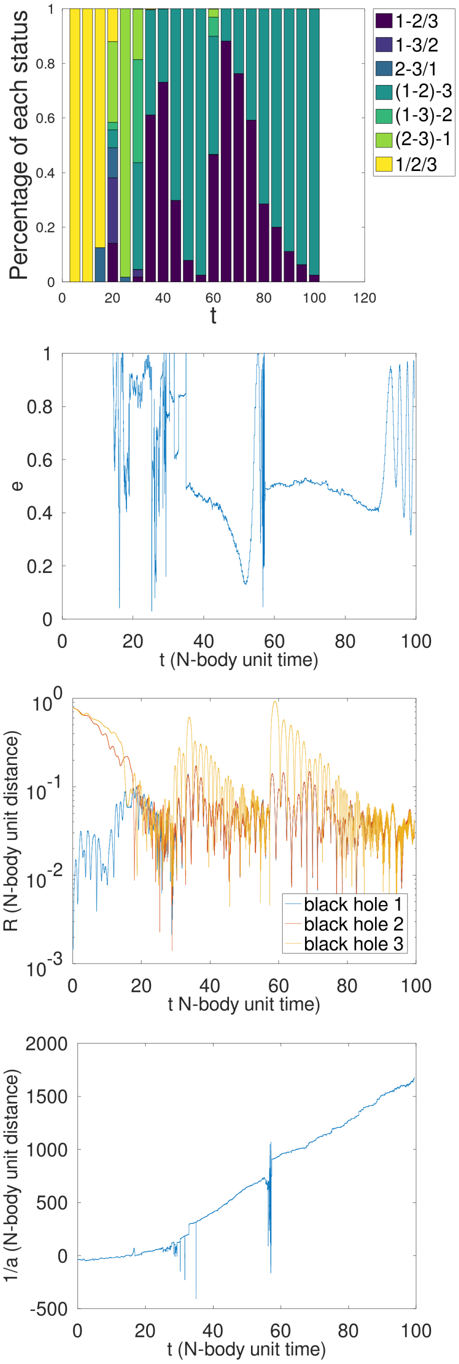

Figure 3.21: Evolution of inner binary black holes in simulation H.

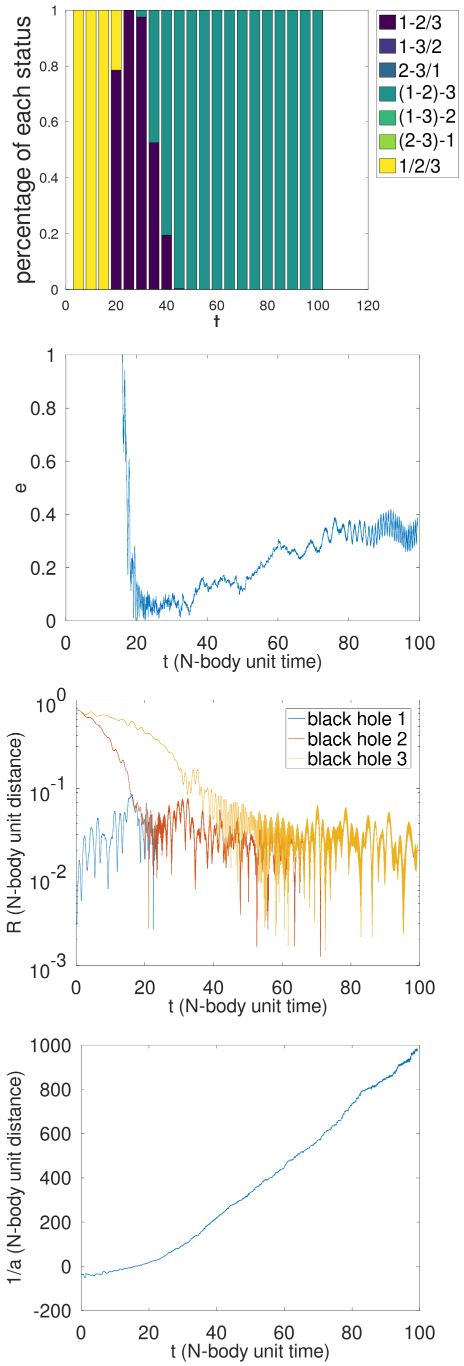

Figure 3.22: Evolution of inner binary black holes in simulation I.

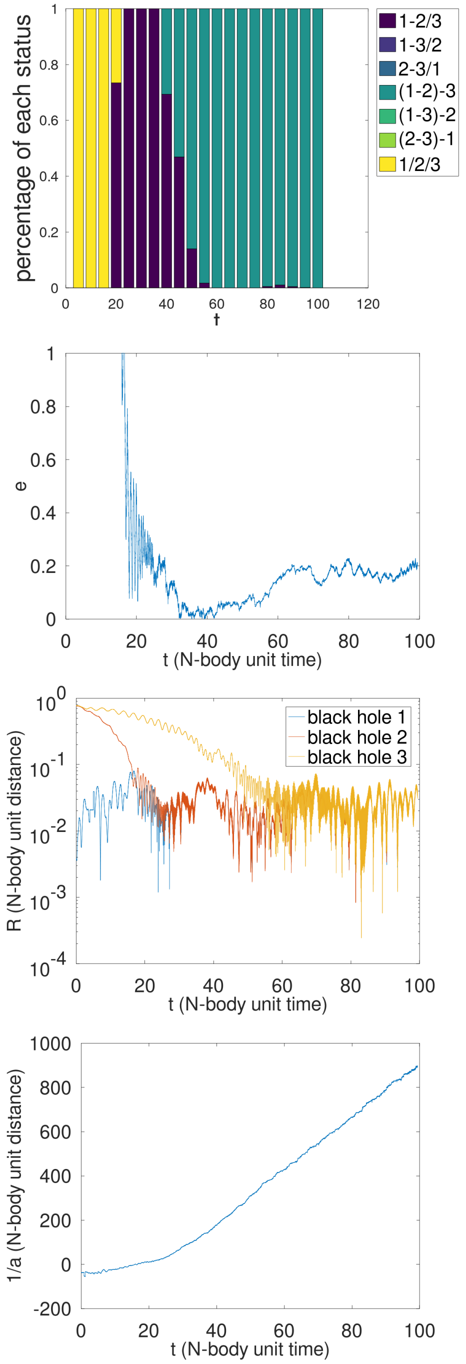

Figure 3.23: Evolution of inner binary black holes in simulation J.

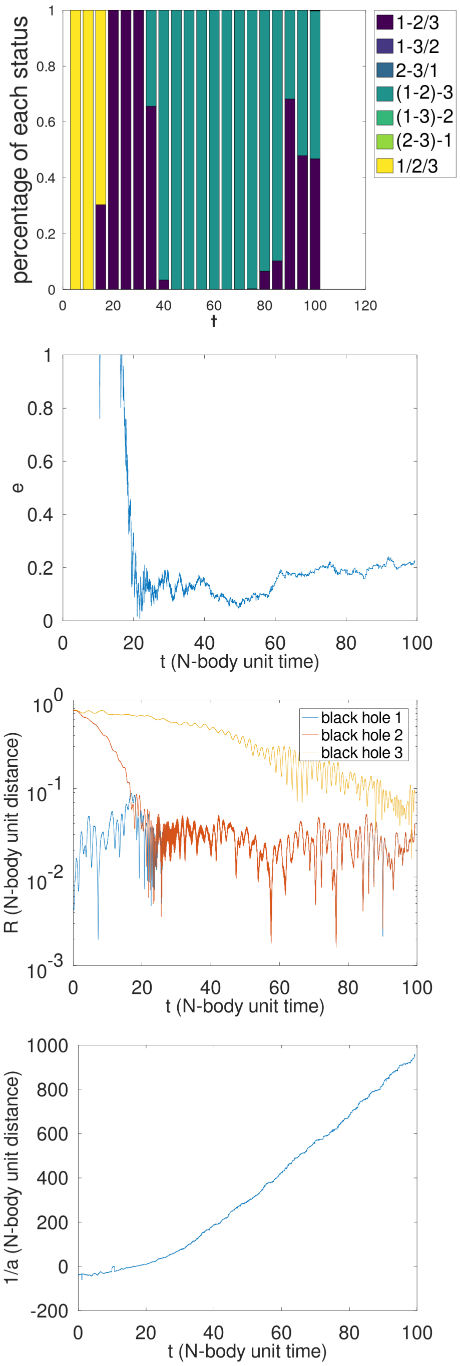

Figure 3.24: Evolution of inner binary black holes in simulation K.

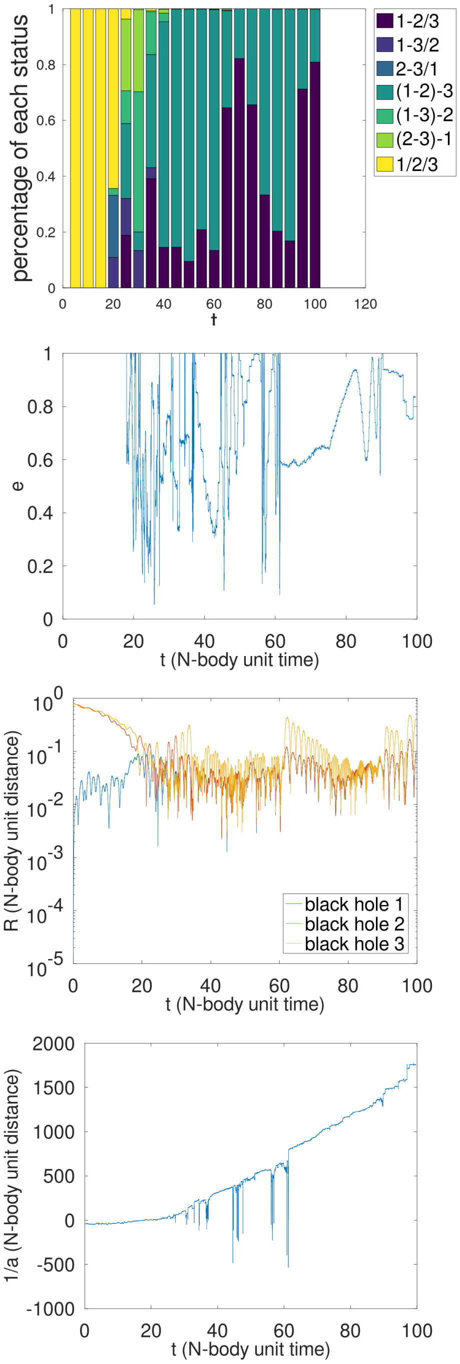

Figure 3.25: Evolution of inner binary black holes in simulation L.

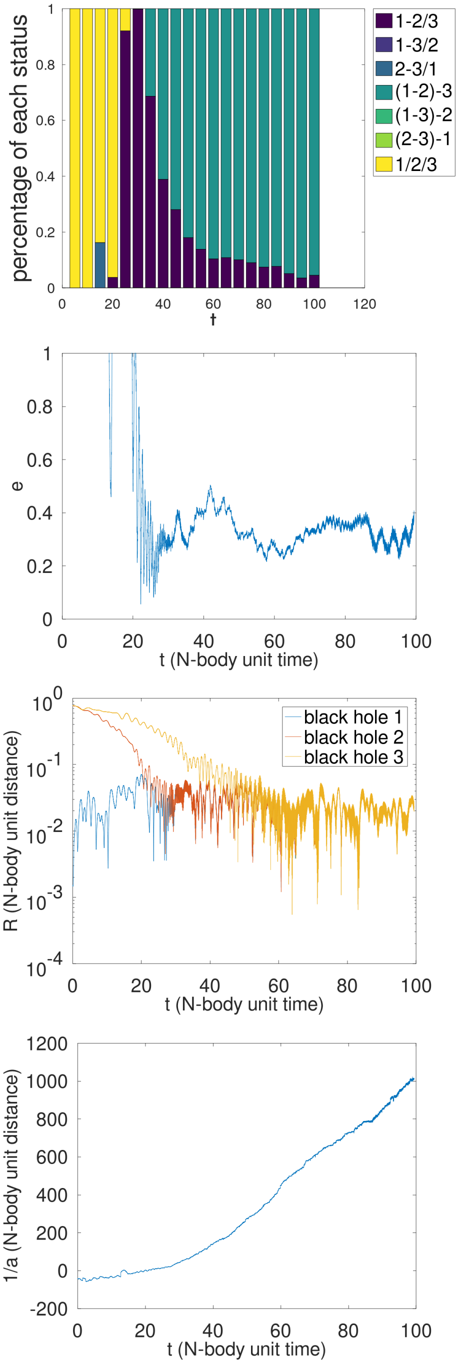

Figure 3.26: Evolution of inner binary black holes in simulation M.

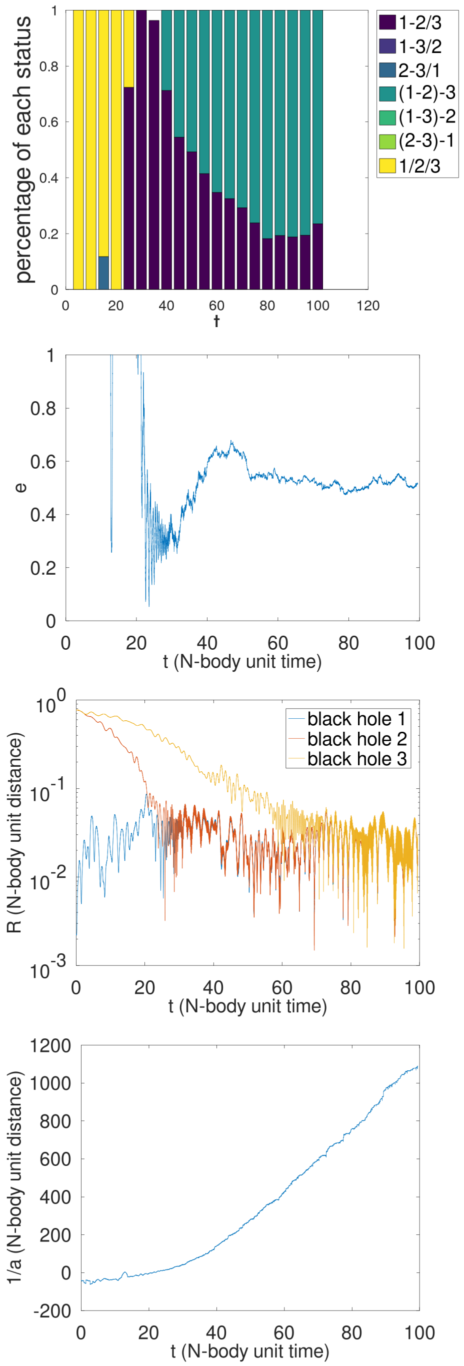

Figure 3.27: Evolution of inner binary black holes in simulation N.

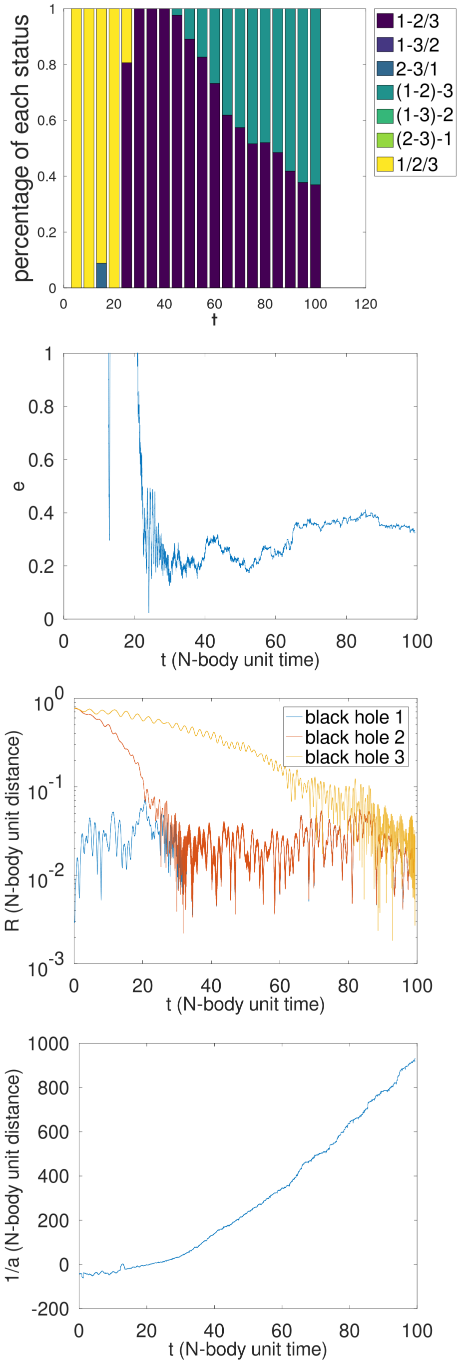

Figure 3.28: Evolution of inner binary black holes in simulation O.

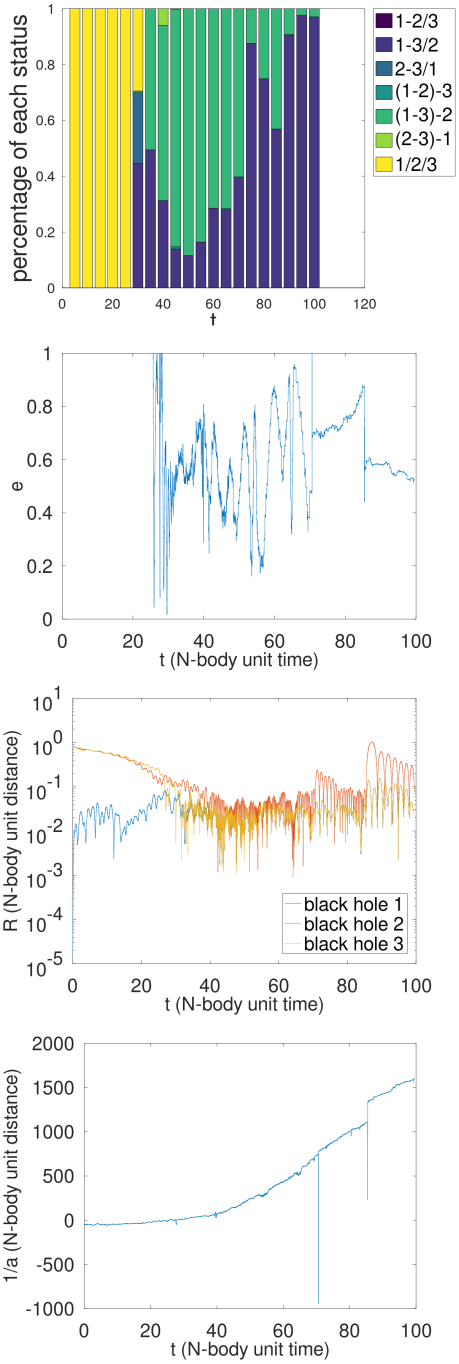

Figure 3.29: Evolution of inner binary black holes in simulation P.

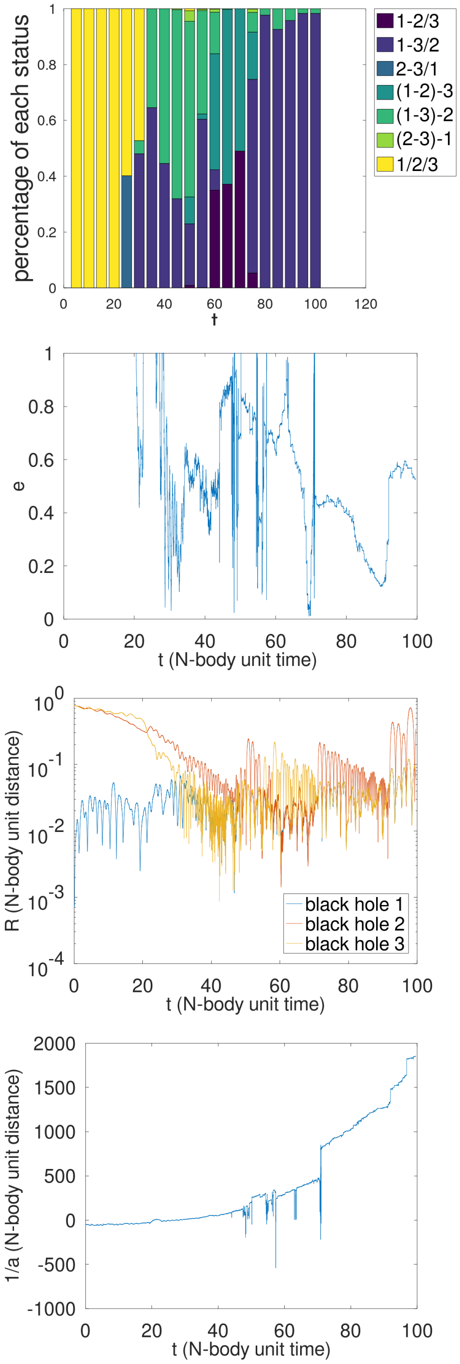

Figure 3.30: Evolution of inner binary black holes in simulation Q.

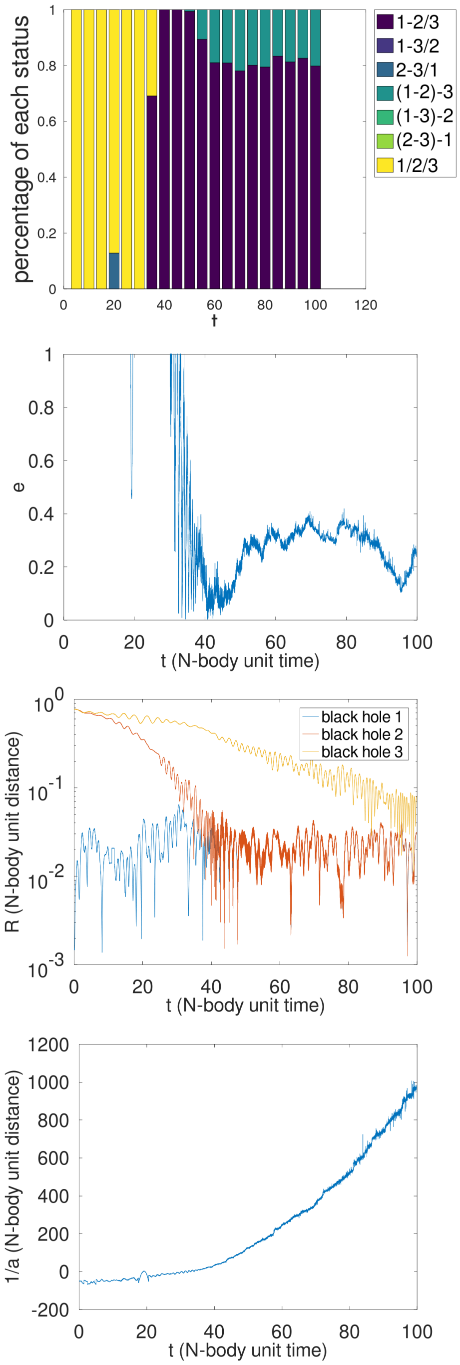

Figure 3.31: Evolution of inner binary black holes in simulation R.

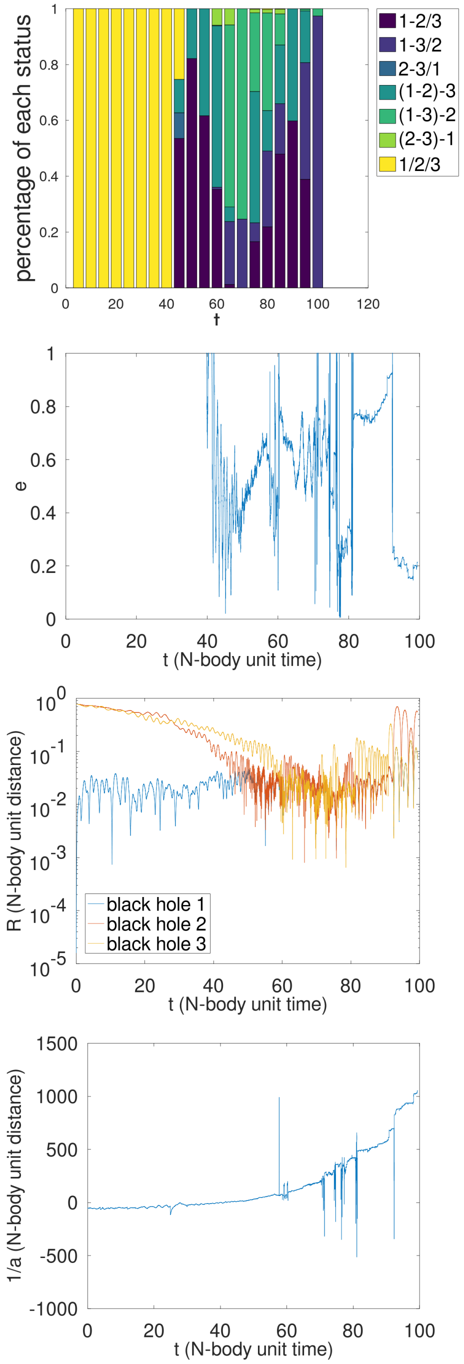

Figure 3.32: Evolution of inner binary black holes in simulation S.

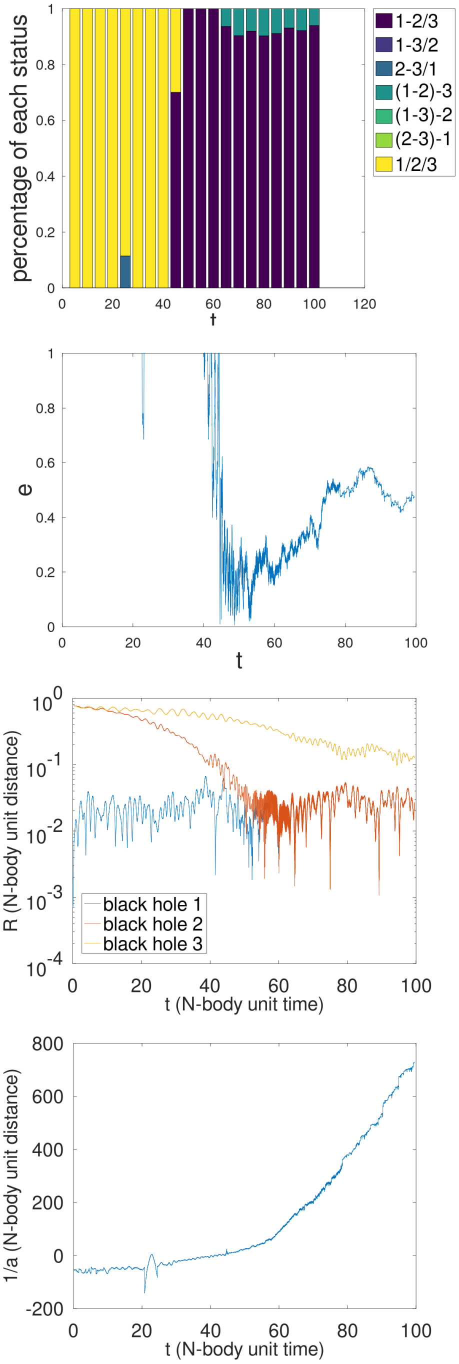

Figure 3.33: Evolution of inner binary black holes in simulation T.

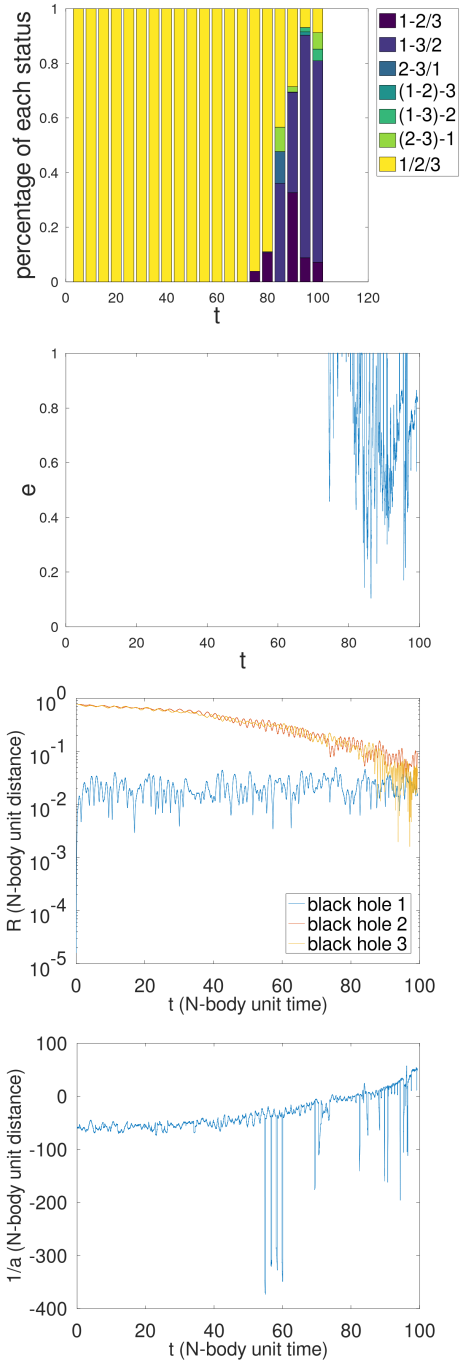

Figure 3.34: Evolution of inner binary black holes in simulation U.

Chapter 4

The dynamical evolution of unequal mass IMBHs in star clusters

This chapter is based on the paper "Unequal intermediate-mass black holes]The dynamical evolution of unequal-mass intermediate-mass black hole triplets in star clusters" to be submitted to the Monthly Notices of the Royal Astronomical Society.

4.1 Introduction

Observations have shown that supermassive black holes (SMBHs) and stellar-mass black holes (SBHs) are common throughout the Universe (Abbott et al. 2019, Casares 2007, Kormendy & Ho 2013, Sahu et al. 2022). However, detecting and confirming intermediate-mass black holes (IMBHs) is significantly more challenging, and a handful of candidates have been reported since (see Greene, Strader, & Ho 2020). The first detection of an IMBH with a mass in the range $10^2\,\mathrm{M}_\odot - 10^3\,\mathrm{M}_\odot$ is the merger product of a gravitational wave event GW190521. The signal of GW190521 originates from a binary stellar-mass black hole with a primary black hole of 85 $\mathrm{M}_\odot$ and secondary mass of 66 $\mathrm{M}_\odot$ (Abbott et al. 2019). The formation process of such a binary system is still under debate. The primary black hole may have formed through stellar collapse or a hierarchical BHs/massive stars merger in a star cluster (Abbott et al. 2020). The scenario of this event has been discussed extensively, including hierarchical mergers in a star cluster (Abbott et al. 2020) and the first generation of Population III stars (Liu & Bromm 2020).

The formation mechanism of IMBHs has been widely discussed. The first proposed scenario is the growth of massive stars via physical collision in the center of a cluster that have migrated with the aid of mass segregation (Freitag, Gürkan, & Rasio 2006, Gürkan, Fregeau, & Rasio 2006, Portegies Zwart & McMillan 2000, Portegies Zwart et al. 2004). Giersz et al. (2015) suggest that an IMBH may form from the remnant of a supermassive star produced by the merger of massive stars in the center of a globular cluster. IMBHs can also form through multiple merger processes of SBHs (Miller & Hamilton 2002). Another IMBH formation channel is the direct collapse of Population III stars or gas clouds. The mass range of IMBHs originating from the gas cloud is $10^4 - 10^6$ $M_\odot$ (Madau & Rees 2001) while IMBH produced by the collapse of Population III stars has a mass range of ≈ 100 $M_\odot$ (Fryer, Woosley, & Heger 2001).

Hubble Space Telescope observations suggest that most star clusters rapidly merge after their formation in starburst regions; examples of such regions include M51, the Antennae galaxy, and Arp 220 (Scoville et al. 2000, 2001, Whitmore et al. 2010, Zhang, Fall, & Whitmore 2001). Current observations suggest that IMBH candidates may be located at the centers of some star clusters (Amaro-Seoane 2006, Amaro-Seoane & Freitag 2006). With very crowded star clusters in a relatively small space, the formation of a binary IMBH (BIMBH) is nearly inevitable. Gürkan, Fregeau, & Rasio (2006) investigated the possibility of forming a BIMBH in the center of dense star clusters with an initial binary fraction $\geq$ 10%, concluding that two very massive stars will form a binary, resulting in the formation of a BIMBH.

Massive BIMBHs may also form via migrating towards each other with the aid of dynamical interaction with surrounding stars when two star clusters merge (Amaro-Seoane & Freitag 2006). The evolutionary process of an IMBH binary may be analogous to the formation of an SMBH binary. In general, IMBHs initially sink towards the center of a recently-merged cluster by dynamical friction, and then shrink their orbit by three-body scattering with a roughly constant hardening rate. When the separation is sufficiently small, gravitational wave emission takes over the role of three-body scattering and the BIMBH effectively evolves in isolation. During the process, a tertiary IMBH embedded in a cluster may migrate towards the merged cluster, resulting in triple-IMBH interactions.

Understanding of the dynamics of IMBHs in dwarf galaxies and globular clusters leaves much space to be explored. A pioneering work of binary IMBH dynamics was performed by Amaro-Seoane & Freitag (2006). Tamfal et al. (2018) utilized collisionless N-body simulations to determine the relation between the dark matter density profile and orbital decay of the IMBH binary. Their study suggests that a steep dark matter density profile is required for forming a hard IMBH binary. Khan & Holley-Bockelmann (2021) conducted the first direct N-body simulation of IMBH binary in nucleated dwarf galaxies. They suggest that IMBH with comparable mass merge very fast in a nucleated dwarf galaxy with host nuclear star clusters destroyed.

There is currently no study on the dynamical evolution of IMBH triplets in globular clusters. Our study presents the first direct N-body simulation of IMBH triplets. In this study we do not focus on the formation of IMBHs, but instead on the dynamical evolution of IMBH triplets in dense stellar environments. This study aims to explore how IMBH triplets evolve dynamically, and how the dynamics is affected by their relative masses. This chapter is organized as follows. Section 4.2 introduces the methods and initial conditions for our simulations. In Section 4.3 we present and analyse the results. Finally, we present and discuss our conclusions in Section 4.4.

4.2 Methods and initial conditions

4.2.1 Numerical simulations

We use N-body simulations to investigate the dynamical evolution of IMBH triples in star clusters. The simulations were conducted with `NBODY6++GPU` (Kamlah et al. 2022), with substantial updates to the original version (Wang et al. 2015), which is in turn an offspring of `NBODY6++` (Spurzem 1999) and `NBODY6GPU` (Nitadori & Aarseth 2012), with MPI (Message Passing Interface) and GPU (Graphical Processing Unit) boost incorporated. We have modified the subroutine `IMBHINIT` to store the kinematic properties of the three IMBHs.

This version of `NBODY6++GPU` uses new recipes for stellar evolution (Kamlah et al. 2022). We adopt stellar evolution level B recipes. The classic recipes for single and binary stellar evolution are explained in Hurley, Pols, & Tout (2000) and Hurley, Tout, & Pols (2002). Electron-capture supernova is enabled using the treatment method from Belczynski et al. (2008). The calculation recipe of remnant mass from delayed and rapid supernovae is adopted from Fryer et al. (2012). Pulsating pair-instability supernovae and pair-instability supernovae are also turned on, following methods from Belczynski et al. (2016). The wind mass-loss prescriptions used are illustrated in Belczynski et al. (2010), with metallicity-dependent wind switched on for massive and hot O- and B- type stars by Vink, de Koter, & Lamers (2001). Collapse-asymmetric-driven kick mechanism was adopted for black hole

Table 4.1: Initial mass ratio scheme for triple intermediate-mass and stellar-mass black holes. Column 1 denotes the identifier of each model. Columns 2 to 4 list the masses of each of the three IMBHs. Column 5 lists the mass ratio q (see equation 4.1).

Model	M_1 ($\mathrm{M}_\odot$)	M_2 ($\mathrm{M}_\odot$)	M_3 ($\mathrm{M}_\odot$)	q
A	370.37	370.37	370.37	2.000
B	370.37	370.37	259.259	1.400
C	370.37	370.37	185.185	1.000
D	370.37	370.37	111.111	0.600
E	370.37	370.37	74.074	0.400
F	370.37	370.37	37.037	0.200
G	370.37	259.259	259.259	1.700
H	370.37	259.259	185.185	1.214
I	370.37	259.259	111.111	0.728
J	370.37	259.259	74.074	0.486
K	370.37	259.259	37.037	0.243
L	370.37	185.185	185.185	1.500
M	370.37	185.185	111.111	0.900
N	370.37	185.185	74.074	0.600
O	370.37	185.185	37.037	0.300
P	370.37	111.111	111.111	1.300
Q	370.37	111.111	74.074	0.867
R	370.37	111.111	37.037	0.433
S	370.37	74.074	74.074	1.200
T	370.37	74.074	37.037	0.600
U	370.37	37.037	37.037	1.100

natal kick (Banerjee et al. 2020), with the same velocity dispersion used for neutron stars (Hobbs et al. 2005).

4.2.2 Initial conditions

We use the Plummer (Plummer 1911) model to initialize the star clusters, each containing 63,997 stars. Stellar masses are randomly drawn from the Kroupa initial mass function (IMF) in the mass range 0.08 $\mathrm{M}_\odot$ to 150 $\mathrm{M}_\odot$ (Kroupa 2001). The total mass of the simulated star clusters is approximately 37 000 $\mathrm{M}_\odot$. We do not include primordial binary systems. We adopt an initial virial radius of 1 pc. We use `NBODY6++GPU`'s standard solar neighbourhood tidal field to represent the tidal field in star clusters. The initial tidal radius of the simulated star cluster is 47.12 pc.

After initializing the stellar population, we add three IMBH to each model. Inspired by Amaro-Seoane (2006) and Amaro-Seoane & Freitag (2006), We place one IMBH (m_1) at rest at the center of the star cluster. The other two IMBHs (m_2 and m_3) are placed at the half-mass radius of the star cluster, and are initially assigned circular velocities. The circular speed at the half-mass radius is 12.6 $\mathrm{km\,s^{-1}}$. Amaro-Seoane et al. (2010) states that massive black hole (MBH) triplet lose their memory of initial condition after the first secular evolution, so the influence of initial conditions on our general conclusion is very little.

We terminate the simulations after 15 Myr (200 N-body time units). As we will show in Section 4.3.3, many of the IMBHs are ejected within 15 Myr. We stop the simulation when one of the IMBHs is ejected from the star cluster. The masses of the IMBHs in each model are listed in Table 4.1.

Following Xu et al. (submitted; hereafter Paper I), we define the triple mass ratio q to determine the effect of tertiary IMBH on the gravitational wave merge timescale of inner BIMBH:

$$q \equiv \frac{m_3}{m_2} + \frac{m_3}{m_1} \quad . \tag{4.1}$$

Here, m_1, m_2, and m_3 are the masses of the three IMBHs, and $m_3 \leq m_2 \leq m_1$. For further details on the orbital parameters and terminology used in this study we refer to Paper I.

4.3 Results

4.3.1 Theoretical background

The typical mechanism in which the IMBH triplet evolves is as follows. When two star clusters merge, IMBHs that may be present at their centers will migrate towards the center of the merged cluster as a consequence of mass segregation.

When two massive bodies find each other in the center of the star cluster, they usually form a binary system. After a BIMBH is formed, its orbit shrinks over time due to three-body scattering with of surrounding stars. The latter process is commonly referred to as *hardening*. This process becomes important when the BIMBH semi-major axis value shrinks to a value below

$$a_h = \frac{GM_2}{4\sigma_c^2} \quad , \tag{4.2}$$

where M_2 is the IMBH with the lower mass in the BIMBH, and σ_c is the velocity dispersion at the globular cluster center. The hardening rate is defined as

$$s = \frac{d(a^{-1})}{dt} \quad , \tag{4.3}$$

where a denotes the semi-major axis of the binary, and t is time. The hardening timescale is

$$t_{\mathrm{harden}} = \frac{\sigma}{HG\rho_c a} \quad , \tag{4.4}$$

Here σ is the velocity dispersion of surrounding stars and ρ_c is the stellar density of the central region. $H \approx 15 - 20$ is a dimensionless constant that depends on the mass ratio and eccentricity of the BIMBH (see Sesana, Haardt, & Madau 2006).

The merger timescale of a Keplerian binary IMBH is calculated as:

The evolution of binary IMBH may be affected by other processes such as a the presence of other bodies in its vicinity, in particular when the masses are comparable. Stellar evolution may also affect the evolution of binary IMBH. When IMBHs form a bound pair and undergoes three-body interaction with the tertiary IMBH, the supernovae explosion from surrounding stars lose its mass. The loss of mass may results in change of gravitational potential change to the inner binary IMBH and the tertiary IMBH. The tidal disruption of stars that approach one of the IMBHs may also affect the evolution of binary IMBH. Tidally-disrupted stars can be partially accreted by an IMBH (and thus increases its mass), and can deliver momentum. This may result in abrupt changes of the orbital parameters of the binary IMBH.

4.3.2 Star cluster evolution

The three IMBHs mutually interact, and also impact the properties of the local stellar population and the global evolution of the cluster itself. This impacts the Lagrangian radii and the stellar neighbour density. The neighbour density affects the migration timescale and the hardening rate of the IMBHB. Studying the evolution of the Lagrangian radii in these simulations allow us to constrain the effect of the IMBH triplet on the evolution of star clusters and vice versa.

The third panels of Figures 4.21-4.35 show the evolution of the Lagrangian radii of the star clusters. In our simulations, all clusters expand because of the mass-loss from the stellar evolution and two-body relaxation process around the IMBH. The stars in the outer regions gain energy from the stars in the inner region and push these stars closer to the

IMBHs.

The 30%-90% Lagrangian radii in simulation A experience an increase at around 4 Myr, with the 95% experience a dramatic increase. This phenomenon corresponds to the ejection of one IMBH. The 30%-90% Lagrangian radii increase steadily, but the 90% Lagrangian radii increases faster than the other radii. This phenomenon indicates that the clusters undergo evaporation process. In Figure 4.1, 4.2, and 4.3, the 90% Lagrangian radii increase dramatically at the end of simulation. In corresponding simulations, two IMBHs is ejected from the core at the same time. We may conclude from these phenomena that the ejection of two IMBH may results in enhanced ejection of field stars. There are several sharp decreases in the evolution of the 0.1% and 1% Lagrangian radii. These sharp decreases indicate that core collapse occurs.

The Lagrangian radii of simulation U show a similar pattern to those of simulation A. The 30%-90% Lagrangian radii also experience a steady increase. The increase in the Lagrangian radii indicates that with the infall of two low-mass IMBHs (m_2 and m_3), the ejection rate of the central stellar population increases. However, the ejection of one of the IMBHs at $t = 10$ Myr did not dramatically increase the 30%-90% Lagrangian radii. This phenomenon probably originates from the nature of low secondary IMBH mass and the constant stellar population ejection rate.

The dynamical evolution of a star cluster is governed by two-body relaxation on a timescale of

$$t_{\rm rh} = \frac{0.138 N^{0.5}}{\ln \Lambda} \sqrt{\frac{{r_{\rm h}}^3}{G\langle m \rangle}}. \tag{4.5}$$

Here $\ln \Lambda$ represents the Coulomb Logarithm (Spitzer 1987). The calculated relaxation time is 98 Myr. Utilizing Equation 2.78, the calculated mass segregation timescale for our star cluster is 1.8 Myr. In Figure 4.4, the collision between IMBH and massive main-sequence stars occur at around 2 Myr, in agreement with the mass segregation timescale calculated above. These main-sequence stars do not have enough time to evolve into BH so there is no IMBH-SBH merger.

4.3.3 Classification of models

We find that in most of the simulations, at least one IMBHs escapes from the star cluster (in contrast to the systems discussed in Paper I). We consider an IMBH as an *escaper* when the distance from the IMBH to the cluster center exceeds two tidal radii. Based on this, we

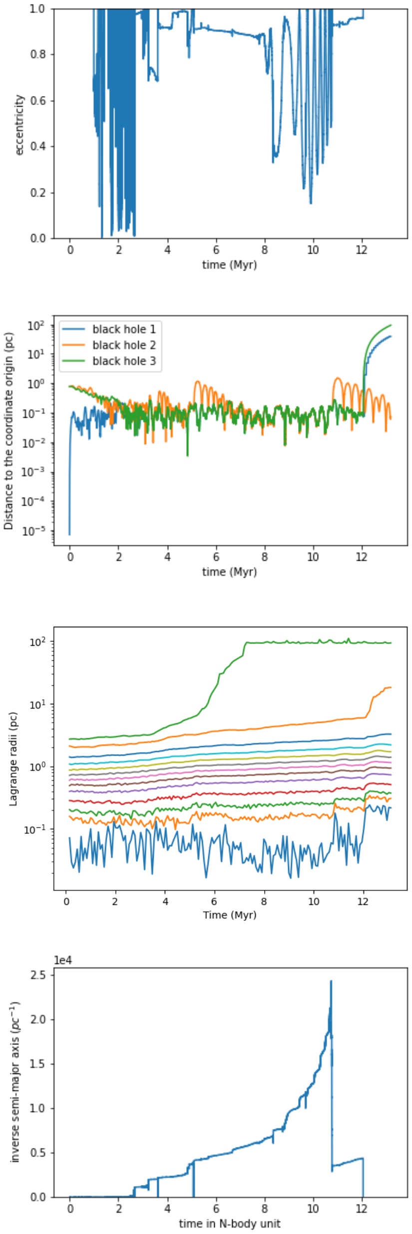

Figure 4.1: Evolution of IMBH triplet and inner binary black holes in simulation L.

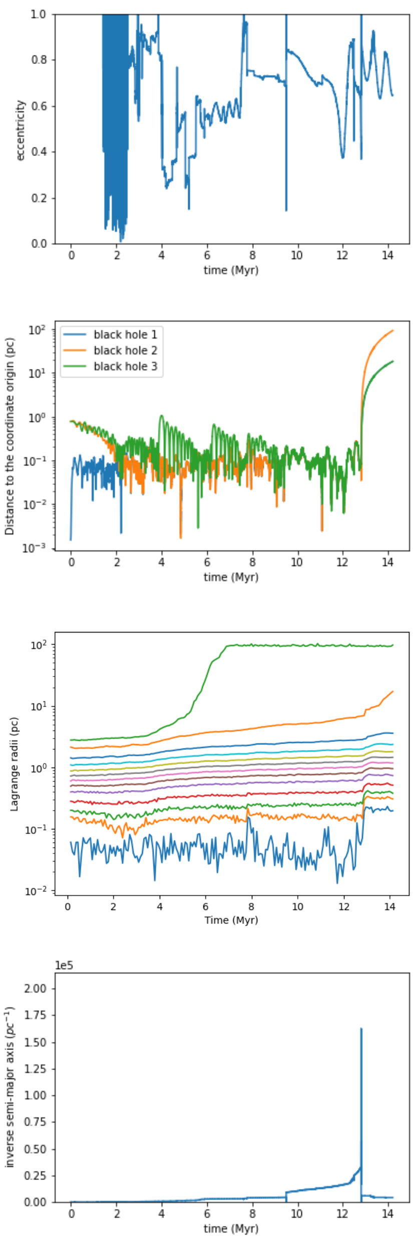

Figure 4.2: Evolution of IMBH triplet and inner binary black holes in simulation M.

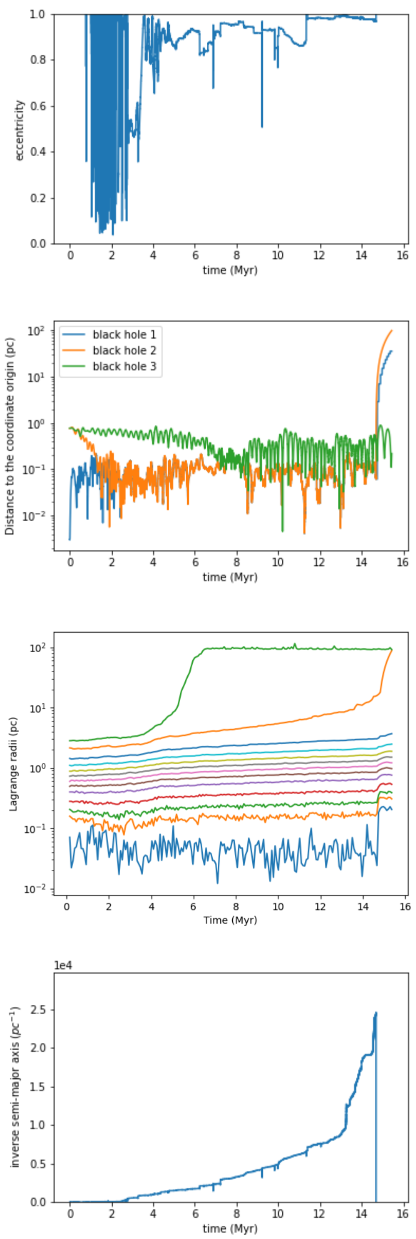

Figure 4.3: Evolution of IMBH triplet and inner binary black holes in simulation O.

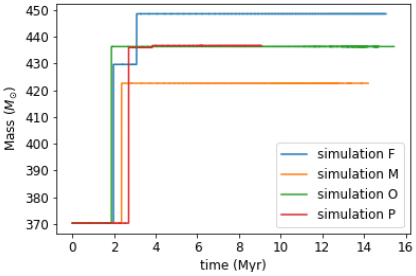

Figure 4.4: Collisions between the central IMBH and surrounding stars in simulation F, M, O, and P. In these 4 simulations, One of the IMBHs collides with massive main-sequence stars. For simulation F, the secondary IMBH collide with a star with a mass of 118 $M_\odot$ at 2 Myrs during its migration to the center, with 59.2 $M_\odot$ added to the IMBH's mass. Shortly after the collision, the secondary IMBH collide with another star with a mass of 38 $M_\odot$, with 18.96 $M_\odot$ added to the IMBH's mass. The central IMBH in simulation P collides with one star with a mass of 131 $M_\odot$ at 3 Myr. The star added 65.66 $M_\odot$ to the mass of IMBH. After 1 Myr, the central IMBH collides with another star with a mass of 1 $M_\odot$, with 0.52 $M_\odot$ added to the mass of the IMBH. The main sequence star collides with the central IMBH in simulations M and O have masses of 105 $M_\odot$ and 132 $M_\odot$, respectively. The two stars added 52.36 $M_\odot$ and 66 $M_\odot$ to the mass of the IMBH in each simulation.

classify the simulations into three categories. Category 1 contains simulations with two IMBH ejected out of the center of the star cluster. Category 1 consists of simulations L, M, O, and T. The evolution of the simulated clusters in Category 1 are shown in Figures 4.1, 4.2, 4.3, and 4.5. In Category 2, no IMBH is ejected. Category 2 only contains simulation B, the results for which are shown in Figure 4.6. The remainder of our simulations constitutes Category 3. Category 3 contains simulations A, C, D, E, F, G, H, I, J, K, N, P, Q, R, S, T, and U. Figures 4.21, 4.22-4.30, 4.31, 4.32 - 4.34, and 4.35 show the evolution of the simulated clusters in Category 3.

4.3.4 Scenario 1: Two IMBHs ejected

In this category of simulated clusters, two IMBHs are ejected from the cluster. BIMBHs are thus unable unable to form after these events. The two IMBHs are initially at the edge of the cluster and migrate into the center of the cluster with the aid of dynamical friction from surrounding stars. After about 1 Myr, two of the IMBHs form a binary.

In Figures 4.1, 4.2, 4.3, and 4.5, two IMBHs are expelled from the center of the cluster.

In simulation L, the value of inverse semi-major axis exceeds 20,000 pc^{-1}, then decreases to about 3,000 pc^{-1}. After a steady increase, the value of the inverse semi-major axis becomes negative, indicating that no binary IMBH is present beyond this time. this phenomenon implies that IMBH may wander in the galaxy with no cluster stars surround it. Simulation M, O, and T share similar characteristics with simulation L. In simulation M, the inverse semi-major axis turns negative after reaching a value of about 160,000 pc^{-1}. After that the inverse semi-major axis remains relatively low. The inverse semi-major axis value in simulation O reaches about 25,000 pc^{-1}, and then becomes negative.

4.3.5 Scenario 2: No IMBH ejected

In this scenario, one IMBH is ejected to the outer regions of the cluster for a short period of time, and then returns to the center of the cluster, where it interacts with the inner binary. The tertiary IMBH shrinks the semi-major axis of the inner binary significantly. Figure 4.6 shows the evolution of binary IMBH in simulation B. In simulation B, no IMBH is expelled from the central region of the star cluster; m_1 is ejected from the cluster centre but remains bound to the system. After a short period, m_1 migrates back to the center of the star cluster. The IMBH triplet is initially in a binary-single status but soon formed a hierarchical triple system. At the end of simulation B, the inner binary reached such a short semi-major axis that the simulation halted due to the energy conservation constraints. The orbit shrinking of the inner binary originates from the presence of m_3. Throughout the simulation, m_3 has removed energy of the inner binary orbit, which resulted in shrinking of the inner binary orbit. This suggests that it is possible to have three tightly-bound IMBHs located in the center of a star cluster for a significant amount of time.

The eccentricity of the inner binary in simulation B experiences frequent changes after ~ 1 Myr, just after the inner binary has formed. These changes continue to occur until ~ 4.5 Myr, when the tertiary black hole is briefly ejected from the core. The eccentricity of the inner binary remains very high when the tertiary returns. The eccentricity remains high until about 8 Myr, when the eccentricity decreases dramatically and the inner binary orbit obtains a nearly-circular orbit.

The inverse semi-major axis of the inner binary in simulation B increases steadily from around 3 Myr to 4.5 Myr. This increase accelerates between 4.5 Myr and 6 Myr. The acceleration of orbit shrinking can be attributed to the repeated scattering of the tertiary black hole. The tertiary black hole removes the angular momentum from the binary black

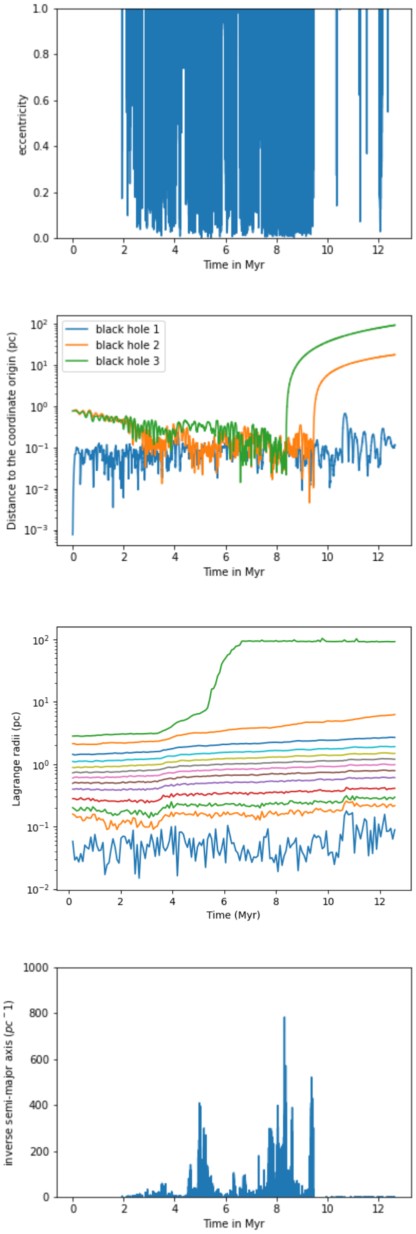

Figure 4.5: Evolution of IMBH triplet and inner binary black holes in simulation T.

hole as it shrinks. From 6 Myr to about 8 Myr, the inverse semi-major axis increases at a more or less constant rate, suggesting that the impact of cluster stars on the hardening rate of the inner binary decreases. After 8 Myr, an exponential increase in the inverse semi-major axis occurs. This is likely the result of complex three-body interaction between the three IMBHs.

4.3.6 Scenario 3: One IMBH ejected

In the remainder of the simulations, one IMBH was ejected from the cluster. In general, after the migration of IMBHs from the edge to the center of the cluster, the three IMBHs forms an unstable system and undergo complex three-body interactions. After some time, one IMBH is usually ejected with a high velocity, leaving the two remaining IMBHs to form a stable binary system. The ejection of one IMBH results in an abrupt shrinking of the inner orbit, and the two remaining IMBHs form a stable binary. The inner binary IMBH is expected to shrink its orbit at a roughly constant rate due to interaction with the surrounding stellar environment.

The eccentricity evolution in this category of simulation is relatively chaotic. This category of simulations can be classified into two subcategories. One subcategory consists of simulations with inner binary IMBHs that remain their high (or low) eccentricity after the ejection of one IMBH. This subcategory consists of simulations A, O, and P. Here, the eccentricity of the inner binary remains high, with no scattering between massive stars and inner binary IMBH. The other subcategory consists of simulations that change inner binary eccentricity after the ejection of one IMBH. This subcategory consists of other simulations. The eccentricity of the inner binary in simulations in this subcategory changes dramatically after scattering with other massive stars, which destabilizes the inner binary.

The semi-major axis evolution in this category of simulation is more smooth than the evolution of the eccentricity. Besides scattering events involving massive stars, the inverse semi-major axis evolution of the inner binary can be approximated with a constant hardening rate.

4.3.7 Hardening rate of inner binary vs mass ratio

Figure 4.7 shows the correlation between the mass ratio and the average hardening rate of the inner binary. There is no clear correlation between the mass ratio and the hardening rate. This indicates that in general, a tertiary IMBH does not aid in the hardening process

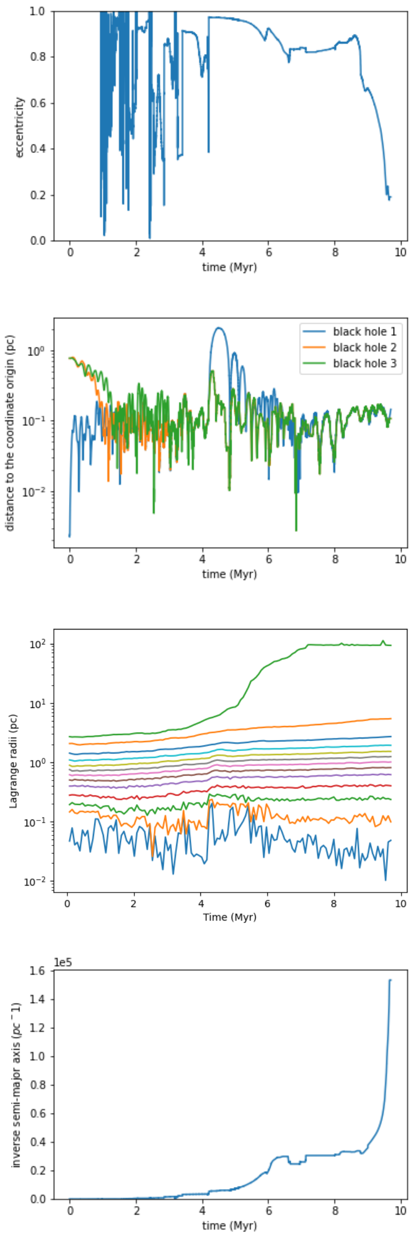

Figure 4.6: Evolution of IMBH triplet and inner binary black holes in simulation B.

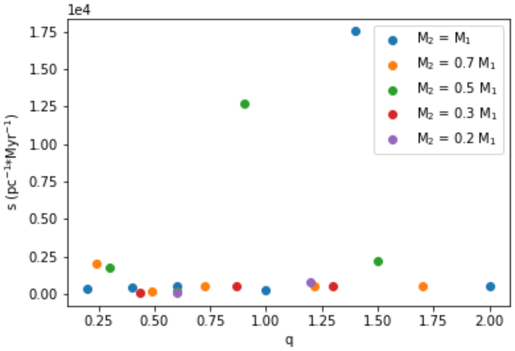

Figure 4.7: The average hardening rate of inner binary in each simulation versus mass ratio in Categories 2 and 3.

of inner binary IMBH because the tertiary IMBH is most likely to be ejected at very early stage of cluster evolution. However, if the tertiary IMBH is not ejected, then the tertiary IMBH will strongly increase the hardening the orbit of inner binary.

4.3.8 Gravitational wave merger timescale for IMBH binary

Figure 4.8 shows the gravitational wave merger timescale for simulations in category 2 and 3 using Equations (2.21) and (2.22). The gravitational wave merger timescale has a weak correlation with the mass ratio q of of the IMBH triplet, implying that an tertiary IMBH does not necessary shorten the merger timescale. This phenomenon originates from the common ejection of one IMBH, which may be caused by frequent very close interaction between massive field stars and IMBH.

4.3.9 Repeated ejections of one IMBH from the core

In both simulations G and Q, one IMBH was ejected from the central region of the cluster. In simulation Q, m_2 was repeatedly ejected from central region of the cluster every roughly 2 Myr, but still remains bound to the cluster. The results of simulation G are similar, but the ejections occur at irregular intervals. This suggests that there may be an IMBH temporarily unbound to binary IMBH but remains bound to the cluster with a very eccentric orbit.

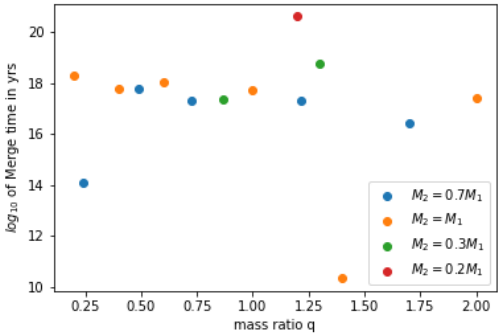

Figure 4.8: Extrapolated gravitational-wave merger timescales for the inner IMBH binary of Simulations in category 2 and 3 at the end of the simulation.

4.3.10 Properties of escaping IMBHs

If IMBH forms during the evolution of cluster, then it may get along with other stellar-mass BH. These stellar-mass BH may interact with IMBH. Although stellar-mass BH may get ejected out of the cluster, it is also possible that IMBH itself may get kicked out of the cluster (Di Carlo et al. 2021). It is thus necessary to study the escape properties of escaped IMBH and the mechanism behind these phenomena.

In 14 out of 21 simulations, one IMBH escaped from the cluster before the simulation ended. It raises much attention to investigating the correlation between the escape parameter of IMBH and the properties of their host cluster. This section discusses the correlation between the parameter of escaped IMBH and the properties of its host cluster.

Figure 4.9 shows the escaped velocity at infinity of IMBH versus escape time for escaped IMBH. In general, the escaped IMBH has a higher escape velocity at a later time. In the center of the cluster, if an IMBH is ejected earlier, the time for IMBH to interact with other stars would be shorter, thus leading to the kinetic energy supplied to the escaped IMBH would be lower, resulting in an escape IMBH with relatively low velocity, leading to escape at a later time. We define the instantaneous escape velocity of an IMBH as its speed just before its ejection from the system. The recipe for calculating the central density of core radius is the prescriptions of Casertano & Hut (1985). The correlation between instantaneous escape velocity and average mass density is shown in Figure 4.10. It is reasonable to infer that there is a positive correlation between initial central density and initial escape velocity. With a higher mass density, the relaxation time is shorter, resulting

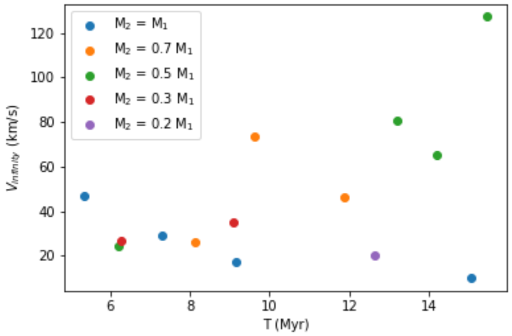

Figure 4.9: The velocity at infinity versus escape time for IMBH that have escaped from the clusters in Category 3.

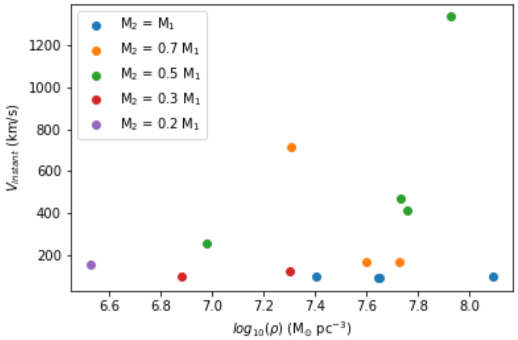

Figure 4.10: The instantaneous velocity versus the local mass density of escaping IMBH prior to the escape event in Category 3.

in a higher frequency of dynamical interactions between IMBHs, and between IMBH and stars. The escaped IMBH gains kinetic energy via this mechanism. Figure 4.11 shows the correlation between the mass ratio and the escape velocity at infinity. It is observable from this figure that the escape velocity has no correlation with mass ratio q. This is reasonable because the IMBH is slowed by surrounding stars, so the escape velocity at infinity is a property of IMBH that is correlated with the properties of surrounding stellar population, but not the binary IMBH.

The correlation between the mass ratio and the instantaneous escape velocity is shown in Figure 4.12. This figure shows that there is no correlation between the mass ratio and the instantaneous escape velocity.

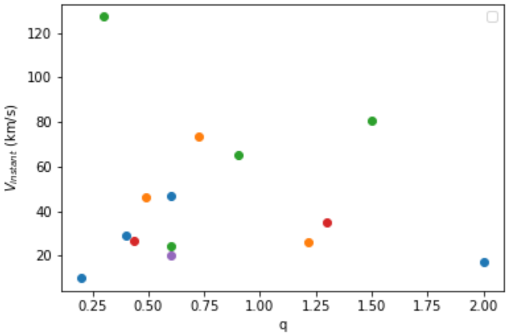

Figure 4.11: The mass ratio versus the escape velocity at infinity for the IMBH that escaped from the cluster in Category 3.

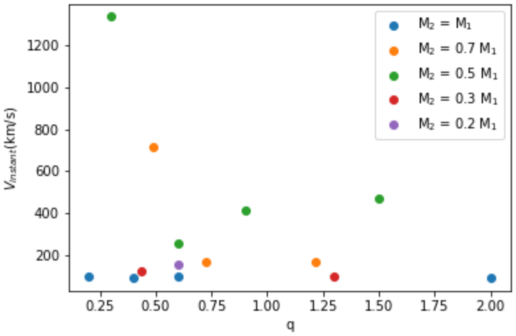

Figure 4.12: The mass ratio versus the instantaneous velocity for IMBH in category escaped out of the cluster in Category 3.

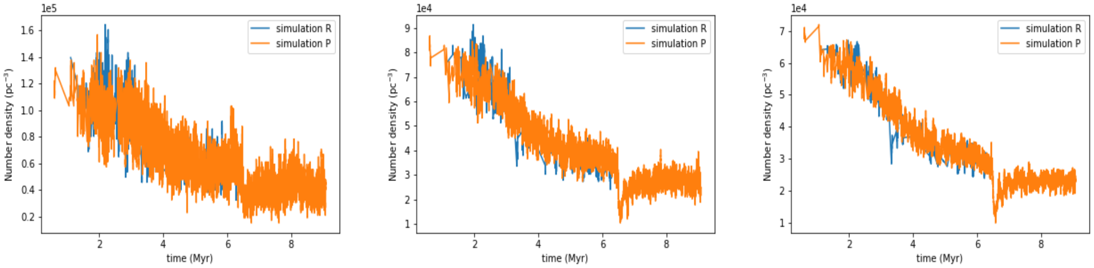

(a) (b) (c)

Figure 4.13: Stellar population number density evolution at $R = 0.05 - 0.15$ pc for simulations A-R. The simulation L, M, Q, and T are omitted.

4.3.11 Interactions between the IMBH binary and surrounding stellar population

Here we discuss the relationship between the number density of the surrounding stellar population of the primary IMBH and the semi-major axis evolution of the inner binary. We define the surrounding stellar population as the stars around the primary IMBH within a set of radius values. These radii form a series of concentric shells.

Figures 4.13-4.14 show the stellar population density evolution within a different radius around m_1. We adopt six different values for the radius of the stellar population density calculation, and find the correlation between stellar population number density and the inverse semi-major axis of the inner binary black hole.

Figure 4.13 shows the stellar population number density evolution for simulations A-P at $R = 0.05 - 0.15$ pc. Initially, the stellar density profile is roughly equal for all four simulations. In simulation A, the stellar density profile decreased dramatically at about 3.8 Myr, then remained steady until around 9 Myr, when the stellar density decreased again. In Figure 4.21, m_2 was temporarily ejected twice, once at 4 Myr and another at 9 Myr. It shows that the repeated ejection of one IMBH results in a temporarily dramatic decrease in stellar density profile around primary IMBH.

Figures 4.14 shows the density evolution of the surrounding stellar population for simulations A-P at $R = 0.20 - 0.30$ pc. The difference between the stellar density profile of simulations A and F is more significant for a larger concentric circle portion surrounding IMBH. The repeated ejection of the more massive tertiary IMBH may result in a more dramatic decrease in surrounding stellar density. The reduction of the surrounding stellar

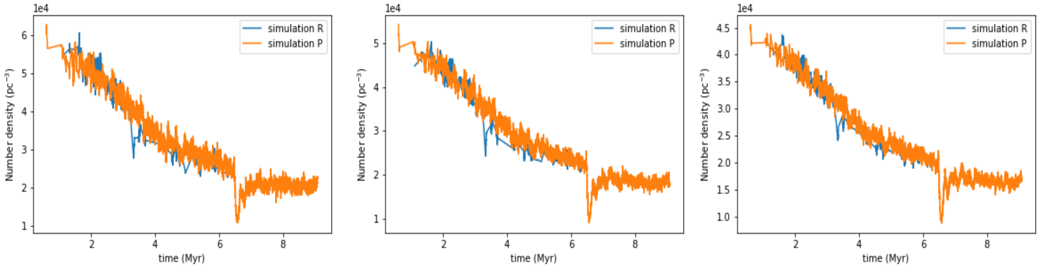

(a) (b) (c)

Figure 4.14: Stellar population number density evolution at R=0.20 - 0.30 pc for simulations A-R. The simulations L, M, Q, and T are omitted

density increases with radii increase.

4.3.12 Physical collisions

Due to the high stellar densities IMBHs may collide with surrounding stars or tidally disrupt surrounding stars, which increases its own mass. The star would be tidally disrupted if the separation between star and IMBH is below a critical distance r_c:

$$r_\mathrm{c} \simeq r_\mathrm{s} \left(\frac{M_\mathrm{BH}}{M_\mathrm{s}} \right)^{1/3}, \tag{4.6}$$

where r_s is the radius of the star, M_BH and M_s are the mass of IMBH and stars, respectively (Kochanek 1992).

We utilize the collision criterion above to determine the collision between IMBHs and stars. Figures 4.4-4.16 show the mass evolution of central IMBH. In these eleven simulations, the central IMBH undergoes collisions with surrounding stars. In simulation F, M, O, P, R, S, and T, the central IMBH collides with very massive main-sequence stars and increase their own mass significantly. Figure 4.4 shows that in simulation F, M, O, and P, the central IMBH collides with surrounding massive stars at around 2 Myr and increase their own mass. In simulation H, I, Q, and U, the central IMBH collides with less massive stars, slightly increase their own mass.

The bottom panel of Figure 4.17 shows that the inverse semi-major axis decreases from 2000 pc^{-1} to nearly 0 pc^{-1}, then jumps back to 2000 pc^{-1} at about 8 Myr. This indicates a temporarily exchange of the inner binary companions. The physical collision occurs

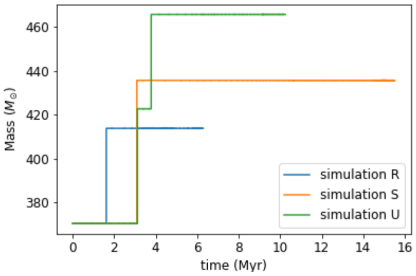

Figure 4.15: Collision between the central IMBH and surrounding stars in simulation R, S, and U. In simulation R, the central IMBH collides with a 87 $M_\odot$ main sequence star at around 1.8 Myr. The merged IMBH collides with a low main-sequence star with a mass of 8 $M_\odot$. The primary IMBH in simulation S collides with a main-sequence star with a mass of 130 $M_\odot$ at around 3 Myr. In simulation U, the primary IMBH collides with a 104 $M_\odot$ main-sequence star at 3 Myr. The merger product collides with another 86 $M_\odot$ main-sequence star after 1 Myr.

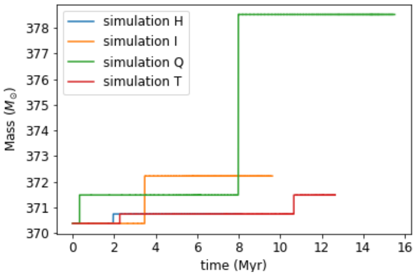

Figure 4.16: Collision between the central IMBH and surrounding stars in simulations H, I, Q, and T. In these 4 simulations, the central IMBH collides with main sequence stars with a low mass.

simultaneously. From these two phenomena, we can conclude that collisions between IMBH and surrounding stars may occur during an exchange event of inner binary companions.

4.3.13 Impact of stochasticity

Stellar systems of the type discussed in this study are highly sensitive to the initial conditions. To characterize the sensitivity of our findings to small differences in the initial conditions, we additionally conduct 19 simulations with different random seeds for the initialization of the stellar positions and velocities. Figures 4.18-4.19 show the distance to the center evolution of the IMBH triplets in simulated clusters. Additionally, the 19 simulations can also be classified into three categories: (1) those with one IMBH ejected from the core, (2) those with two IMBHs ejected, and (3) those with no IMBH ejected.

Merged star clusters that have evolved from star cluster complexes can thus have one or more IMBHs in their center, but this number is highly sensitive on the initial conditions. In simulations where no IMBH is ejected, the inverse semi-major axis is much higher than in those with one IMBH ejected. This suggests that the presence of tertiary IMBH can provide significant aid in shrinking the orbit of BIMBH. For the plot in the middle of the first row of Figure 4.18, the simulation is terminated at 10 Myr, the time at which the central IMBH coalesces with a red giant.

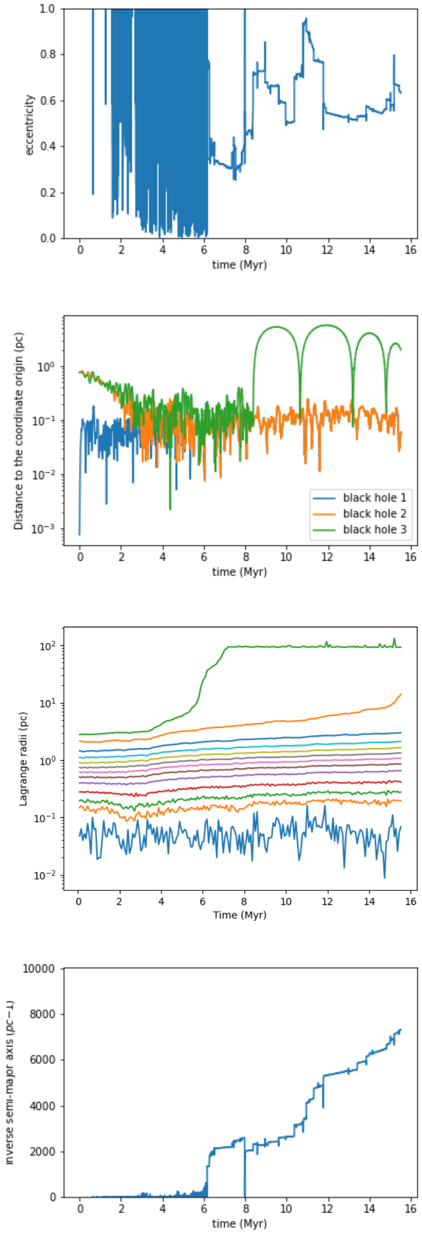

Figure 4.17: Evolution of IMBH triplet and inner binary black holes in simulation Q.

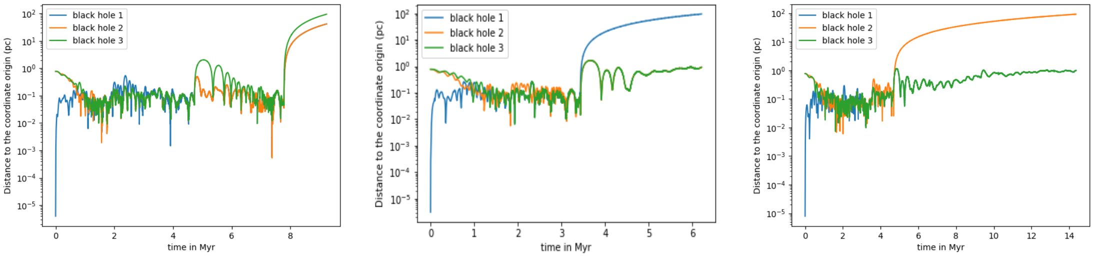

(a) (b) (c)

Figure 4.18: Distance evolution of simulations with different random seed.

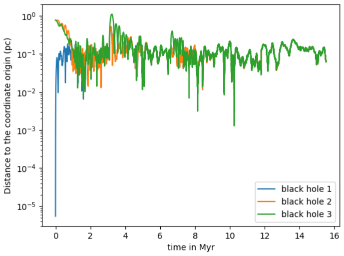

(a)

Figure 4.19: Distance evolution of simulations with different random seeds.

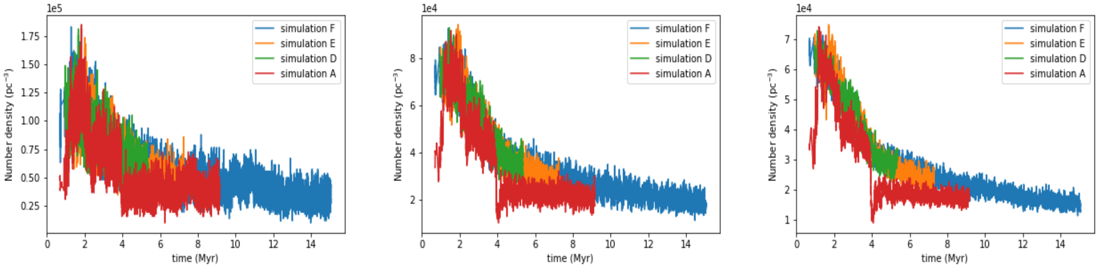

(a) (b) (c)

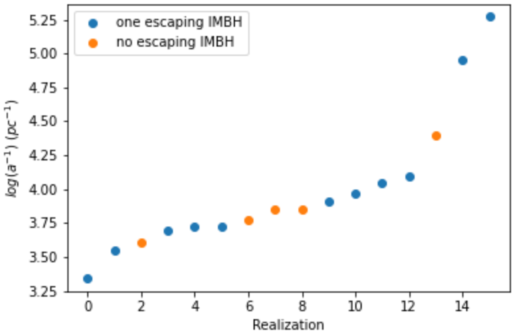

Figure 4.20: The inverse semi-major axis of inner binary for different realisations of simulation A.

Figure 4.20 shows the inverse semi-major axis of the inner binary for different random seeds. The simulations were divided into three categories. Category 1 contains simulations with one IMBH escape (or will escape) from the cluster. Category 2 consists of simulations with no IMBH escaping from the cluster. Simulations with two IMBHs that will escape are classified as Category 3. There are three simulations in Category 3, five simulations with no IMBH escaping, and eleven simulations with one IMBH escaping. The proportion of each category is 16%, 26%, and 58%, respectively. This suggests that in most cases, one IMBH will escape from the merged cluster remnant after star clusters collide, but two escaping IMBHs and no escape IMBH (within a timescale comparable to those of our simulations) are also possible. Figure 4.20 shows that the existence of tertiary IMBH does not necessarily result in a dramatic increase in inverse semi-major axis. In Category 2, there are simulations that have IMBH repeatedly ejected but still bound to the system. In these cases, the tertiary IMBH does not aid much in helping the inner binary IMBH shrink its orbit.

4.3.14 Implication for IMBH binary observations

In all of our simulations, the gravitational wave merger timescale is substantially longer than a Hubble time, suggesting that the IMBH binary may not reach coalescence in a Hubble time. The simulation suggests that an IMBH binary merger event with each component mass in the range $100 - 1000\ \mathrm{M}_{\odot}$ is unlikely to occur in a star cluster. This is in agreement with current understanding of IMBH observation (Greene, Strader, & Ho 2020).

4.4 Conclusions

We have conducted a series of N-body simulations of triple IMBHs in star clusters with different configurations of mass. The orbital parameters of the three IMBHs with the secondary and tertiary IMBH mass ranging from 10% to 100% of the primary black hole. The evolution of the inverse semi-major axis of mutually closest black holes were also investigated. The code `NBODY6++GPU` was utilized to carry out the N-body simulations. Our conclusion can be summarized as follows:

1. In most of the simulations, one IMBH is ejected through the slingshot mechanism, leaving two IMBHs remaining in the center of the cluster. However, it is also possible that two IMBH are expelled from the cluster, suggesting that a single wandering IMBH may be common in the interstellar medium between globular clusters.

2. The existence of a non-ejected tertiary IMBH can greatly enhance the hardening rate of the inner binary IMBH, decreases the gravitational-wave merger timescale to the same order of magnitude as a Hubble time.

3. In simulated clusters, there is a positive correlation between the initial escape velocity of IMBH and the average mass density within the core radius. The positive correlation between IMBH escape velocity at infinity and escape time also exists. There is positive correlation between mass ratio q and escape velocity of IMBH at infinity, as well as the instantaneous escape velocity.

4. We observe no notable correlation between the gravitational wave merger timescale of the inner binary and the mass ratio, q, of the IMBH triplet.

5. In different clusters with equal-mass triple IMBHs, it is very likely that one IMBH is expelled from the center of the cluster, but still remains bound to the cluster. It is also possible to have zero, one, or two IMBH ejected out of the cluster. In simulations with zero or one IMBH ejected, the value of the inverse semi-major axis of the inner binary in different clusters varies a lot between different realisations of the same cluster, with a minimum of about 2,200 pc^{-1} and a maximum of about 186,700 pc^{-1}.

6. The repeated ejection from the cluster core and subsequent return of IMBHs may result in enhanced ejection of surrounding stellar population. The stellar ejection rate increase With a more massive tertiary IMBH repeatedly ejected.

Throughout the simulations, the three IMBHs maintain mutual distances in which relativistic effects are negligible. Therefore we have not introduced Post-Newtonian treatment in this study. The next step will be introducing the rotation factor in a star cluster to investigate how the rotation factor affects the evolution of intermediate-mass black hole triplets. Different particle numbers and initial mass function of simulated star clusters could also be very interesting topics, leaving to be explored.

4.5 Evolution of IMBH triplets

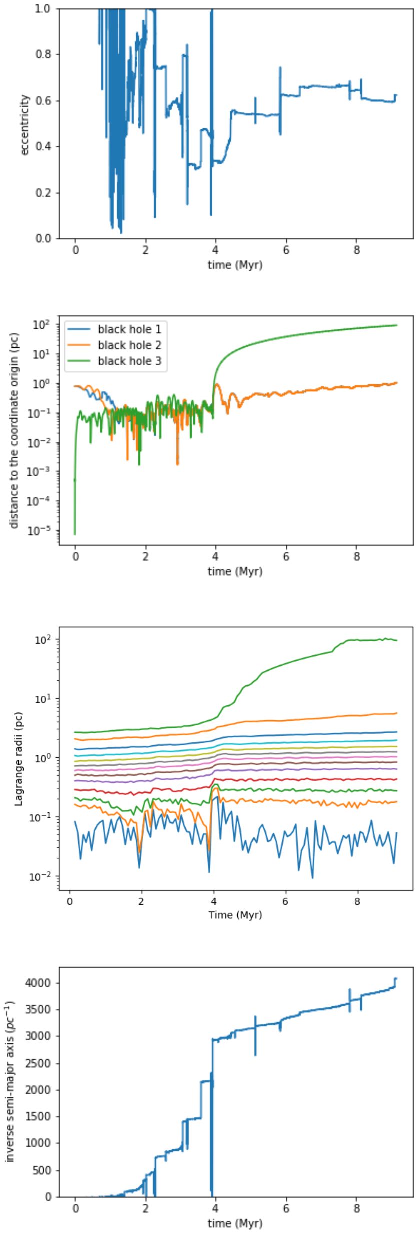

Figure 4.21: Evolution of IMBH triplet and inner binary black holes in simulation A. The first panel is the eccentricity evolution of inner binary IMBH. Distance to the center evolution of triple IMBHs system is described in the second panel. The Lagrangian radii evolution of the cluster's current total mass is depicted in the third panel. The bottom panel shows the inverse semi-major axis evolution of inner binary IMBH. From bottom to top, the mass fraction are 1%, 3%, 5%, 10%, 20%, 30%, ..., 90%, and 95%.

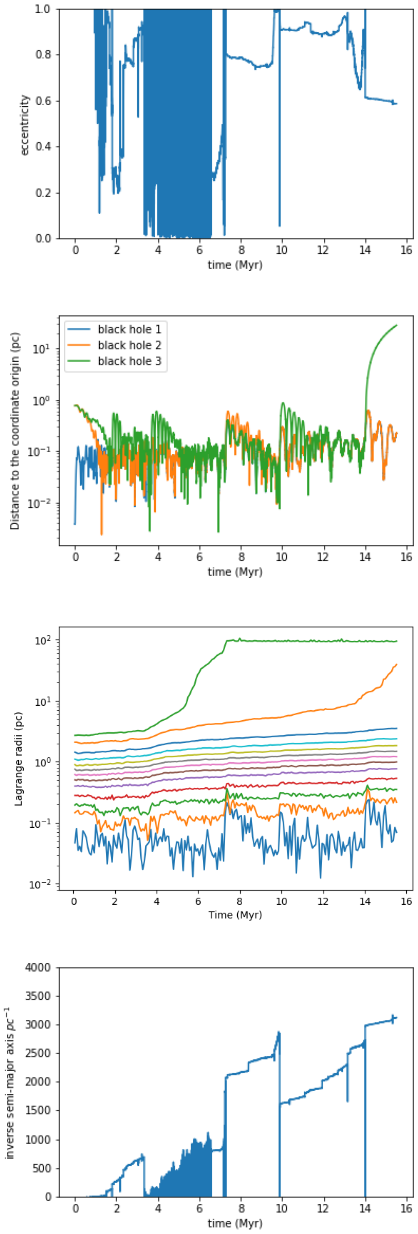

Figure 4.22: Evolution of IMBH triplet and inner binary black holes in simulation C.

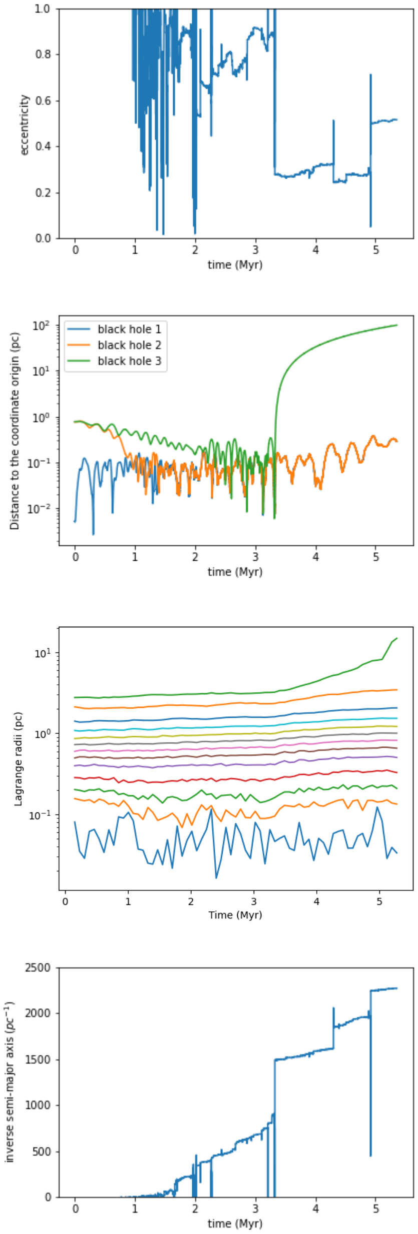

Figure 4.23: Evolution of IMBH triplet and inner binary black holes in simulation D.

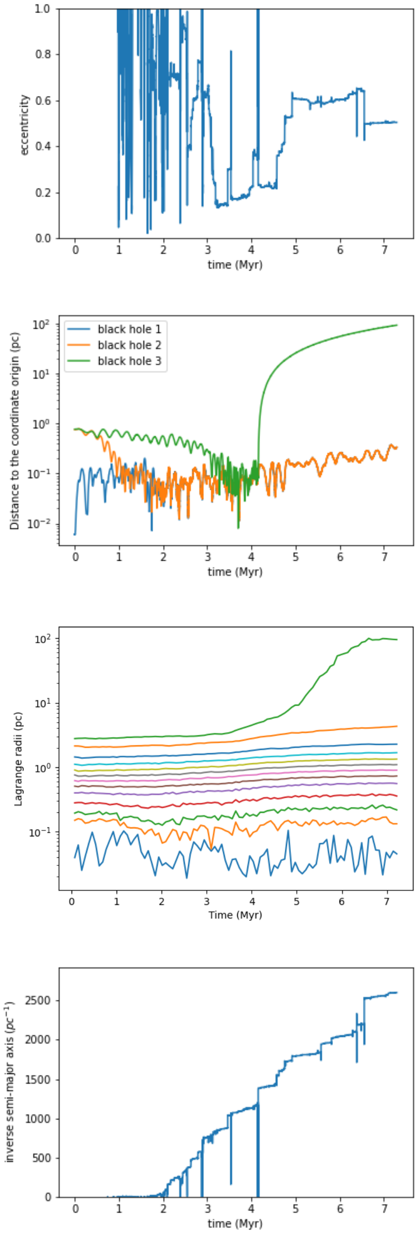

Figure 4.24: Evolution of IMBH triplet and inner binary black holes in simulation E.

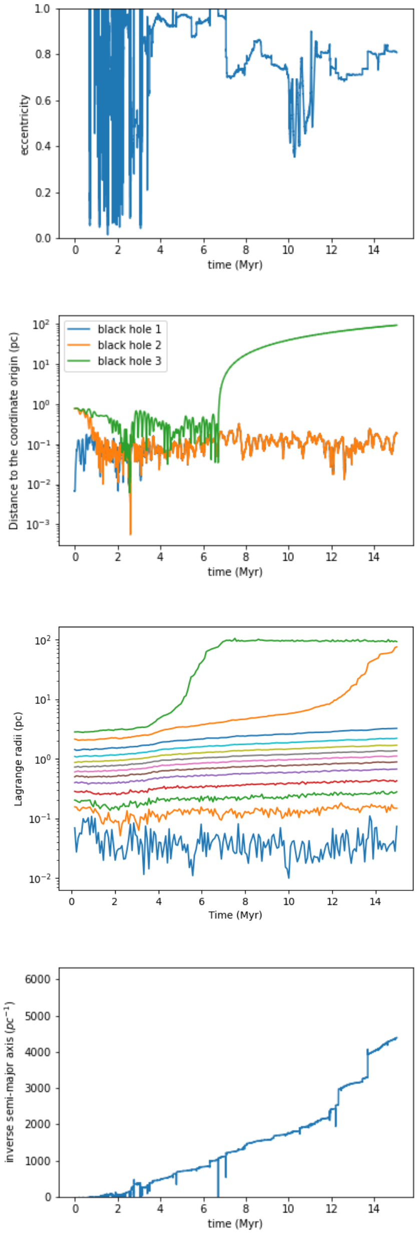

Figure 4.25: Evolution of IMBH triplet and inner binary black holes in simulation F.

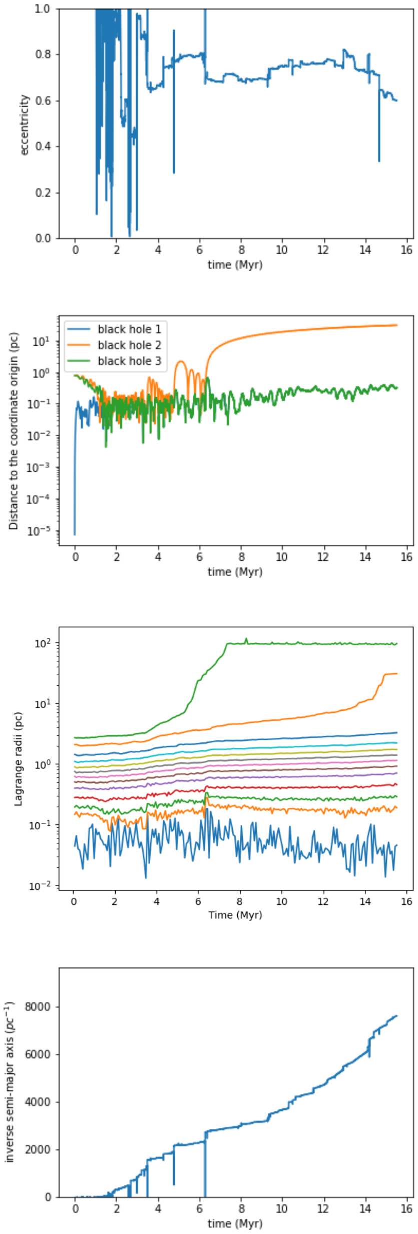

Figure 4.26: Evolution of IMBH triplet and inner binary black holes in simulation G.

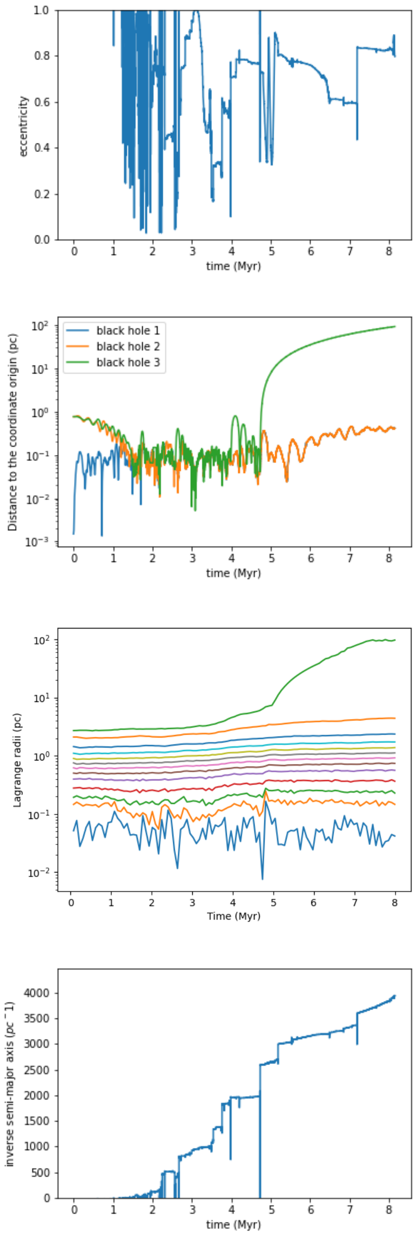

Figure 4.27: Evolution of IMBH triplet and inner binary black holes in simulation H.

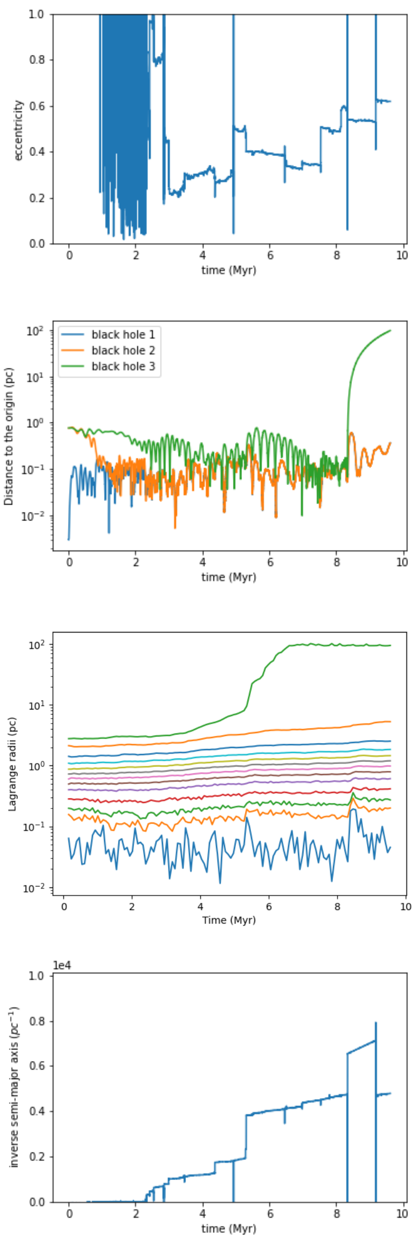

Figure 4.28: Evolution of IMBH triplet and inner binary black holes in simulation I.

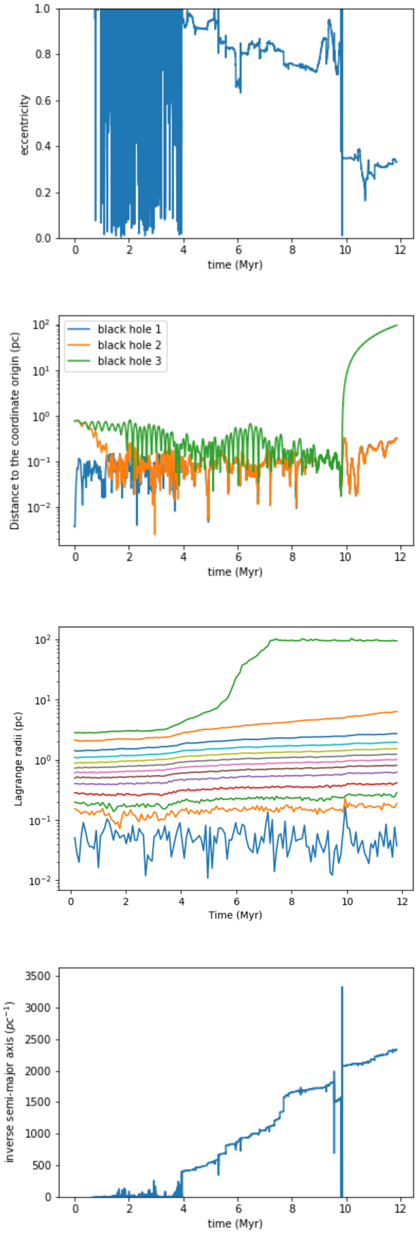

Figure 4.29: Evolution of IMBH triplet and inner binary black holes in simulation J.

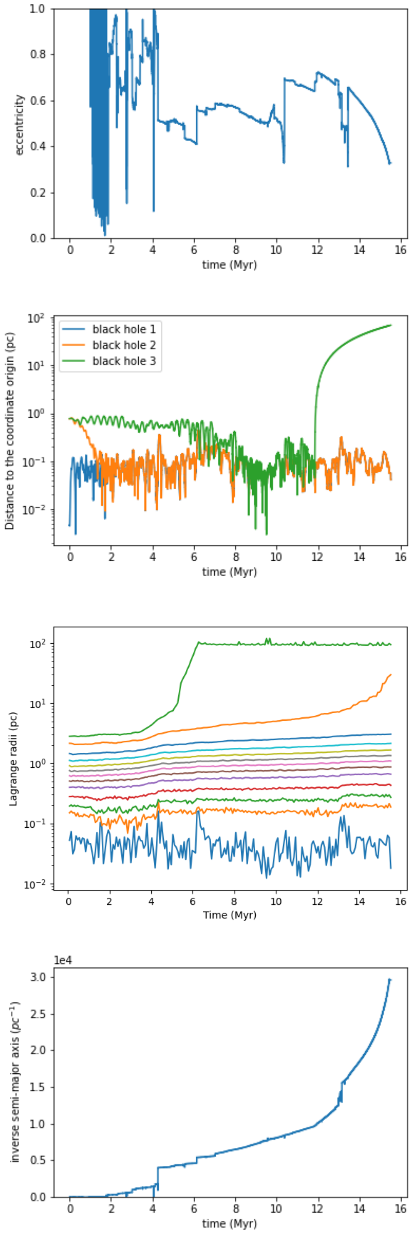

Figure 4.30: Evolution of IMBH triplet and inner binary black holes in simulation K.

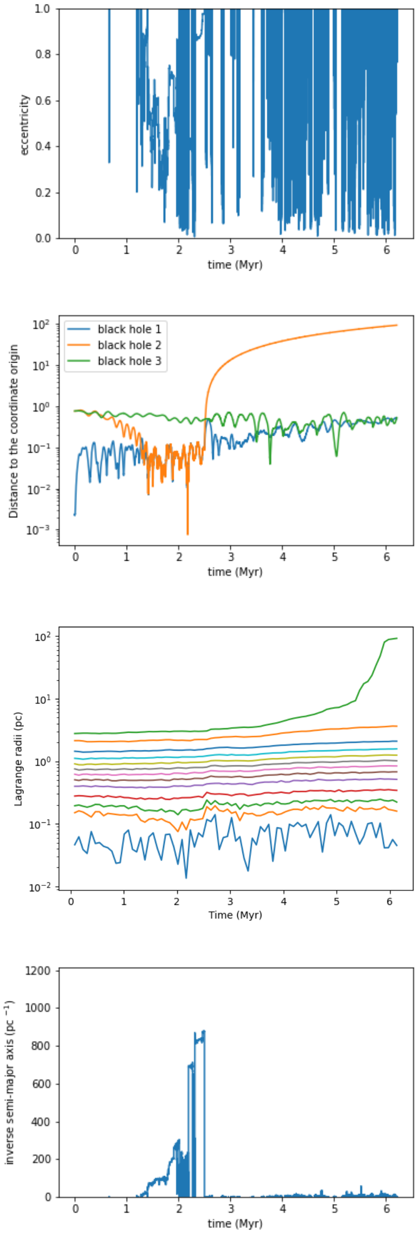

Figure 4.31: Evolution of IMBH triplet and inner binary black holes in simulation N.

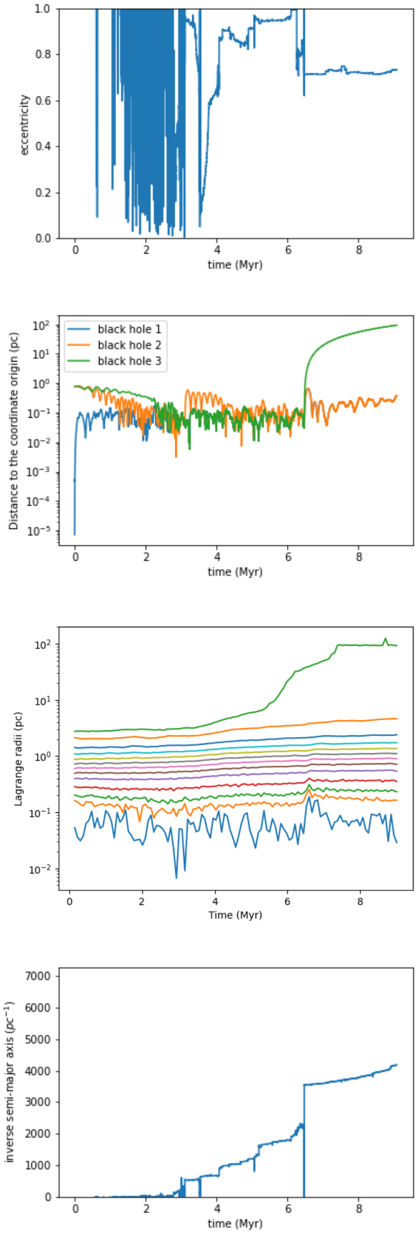

Figure 4.32: Evolution of IMBH triplet and inner binary black holes in simulation P.

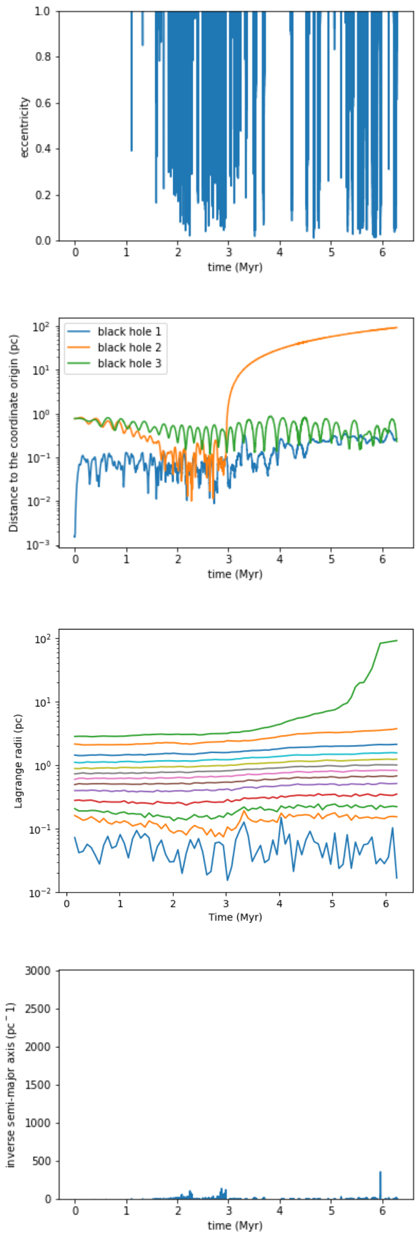

Figure 4.33: Evolution of IMBH triplet and inner binary black holes in simulation R.

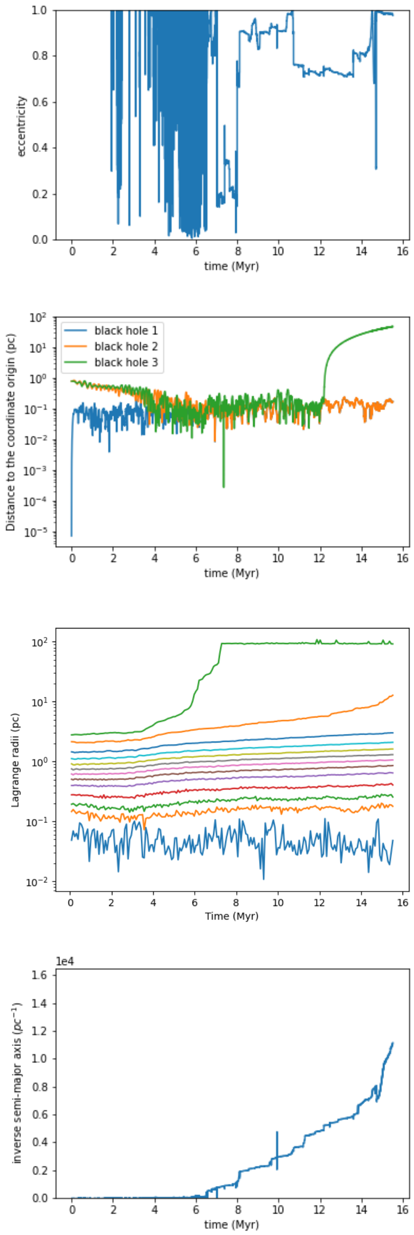

Figure 4.34: Evolution of IMBH triplet and inner binary black holes in simulation S.

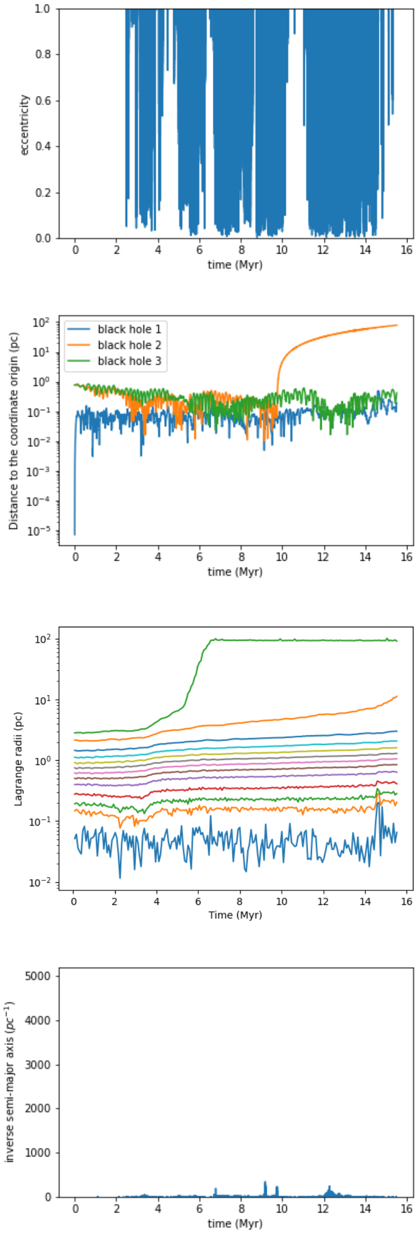

Figure 4.35: Evolution of IMBH triplet and inner binary black holes in simulation U.

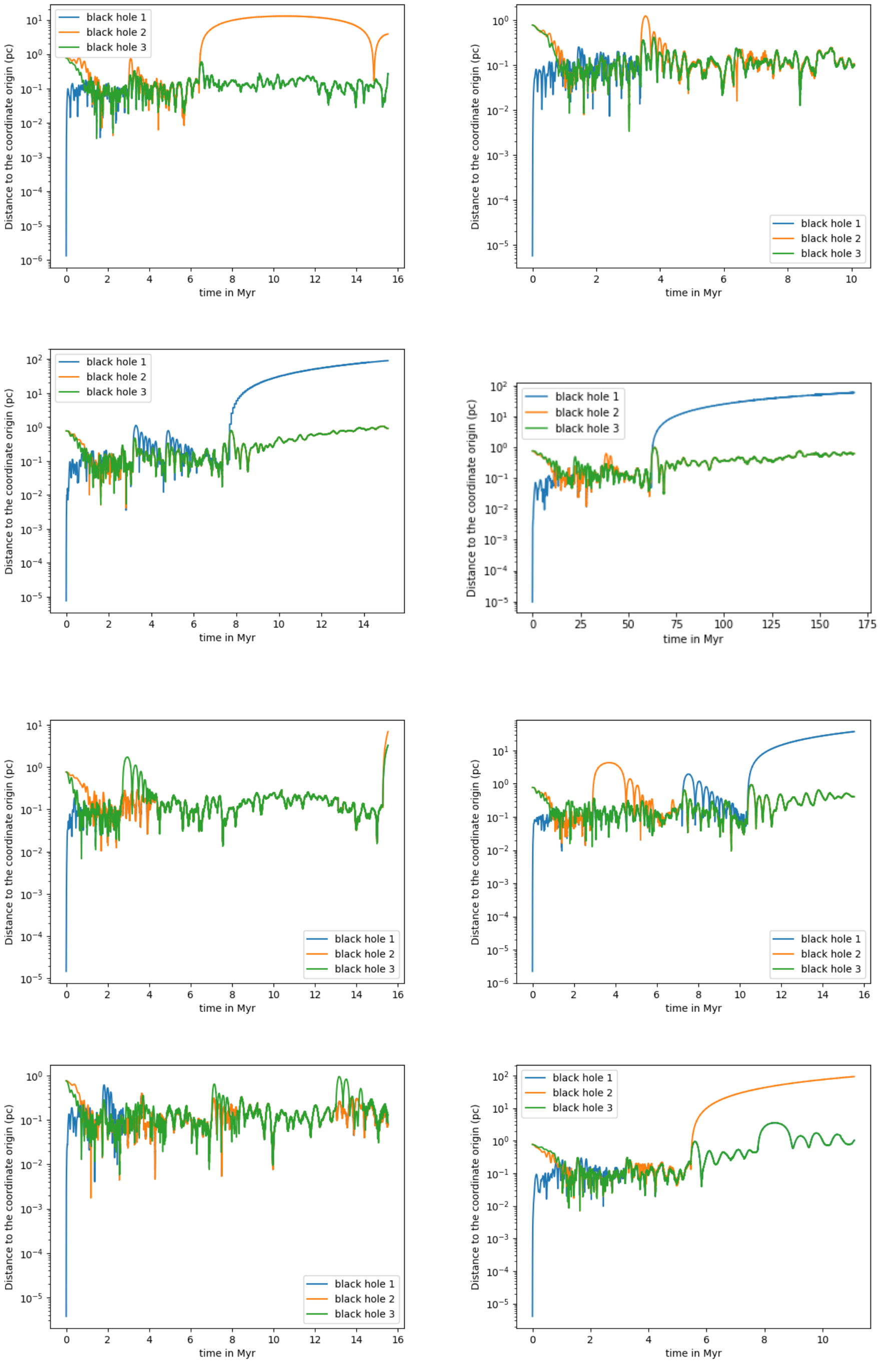

Figure 4.36: Distance evolution of IMBH triplet with different random seed

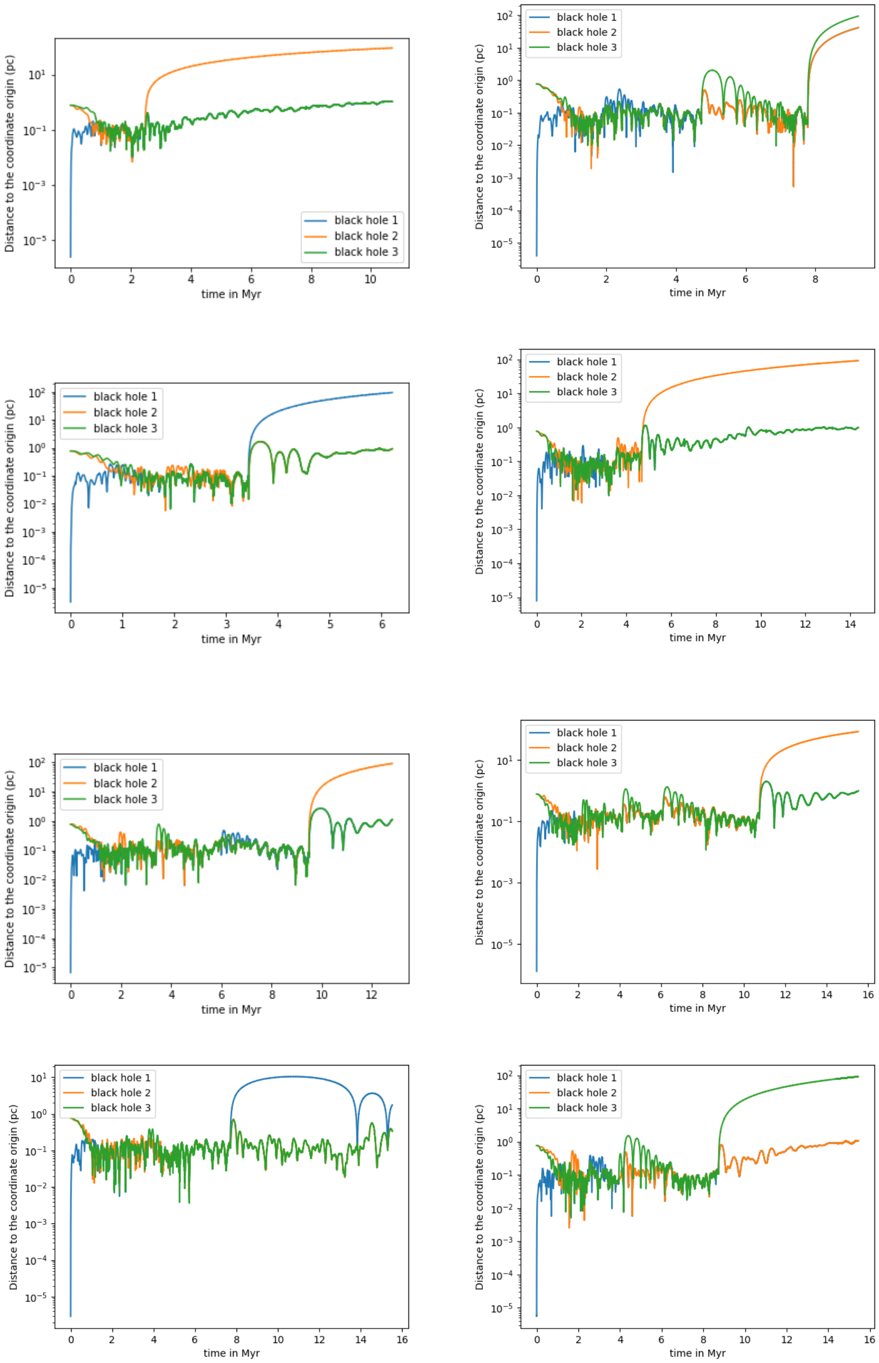

Figure 4.37: Distance evolution of IMBH triplet with different random seed

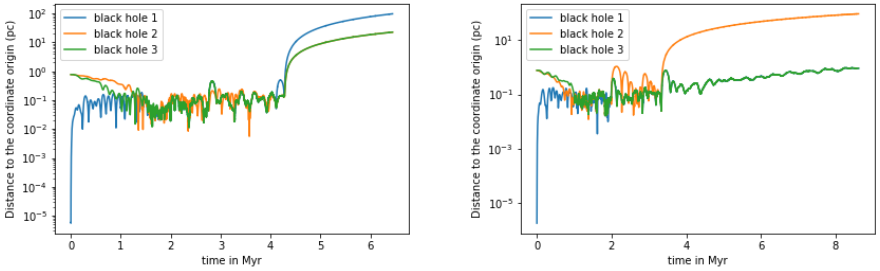

Figure 4.38: Distance evolution of IMBH triplet with different random seed

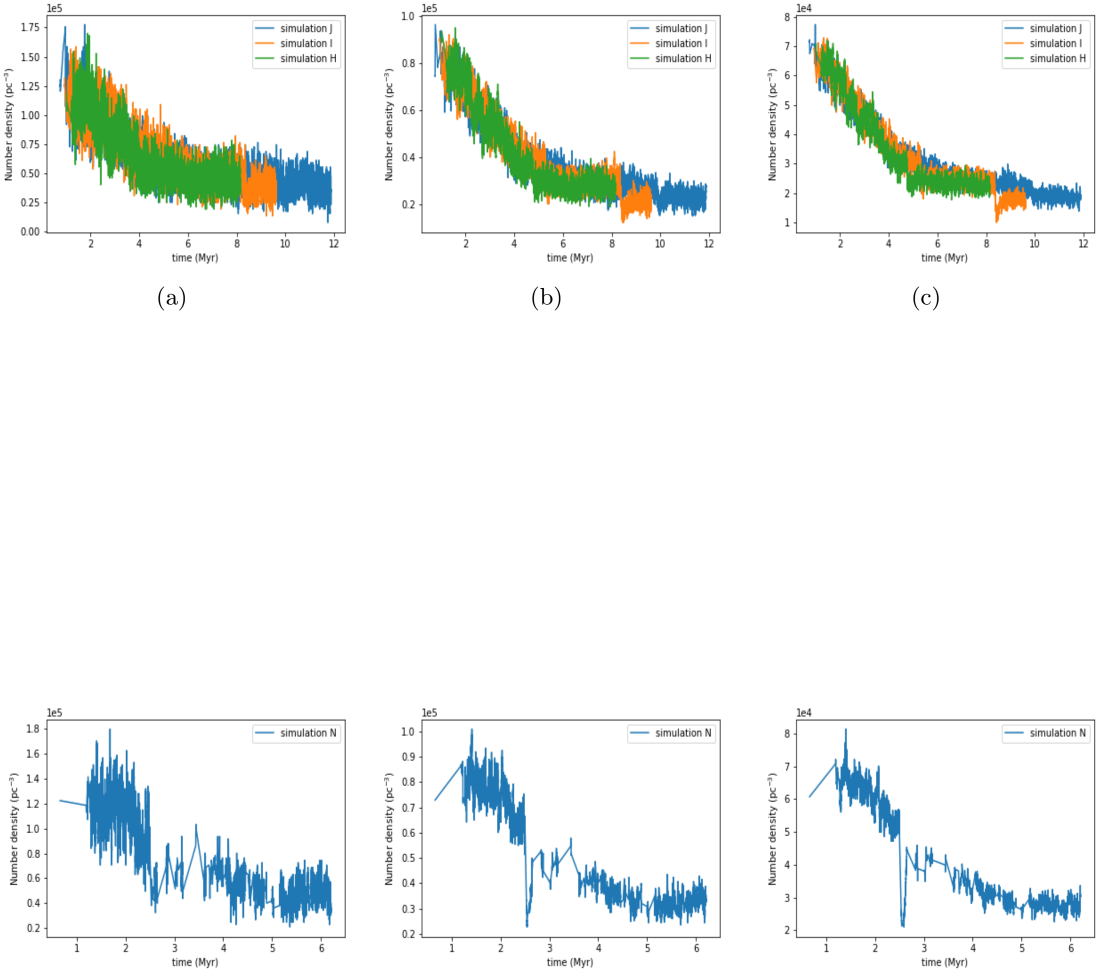

(a) (b) (c)

(d) (e) (f)

Figure 4.39: Stellar population number density evolution at R=0.20 - 0.30 pc for simulations A-R. The simulations L, M, Q, and T are omitted

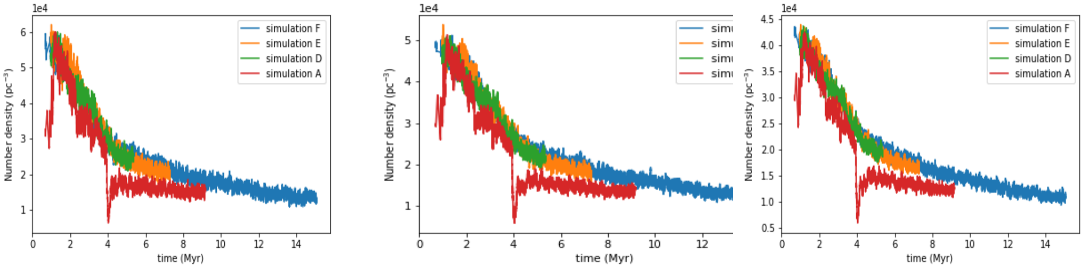

(a) (b) (c)

Figure 4.40: Stellar population number density evolution at R=0.20 - 0.30 pc for simulations A-F.

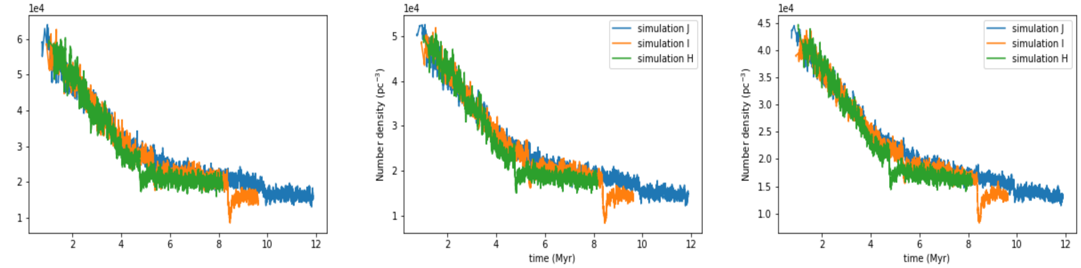

(a) (b) (c)

Figure 4.41: Stellar population number density evolution at R=0.20 - 0.30 pc for simulations G-K.

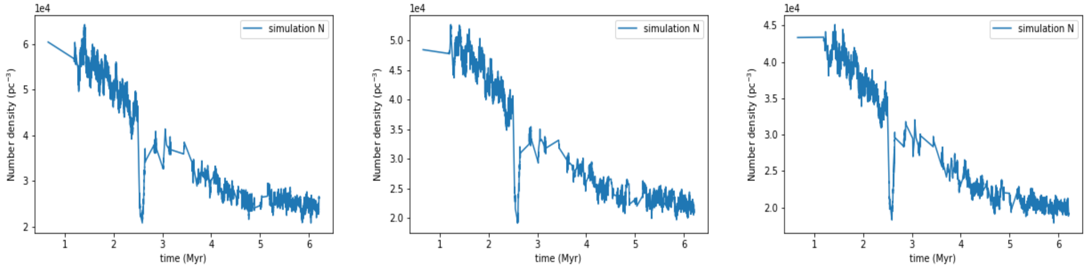

(a) (b) (c)

Figure 4.42: Stellar population number density evolution at R=0.20 - 0.30 pc for simulations L-O.

Chapter 5

Dynamical evolution of IMBH triplets in rotating star clusters

5.1 Introduction

In the past, globular clusters are believed to be non-rotating, spherical systems. However, the utilization of advanced detectors, such as Gaia, and modern data processing tools has proved that classically non-rotating globular clusters are indeed rotating, allowing the revelation of global rotation and individual star motion (Vasiliev 2019). It is believed that IMBHs are located in the center of globular clusters, such as G1 in the Andromeda galaxy (Kong et al. 2010, Pooley & Rappaport 2006, Ulvestad, Greene, & Ho 2007), and 47 Tucanae in the Milky Way (Freire et al. 2017, Kızıltan, Baumgardt, & Loeb 2017, Ridolfi et al. 2016). Current observations suggest that IMBH candidates may be located at the centers of some star clusters (Amaro-Seoane 2006, Amaro-Seoane & Freitag 2006). With very crowded star clusters in a relatively small space, the formation of a binary IMBH (BIMBH) is nearly inevitable. The evolutionary process of an IMBH binary may be analogous to the formation of an SMBH binary. In general, IMBHs initially sink towards the center of a recently-merged cluster by dynamical friction and then shrink their orbit by three-body scattering at a roughly constant hardening rate. If the separation becomes sufficiently small, gravitational wave emission takes over the role of three-body scattering, and the BIMBH effectively evolves in isolation. In this process, a tertiary IMBH may join the process and affect the merger process of the progenitor binary IMBH. In this chapter, we study the effect of rotation, central density, and the tertiary IMBH on the gravitational wave merger

Table 5.1: Initial conditions for the star clusters in this study. Column 1 denotes the identifier of each model. Column 2 shows the concentration parameter of the King model. Column 3 shows the rotation parameter of the King model. Column 4 lists the properties of the mass distribution of the stellar population.

Model ID	W_0	ω_0	IMF
A	3	0.0	equal-mass
B	3	0.3	equal-mass
C	3	0.6	equal-mass
D	6	0.0	equal-mass
E	6	0.3	equal-mass
F	6	0.6	equal-mass
G	6	0.8	equal-mass
H	6	1.2	equal-mass
I	6	1.4	equal-mass
J	6	1.8	equal-mass
K	3	0.0	Kroupa (2001) IMF
L	3	0.3	Kroupa (2001) IMF
M	3	0.6	Kroupa (2001) IMF
N	6	0.0	Kroupa (2001) IMF
O	6	0.3	Kroupa (2001) IMF
P	6	0.6	Kroupa (2001) IMF
Q	6	0.8	Kroupa (2001) IMF
R	6	1.2	Kroupa (2001) IMF
S	6	1.4	Kroupa (2001) IMF
T	6	1.8	Kroupa (2001) IMF

timescale of binary IMBH. The impact of IMBH on cluster evolution is also studied. This chapter is organized as follows. Section 5.2 describes the numerical methods and initial conditions. In Section 5.3, we analyze the outcomes of the simulations and present our results. Finally, our conclusions and discussion are presented in Section 5.4.

5.2 Methods and initial conditions

5.2.1 Initial conditions: star clusters

In this study, we investigate the dynamical evolution of IMBH triplets in intermediate-mass star clusters with an initial total mass of $M_c = 32000\,M_\odot$. The star clusters modeled in this study contain 64 000 particles, of which 63 997 are stars, while the other three are IMBHs.

Each IMBH has a mass that is 1% of the total cluster mass. We model star clusters with different initial central concentration parameters (W_0), different rotation parameters (ω_0), and different stellar mass spectra. The mass spectrum of our simulated cluster are listed in Table 5.1 and discussed below.

In simulations A-J, all stars are assigned identical masses of $\mathrm{m} = 0.5\,\mathrm{M}_\odot$. In simulations K-T, the stellar masses are drawn from the Kroupa (2001) initial mass function (IMF) in the mass range $0.08\,\mathrm{M}_\odot - 150\,\mathrm{M}_\odot$. All clusters are initialized in virial equilibrium, with a virial radius of 1 pc. None of the simulations include primordial binaries or gas. We do not include the tidal field because the tidal disruption of stars onto IMBH may result in a mass change of IMBH, which may change the outcome of IMBH triplet evolution. The systems are evolved for 16.7 Myrs. (or 200 N-body time units (Heggie & Mathieu 1986)) to ensure that at least one IMBH is ejected from the cluster. Stellar evolution is not included, both for a better understanding of the dynamical processes in the systems and also because stellar evolution plays only a minor role at the timescale we investigate in this study.

The positions and velocities of the stars initialized from the rotating King (1966) model, which is defined by the central concentration parameter W_0 and the rotation factor ω_0. We utilize the phase-space distributions described in Goodman (1983) to generate the initial position and velocities. We adopt a Cartesian coordinate system in which the initial net angular momentum of the star cluster points in the positive z-direction.

The half-mass radius of the King model with $W_0 = 6$ is nearly the same as the half-mass radius of the Plummer model with $n = 5$ polytrope, with $R_\mathrm{h} \approx 0.768 R_\mathrm{v}$ (see, e.g., Heggie & Hut 2003). The circular velocity at the half-mass radius of the King model is $V_\mathrm{c} = \sqrt{GM_\mathrm{c}/2R_\mathrm{h}} \approx 9.43 \quad \mathrm{km/s}$, where M_c is the total mass of the cluster.

The stellar distribution function of energy E and z-component angular momentum J_z is expressed as:

$$f_\mathrm{rk} = \mathrm{constant} \times (\mathrm{e}^{-\beta \mathrm{E}} - 1) \times (\mathrm{e}^{-\beta \Omega \mathrm{J_z}}) \quad , \tag{5.1}$$

where $\beta = 1/(m\sigma_c^2)$. m is the mass of one star and σ_c is the one-dimension velocity dispersion. The rotation factor, or dimensionless angular velocity Ω_0, is defined as

$$\omega_0 \equiv \sqrt{2.25\pi G n_c} \Omega_0 \quad , \tag{5.2}$$

where G is the gravitational constant, n_c is a distribution function from Goodman (1983) that needs to be specified in the model.

The central concentration W_0 is defined as

$$W_0 = \beta m(\phi - \phi_t) \tag{5.3}$$

where ϕ is the central potential and ϕ_t being the potential at the cut-off radius. We pick two different W_0 to discover the effect of W_0 on the hardening rate of binary IMBH. Seven values of ω_0 were chosen to investigate the effect of ω_0 on the hardening rate of binary IMBH.

5.2.2 Initial conditions: IMBHs

We initialize each star cluster with three IMBHs. All three black holes are assigned equal masses of $m = 320\,\mathrm{M}_\odot$ One IMBH (m_1) is placed at the coordinate origin of the cluster with zero velocity. The other two IMBHs (m_2 and m_3) are placed at opposite sides of the cluster center in the equatorial plane of the star cluster, at the half-mass radius of the King model. They are assigned circular orbits in the equatorial plane, with their velocity vectors oriented such that their angular momentum with respect to the cluster center points along the positive z-axis. The dynamical time for a rotating star cluster is

$$t_0 = \sqrt{\frac{r_c^3}{GM}}\frac{(GM)^2}{4\pi\Gamma}\frac{1}{N} \tag{5.4}$$

with $\Gamma = 4\pi(Gm)^2 \ln\Lambda$. N is the total number of particles, and m is the mass of a single star (average mass if an IMF exists). $\ln\Lambda$ is the Coulomb logarithm. Usually, λ is assumed to be 0.4 N. r_c is the radius of the core (Cohn 1979). The initial half-mass relaxation time is 32.5 t_0 (Spitzer & Hart 1971).

5.2.3 Numerical method

We use the code FOPAX (Einsel & Spurzem 1999) to generate the initial conditions of the stellar populations. FOPAX utilized the distribution function of the stellar population from Lupton, Gunn, & Griffin (1987). By extending the solver for the 2D Fokker-Planck equation in Goodman (1983), FOPAX creates a rotating King model characterized by central concentration parameter W_0 and rotation factor ω_0. After initialization, we use the direct N-body simulation code `NBODY6++GPU` to dynamically evolve the rotating stellar system (Kamlah et al. 2022, Wang et al. 2015). Kustaanheimo-Stiefel (KS) regularization is used in `NBODY6++GPU` to avoid force calculation error in close binaries (Kustaanheimo & Stiefel 1965).

5.3 Results

This section presents our results and discuss the impact of rotation, central concentration, and initial mass spectrum on the gravitational wave merger timescale of inner binary IMBH.

5.3.1 Total cluster mass and other global properties

Figure 5.1 shows the evolution of the total cluster mass in simulation A-T. The top panel indicates that clusters with an IMF eject more mass than the clusters with equal-mass stars. A comparison between simulations A-C with simulations D-F in the middle panel of the figure shows that clusters with a higher initial central concentration lose mass faster than clusters with a lower central concentration. Since stellar evolution is not included, this mass loss is caused only by escaping stars. We may conclude that mass segregation and higher central concentration speed up the mass loss.

The half-mass radius evolution in simulations A-T exhibits an interesting pattern. The top panel of Figure 5.2 shows the evolution of half-mass radius in simulations A-C and K-M. We observe an abrupt increase in half-mass radius for simulation B at around 10 Myr. At the same time, an IMBH was ejected from the system. A similar pattern occurs for simulations O and P in the middle panel. In the bottom panel of Figure 5.2, clusters with a higher degree of rotation and IMF expand faster. A cluster with an IMF and a low degree of rotation expands faster than a cluster with the highest degree of rotation and no IMF, suggesting that mass segregation is more effective in driving the expansion of the cluster than rotation.

Figure 5.3 shows the evolution of the core mass in simulations A-T. As shown in the top panel, an abrupt increase of core mass occurred at around 10 Myr for simulation B. At that time, an IMBH was ejected from the system. A similar pattern occurs at around 9 Myr for simulation J. In the bottom panel, an abrupt increase in core mass occurs shortly after the start of the simulation. By inspecting the top panel of Figure 5.4, we find that the IMBHs located at the half-mass radius have difficulty migrating to the center of the clusters. The two IMBHs wander for 1.5 Myr before sinking to the center. The unusual increase in core size and half-mass radius is probably an artificial phenomenon brought

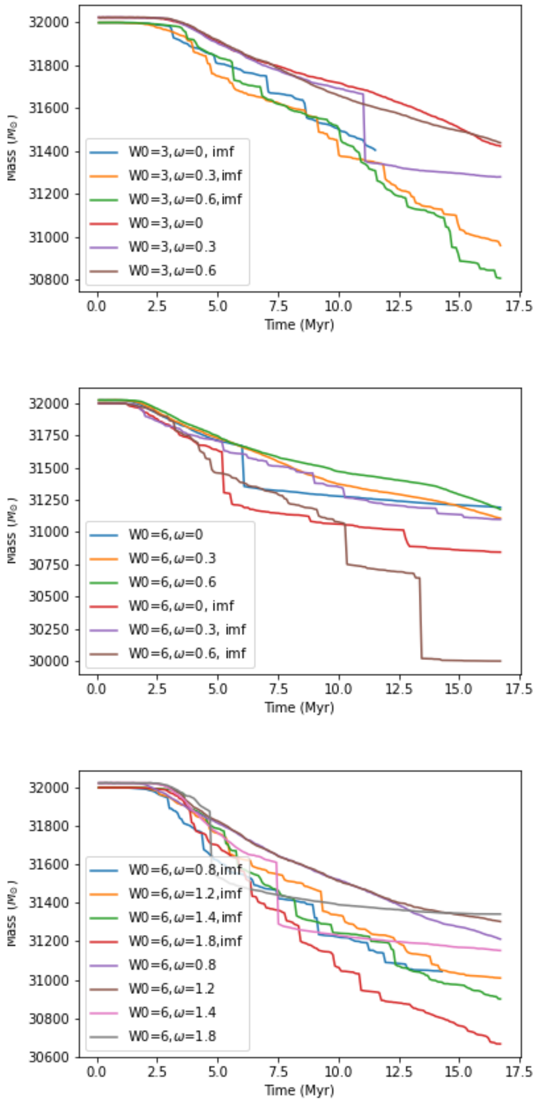

Figure 5.1: The evolution of total cluster mass in simulation A-T. The first panel shows the total cluster mass comparison between simulations A-C and K-M. The second panel shows the total cluster mass comparison between simulations D-F and N-P. The last panel shows the total cluster mass comparison between G-J and Q-T.

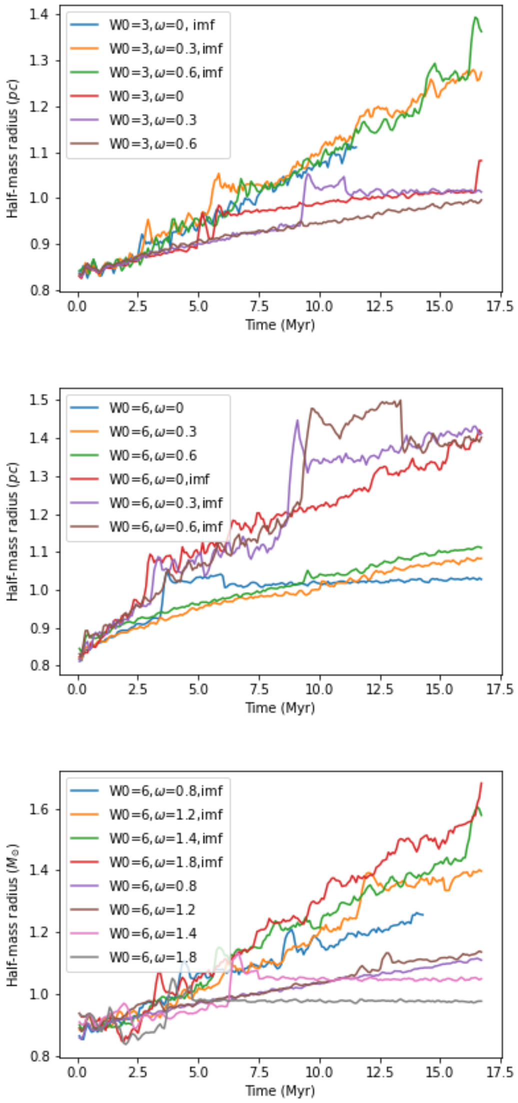

Figure 5.2: The evolution of half-mass radius in simulation A-T. The first panel shows the half-mass radius comparison between simulations A-C and K-M. The second panel shows the half-mass radius comparison between simulations D-F and N-P. The last panel shows the half-mass comparison between simulation G-J and Q-T.

by the calculation recipes. The recipes use a density-weighted average of the positions of particles to obtain core radius. The IMBH brings a very high mass density to surrounding stars, so the core and half-mass radius is unusually large at some time.

5.3.2 Evolution of the BIMBH semi-major axis

5.3.2.1 The effect of central concentration, IMF, and rotation

IMBH triplets in the center of globular clusters undergo complex three-body interaction, which may result in a permanent or temporary ejection of an IMBH from the center of the star cluster. In this study, the evolution of the orbital parameters of the binary IMBH is still monitored after the permanent ejection of one IMBH, but its distance to the cluster's coordinates of origin is not calculated. The evolution of BIMBH depends on the global properties of the embedded cluster, such as the surrounding stellar density profile, mass spectrum, and degree of rotation. This section describes the inverse semi-major axis evolution of the inner binary IMBH and investigates how central concentration, IMF, and how the degree of rotation affect the hardening rate.

The bottom panels of Figures 5.5 and 5.6 show the evolution of the inverse semi-major axis of the inner binary IMBH in simulations C and F. These models have different W_0 but identical ω_0. In both simulations, one IMBH was ejected from the cluster. The hardening rate of the IMBH binary after the ejection of one IMBH is interpolated.

For simulations C and F, the period between 12.5 Myr and 15 Myr was adopted to investigate the hardening rate of the inner binary. The average hardening rate for simulation C is $s = \Delta(a^{-1})/\Delta t = 103\,\mathrm{pc}^{-1}\,\mathrm{Myr}^{-1}$. For simulation F, the hardening rate is $389\,\mathrm{pc}^{-1}\,\mathrm{Myr}^{-1}$. This suggests that in a rotating cluster with three IMBHs embedded in the center, a higher central concentration results in a higher hardening rate. This is reasonable because a higher central concentration implies more stars enter the loss cone of the inner binary IMBH. Hence the hardening rate is higher.

The bottom panels of Figures 5.7 and 5.8 show the inverse semi-major axis evolution of the inner binary IMBH in simulations D and N. These models have identical W_0 and ω_0, but a different mass spectrum. In both simulations, one IMBH was ejected from the cluster. The hardening rate of the inner IMBH binary after the ejection of one IMBH interpolated to investigate the effect of IMF on the hardening rate. For simulation D, the period between 4 Myr and 6 Myr was adopted, while for simulation N, the period between 3 Myr and 5 Myr was adopted. The average hardening rate for simulation D is $s = 201\,\mathrm{pc}^{-1}\,\mathrm{Myr}^{-1}$. For

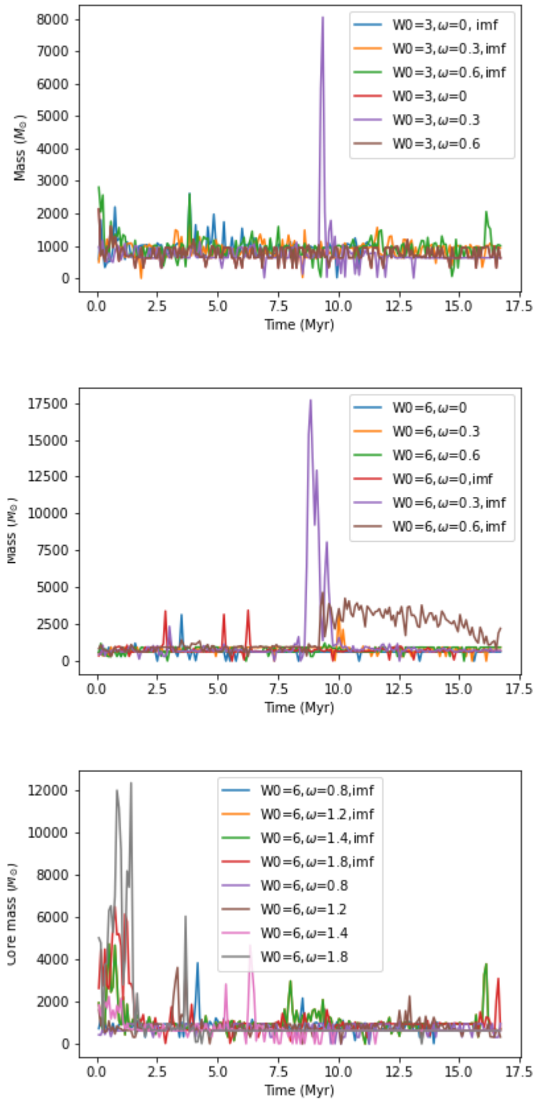

Figure 5.3: The evolution of core mass in simulations A-T. The top panel shows the core mass comparison between simulations A-C and K-M. The middle panel shows the core mass comparison between simulations D-F and N-P. The bottom panel shows the core comparison between simulations G-J and Q-T.

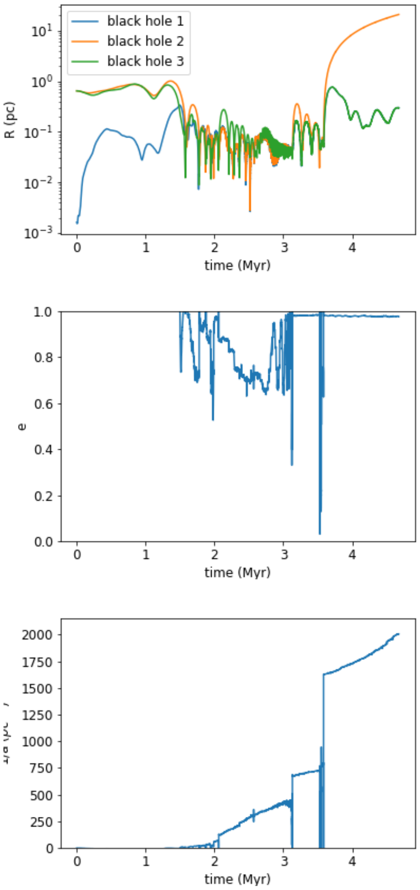

Figure 5.4: Evolution of inner binary black holes and cluster properties in simulation J.

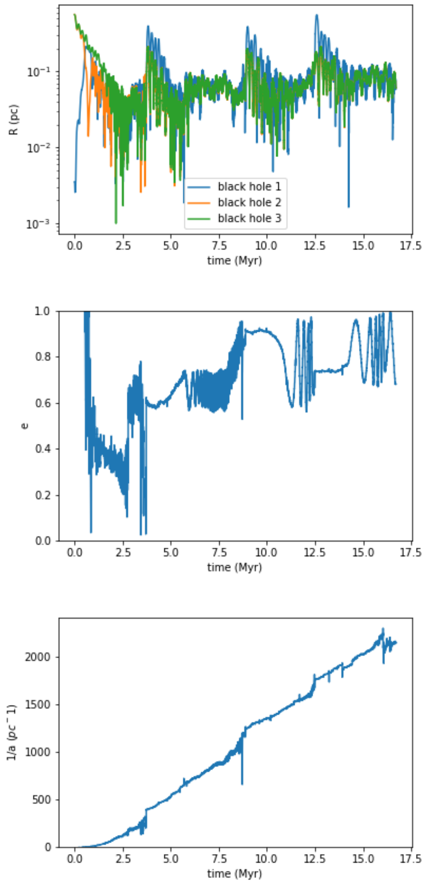

Figure 5.5: Evolution of inner binary black holes in simulation C.

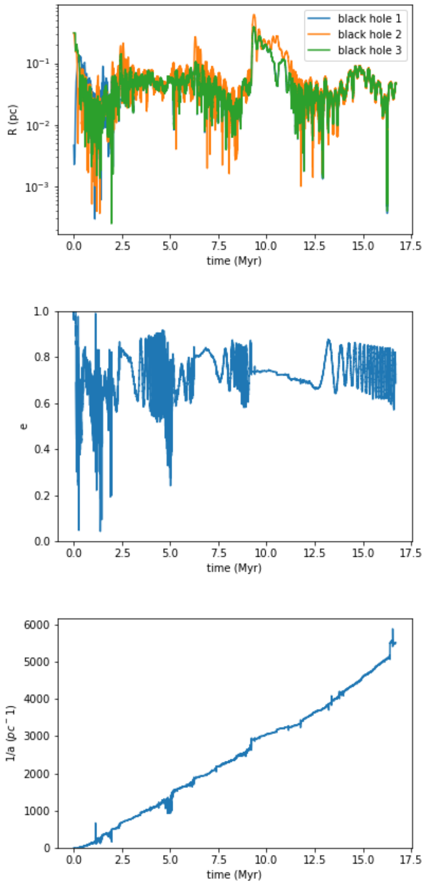

Figure 5.6: Evolution of inner binary black holes and cluster properties in simulation F.

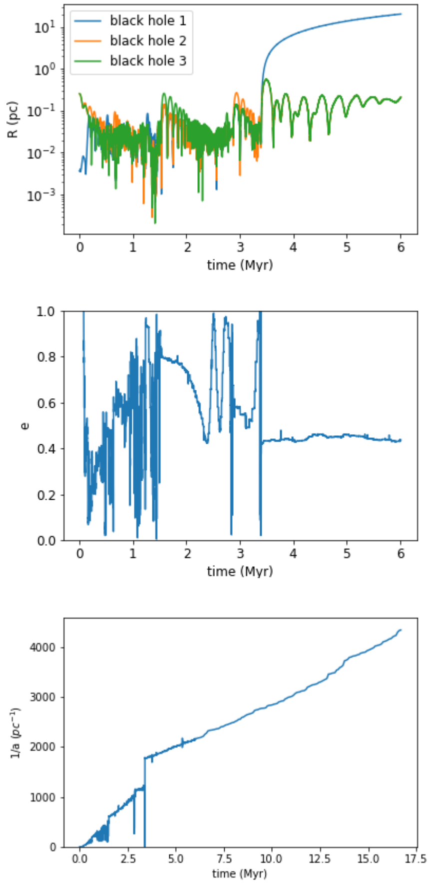

Figure 5.7: Evolution of inner binary black holes and cluster properties in simulation D.

simulation N, the hardening rate is 211 $\mathrm{pc}^{-1}\,\mathrm{Myr}^{-1}$. It suggests that in a rotating cluster with a binary IMBH embedded, the inclusion of IMF increases the hardening rate of the IMBH binary.

The increase in hardening rate likely originates from the difference in the phase-space distribution of the cluster stars. The initial condition also affects the hardening rate of the inner binary.

The bottom panel of Figure 5.4 shows the inverse semi-major axis evolution of simulation I. For simulations D and I, the period from the ejection of one IMBH to the end of the simulation was adopted for extrapolating the value of the inverse semi-major axis. The average hardening rate for simulation D is 201 $\mathrm{pc}^{-1}\,\mathrm{Myr}^{-1}$, and 186 $\mathrm{pc}^{-1}\,\mathrm{Myr}^{-1}$ for

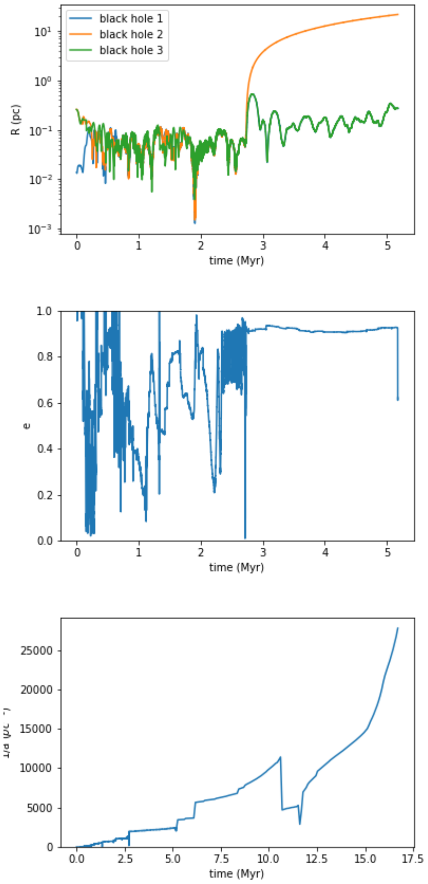

Figure 5.8: Evolution of inner binary black holes and cluster properties in simulation N.

simulation I. The difference in the hardening rate between the two simulations implies that the hardening rate of the IMBH binary decreases as the degree of rotation increases.

5.3.2.2 The effect of a tertiary IMBH

The outcome of IMBH triplets in the center of globular clusters may vary a lot. One IMBH may get ejected after violent three-body interaction. Our simulations can be divided into three categories. In the first category, one IMBH is ejected out of the cluster, including simulations B, D, I, J, and N. The second category contains simulations with two IMBH ejected from the cluster, such as simulation P. The rest of our simulations fall in the third category. The third panel of Figure 5.13 - 5.4 shows the evolution of the inverse semi-major axis in simulation A-J. It is observable that the inner binaries with a higher final inverse semi-major axis value are from simulations with no IMBH ejected. This phenomenon suggests that in a rotating cluster, a non-escape tertiary IMBH may increase the hardening rate of the inner binary IMBH. The member exchange of inner binary IMBH and the ejection of one IMBH, however, does not aid much in the shrinking of the inner binary orbit. The increase of hardening rate by a non-escape tertiary IMBH is analogous to the mechanism stated by Blaes, Lee, & Socrates (2002), suggesting that a non-escape tertiary SMBH helps increase the hardening rate of inner binary SMBH. For simulation K-T, the mechanism is not valid because mass segregation and the existence of massive stars with masses comparable to the IMBH break the assumption of the standard binary IMBH hardening process.

5.3.3 Evolution of the Lagrangian radii

The inclusion of three IMBH in a rotating cluster not only evolves via binary-single interaction but also impacts the global properties of the rotating cluster. Figures 5.9 and 5.10 show the evolution of the core radii and 50% Lagrangian radii of simulations A-T. In general, the clusters with a stellar mass spectrum expand faster than those clusters with identical stellar masses, implying that mass segregation plays a role in the expansion of the clusters. Clusters with a higher degree of rotation expand faster than those with lesser rotation.

All modeled clusters experience core collapse, but the time at which the core collapse takes place varies with the properties of the clusters. The top panel of Figure 5.9 shows that simulations A-C undergo core collapse for the first time at around 2.5 Myr. Unlike cluster

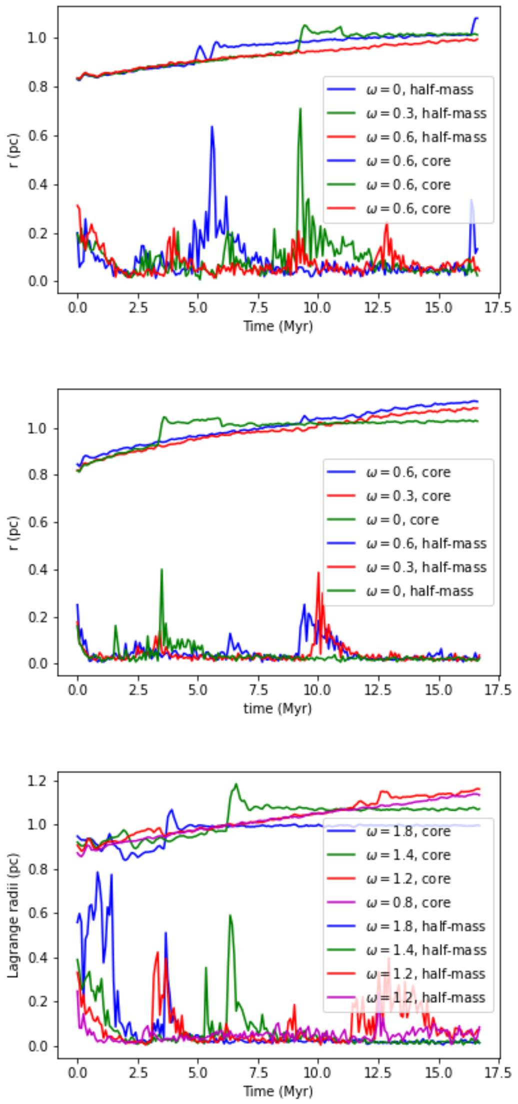

Figure 5.9: The evolution of the 50% Lagrangian and core radii in simulations A-C (top), D-F (middle), and G-J (bottom). The curves start at the top denotes half-mass radius, and the curve start at the bottom represents core radius.

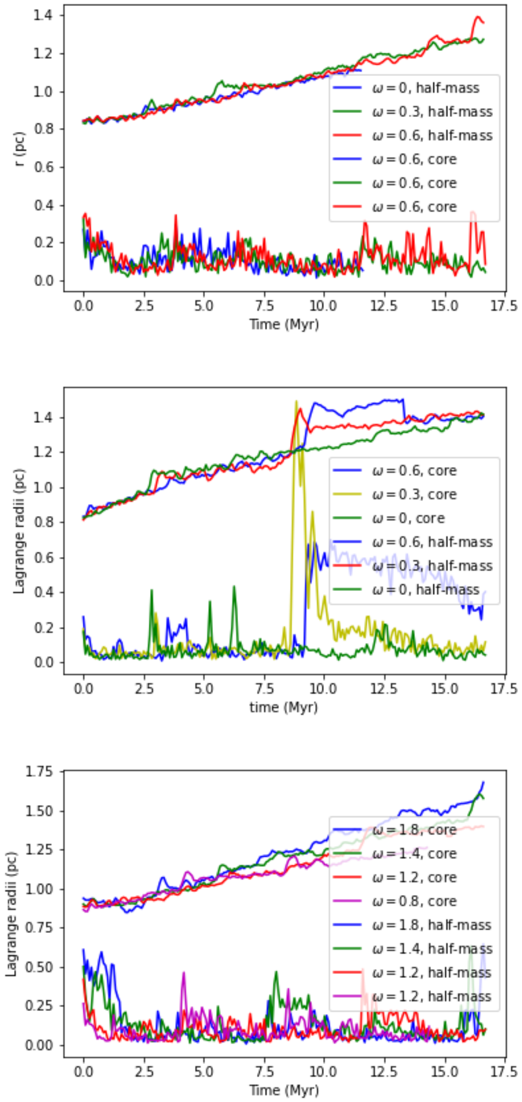

Figure 5.10: The evolution of the 50% Lagrangian and core radii in simulations K-M (top), N-P (middle), and Q-T (bottom).

Model ID	Ejection rate (N_{esc}/Myr)	Average escape speed (km/s)
A	74	22.56
B	53	22.71
C	72	22.23
D	60	31.62
E	113	24.87
F	105	25.78
K	91	20.9
L	78	19.6
M	88	19.74

Table 5.2: The ejection rates and average escape speeds for simulations A-F and simulations K-M. We define the ejection rate as the number of ejected stars N_{esc} per Myr.

simulation C, which has a small core until the end, the core of the cluster in simulations A and B experiences a sharp expansion and contraction. The cluster core in simulation A expands and contracts at around 6 Myr. The expansion and contraction of the cluster core probably originate from the temporary ejection of two of the IMBHs (m_1 and m_3), which is an artificial phenomenon brought by the core radius calculation recipes from Casertano & Hut (1985). Similarly, the expansion and contraction of the cluster core in simulation B is also an artificial phenomenon that is brought by the permanent escape of an IMBH.

The middle panel of Figure 5.9 shows the evolution of core and half-mass radii in simulations D-F. The core collapse timescale in this set of simulations is about 0.5 Myr, much shorter than the simulations depicted in the panel above. We may conclude that higher central concentration results in a much shorter core collapse timescale.

The bottom panel of Figure 5.10 shows the evolution of core radius and half-mass radius in simulation G-J. The core collapse timescale in this set of simulations is about 2.5 Myr, nearly the same as the timescale in simulations A-C and much longer than the timescale in simulations D-F. This implies that a high degree of rotation may delay the core collapse process.

5.3.4 Runaway IMBHs and stars

The ejection of stars can be utilized to analyze the effect of different host cluster properties on the evolution of binary IMBH. Figure 5.11 shows the escape velocity at infinity of stars versus their escape time. The first, second, and third rows show the escape velocity at

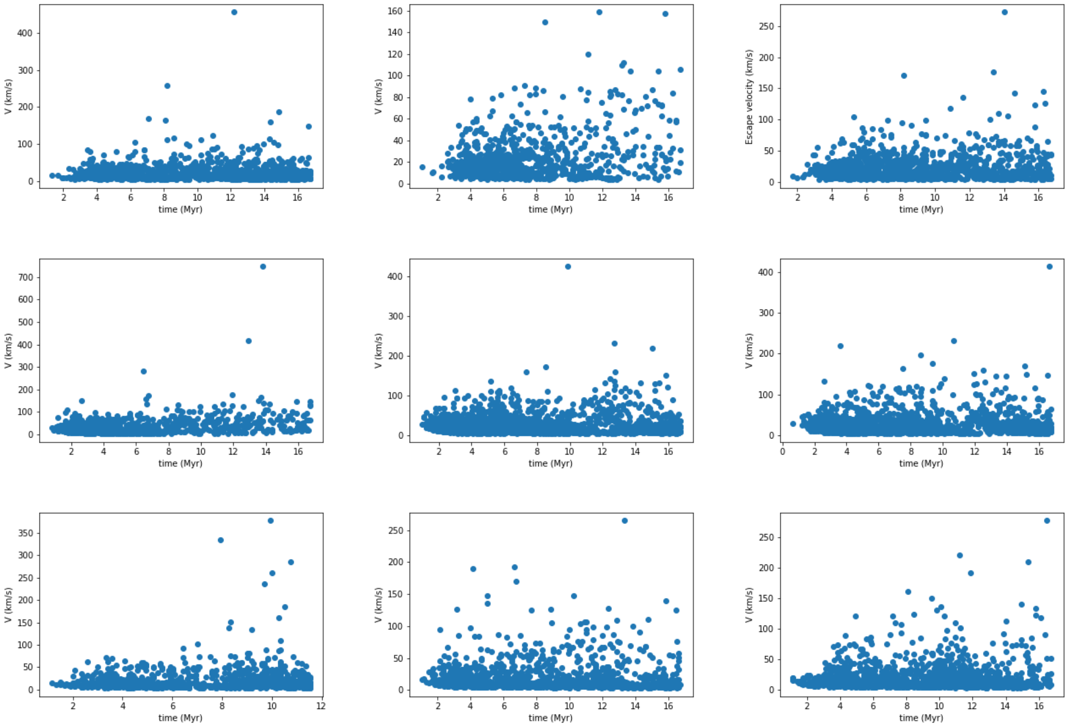

Figure 5.11: Escape speeds of stars at infinity versus escape time.The first row denotes simulations A-C, from left to right. The second row shows simulation D-F, from left to right. The third row represents simulation K-M.

infinity versus escape time for the stars in simulations A-C, D-F, and K-M. Table 5.2 shows the profile of escape velocity at infinity for average ejection rates for simulations A-F and K-M. Simulation A-C shares a similar escape velocity profile, but the ejection rate of simulation B is much lower than the other two simulations. It is reasonable because the evolution of the inner binary black hole requires surrounding stellar ejection to shrink their orbit. In simulation B, one IMBH is ejected. But no IMBH is ejected from the cluster in simulation A and C, so more mass need to be ejected from the loss cone of binary IMBH in simulation A and C. The escape velocity profile in simulation A-C is similar, with a tiny difference. In general, The ejection rate of simulations D-F is higher than simulations A and C. The ejection rate in simulation D is somewhat lower than simulation A because an IMBH is also ejected from the cluster in simulation D. The ejection speed in simulations D-F is also higher than simulations A-C, indicating that clusters with a high

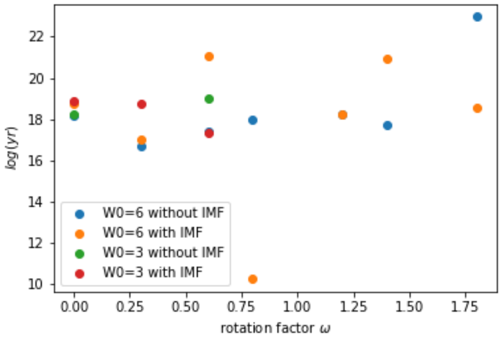

Figure 5.12: Gravitational wave merger timescale for simulations A-T. The horizontal axis indicates the initial rotation parameter ω_0. The vertical axis denotes the logarithmic scale of merger time with base 10.

central concentration have a higher escape speed.

The average escape velocity in simulation D is much higher than in simulations E and F. This is inconsistent with the gravo-gyro catastrophe, which indicates that stars in a rotating stellar system have a higher ejection speed compared to stars in a non-rotating stellar system. The high escape velocity in simulation D is probably due to a violent three-body interaction between the IMBH.

The violent three-body interaction in simulation D heat up the surrounding stars, allowing these surrounding stars to heat up and have high kinetic energy. The average ejection rate in simulations K-M is higher than in simulations A-C, but the escape velocity is slightly lower than in simulation A-C. The high ejection rate suggests that mass segregation may be an aid in accelerating the surrounding stellar ejections of the inner binary IMBH.

5.3.5 Merger timescale of inner binary

Figure 5.12 shows the merger timescale of inner binary IMBH when the corresponding simulation stops. It is observable that there is no clear correlation between the merger timescale, the rotation factor, and the central concentration factor. The unclear correlation between the merger timescale, the rotational factor, and the central concentration primary originates from the stochastic nature of the inner binary IMBH eccentricity.

5.4 Conclusions

In this study, we investigated the evolution of IMBH triplets in rotating clusters with different parameters in order to find out the effect of a tertiary IMBH on the gravitational wave merger timescale of progenitor binaries. The impact of initial bulk rotation on the cluster's global properties and member stars was also investigated. Our conclusion can be summarized as follows.

1. The inclusion of initial bulk rotation accelerates the violent relaxation of globular clusters. Globular clusters undergo violent relaxation faster with a higher degree of rotation.

2. Globular clusters with an IMF undergo violent relaxation faster than clusters with a single mass function. Mass segregation accelerates the violent relaxation of globular clusters.

3. The hardening rate of inner binary IMBH increases with central concentration factor W_0 increases. However, the hardening rate may decrease with rotation factor ω_0 increase. The existence of an IMF may also increase the hardening rate of the inner binary IMBHs.

4. There is no clear correlation between the merger timescale and rotational factor, nor merger timescale nor central concentration. The lack of clear correlation primarily originates from the stochastic nature of the eccentricity of the inner binary IMBH.

5. The presence of IMF may enhance the mass ejection rate of globular clusters. However, the mass ejection rate does not necessarily increase with W_0 and ω_0 increase.

6. The repeated dynamical interaction between the tertiary IMBH and the inner binary IMBH does not necessarily harden the inner binary efficiently. In fact, a tertiary IMBH that is gravitationally bound to the binary IMBH may be more effective in the hardening process of the inner binary IMBH.

7. Globular clusters with a higher central concentration experience core collapse on a much shorter timescale compare to clusters with a shallow density cusp. Globular clusters with a high degree of rotation may delay the core collapse process compared to non-rotating clusters

In our follow-up study, we plan to replace the tertiary IMBH with other massive objects, such as a giant molecular cloud or a nuclear star cluster. The IMBH may embed in the center of a gas disc, so a further study of the IMBH binary with a gas disc is also possible.

5.5 Appendix

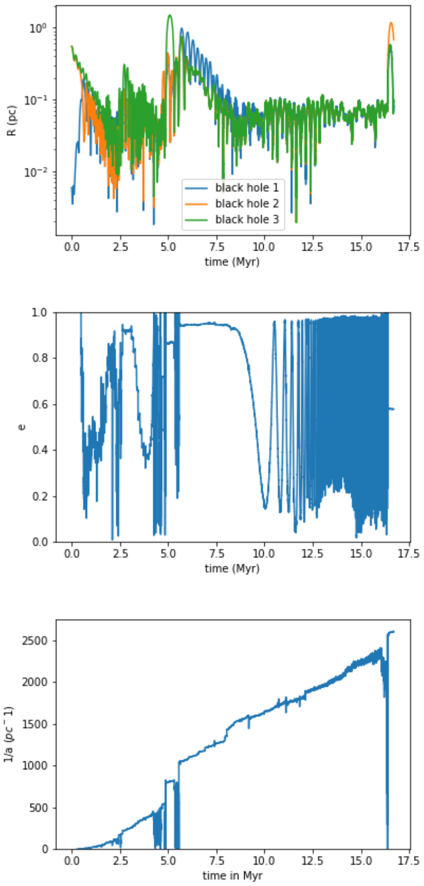

Figure 5.13: Evolution of inner binary black holes and cluster properties in simulation A. The top, middle, and bottom panels show the evolution of the eccentricity, the distance to the center, and the inverse semi-major axis, respectively.

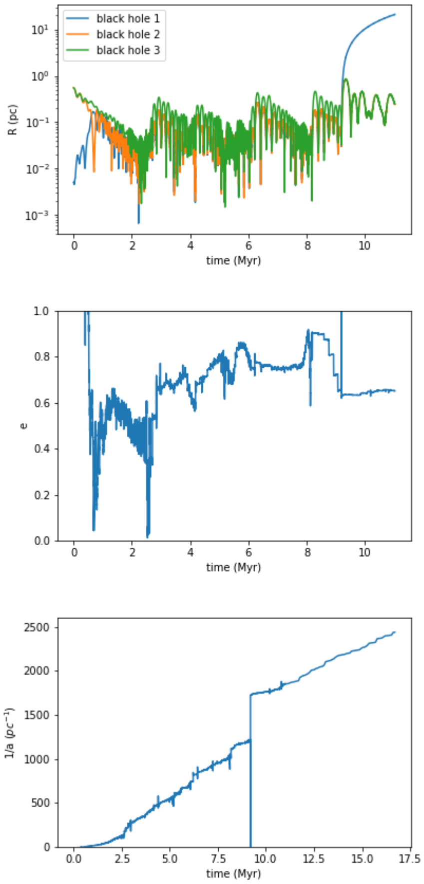

Figure 5.14: Evolution of inner binary black holes and cluster properties in simulation B.

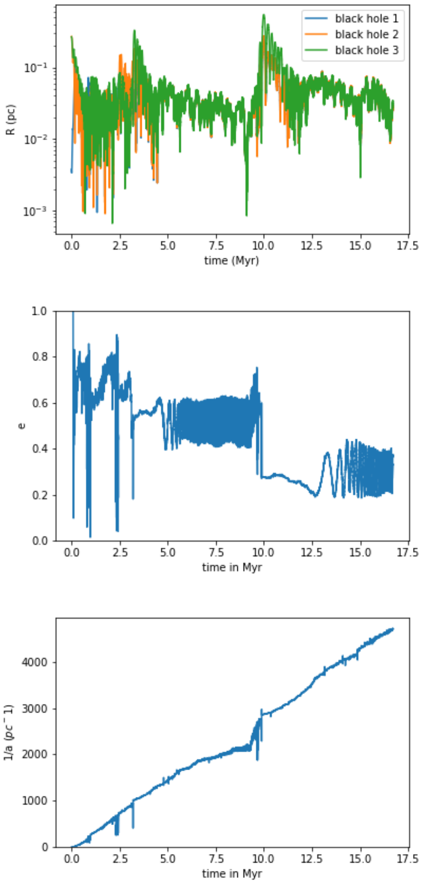

Figure 5.15: Evolution of inner binary black holes and cluster properties in simulation E.

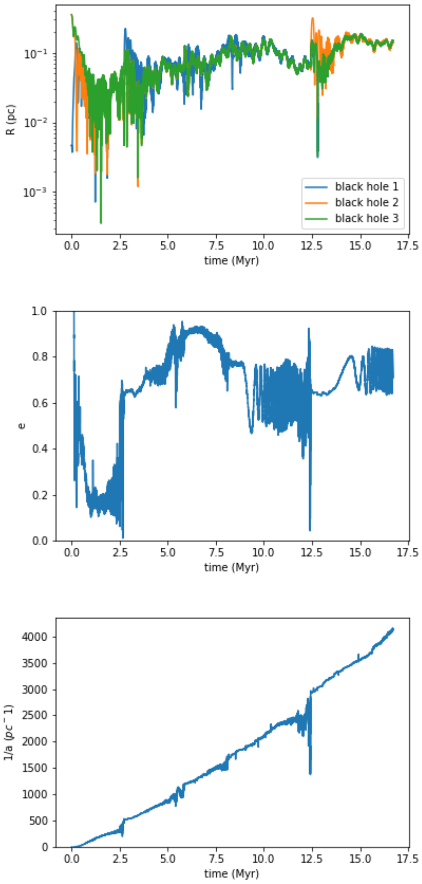

Figure 5.16: Evolution of inner binary black holes and cluster properties in simulation G.

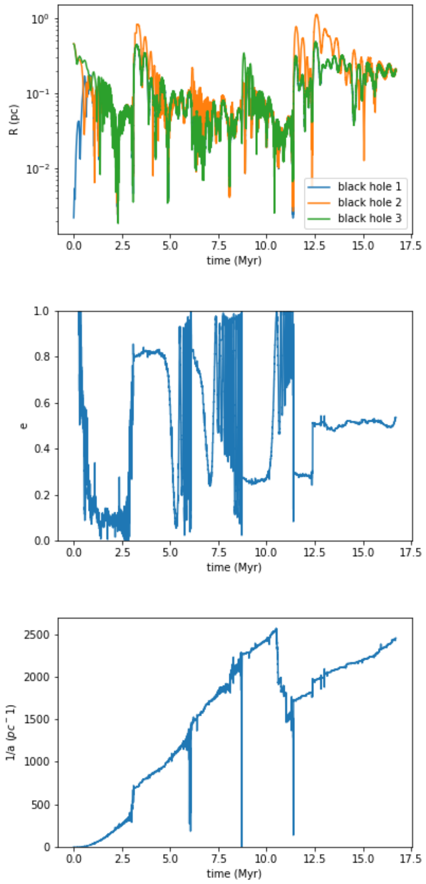

Figure 5.17: Evolution of inner binary black holes and cluster properties in simulation H.

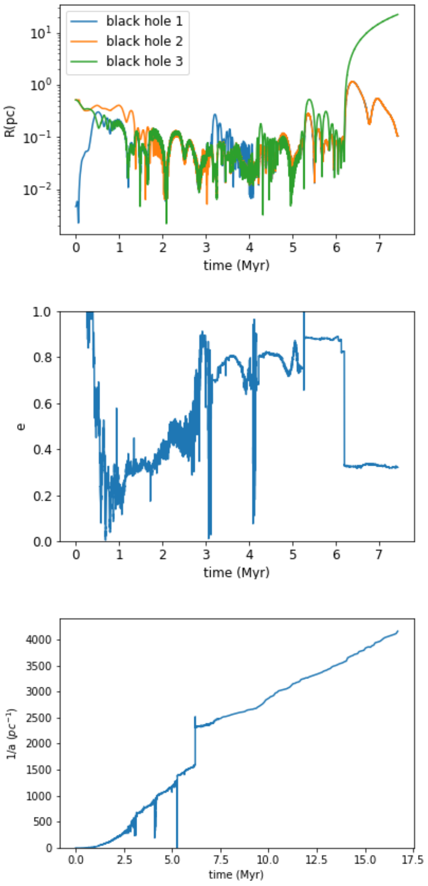

Figure 5.18: Evolution of inner binary black holes and cluster properties in simulation I.

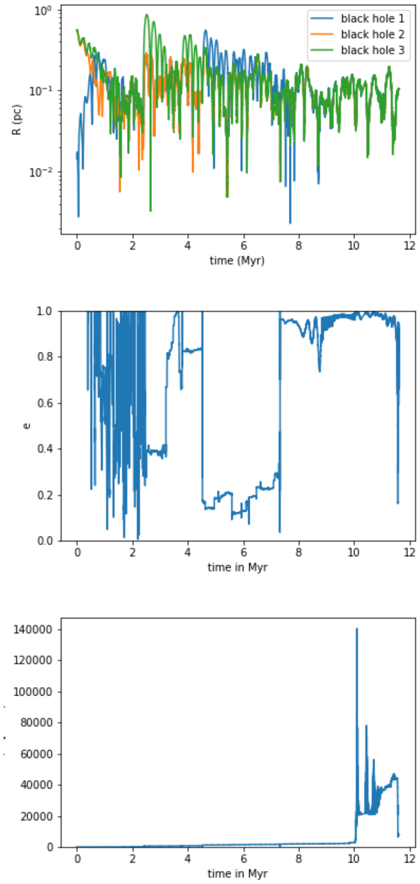

Figure 5.19: Evolution of inner binary black holes and cluster properties in simulation K.

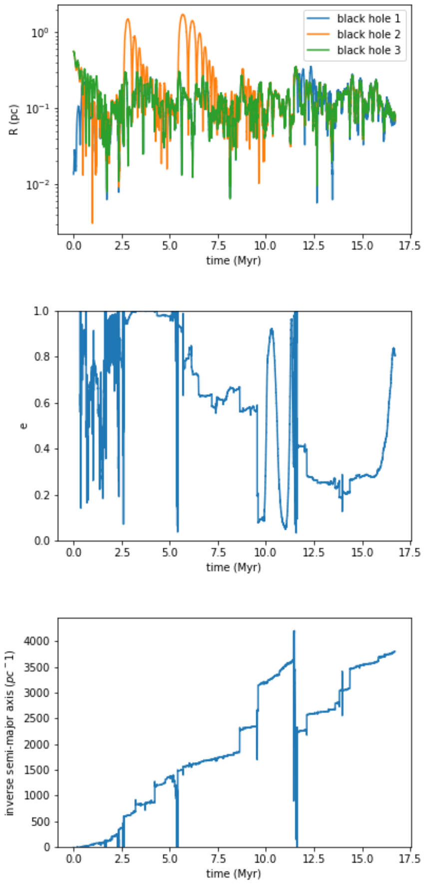

Figure 5.20: Evolution of inner binary black holes and cluster properties in simulation L.

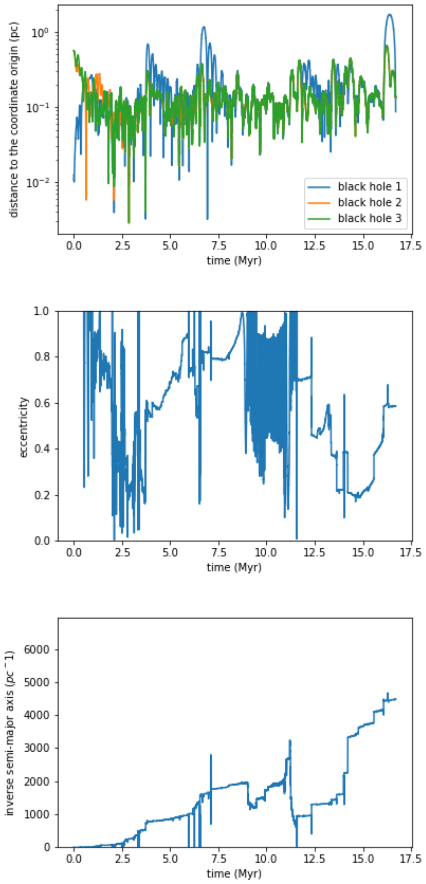

Figure 5.21: Evolution of inner binary black holes and cluster properties in simulation M.

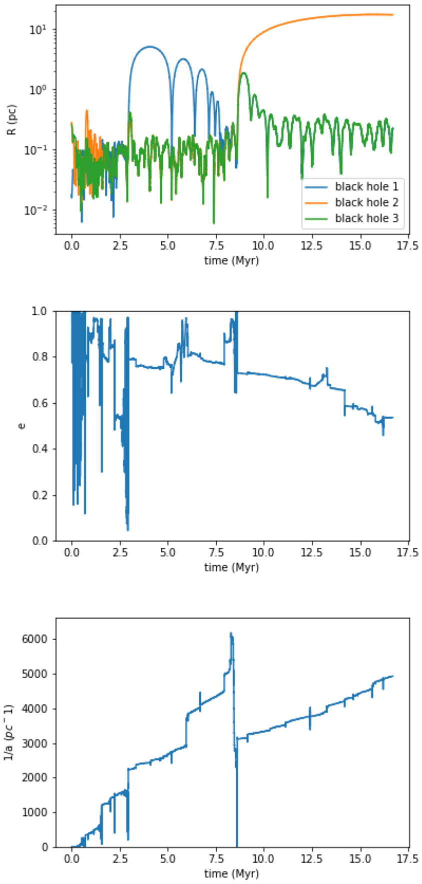

Figure 5.22: Evolution of inner binary black holes and cluster properties in simulation O.

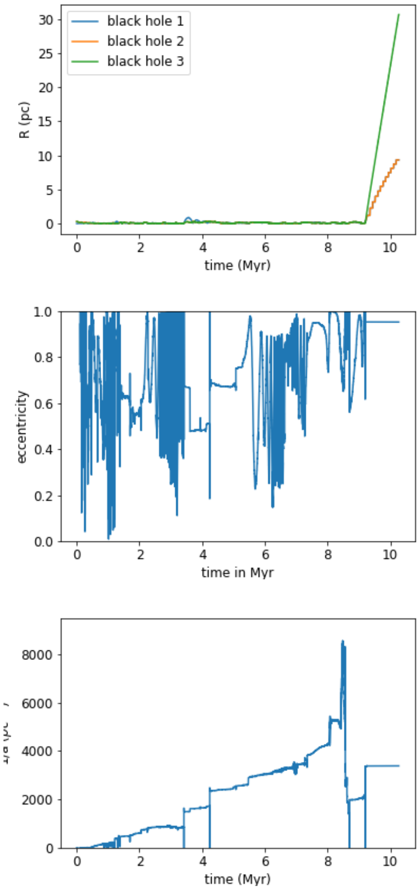

Figure 5.23: Evolution of inner binary black holes and cluster properties in simulation P.

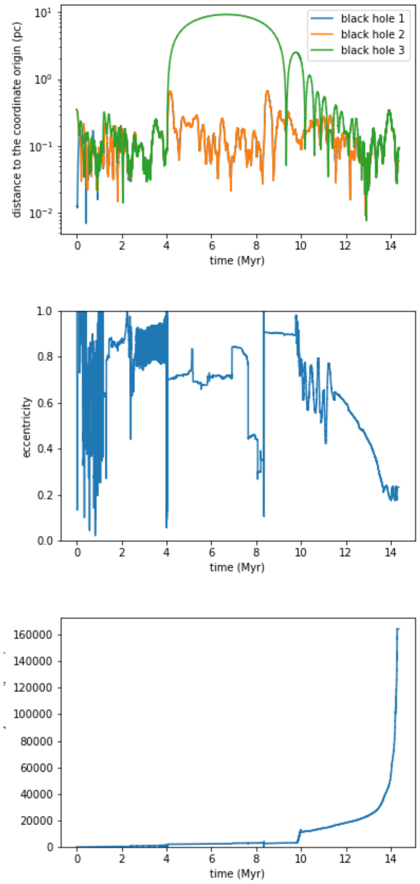

Figure 5.24: Evolution of inner binary black holes and cluster properties in simulation Q.

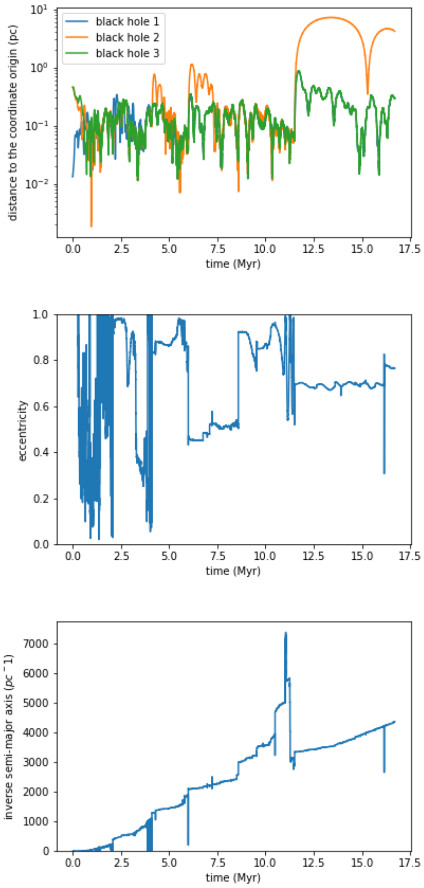

Figure 5.25: Evolution of inner binary black holes and cluster properties in simulation R.

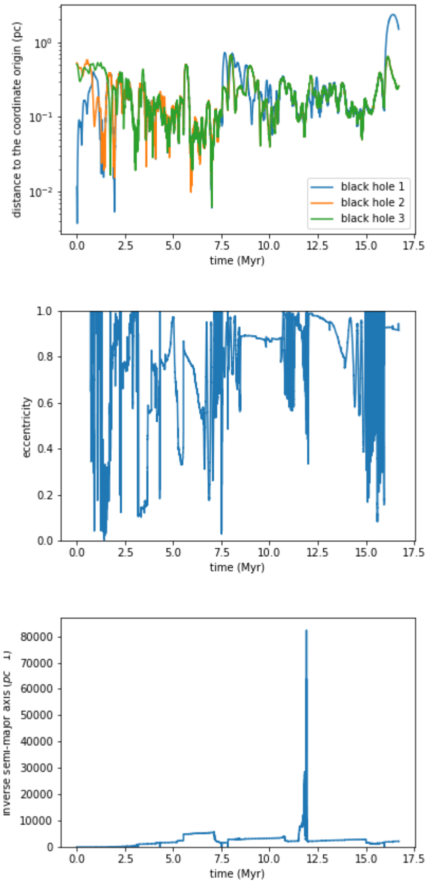

Figure 5.26: Evolution of inner binary black holes and cluster properties in simulation S.

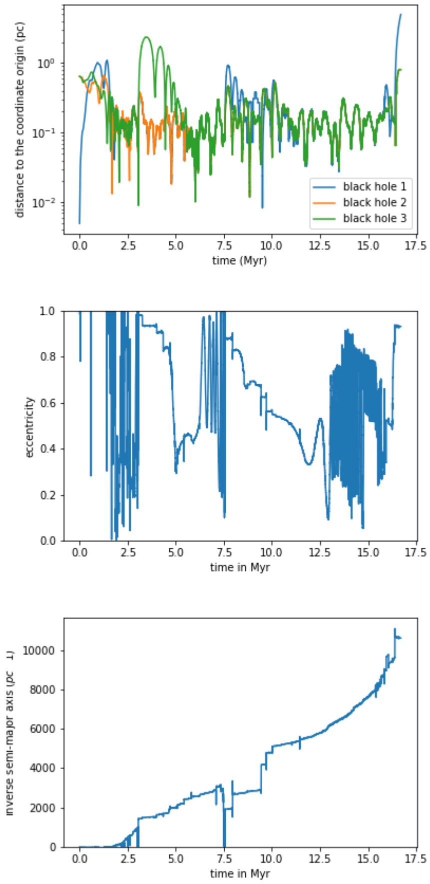

Figure 5.27: Evolution of inner binary black holes and cluster properties in simulation T.

Chapter 6

Conclusions

In this thesis, I have investigated the effect of a tertiary massive black hole (MBH) on the dynamical evolution of a binary MBH and how this interaction depends on the properties of the surrounding stellar environment. The aims of the study were to investigate: (I) the effect of a tertiary SMBH on the merger timescale of a binary SMBH in galaxy mergers; (II) how a tertiary IMBH influences the merger timescale of a binary IMBH in globular clusters and its effect on the surrounding stellar environment; and (III) how the hardening rate and merger timescale of a binary IMBH is influenced by the presence of a tertiary IMBH in different star cluster environments.

6.1 Supermassive black hole triplets in galaxy centers

In Chapter 3, we have investigated the effect of a tertiary SMBH on the GW-merger timescale of a binary SMBH in galaxy centers. Triple SMBHs have been observed or proposed in a number of galaxies, such as NGC 6240. Given sufficient time, two of the SMBHs will form a binary, shrink, and may ultimately merge. This process can be accelerated by the presence of a third SMBH, and the merger timescale may depend on the mass ratio of the triple SMBH and on the properties of the surrounding stellar population. Understanding the merger process involving a triple SMBH remains critical for understanding the evolutionary process of galaxies. We use N-body simulations to study the dynamical evolution of triple SMBHs in galactic centers with a range of initial SMBH masses. We find that both the binary exchange frequency and the merger timescale depend strongly on the mass ratio of the SMBH triplet. A more massive tertiary SMBH can shorten the merger timescale of binary SMBH via two mechanisms: (i) a third SMBH gravitationally bound to the binary SMBH may force the binary SMBH to wander in the galactic center and enhances the hardening rate by further driving inner binary to interact with surrounding stars, and (ii) repeated dynamical interactions between the tertiary SMBH and the inner binary results in repeated hardening of the inner binary, cause the semi-major axis to shrink abruptly. In our simulations, the Kozai resonance does not play an important role in increasing the eccentricity of the inner binary.

6.2 Intermediate-mass black hole triplets in star clusters

Hubble Space Telescope observations suggest the existence of potential merged star clusters in certain galaxies. If each star cluster holds an intermediate-mass black hole (IMBH) in its center, the formation and merger of a bound binary IMBH as their host cluster merge are inevitable. During this process, a third IMBH may move toward the binary, forming a triple system. The effect of a tertiary IMBH on the merge timescale of binary IMBH is unknown. In Chapter 4, we perform a study of the dynamical evolution of IMBH triplets in realistic merged clusters and their impact on the cluster properties, using direct N-body simulations. Stellar evolution, tidal field, and initial mass function were incorporated. We find that in most of our cases, one or two IMBHs escape from the cluster. Positive correlations exist between escape velocity at infinity and combined mass ratio q, instantaneous escape velocity, and central stellar mass density. The ejection of one of the IMBHs results in a shallower stellar density cusp. The ejected IMBH may also enlarge the outer region of the cluster. In some simulations, expansion occurs at the end of the simulation after the cluster fills its Roche Lobe. The gravitational wave merger timescale of a binary IMBH shows no apparent correlation with the mass of a tertiary IMBH. This lack of correlation between the gravitational wave merger timescale and the mass of a tertiary IMBH probably originates from the very early ejection of the tertiary IMBH from the cluster center.

6.3 Intermediate-mass black holes in different environments

Globular clusters are often modeled as non-rotating, spherical systems. However, the utilization of advanced detectors, such as Gaia, and modern data processing tools has proved that classically non-rotating globular clusters are indeed rotating, allowing the revelation of global rotation and individual star motion (Vasiliev 2019). It is believed that some globular clusters may host IMBHs in their center. This includes, for example, G1 in the Andromeda galaxy (Kong et al. 2010, Pooley & Rappaport 2006, Ulvestad, Greene, & Ho 2007), and 47 Tucanae in the Milky Way. According to Hubble Space Telescope observations, globular clusters rapidly merge after their formation in starburst regions such as M51, the Antennae galaxy, and Arp 220 (Freire et al. 2017, Kızıltan, Baumgardt, & Loeb 2017, Ridolfi et al. 2016). Chapter 5 investigated the dynamical evolution of IMBH triplet in rotating globular clusters with different degrees of rotation, central concentration, and mass function. We draw the following conclusions from this study. (1) Globular clusters with an initial rotation experience more violent relaxation. Higher degrees of rotation accelerates the violent relaxation process. (2) The mass segregation process accelerates the process of violent relaxation in globular clusters. (3) The hardening rate of the inner binary IMBH is higher when the initial central concentration (W_0) is larger. The hardening rate decreases with a higher degree of initial rotation (ω_0). The inclusion a stellar mass spectrum (IMF) may also speed up the hardening process. (4) The merger timescale of inner binary IMBH does not show a clear correlation with central concentration or degree of rotation. The inclusion of a stellar mass spectrum may increase the ejection rate, but there is no clear correlation between ejection rate, degree of rotation, and central concentration. (5) The presence of a bound tertiary IMBH can increase the hardening rate of the inner binary IMBH. This is analogous to the mechanism proposed by Blaes, Lee, & Socrates (2002). This mechanism is more effective than that of chaotic three-body interactions between the binary IMBH and an unbound tertiary IMBH because the exchange between the binary IMBH and an unbound tertiary IMBH did not cause an abrupt decrease in the semi-major axis.

6.4 Future work

Throughout the studies presented in this thesis, MBHs are assumed to be initially located at the center and at the half-mass radius of different stellar systems without gas. However, gas may be an important factor in driving the merge of binary SMBH. Our next study will introduce gas circumbinary disk to SMBH triplet and simulate more realistic triple AGNs. Another potential study will introduce Post-Newtonian correction to the evolution of the SMBH triplet system. This will lead to a better understanding of the effect of a tertiary SMBH on the merger timescale of binary SMBH during the final stages of the merger process.

Last but not least, a major step forward in understanding the evolution of IMBH triplets in globular clusters would be to extend our simulation to a smaller scale, such as 10^{-7} pc with the combination of ARCHAIN and other numerical relativity code, when the gravitational wave emission itself becomes the dominant factor in the evolution of a black hole binary. This study predicts the existence of free-floating SMBHs and IMBHs, and provides insight to the observation of triple AGN and IMBH subsystems in globular clusters. For example, van Dokkum et al. (2023) proves the existence of a wandering SMBH with a high velocity. Our simulations suggest that such SMBHs may be more common than we thought. The observations of HLX-1 and M82 X-1 suggest that it is possible to have free-floating IMBHs wandering in galaxies, in agreement with our findings in Chapter 4 (Farrell et al. 2009, Feng & Kaaret 2010).

Bibliography

Aarseth S. J., 1963, MNRAS, 126, 223. doi:10.1093/mnras/126.3.223

Aarseth S. J., Zare K., 1974, CeMec, 10, 185. doi:10.1007/BF01227619

Aarseth S. J., 1985, Multiple Time Scales. Academic Press, Cambridge, MA, p. 442

Aarseth S. J., 1999, CeMDA, 73, 127. doi:10.1023/A:1008390828807

Aarseth S. J., 1999, PASP, 111, 1333. doi:10.1086/316455

Aarseth S. J., 2003, Gravitational N-Body Simulations. Cambridge Univ. Press, Cambridge, UK, p. 430

Aarseth S. J., Henon M., Wielen R., 1974, A&A, 37, 183

Aarseth S. J., Tout C. A., Mardling R. A., 2008, LNP. doi:10.1007/978-1-4020-8431-7

Abbott D. C., 1982, ApJ, 259, 282. doi:10.1086/160166

Abbott B. P., Abbott R., Abbott T. D., Abernathy M. R., Acernese F., Ackley K., Adams C., et al., 2016, PhRvL, 116, 061102. doi:10.1103/PhysRevLett.116.061102

Abbott B. P., Abbott R., Abbott T. D., Abernathy M. R., Acernese F., Ackley K., Adams C., et al., 2016, PhRvL, 116, 241103. doi:10.1103/PhysRevLett.116.241103

Abbott B. P., Abbott R., Abbott T. D., Acernese F., Ackley K., Adams C., Adams T., et al., 2017, PhRvL, 119, 161101. doi:10.1103/PhysRevLett.119.161101

Abbott B. P., Abbott R., Abbott T. D., Acernese F., Ackley K., Adams C., Adams T., et al., 2017, ApJL, 851, L35. doi:10.3847/2041-8213/aa9f0c

Abbott B. P., Abbott R., Abbott T. D., Acernese F., Ackley K., Adams C., Adams T., et al., 2017, PhRvL, 118, 221101. doi:10.1103/PhysRevLett.118.221101

Abbott B. P., Abbott R., Abbott T. D., Acernese F., Ackley K., Adams C., Adams T., et al., 2017, PhRvL, 119, 141101. doi:10.1103/PhysRevLett.119.141101

Abbott B. P., Abbott R., Abbott T. D., Abraham S., Acernese F., Ackley K., Adams C., et al., 2019, ApJL, 882, L24. doi:10.3847/2041-8213/ab3800

Abbott R., Abbott T. D., Abraham S., Acernese F., Ackley K., Adams C., Adhikari R. X., et al., 2020, PhRvD, 102, 043015. doi:10.1103/PhysRevD.102.043015

Abbott R., Abbott T. D., Abraham S., Acernese F., Ackley K., Adams C., Adhikari R. X., et al., 2020, PhRvL, 125, 101102. doi:10.1103/PhysRevLett.125.101102

Abbott B. P., Abbott R., Abbott T. D., Abraham S., Acernese F., Ackley K., Adams C., et al., 2020, ApJL, 892, L3. doi:10.3847/2041-8213/ab75f5

Abbott R., Abbott T. D., Abraham S., Acernese F., Ackley K., Adams C., Adhikari R. X., et al., 2020, ApJL, 896, L44. doi:10.3847/2041-8213/ab960f

Abbott R., Abbott T. D., Abraham S., Acernese F., Ackley K., Adams C., Adhikari R. X., et al., 2020, ApJL, 900, L13. doi:10.3847/2041-8213/aba493

Abbott R., Abbott T. D., Abraham S., Acernese F., Ackley K., Adams A., Adams C., et al., 2021, ApJL, 915, L5. doi:10.3847/2041-8213/ac082e

Ahmad A., Cohen L., 1973, JCoPh, 12, 389. doi:10.1016/0021-9991(73)90160-5

Akiyama K., Sugimoto D., 1989, PASJ, 41, 991

Amaro-Seoane P., 2006, AIPC, 873, 250. doi:10.1063/1.2405051

Amaro-Seoane P., Freitag M., 2006, ApJL, 653, L53. doi:10.1086/510405

Amaro-Seoane P., Sesana A., Hoffman L., Benacquista M., Eichhorn C., Makino J., Spurzem R., 2010, MNRAS, 402, 2308. doi:10.1111/j.1365-2966.2009.16104.x

Amaro-Seoane P., Audley H., Babak S., Baker J., Barausse E., Bender P., Berti E., et al., 2017, arXiv, arXiv:1702.00786

Antonov V. A., 1961, SvA, 4, 859

Antognini J. M. O., 2015, MNRAS, 452, 3610. doi:10.1093/mnras/stv1552

Arp H., 1966, Atlas of Peculiar Galaxies. California Institute of Technology, Pasadena, CA

Ashman K. M., Zepf S. E., 1992, ApJ, 384, 50. doi:10.1086/170850

Banerjee S., Belczynski K., Fryer C. L., Berczik P., Hurley J. R., Spurzem R., Wang L., 2020, A&A, 639, A41. doi:10.1051/0004-6361/201935332

Barth A. J., Martini P., Nelson C. H., Ho L. C., 2003, ApJL, 594, L95. doi:10.1086/378735

Baumgardt H., 2001, MNRAS, 325, 1323. doi:10.1046/j.1365-8711.2001.04272.x

Begelman M. C., Blandford R. D., Rees M. J., 1980, Natur, 287, 307

Belczynski K., Kalogera V., Rasio F. A., Taam R. E., Zezas A., Bulik T., Maccarone T. J., et al., 2008, ApJS, 174, 223. doi:10.1086/521026

Belczynski K., Bulik T., Fryer C. L., Ruiter A., Valsecchi F., Vink J. S., Hurley J. R., 2010, ApJ, 714, 1217. doi:10.1088/0004-637X/714/2/1217

Belczynski K., Heger A., Gladysz W., Ruiter A. J., Woosley S., Wiktorowicz G., Chen H.-Y., et al., 2016, A&A, 594, A97. doi:37.037.1051/0004-6361/201628980

Belczynski K., 2020, ApJL, 905, L15. doi:10.3847/2041-8213/abcbf1

Bellovary J. M., Cleary C. E., Munshi F., Tremmel M., Christensen C. R., Brooks A., Quinn T. R., 2019, MNRAS, 482, 2913. doi:10.1093/mnras/sty2842

Berczik P., Merritt D., Spurzem R., 2005, ApJ, 633, 680. doi:10.1086/491598

Berczik P., Merritt D., Spurzem R., Bischof H.-P., 2006, ApJL, 642, L21. doi:10.1086/504426

Berczik P., Nitadori K., Zhong S., Spurzem R., Hamada T., Wang X., Berentzen I., et al., 2011, hpc..conf, 8

Binney J., Tremaine S., 1987, Galactic Dynamics. Princeton Univ. Press, Princeton

Binney J., Tremaine S., 2008, Galactic Dynamics, 2nd edn. Princeton Univ. Press, Princeton, NJ

Blaes O., Lee M. H., Socrates A., 2002, ApJ, 578, 775. doi:10.1086/342655

Bon E., Jovanović P., Marziani P., Shapovalova A. I., Bon N., Borka Jovanović V., Borka D., et al., 2012, ApJ, 759, 118. doi:10.1088/0004-637X/759/2/118

Bonetti M., Haardt F., Sesana A., Barausse E., 2016, MNRAS, 461, 4419. doi:10.1093/mnras/stw1590

Bonetti M., Haardt F., Sesana A., Barausse E., 2018, MNRAS, 477, 3910. doi:10.1093/mnras/sty896

Bonetti M., Sesana A., Barausse E., Haardt F., 2018, MNRAS, 477, 2599. doi:10.1093/mnras/sty874

Bonetti M., Sesana A., Haardt F., Barausse E., Colpi M., 2019, MNRAS, 486, 4044. doi:10.1093/mnras/stz903

Bonetti M., Rasskazov A., Sesana A., Dotti M., Haardt F., Leigh N. W. C., Arca Sedda M., et al., 2020, MNRAS, 493, L114. doi:10.1093/mnrasl/slaa018

Boroson T. A., Lauer T. R., 2009, Natur, 458, 53. doi:10.1038/nature07779

Bortolas E., Gualandris A., Dotti M., Spera M., Mapelli M., 2016, MNRAS, 461, 1023. doi:10.1093/mnras/stw1372

Bruzual A. G., 2010, RSPTA, 368, 783. doi:10.1098/rsta.2009.0258

Cackett E. M., Bentz M. C., Kara E., 2021, iSci, 24, 102557. doi:10.1016/j.isci.2021.102557

Bruzual A. G., 2010, IAUS, 262, 55. doi:10.1017/S1743921310002528

Casares J., 2007, IAUS, 238, 3. doi:10.1017/S1743921307004590

Casertano S., Hut P., 1985, ApJ, 298, 80. doi:10.1086/163589

Cervantes-Cota J., Galindo-Uribarri S., Smoot G., 2016, Univ, 2, 22. doi:10.3390/universe2030022

Chatterjee P., Hernquist L., Loeb A., 2003, ApJ, 592, 32. doi:10.1086/375552

Chen X., Sesana A., Madau P., Liu F. K., 2011, ApJ, 729, 13. doi:10.1088/0004-637X/729/1/13

Chandrasekhar S., 1943, ApJ, 97, 255. doi:10.1086/144517

Cohn H., 1979, ApJ, 234, 1036. doi:10.1086/157587

Cohn H., 1980, ApJ, 242, 765. doi:10.1086/158511

Cuadra J., Armitage P. J., Alexander R. D., Begelman M. C., 2009, MNRAS, 393, 1423. doi:10.1111/j.1365-2966.2008.14147.x

Cuntz M., Wang Z., 2018, RNAAS, 2, 19. doi:10.3847/2515-5172/aaaa67

Davidson K., Netzer H., 1979, RvMP, 51, 715. doi:10.1103/RevModPhys.51.715

Dahal P. K., 2020, JApA, 41, 8. doi:10.1007/s12036-020-9625-y

de Laplace P. S., Harte H. H., 1830, sywo.book

Deane R. P., Paragi Z., Jarvis M. J., Coriat M., Bernardi G., Fender R. P., Frey S., et al., 2014, Natur, 511, 57. doi:10.1038/nature13454

Di Carlo U. N., Mapelli M., Pasquato M., Rastello S., Ballone A., Dall'Amico M., Giacobbo N., et al., 2021, MNRAS, 507, 5132. doi:10.1093/mnras/stab2390

Dietrich M., Hamann F., Shields J. C., Constantin A., Vestergaard M., Chaffee F., Foltz C. B., et al., 2002, ApJ, 581, 912. doi:10.1086/344410

Dotti M., Colpi M., Haardt F., Mayer L., 2007, MNRAS, 379, 956. doi:10.1111/j.1365-2966.2007.12010.x

Dubois Y., Volonteri M., Silk J., Devriendt J., Slyz A., Teyssier R., 2015, MNRAS, 452, 1502. doi:10.1093/mnras/stv1416

Duric N., 2003, Advanced Astrophysics. Cambridge University Press, Cambridge

Einsel C., Spurzem R., 1999, MNRAS, 302, 81. doi:10.1046/j.1365-8711.1999.02083.x

Einstein A., 1916, AnP, 354, 769. doi:10.1002/andp.19163540702

Einstein A., 1916, SPAW, 688

Ebisuzaki T., Makino J., Okumura S. K., 1991, Natur, 354, 212. doi:10.1038/354212a0

eLISA Consortium, Amaro Seoane P., Aoudia S., Audley H., Auger G., Babak S., Baker J., et al., 2013, arXiv, arXiv:1305.5720

Elmegreen B. G., Efremov Y. N., 1997, ApJ, 480, 235. doi:10.1086/303966

Escala A., Larson R. B., Coppi P. S., Mardones D., 2004, ApJ, 607, 765. doi:10.1086/386278

Escala A., Larson R. B., Coppi P. S., Mardones D., 2005, ApJ, 630, 152. doi:10.1086/431747

Event Horizon Telescope Collaboration, Akiyama K., Alberdi A., Alef W., Asada K., Azulay R., Baczko A.-K., et al., 2019, ApJL, 875, L1. doi:10.3847/2041-8213/ab0ec7

Event Horizon Telescope Collaboration, Akiyama K., Alberdi A., Alef W., Asada K., Azulay R., Baczko A.-K., et al., 2019, ApJL, 875, L5. doi:10.3847/2041-8213/ab0f43

Fabbiano G., Wang J., Elvis M., Risaliti G., 2011, Natur, 477, 431. doi:10.1038/nature10364

Fan X., 2006, NewAR, 50, 665. doi:10.1016/j.newar.2006.06.077

Farrell S. A., Webb N. A., Barret D., Godet O., Rodrigues J. M., 2009, Natur, 460, 73. doi:10.1038/nature08083

Farrell S. A., Servillat M., Gladstone J. C., Webb N. A., Soria R., Maccarone T. J., Wiersema K., et al., 2014, MNRAS, 437, 1208. doi:10.1093/mnras/stt1924

Feng H., Kaaret P., 2010, ApJL, 712, L169. doi:10.1088/2041-8205/712/2/L169

Fiestas J., Spurzem R., Kim E., 2006, MNRAS, 373, 677. doi:10.1111/j.1365-2966.2006.11036.x

Foord A., Gültekin K., Runnoe J. C., Koss M. J., 2021, ApJ, 907, 72. doi:10.3847/1538-4357/abce5e

Freitag M., Gürkan M. A., Rasio F. A., 2006, MNRAS, 368, 141. doi:10.1111/j.1365-2966.2006.10096.x

Ferland G. J., Mushotzky R. F., 1982, ApJ, 262, 564. doi:10.1086/160448

Freire P. C. C., Ridolfi A., Kramer M., Jordan C., Manchester R. N., Torne P., Sarkissian J., et al., 2017, MNRAS, 471, 857. doi:10.1093/mnras/stx1533

Fryer C. L., Woosley S. E., Heger A., 2001, ApJ, 550, 372. doi:10.1086/319719

Fryer C. L., Belczynski K., Wiktorowicz G., Dominik M., Kalogera V., Holz D. E., 2012, ApJ, 749, 91. doi:37.037.1088/0004-637X/749/1/91

Fukushige T., Ebisuzaki T., Makino J., 1992, PASJ, 44, 281

Fukushige T., Heggie D. C., 2000, MNRAS, 318, 753. doi:10.1046/j.1365-8711.2000.03811.x

Genzel R., Eisenhauer F., Gillessen S., 2010, RvMP, 82, 3121. doi:10.1103/RevModPhys.82.3121

Ghez A. M., Salim S., Weinberg N. N., Lu J. R., Do T., Dunn J. K., Matthews K., et al., 2008, ApJ, 689, 1044. doi:10.1086/592738

Giersz M., Heggie D. C., Hurley J. R., Hypki A., 2013, MNRAS, 431, 2184. doi:10.1093/mnras/stt307

Giersz M., Leigh N., Hypki A., Lützgendorf N., Askar A., 2015, MNRAS, 454, 3150. doi:10.1093/mnras/stv2162

Goodman J. J., 1983, PhD thesis, Princeton University, NJ

Gualandris A., Merritt D., 2008, ApJ, 678, 780. doi:10.1086/586877

Gültekin K., Richstone D. O., Gebhardt K., Lauer T. R., Tremaine S., Aller M. C., Bender R., et al., 2009, ApJ, 698, 198. doi:10.1088/0004-637X/698/1/198

Graham M. J., Djorgovski S. G., Stern D., Drake A. J., Mahabal A. A., Donalek C., Glikman E., et al., 2015, MNRAS, 453, 1562. doi:10.1093/mnras/stv1726

Greene J. E., Strader J., Ho L. C., 2020, ARA&A, 58, 257. doi:10.1146/annurev-astro-032620-021835

Gürkan M. A., Fregeau J. M., Rasio F. A., 2006, ApJL, 640, L39. doi:10.1086/503295

Haardt F., Gorini V., Moschella U., Treves A., Colpi M., 2016, LNP. doi:10.1007/978-3-319-19416-5

Hachisu I., 1979, PASJ, 31, 523

Haiman Z., 2013, ASSL, 396, 293. doi:10.1007/978-3-642-32362-1_6

Hansen C. J., Kawaler S. D., 1994, Stellar Interiors. Physical Principles, Structure, and Evolution. Springer-Verlag, Berlin Heidelberg doi:10.1007/978-1-4419-9110-2

Harfst S., Gualandris A., Merritt D., Spurzem R., Portegies Zwart S., Berczik P., 2007, NewA, 12, 357. doi:10.1016/j.newast.2006.11.003

Hawking S. W., Israel W., 1989, Three Hundred Years of Gravitation. Cambridge University Press, Cambridge

Hayashi C., 1961, PASJ, 13, 450

Heckman T. M., Best P. N., 2014, ARA&A, 52, 589. doi:10.1146/annurev-astro-081913-035722

Heger A., Fryer C. L., Woosley S. E., Langer N., Hartmann D. H., 2003, ApJ, 591, 288. doi:10.1086/375341

Heggie D. C., Mathieu R. D., 1986, LNP, 267, 233, LNP...267

Heggie D., Hut P., 2003, The Gravitational Million-Body Problem: A Multidisciplinary Approach To Star Cluster Dynamics. Cambridge Univ. Press, Cambridge

Hénon M. H., 1971, Ap&SS, 14, 151. doi:10.1007/BF00649201

Henyey L. G., Lelevier R., Levée R. D., 1955, PASP, 67, 154. doi:10.1086/126791

Henyey L. G., Wilets L., Böhm K. H., Lelevier R., Levee R. D., 1959, ApJ, 129, 628. doi:10.1086/146661

Hobbs G., Lorimer D. R., Lyne A. G., Kramer M., 2005, MNRAS, 360, 974. doi:10.1111/j.1365-2966.2005.09087.x

Hoffman L., Loeb A., 2007, MNRAS, 377, 957. doi:10.1111/j.1365-2966.2007.11694.x

Holley-Bockelmann K., Sigurdsson S., 2006, arXiv, astro-ph/0601520

Holley-Bockelmann K., Khan F. M., 2015, ApJ, 810, 139. doi:10.1088/0004-637X/810/2/139

Holman M., Touma J., Tremaine S., 1997, Natur, 386, 254. doi:10.1038/386254a0

Holmberg E., 1941, ApJ, 94, 385. doi:10.1086/144344

Hulse R. A., Taylor J. H., 1975, ApJL, 195, L51. doi:10.1086/181708

Hurley J. R., Pols O. R., Tout C. A., 2000, MNRAS, 315, 543. doi:10.1046/j.1365-8711.2000.03426.x

Hurley J. R., Tout C. A., Pols O. R., 2002, MNRAS, 329, 897. doi:10.1046/j.1365-8711.2002.05038.x

Inagaki S., Hachisu I., 1978, PASJ, 30, 39

Inayoshi K., Visbal E., Haiman Z., 2020, ARA&A, 58, 27. doi:10.1146/annurev-astro-120419-014455

Iwasawa M., Funato Y., Makino J., 2006, ApJ, 651, 1059

Iwasawa M., Funato Y., Makino J., 2008, arXiv, arXiv:0801.0859

Iwasawa M., An S., Matsubayashi T., Funato Y., Makino J., 2011, ApJL, 731, L9. doi:10.1088/2041-8205/731/1/L9

Joshi K. J., Rasio F. A., Portegies Zwart S., 2000, ApJ, 540, 969. doi:10.1086/309350

Kamlah A. W. H., Leveque A., Spurzem R., Arca Sedda M., Askar A., Banerjee S., Berczik P., et al., 2022, MNRAS, 511, 4060. doi:10.1093/mnras/stab3748

Kamlah A. W. H., Spurzem R., Berczik P., Sedda M. A., Flammini Dotti F., Neumayer N., Pang X., et al., 2022, MNRAS, 516, 3266. doi:10.1093/mnras/stac2281

Kahn F. D., Woltjer L., 1959, ApJ, 130, 705. doi:10.1086/146762

Kauffmann G., Haehnelt M., 2000, MNRAS, 311, 576. doi:10.1046/j.1365-8711.2000.03077.x

Kaspi S., Brandt W. N., Maoz D., Netzer H., Schneider D. P., Shemmer O., 2007, ApJ, 659, 997. doi:10.1086/512094

Kerr R. P., 1963, PhRvL, 11, 237. doi:10.1103/PhysRevLett.11.237

Kerr F. J., Lynden-Bell D., 1986, MNRAS, 221, 1023. doi:10.1093/mnras/221.4.1023

Khan F. M., Preto M., Berczik P., Berentzen I., Just A., Spurzem R., 2012, ApJ, 749, 147. doi:10.1088/0004-637X/749/2/147

Khan F. M., Berentzen I., Berczik P., Just A., Mayer L., Nitadori K., Callegari S., 2012, ApJ, 756, 30. doi:10.1088/0004-637X/756/1/30

Khan F. M., Holley-Bockelmann K., Berczik P., Just A., 2013, ApJ, 773, 100. doi:10.1088/0004-637X/773/2/100

Khan F. M., Berczik P., Just A., 2018, A&A, 615, A71. doi:10.1051/0004-6361/201730489

Khan F. M., Holley-Bockelmann K., 2021, MNRAS, 508, 1174. doi:10.1093/mnras/stab2646

Khan F. M., Holley-Bockelmann K., Berczik P., 2015, ApJ, 798, 103. doi:10.1088/0004-637X/798/2/103

Khan F. M., Just A., Merritt D., 2011, ApJ, 732, 89. doi:10.1088/0004-637X/732/2/89

Kharb P., Lal D. V., Merritt D., 2017, NatAs, 1, 727. doi:10.1038/s41550-017-0256-4

King I. R., 1966, AJ, 71, 64. doi:10.1086/109857

Kızıltan B., Baumgardt H., Loeb A., 2017, Natur, 542, 203. doi:10.1038/nature21361

Kochanek C. S., 1992, ApJ, 385, 604. doi:10.1086/170966

Koliopanos F., 2017, Proc. Sci., XII Multifrequency Behaviour of High Energy Cosmic Sources Workshop (MULTIF2017). SISSA, Trieste, PoS#051

Kollatschny W., Weilbacher P. M., Ochmann M. W., Chelouche D., Monreal-Ibero A., Bacon R., Contini T., 2020, A&A, 633, A79

Kollmeier J. A., Onken C. A., Kochanek C. S., Gould A., Weinberg D. H., Dietrich M., Cool R., et al., 2006, ApJ, 648, 128. doi:10.1086/505646

Komossa S., 2006, MmSAI, 77, 733

Kong A. K. H., Heinke C. O., di Stefano R., Cohn H. N., Lugger P. M., Barmby P., Lewin W. H. G., et al., 2010, MNRAS, 407, L84.

Kormendy J., Richstone D., 1995, ARA&A, 33, 581. doi:10.1146/annurev.aa.33.090195.003053

Kormendy J., Fisher D. B., Cornell M. E., Bender R., 2009, ApJS, 182, 216. doi:10.1088/0067-0049/182/1/216

Kormendy J., Ho L. C., 2013, ARA&A, 51, 511. doi:10.1146/annurev-astro-082708-101811

Kozai Y., 1962, AJ, 67, 591. doi:10.1086/108790

Kroupa P., Tout C. A., Gilmore G., 1993, MNRAS, 262, 545. doi:10.1093/mnras/262.3.545

Kroupa P., 2001, MNRAS, 322, 231. doi:10.1046/j.1365-8711.2001.04022.x

Kroupa P., 2008, LNP, 181. doi:10.1007/978-1-4020-8431-7_8

Kroupa P., Jerabkova T., 2019, NatAs, 3, 482. doi:10.1038/s41550-019-0793-0

Kumar S. S., 1962, AJ, 67, 579. doi:10.1086/108658

Küpper A. H. W., Maschberger T., Kroupa P., Baumgardt H., 2011, MNRAS, 417, 2300. doi:10.1111/j.1365-2966.2011.19412.x

Kustaanheimo P., Stiefel E., 1965, J. Reine Angew. Math., 10.1515/crll.1965.218.204, 218, 204

Larson R. B., 1970, MNRAS, 147, 323. doi:10.1093/mnras/147.4.323

Laor A., 1998, ApJL, 505, L83. doi:10.1086/311619

Lehto H. J., Valtonen M. J., 1996, ApJ, 460, 207. doi:10.1086/176962

Li Y.-R., Wang J.-M., Ho L. C., Lu K.-X., Qiu J., Du P., Hu C., et al., 2016, ApJ, 822, 4. doi:10.3847/0004-637X/822/1/4

Li Y.-R., Wang J.-M., Zhang Z.-X., Wang K., Huang Y.-K., Lu K.-X., Hu C., et al., 2019, ApJS, 241, 33. doi:10.3847/1538-4365/ab0ec5

Lidov M. L., 1962, P&SS, 9, 719. doi:10.1016/0032-0633(62)90129-0

Livernois A. R., Vesperini E., Varri A. L., Hong J., Tiongco M., 2022, MNRAS, 512, 2584. doi:10.1093/mnras/stac651

Liu B., Bromm V., 2020, ApJL, 903, L40. doi:10.3847/2041-8213/abc552

Liu F. K., Wu X.-B., Cao S. L., 2003, MNRAS, 340, 411. doi:10.1046/j.1365-8711.2003.06235.x

Lodato G., Nayakshin S., King A. R., Pringle J. E., 2009, MNRAS, 398, 1392. doi:10.1111/j.1365-2966.2009.15179.x

Lousto C. O., Campanelli M., Zlochower Y., Nakano H., 2010, CQGra, 27, 114006. doi:10.1088/0264-9381/27/11/114006

Lupton R. H., Gunn J. E., Griffin R. F., 1987, AJ, 93, 1114. doi:10.1086/114395

Lützgendorf N., Kissler-Patig M., Neumayer N., Baumgardt H., Noyola E., de Zeeuw P. T., Gebhardt K., et al., 2013, A&A, 555, A26. doi:10.1051/0004-6361/201321183

Luo J., Chen L.-S., Duan H.-Z., Gong Y.-G., Hu S., Ji J., Liu Q., et al., 2016, CQGra, 33, 035010. doi:10.1088/0264-9381/33/3/035010

Lynden-Bell D., 1967, MNRAS, 136, 101. doi:10.1093/mnras/136.1.101

Lynden-Bell D., Wood R., 1968, MNRAS, 138, 495. doi:10.1093/mnras/138.4.495

Lynden-Bell D., 1969, Natur, 223, 690. doi:10.1038/223690a0

Madau P., Rees M. J., 2001, ApJL, 551, L27. doi:10.1086/319848

Makino J., Aarseth S. J., 1992, PASJ, 44, 141

Makino J., Ebisuzaki T., 1994, ApJ, 436, 607. doi:10.1086/174935

Makino J., Funato Y., 2004, ApJ, 602, 93. doi:10.1086/380917

Makino J., Hut P., 1988, ApJS, 68, 833. doi:10.1086/191306

Makino J., Fukushige T., Okumura S. K., Ebisuzaki T., 1993, PASJ, 45, 303

Maness H. L., Taylor G. B., Zavala R. T., Peck A. B., Pollack L. K., 2004, ApJ, 602, 123. doi:10.1086/380919

Mapelli M., 2016, MNRAS, 459, 3432. doi:10.1093/mnras/stw869

Mapelli M., Santoliquido F., Bouffanais Y., Arca Sedda M. A., Artale M. C., Ballone A., 2021, Symm, 13, 1678. doi:10.3390/sym13091678

Mapelli M., Dall'Amico M., Bouffanais Y., Giacobbo N., Arca Sedda M., Artale M. C., Ballone A., et al., 2021, MNRAS, 505, 339. doi:10.1093/mnras/stab1334

Matsui H., Habe A., 2009, PASJ, 61, 421. doi:10.1093/pasj/61.3.421

Mayer L., Kazantzidis S., Madau P., Colpi M., Quinn T., Wadsley J., 2007, Sci, 316, 1874. doi:10.1126/science.1141858

Mazzali P. A., Röpke F. K., Benetti S., Hillebrandt W., 2007, Sci, 315, 825. doi:10.1126/science.1136259

McLure R. J., Jarvis M. J., 2002, MNRAS, 337, 109. doi:10.1046/j.1365-8711.2002.05871.x

McMillan S., Baumgardt H., Portegies Zwart S., Hut P., Makino J., 2004, ASPC, 322, 449

Merritt D., Poon M. Y., 2004, ApJ, 606, 788. doi:10.1086/382497

Merritt D., 2013, CQGra, 30, 244005. doi:10.1088/0264-9381/30/24/244005

Michell J., 1784, RSPT, 74, 35

Miholics M., Webb J. J., Sills A., 2016, MNRAS, 456, 240. doi:10.1093/mnras/stv2680

Mikkola S., Aarseth S. J., 1990, CeMDA, 47, 375

Mikkola S., Aarseth S. J., 1993, CeMDA, 57, 439. doi:10.1007/BF00695714

Mikkola S., Aarseth S. J., 1996, CeMDA, 64, 197. doi:10.1007/BF00728347

Mikkola S., Aarseth S. J., 1998, NewA, 3, 309. doi:10.1016/S1384-1076(98)00018-9

Mikkola S., Valtonen M. J., 1990, ApJ, 348, 412. doi:10.1086/168250

Miller M. C., Hamilton D. P., 2002, MNRAS, 330, 232. doi:10.1046/j.1365-8711.2002.05112.x

Miller G. E., Scalo J. M., 1979, ApJS, 41, 513. doi:10.1086/190629

Milosavljević M., Merritt D., 2001, ApJ, 563, 34. doi:10.1086/323830

Milosavljević M., Merritt D., 2003, AIPC, 686, 201. doi:10.1063/1.1629432

Mirza M. A., Tahir A., Khan F. M., Holley-Bockelmann H., Baig A. M., Berczik P., Chishtie F., 2017, MNRAS, 470, 940. doi:10.1093/mnras/stx1248

Naab T., Khochfar S., Burkert A., 2006, ApJL, 636, L81. doi:10.1086/500205

Nitadori K., Aarseth S. J., 2012, MNRAS, 424, 545. doi:10.1111/j.1365-2966.2012.21227.x

Padmanabhan T., 1990, PhR, 188, 285. doi:10.1016/0370-1573(90)90051-3

Portegies Zwart S. F., McMillan S. L. W., 2000, ApJL, 528, L17. doi:10.1086/312422

Sahu K. C., Anderson J., Casertano S., Bond H. E., Udalski A., Dominik M., Calamida A., et al., 2022, arXiv, arXiv:2201.13296

Salaris M., Cassisi S., 2006, Evolution of Stars and Stellar Populations. Wiley-VCH, Chichester, UK

Sigurdsson S., Phinney E. S., 1993, ApJ, 415, 631. doi:10.1086/173190

Soderhjelm S., 1984, A&A, 141, 232

Tamfal T., Capelo P. R., Kazantzidis S., Mayer L., Potter D., Stadel J., Widrow L. M., 2018, ApJL, 864, L19. doi:37.037.3847/2041-8213/aada4b

Tiongco M. A., Vesperini E., Varri A. L., 2022, MNRAS, 512, 1584. doi:10.1093/mnras/stac643

Newman E. T., Couch E., Chinnapared K., Exton A., Prakash A., Torrence R., 1965, JMP, 6, 918. doi:10.1063/1.1704351

Nordström G., 1918, KNAB, 20, 1238

Norman C., Silk J., 1983, ApJ, 266, 502. doi:10.1086/160798

Oppenheimer J. R., Volkoff G. M., 1939, PhRv, 55, 374. doi:10.1103/PhysRev.55.374

Özel F., Psaltis D., Narayan R., McClintock J. E., 2010, ApJ, 725, 1918. doi:10.1088/0004-637X/725/2/1918

Palla F., 2012, AIPC, 1480, 22. doi:10.1063/1.4754323

Parma P., Ekers R. D., Fanti R., 1985, A&AS, 59, 511

Pechetti R., Seth A., Kamann S., Caldwell N., Strader J., den Brok M., Luetzgendorf N., et al., 2022, ApJ, 924, 48. doi:10.3847/1538-4357/ac339f

Penrose R., 1996, JApA, 17, 213. doi:10.1007/BF02702305

Peterson B. M., 1993, PASP, 105, 247. doi:10.1086/133140

Peterson B. M., Wandel A., 1999, ApJL, 521, L95. doi:10.1086/312190

Pfeifle R. W., Satyapal S., Manzano-King C., Cann J., Sexton R. O., Rothberg B., Canalizo G., et al., 2019, ApJ, 883, 167. doi:10.3847/1538-4357/ab3a9b

Plummer H. C., 1911, MNRAS, 71, 460

Perets H. B., Alexander T., 2008, ApJ, 677, 146. doi:10.1086/527525

Preto M., Berentzen I., Berczik P., Spurzem R., 2011, ApJL, 732, L26. doi:10.1088/2041-8205/732/2/L26

Preto M., Berentzen I., Berczik P., Merritt D., Spurzem R., 2009, JPhCS, 154, 012049. doi:10.1088/1742-6596/154/1/012049

Pooley D., Rappaport S., 2006, ApJL, 644, L45. doi:10.1086/505344

Poon M. Y., Merritt D., 2001, ApJ, 549, 192. doi:10.1086/319060

Portegies Zwart S. F., Baumgardt H., Hut P., Makino J., McMillan S. L. W., 2004, Natur, 428, 724. doi:10.1038/nature02448

Quinlan G. D., 1996, NewA, 1, 35. doi:10.1016/S1384-1076(96)00003-6

Rasskazov A., Merritt D., 2017, ApJ, 837, 135. doi:10.3847/1538-4357/aa6188

Rasskazov A., Kocsis B., 2019, ApJ, 881, 20. doi:10.3847/1538-4357/ab2c74

Reinoso B., Schleicher D. R. G., Fellhauer M., Klessen R. S., Boekholt T. C. N., 2018, A&A, 614, A14. doi:10.1051/0004-6361/201732224

Reissner H., 1916, AnP, 355, 106. doi:10.1002/andp.19163550905

Renaud F., Gieles M., 2015, MNRAS, 448, 3416. doi:10.1093/mnras/stv245

Renaud F., Gieles M., Boily C. M., 2011, MNRAS, 418, 759. doi:10.1111/j.1365-2966.2011.19531.x

Renaud F., Gieles M., 2013, MNRAS, 431, L83. doi:10.1093/mnrasl/slt013

Ridolfi A., Freire P. C. C., Torne P., Heinke C. O., van den Berg M., Jordan C., Kramer M., et al., 2016, MNRAS, 462, 2918. doi:10.1093/mnras/stw1850

Rieger F. M., 2004, ApJL, 615, L5. doi:10.1086/426018

Rizzuto F. P., Naab T., Spurzem R., Giersz M., Ostriker J. P., Stone N. C., Wang L., et al., 2021, MNRAS, 501, 5257. doi:10.1093/mnras/staa3634

Rodriguez C., Taylor G. B., Zavala R. T., Peck A. B., Pollack L. K., Romani R. W., 2006, ApJ, 646, 49. doi:10.1086/504825

Roos N., 1988, ApJ, 334, 95. doi:10.1086/166820

Sesana A., Gualandris A., Dotti M., 2011, MNRAS, 415, L35. doi:10.1111/j.1745-3933.2011.01073.x

Roos N., Kaastra J. S., Hummel C. A., 1993, ApJ, 409, 130. doi:10.1086/172647

Ruan W.-H., Guo Z.-K., Cai R.-G., Zhang Y.-Z., 2020, IJMPA, 35, 2050075. doi:10.1142/S0217751X2050075X

Sahu K. C., Anderson J., Casertano S., Bond H. E., Udalski A., Dominik M., Calamida A., et al., 2022, ApJ, 933, 83. doi:10.3847/1538-4357/ac739e

Salpeter E. E., 1955, ApJ, 121, 161. doi:10.1086/145971

Salpeter E. E., 1964, ApJ, 140, 796. doi:10.1086/147973

Schiavi R., Capuzzo-Dolcetta R., Arca-Sedda M., Spera M., 2020, A&A, 642, A30. doi:10.1051/0004-6361/202038674

Schoenmakers A. P., de Bruyn A. G., Röttgering H. J. A., van der Laan H., Kaiser C. R., 2000, MNRAS, 315, 371. doi:10.1046/j.1365-8711.2000.03430.x

Schwarzschild K., 1999, arXiv, physics/9905030

Scoville N. Z., Evans A. S., Thompson R., Rieke M., Hines D. C., Low F. J., Dinshaw N., et al., 2000, AJ, 119, 991. doi:10.1086/301248

Scoville N. Z., Polletta M., Ewald S., Stolovy S. R., Thompson R., Rieke M., 2001, AJ, 122, 3017. doi:10.1086/323445

Sesana A., Haardt F., Madau P., 2006, ApJ, 651, 392. doi:10.1086/507596

Sesana A., Haardt F., Madau P., 2007, ApJ, 660, 546. doi:10.1086/513016

Sesana A., Haardt F., Madau P., 2008, ApJ, 686, 432. doi:10.1086/590651

Sesana A., Khan F. M., 2015, MNRAS, 454, L66. doi:10.1093/mnrasl/slv131

Sigurdsson S., Hernquist L., 1993, Natur, 364, 423. doi:10.1038/364423a0

Silk J., Rees M. J., 1998, A&A, 331, L1. doi:10.48550/arXiv.astro-ph/9801013

Sobolenko M., Berczik P., Spurzem R., 2021, A&A, 652, A134. doi:10.1051/0004-6361/202039859

Spitzer L., Hart M. H., 1971, ApJ, 164, 399. doi:10.1086/150855

Spitzer L., 1987, Dynamical evolution of globular clusters. Princeton University Press

Spurzem R., 1994, LNP, 170. doi:10.1007/BFb0058104

Spurzem R., 1996, IAUS, 174, 111

Spurzem R., 1999, JCoAM, 109, 407

Stahler S. W., Palla F., 2004, The Formation of stars. Wiley-VCH, Weinheim Germany

Straub O., Godet O., Webb N., Servillat M., Barret D., 2014, A&A, 569, A116. doi:10.1051/0004-6361/201423874

Takahashi K., 1995, PASJ, 47, 561

Tanikawa A., Kinugawa T., Yoshida T., Hijikawa K., Umeda H., 2021, MNRAS, 505, 2170. doi:10.1093/mnras/stab1421

Tremaine S., Gebhardt K., Bender R., Bower G., Dressler A., Faber S. M., Filippenko A. V., et al., 2002, ApJ, 574, 740. doi:10.1086/341002

Tout C. A., Aarseth S. J., Pols O. R., Eggleton P. P., 1997, MNRAS, 291, 732. doi:10.1093/mnras/291.4.732

Ulvestad J. S., Greene J. E., Ho L. C., 2007, ApJL, 661, L151. doi:10.1086/518784

Vanden Berk D. E., Wilhite B. C., Kron R. G., Anderson S. F., Brunner R. J., Hall P. B., Ivezić Ž., et al., 2004, ApJ, 601, 692. doi:10.1086/380563

van der Marel R. P., Fardal M. A., Sohn S. T., Patel E., Besla G., del Pino A., Sahlmann J., et al., 2019, ApJ, 872, 24. doi:10.3847/1538-4357/ab001b

van Dokkum P., Pasha I., Buzzo M. L., LaMassa S., Shen Z., Keim M. A., Abraham R., et al., 2023, ApJL, 946, L50. doi:10.3847/2041-8213/acba86

Valtonen M. J., Mikkola S., Heinamaki P., Valtonen H., 1994, ApJS, 95, 69. doi:10.1086/192094

Valtonen M. J., 1996, MNRAS, 278, 186. doi:10.1093/mnras/278.1.186

Valtonen M. J., Lehto H. J., Nilsson K., Heidt J., Takalo L. O., Sillanpää A., Villforth C., et al., 2008, Natur, 452, 851. doi:10.1038/nature06896

Varisco L., Bortolas E., Dotti M., Sesana A., 2021, MNRAS, 508, 1533. doi:10.1093/mnras/stab2649

Vasiliev E., Antonini F., Merritt D., 2014, ApJ, 785, 163. doi:10.1088/0004-637X/785/2/163

Vasiliev E., Antonini F., Merritt D., 2015, ApJ, 810, 49. doi:10.1088/0004-637X/810/1/49

Vasiliev E., 2014, CQGra, 31, 244002. doi:10.1088/0264-9381/31/24/244002

Vasiliev E., 2019, MNRAS, 489, 623. doi:10.1093/mnras/stz2100

Vestergaard M., 2002, ApJ, 571, 733. doi:10.1086/340045

Vestergaard M., 2004, ApJ, 601, 676. doi:10.1086/379758

Vestergaard M., Peterson B. M., 2006, ApJ, 641, 689. doi:10.1086/500572

Vink J. S., de Koter A., Lamers H. J. G. L. M., 2001, A&A, 369, 574. doi:10.1051/0004-6361:20010127

Volonteri M., 2010, A&ARv, 18, 279. doi:10.1007/s00159-010-0029-x

Volonteri M., Habouzit M., Colpi M., 2021, NatRP, 3, 732. doi:10.1038/s42254-021-00364-9

von Hoerner S., 1960, ZA, 50, 184

Wandel A., Peterson B. M., Malkan M. A., 1999, ApJ, 526, 579. doi:10.1086/308017

Wang L., Spurzem R., Aarseth S., Nitadori K., Berczik P., Kouwenhoven M. B. N., Naab T., 2015, MNRAS, 450, 4070

Wang J.-M., Li Y.-R., 2020, RAA, 20, 160. doi:10.1088/1674-4527/20/10/160

Weinstein G., 2016, arXiv, arXiv:1602.04040

Whitmore B. C., Chandar R., Schweizer F., Rothberg B., Leitherer C., Rieke M., Rieke G., et al., 2010, AJ, 140, 75. doi:10.1088/0004-6256/140/1/75

Wilson B., 2003, eaa..book, E5521. doi:10.1888/0333750888/5521

Wilson C. D., Harris W. E., Longden R., Scoville N. Z., 2006, ApJ, 641, 763. doi:10.1086/500577

Woosley S., Janka T., 2005, NatPh, 1, 147. doi:10.1038/nphys172

Yan C.-S., Lu Y., Dai X., Yu Q., 2015, ApJ, 809, 117. doi:10.1088/0004-637X/809/2/117

Yu Q., 2002, MNRAS, 331, 935. doi:10.1046/j.1365-8711.2002.05242.x

Zier C., 2005, MNRAS, 364, 583. doi:10.1111/j.1365-2966.2005.09586.x

Zhang Q., Fall S. M., Whitmore B. C., 2001, ApJ, 561, 727. doi:10.1086/322278

Zheng Z.-Y., Butler N. R., Shen Y., Jiang L., Wang J.-X., Chen X., Cuadra J., 2016, ApJ, 827, 56. doi:10.3847/0004-637X/827/1/56

Zwick L., Capelo P. R., Bortolas E., Mayer L., Amaro-Seoane P., 2020, MNRAS, 495, 2321. doi:10.1093/mnras/staa1314